

Springer Theses

Recognizing Outstanding Ph.D. Research

Jian Wang

QCD Higher-Order Effects and Search for New Physics

 Springer

Springer Theses

Recognizing Outstanding Ph.D. Research

Aims and Scope

The series “Springer Theses” brings together a selection of the very best Ph.D. theses from around the world and across the physical sciences. Nominated and endorsed by two recognized specialists, each published volume has been selected for its scientific excellence and the high impact of its contents for the pertinent field of research. For greater accessibility to non-specialists, the published versions include an extended introduction, as well as a foreword by the student’s supervisor explaining the special relevance of the work for the field. As a whole, the series will provide a valuable resource both for newcomers to the research fields described, and for other scientists seeking detailed background information on special questions. Finally, it provides an accredited documentation of the valuable contributions made by today’s younger generation of scientists.

Theses are accepted into the series by invited nomination only and must fulfill all of the following criteria

- They must be written in good English.
- The topic should fall within the confines of Chemistry, Physics, Earth Sciences, Engineering and related interdisciplinary fields such as Materials, Nanoscience, Chemical Engineering, Complex Systems and Biophysics.
- The work reported in the thesis must represent a significant scientific advance.
- If the thesis includes previously published material, permission to reproduce this must be gained from the respective copyright holder.
- They must have been examined and passed during the 12 months prior to nomination.
- Each thesis should include a foreword by the supervisor outlining the significance of its content.
- The theses should have a clearly defined structure including an introduction accessible to scientists not expert in that particular field.

More information about this series at <http://www.springer.com/series/8790>

Jian Wang

QCD Higher-Order Effects and Search for New Physics

Doctoral Thesis accepted by
Peking University, Beijing, China

 Springer

Author

Dr. Jian Wang
Johannes Gutenberg University
Mainz
Germany

Supervisor

Prof. Chong Sheng Li
Peking University
Beijing
China

ISSN 2190-5053

Springer Theses

ISBN 978-3-662-48671-9

DOI 10.1007/978-3-662-48673-3

ISSN 2190-5061 (electronic)

ISBN 978-3-662-48673-3 (eBook)

Library of Congress Control Number: 2015953252

Springer Heidelberg New York Dordrecht London

© Springer-Verlag Berlin Heidelberg 2016

This work is subject to copyright. All rights are reserved by the Publisher, whether the whole or part of the material is concerned, specifically the rights of translation, reprinting, reuse of illustrations, recitation, broadcasting, reproduction on microfilms or in any other physical way, and transmission or information storage and retrieval, electronic adaptation, computer software, or by similar or dissimilar methodology now known or hereafter developed.

The use of general descriptive names, registered names, trademarks, service marks, etc. in this publication does not imply, even in the absence of a specific statement, that such names are exempt from the relevant protective laws and regulations and therefore free for general use.

The publisher, the authors and the editors are safe to assume that the advice and information in this book are believed to be true and accurate at the date of publication. Neither the publisher nor the authors or the editors give a warranty, express or implied, with respect to the material contained herein or for any errors or omissions that may have been made.

Printed on acid-free paper

Springer-Verlag GmbH Berlin Heidelberg is part of Springer Science+Business Media
(www.springer.com)

Supervisor's Foreword

The standard model (SM) of particle physics successfully describes the electromagnetic, weak and strong interactions in a unified way, and has been validated by a number of experimental tests. After a three-year running of the Large Hadron Collider (LHC), the ATLAS and CMS Collaborations at the LHC announced the discovery of a new particle with a mass of around 125 GeV. All the current experimental results and analyses show that the properties of the new particle match those of the SM Higgs boson, which means the last block of the model has been established.

In spite of the great success, the SM suffers from intrinsic problems, e.g., the gauge hierarchy problem. Moreover, it cannot describe gravity, cannot interpret the origin of dark matter as well as the matter and anti-matter asymmetry, etc. All these problems suggest that the SM is not an ultimate theory, but just an effective theory in the present energy region. The proton-proton collider LHC has the highest energy in the world to explore the hitherto untouched landscapes, and thus enable us to test the SM and search for new physics. Meanwhile, the QCD higher-order effects are crucial for precise predictions on the scattering processes at the LHC. This thesis is devoted to discovering the signals of new physics at the LHC and to estimating the effects of QCD higher-order effects on the theoretical predictions.

There are three main topics studied in this thesis. The first is about the dark matter. Most of the mass density in the universe is in the form of dark matter, the properties of which are unclear to our knowledge. It is of high importance to study the probability of producing dark matter directly at the LHC. In this thesis, the potential of the LHC to discover the signal of dark matter associated production with a photon is studied. In particular, the QCD next-to-leading order effects are taken into account for the first time. After calculating the relic density of dark matter to find out the allowed parameter regions, the main backgrounds from the SM, i.e., Z boson and a photon associated production with invisible decay of Z boson, and Z boson and a jet production with the jet misidentified as a photon are investigated. Important kinematic distributions of both the signal and backgrounds are also compared. It is found that the photon's transverse momentum distributions

of the backgrounds decrease faster than that of the signal, and that the photon's rapidity distribution of the signal is more concentrated in the central region than those of the backgrounds. These features may help to select the events in experiments. Finally, the parameter regions corresponding to a 5σ discovery and a 3σ exclusion are presented.

The single top quark production is not only one of the main backgrounds in searches for new physics, but is also a unique channel to measure the CKM matrix element and sensitiveness to new physics. It is important to give most precise predictions on its production at the hadron colliders. In this thesis, the collinear and soft gluon effects in the t -channel single top quark production at both the Tevatron and LHC are resummed to all orders in the strong interaction coupling α_s . The resummation is based on the factorization of the cross section into hard, jet, soft, and parton distribution functions near the threshold region. Moreover, the NLO soft functions for this process are first calculated. The resummation is performed by evolving the different functions to a common scale by the renormalization group equations. The results show that the resummation effects increase the NLO results by about $9 \sim 13\%$ and $4 \sim 9\%$ when the top quark transverse momentum is larger than 50 and 70 GeV at the Tevatron and the 8 TeV LHC, respectively. This prediction is important in searching for new physics, e.g., a heavy W' which can decay into a top quark and a jet.

The top quark mass is close to the energy scale of electroweak symmetry breaking, and thus can be considered as a good probe of new physics. The monotonop signal, i.e., only a top quark and missing energy in the final state, is special and exists in many models such as R -parity violating supersymmetry or $SU(5)$ grand unification model, etc. In this thesis, the potential of the early LHC to discover the signal of monotonop is investigated. First, the general renormalizable Lagrangian that can describe the production of monotonop signal is proposed. Then the parameter spaces of the model are constrained by the $K^0 - \bar{K}^0$ mixing, the Z boson hadronic decay branching ratio, and dijet productions at the LHC. Furthermore, the discovery potential of the signal is studied in both the hadronic and semileptonic modes. The parameter regions corresponding to a discovery of the signal at different integrated luminosities are given.

All these results have been published in international recognized journals and have attracted the interests of both theorists and experimentalists. This thesis has been well written and presents many backgrounds and calculation details in the research, which can be taken as examples by interested readers, especially graduate students, to carry out studies on the frontiers of particle physics.

Beijing, China
September 2015

Prof. Chong Sheng Li

Preface

“What are the elementary building blocks of the world and ourselves?” is a question occurring in the human mind from ancient times. Aristotle, one of the great Greek philosophers, believed that the world is made of Earth, Air, Fire, and Water. In ancient China, people thought that everything arises as a composition of the five elements of Earth, Wood, Fire, Metal, and Water. However, most of these thoughts are in the sense of philosophy. It became a scientific problem since the proposal and discovery of *molecules* and *atoms*. As the technique of probing the structure of matter improves, atoms are found to be composed of more fundamental elements, i.e., the nucleus and electrons. Such a decomposition line extends continuously, and nowadays the most fundamental elements are electrons and quarks, the latter of which make up the baryons and mesons. The typical size of electrons and quarks is less than 10^{-15} meter. It is such a small size that one cannot imagine it ordinarily. These elements are called *particles* academically.

Another important discovery in probing the structure of matter is that the rules to govern the particles are very different from those in the macro-world. They are so weird that even scientists cannot understand them intuitively. For example, the state of a particle cannot be measured accurately in a fixed space. They can move with unspecified momentum. In other words, the momentum is not fixed before a measurement. Furthermore, particles possess a special property, called *spin*, which seems related to the rotation of something in particles. But in fact spin is not so simple and just a unique property in the micro-world. Especially, the value of a particle’s spin is fixed all the time and takes only integers or half integers. The known particles have only spins of 0, 1/2 or 1. The spin-1/2 particles include electrons and quarks while the spin-1 particles are mediators of the forces among the spin-1/2 particles, such as photons. The only spin-0 particle was newly discovered in 2012, which plays a crucial role in explaining the masses of spin-1 and spin-1/2 particles.

It is a fantastic work to establish such a framework, called the standard model of particle physics, about the construction of the world. People are confident to describe and explain almost every phenomenological event with this framework in hand. However, it is not the final and perfect theory about the world, though the

framework has been indeed tested by a number of experiments. There are some phenomena that cannot be explained in the framework. Pursuing a more complete theory is still an existing aim of scientists.

In order to look into the inner structure of tiny particles, the only way is to let other particles collide with them to break them apart. The more energy there is in the collision, the finer the structure people can see. Since protons are heavier than electrons, it is easier to accelerate them with high energy. Quarks are the building blocks of protons, and therefore a precise understanding of the interaction involving quarks is the basis for discovery of any new physics. Quantum Chromodynamics (QCD) is the theory to describe the interaction involving quarks. However, it is so complicated that exact solutions cannot be obtained. The prediction made by QCD can only become more and more precise after including more and more corrections. As a consequence, it is important to consider QCD high-order corrections in searching for new physics.

This is the motivation for my Ph.D. thesis. Most of the contents in this thesis have been published in the form of academic papers. However, I provide in this book more updated introductions to the backgrounds and recent developments in the relevant fields, and show more useful details in my research that are not appropriate for publication in scientific journals. Thus, I believe that graduate students can benefit from this book.

The main contents of this thesis are arranged as follows. We first introduce the present knowledge about the micro-world, the standard model of particle physics in Chap. 1. In Chap. 2, the bases of Quantum Chromodynamics, including the history, quantization, and renormalization, are reviewed. Then in Chap. 3 the perturbative QCD calculation of the scattering processes at hadron colliders is described, especially the factorization, infrared safety, QCD higher-order effects, and resummation methods. In Chap. 4, the potential of the LHC to discover the signal of dark matter associated production with a photon in an effective theory is studied. In Chap. 5, the factorization and resummation of the prediction for the top quark transverse momentum distribution at large p_T at both the Tevatron and the LHC are discussed with soft-collinear effective theory. In Chap. 6, the potential of the early LHC to discover the signal of monotops, which can be decay products of some resonances in models such as R -parity violating supersymmetry (SUSY) or $SU(5)$ grand unification model, is investigated. Chapter 7 is a summary of this thesis and also an outlook is presented. Some calculation details and parameters used in the calculation are given in the appendices.

Acknowledgments

It was not easy for me to get through the period of earning my Ph.D. I feel very lucky and grateful after achieving this.

First of all, I would like to thank my supervisor, Prof. Chong Sheng Li, who gave me the opportunity to join his group and encouraged me to explore the amazing field of high energy physics. I still remember the summer when Prof. Li told me to buy the book “An Introduction to Quantum Field Theory” by M.E. Peskin and D.V. Schroeder. Then I spent a whole year to read it. Though I got very confused, I was interested in the method to describe the actions in the micro-world. Later, I began my own research under his supervision. The first paper was difficult to write and he helped me to revise every sentence. I was deeply impressed by his strict manner. Thanks to his instruction, I grew from a layman to a freshman who could carry out studies independently. I was very pleased to take his instructions.

I wish to thank the teachers at the institute of theoretical physics at Peking University, including Profs. Kuang-Ta Chao, Xing-Chang Song, Bo-Qiang Ma, Chuan Liu, Han-Qing Zheng, Shi-Lin Zhu, Shou-Hua Zhu, Bin Chen, Zhong-Shui Ma, Zhi-Xin Qian, and Da-Xin Zhang. I learned a lot from their classes and reports. The collaboration and communication with Prof. C.P. Yuan, Qing-Hong Cao, Li Lin Yang were enjoyable.

I would also like to thank my colleagues at Peking University for their kind help and friendship, especially the group members, Zhao Li, Xiang Dong Gao, Jia Jun Zhang, Hao Zhang, Jun Gao, Hua Xing Zhu, Bo Hua Li, Yue Zhang, Ding Yu Shao, Yan Wang, Fa Peng Huang, Hai Tao Li, Yong Chuan Zhan, Ze Long Liu, and Shi Ang Li.

Lastly, I am grateful to my parents for their patience and *love*. Without them I could never keep on studying physics. I am indebted to my wife for her understanding and support.

Supplementary Note Several parts of this thesis were published in the following articles and reused with permission:

1. Jian Wang, Chong Sheng Li, Ding Yu Shao, and Hao Zhang, Next-to-leading order QCD predictions for the signal of dark matter and photon associated production at the LHC, *Phys. Rev. D* 84, 075011—Published 13 October 2011. Copyright ©2011 American Physical Society
2. Jian Wang, Chong Sheng Li, Ding Yu Shao, and Hao Zhang, Search for the signal of monoton production at the early LHC, *Phys. Rev. D* 86, 034008—Published 6 August 2012. Copyright ©2012 American Physical Society
3. Jian Wang, Chong Sheng Li, and Hua Xing Zhu, Resummation prediction on top quark transverse momentum distribution at large p_T , *Phys. Rev. D* 87, 034030—Published 19 February 2013. Copyright ©2013 American Physical Society

However, I have taken this opportunity to update some new materials and references in this thesis to introduce some subsequent progress on several problems studied in this thesis after their publications.

Contents

1	Introduction to the Standard Model of Particle Physics	1
1.1	Particles	1
1.2	The Electroweak Theory	2
1.3	Quantum Chromodynamics	8
1.4	Open Questions	9
	References	10
2	Foundations of the Quantum Chromodynamics	11
2.1	Origin of QCD	11
2.2	Lagrangian of QCD and Feynman Rules	14
2.3	Renormalization	18
	References	21
3	QCD Perturbative Calculation of the Scattering Processes at Hadron Colliders	23
3.1	Factorization	24
3.2	Infrared Safety	26
3.3	QCD Higher-Order Effects	28
3.4	Resummation Methods	31
	3.4.1 Traditional Resummation Method	33
	3.4.2 Resummation with SCET	38
	References	40
4	QCD NLO Prediction on the Dark Matter and Photon Associated Production at the LHC	47
4.1	Introduction	47
4.2	Effective Operators	50
4.3	Relic Density	51
4.4	DM and Photon Associated Production at the LHC	56
	4.4.1 LO Results	56
	4.4.2 NLO Results	58
	4.4.3 Numerical Results	63

4.5	Backgrounds and Discovery Potential.	66
4.6	Conclusions and Comments	68
	References	69
5	Resummation Prediction on Top Quark Transverse Momentum	
	Distribution at Large p_T.	73
5.1	Introduction	73
5.2	Analysis of Kinematics.	77
5.3	Factorization and Resummation Formalism	80
5.4	Hard, Soft, and Jet Functions at NLO.	86
	5.4.1 Hard Functions	87
	5.4.2 Soft Function	88
	5.4.3 Jet Function	91
	5.4.4 Scale Invariance	93
	5.4.5 Final RG Improved Differential Cross Section.	95
5.5	Numerical Results	97
5.6	Conclusions and Comments	101
	References	103
6	Search for the Signal of Monotop Production at the Early LHC . . .	107
6.1	Introduction	107
6.2	Experiment Constraints.	109
	6.2.1 $K^0 - \bar{K}^0$ Mixing	109
	6.2.2 Z Hadronic Decay Branching Ratio	112
	6.2.3 Dijet Production at the LHC.	115
6.3	Signals and Backgrounds	118
	6.3.1 Hadronic Decay Mode	121
	6.3.2 Semileptonic Decay Mode	124
6.4	Conclusions and Comments	126
	References	127
7	Summary and Outlook.	131
	Erratum to: Foundations of the Quantum Chromodynamics.	E1
	Appendix A: Phase Space Integration	133
	Appendix B: Calculation of the Soft Functions	137
	Appendix C: Anomalous Dimensions	141

Chapter 1

Introduction to the Standard Model of Particle Physics

The Standard Model (SM) of particle physics is a gauge field theory based on the gauge group $SU(3)_C \otimes SU(2)_L \otimes U(1)_Y$ that describes the fundamental electromagnetic, weak and strong interactions. It is established after immense experimental and inspired theoretical efforts in pursuing the answer to the question of what are the ultimate constituents of matter.

1.1 Particles

In the SM, all matter in the Universe is made up of elementary particles, which can be classified according to the spin and character under interaction. They are listed in Fig. 1.1. In general, there are four categories of particles in the SM, i.e., quarks, leptons, gauge bosons, and Higgs boson. The quarks are components of hadrons and carry fractional charges, which means they can interact via photons (one kind of gauge bosons), denoted by γ . This interaction is rather weak compared to another interaction that is mediated by gluons (one kind of gauge bosons), denoted by g . Moreover, quarks translate to each other in nucleon decays, in which the gauge boson W plays a role. The Z boson is a sister of the W boson but carries a force similar to γ . The prediction and confirmation by experiments of the Z boson provide strong evidence of taking the SM as a correct theory to describe the interactions in Nature. The leptons can interact by mediating a γ , W , or Z bosons, but do not couple via gluons. This is the main difference between leptons and quarks. The four gauge bosons are all force carriers and should be massless in the language of gauge field theory. In practice, γ and g are massless, but W and Z bosons are massive, with a mass of $\mathcal{O}(100 \text{ GeV})$. This phenomenon is called the *electroweak gauge symmetry breaking*. In order to generate such a mechanism, an additional particle, i.e., the Higgs boson, was proposed to exist [1–5]. It was indeed discovered about three years ago after being searched for about half a century [6, 7], and it makes the SM a closed theory by itself. Although its mass is a free parameter theoretically, it turns out to have a mass near the W and Z boson masses.

spin- $\frac{1}{2}$	Quarks	u	c	t
		d	s	b
spin- $\frac{1}{2}$	Leptons	ν_e	ν_μ	ν_τ
		e	μ	τ
spin-1	Gauge bosons	γ	Z	W g
spin-0	Higgs boson	H		

Fig. 1.1 The particles in the SM

1.2 The Electroweak Theory

As shown by the gauge group, the SM consists of two separate parts. The first part is the electroweak theory dictated by the gauge group $SU(2)_L \otimes U(1)_Y$ [8–10]. The gauge group $SU(2)_L$ has three generators, for example, taken to be $\sigma^a/2$ with σ^a ($a = 1, 2, 3$) the Pauli spin matrices, to represent the independent gauge transformations under this group. And each generator is associated with a gauge boson, denoted by W^1 , W^2 , and W^3 respectively. The gauge group $U(1)_Y$ has only one generator and one associating gauge boson B . Two of the gauge bosons in $SU(2)_L$ combine linearly to the mass eigenstates W^\pm as

$$W^+ = \frac{1}{\sqrt{2}}(W^1 - iW^2), \quad (1.1)$$

$$W^- = \frac{1}{\sqrt{2}}(W^1 + iW^2). \quad (1.2)$$

The third mixes with the gauge boson in $U(1)_Y$ because they have the same quantum numbers and couple with quarks or leptons in the same way. Thus an additional parameter may be introduced to describe the extent of mixing. It is convenient to express the mixing in an angle θ_w , called the Weinberg angle, and the resulting mass eigenstates are

$$Z = W^3 \cos \theta_w - B \sin \theta_w, \quad (1.3)$$

$$A = W^3 \sin \theta_w + B \cos \theta_w. \quad (1.4)$$

The gauge boson A is massless, corresponding to the photon. But the gauge boson Z is massive after the electroweak symmetry breaking. The mass difference between the W^\pm and Z bosons determines the Weinberg angle. In the SM, the electroweak

symmetry breaking is triggered by a complex scalar doublet, so a simple relation follows:

$$\cos \theta_w = \frac{M_W}{M_Z}. \quad (1.5)$$

Since their masses are measured to be close to each other, the Weinberg angle is small, about 30° . Actually, the Weinberg angle is also related to the ratio of the couplings g_2 and g_1 that associates with the gauge bosons W^i ($i = 1, 2, 3$) and B respectively,

$$\tan \theta_w = \frac{g_1}{g_2}. \quad (1.6)$$

The couplings g_2 and g_1 appear in the covariant derivative

$$D_\mu = \partial_\mu - i \frac{g_1}{2} B_\mu - i \frac{g_2}{2} W_\mu^i \sigma^i. \quad (1.7)$$

The usual coupling between photons and electrons, denoted by e , is not an explicit constant in the SM gauge group, but a combination of g_1 and g_2 ,

$$e = \frac{g_1 g_2}{\sqrt{g_1^2 + g_2^2}}. \quad (1.8)$$

Therefore, the coupling structure of the electroweak part in the SM, represented by g_1 and g_2 , can just be determined by three experimental measurements of M_W , M_Z , and $\alpha = e^2/4\pi$. Taking $M_W = 80.385$ GeV, $M_Z = 91.1876$ GeV and $\alpha = 1/137$, gives $g_1 = 0.344$ and $g_2 = 0.641$.

Meanwhile, the interactions involving the gauge bosons are fixed by gauge invariance of the theory and the quantum numbers of relevant quarks and leptons. Specifically, there are electromagnetic, weak charged and weak neutral interactions, given as

$$\mathcal{L} = e A_\mu J_{EM}^\mu + \frac{g_2}{\sqrt{2}} (W_\mu^+ J_W^{\mu+} + W_\mu^- J_W^{\mu-}) + \frac{g_2}{\cos \theta_w} Z_\mu J_Z^\mu, \quad (1.9)$$

where¹

$$J_{EM}^\mu = (-1) \bar{e} \gamma^\mu e + \left(\frac{2}{3}\right) \bar{u} \gamma^\mu u + \left(-\frac{1}{3}\right) \bar{d} \gamma^\mu d, \quad (1.10)$$

$$J_W^{\mu+} = \bar{\nu}_L \gamma^\mu e_L + \bar{u}_L \gamma^\mu d_L, \quad (1.11)$$

$$J_W^{\mu-} = \bar{e}_L \gamma^\mu \nu_L + \bar{d}_L \gamma^\mu u_L, \quad (1.12)$$

¹We take the first generation as an example and assume that the Cabibbo-Kobayashi-Maskawa matrix is diagonal.

$$\begin{aligned}
J_Z^\mu = & \left(\frac{1}{2}\right) \bar{\nu}_L \gamma^\mu \nu_L \\
& + \left(-\frac{1}{2} + \sin^2 \theta_w\right) \bar{e}_L \gamma^\mu e_L + (\sin^2 \theta_w) \bar{e}_R \gamma^\mu e_R \\
& + \left(\frac{1}{2} - \frac{2}{3} \sin^2 \theta_w\right) \bar{u}_L \gamma^\mu u_L + \left(-\frac{2}{3} \sin^2 \theta_w\right) \bar{u}_R \gamma^\mu u_R \\
& + \left(-\frac{1}{2} + \frac{1}{3} \sin^2 \theta_w\right) \bar{d}_L \gamma^\mu d_L + \left(\frac{1}{3} \sin^2 \theta_w\right) \bar{d}_R \gamma^\mu d_R. \quad (1.13)
\end{aligned}$$

Here, we have denoted the electrons of left- and right-handed chirality as e_L and e_R , respectively. So does u_L , d_L , and u_R , d_R . It is obvious from these expressions that the electromagnetic interaction does not distinguish the chirality while weak charged current involves only left-handed particles. The theory describing the electromagnetic interaction is conventionally called quantum electrodynamics (QED), which has successfully explained a lot of experiments, such as the anomalous magnetic moment of the electron and Lamb shift of the energy levels of hydrogen.

If the mediator W^\pm is heavy enough compared to the external momenta in a process, then the two charged currents can be merged together to reproduce the four fermion operator,

$$\mathcal{L}_W \approx \frac{g_2^2}{2M_W^2} J_W^{\mu-} J_{\mu W}^+. \quad (1.14)$$

Thus the conventional Fermi constant can be written as

$$G_F = \frac{g_2^2}{4\sqrt{2}M_W^2} = \frac{e^2}{4\sqrt{2}M_W^2 \sin^2 \theta_w}. \quad (1.15)$$

The weak neutral current couples with both chiralities but in different sizes. In particular, the difference between the left- and right-handed down-type quarks is most significant. One may have noticed that the right-handed neutrino does not take part in any interaction. In the limit $\theta_w \rightarrow 0$, there are no right-handed particles in the weak neutral current, as expected. As a consequence, the Weinberg angle can be obtained by measuring the rates of processes induced by the weak neutral current, especially the angular distributions in the processes. Historically, since the Fermi constant has been measured to very high precision, the knowledge of G_F and θ_w was used to predict the masses of the W^\pm and Z bosons, and then the CERN proton–proton collider was built to discover them.

In quantum field theory, the mass of the mediator reflects the range of the interaction. The range is proportional to the inverse of the mass, about $1 \text{ fm} \sim 1/0.2 \text{ GeV}$. The photon is massless, so the range of the electromagnetic interaction is infinite. The W boson is massive, so the weak interaction happens typically in the range of $\sim 2.5 \times 10^{-15} \text{ m}$.

From the description in the above paragraphs, the couplings involving the photon and W boson, e and $g_2/\sqrt{2}$, are of the same order. The strength of the weak interaction appears “weak” because of the suppression of the heavy mass M_W in low energy phenomena. In high energy scattering, when the heavy boson could be on-shell produced, the weak interaction does not necessarily appear weak compared to the electromagnetic interaction.

The massive gauge bosons are naively problematic objects in gauge field theory because their corresponding mass terms would violate the gauge invariance, which is crucial to ensure the behavior of the scattering rate in high energy ranges. In the case of nothing else added, the amplitude of the scattering involving double W bosons is proportional to the square of the center-of-mass energy in high energy limit, violating the unitarity of the cross section. This is unacceptable and therefore there must be something else taking part in this process to restore unitarity. Given the measured value of the W boson mass, this unitarity constraint requires the existence of some particles of masses below the unitarity bound ~ 1 TeV or the theory becomes non-perturbative above the unitarity bound [11]. In the SM, the solution is adding a scalar, the Higgs boson, whose coupling with the W boson is proportional to the square of the W boson mass and whose mass is around $\mathcal{O}(100 \text{ GeV})$ if the theory is still perturbative. At the same time, the mass term of the W boson does not exist explicitly in the Lagrangian but appears spontaneously after incorporating the Higgs boson in a doublet which transforms under the $SU(2)_L$ gauge transformation but takes a nonvanishing vacuum expectation value. In this way, the gauge invariance of the Lagrangian is maintained. This kind of realization of the massive gauge boson’s mass term is called the *Higgs mechanism* [1–5].

The core of the Higgs mechanism is a proposed Higgs field taking a nonvanishing vacuum expectation value. This can be realized by imposing special potential terms of the field, for example,

$$V(\phi) = -\mu^2 \phi^\dagger \phi + \lambda(\phi^\dagger \phi)^2, \quad (1.16)$$

where ϕ is the Higgs field, parameterized by

$$\phi(x) = U(x) \frac{1}{\sqrt{2}} \begin{pmatrix} 0 \\ v + h(x) \end{pmatrix}. \quad (1.17)$$

Here $U(x)$ is a general $SU(2)_L$ gauge transformation and can be chosen to be 1, i.e., the unitary gauge, without any effect on physical observables.² The factor $1/\sqrt{2}$ comes as a convention. The real-valued field $h(x)$ is physical with the vacuum expectation value $\langle h(x) \rangle = 0$, the quantization of which is just the Higgs boson. The parameter λ is positive so that the potential generates a stable vacuum. The parameter μ^2 should be also positive in order to induce a nonvanishing vacuum. Notice that

²The other parts of the SM should be changed correspondingly.

in the mass term of a usual scalar field, the coefficient $-\mu^2$ is positive. Under these assumptions, the minimum of the potential occurs at

$$v = \left(\frac{\mu^2}{\lambda} \right)^{1/2}. \quad (1.18)$$

Then the potential terms take the form

$$\begin{aligned} V(h) &= \mu^2 h^2 + \lambda v h^3 + \frac{1}{4} \lambda h^4 \\ &= \frac{1}{2} m_H^2 h^2 + \sqrt{\frac{\lambda}{2}} m_H h^3 + \frac{1}{4} \lambda h^4. \end{aligned} \quad (1.19)$$

In the second line of the above equation, we have written the coefficients in terms of two parameters m_h and λ , which are more closely related to physical observables. The relations are

$$m_H = \sqrt{2} \mu = \sqrt{2 \lambda} v. \quad (1.20)$$

In principle, there are two independent parameters in the potential energy that need to be determined experimentally. However, as mentioned above, the purpose of the Higgs mechanism is to provide mass terms of massive gauge bosons. Thus the vacuum expectation value of the Higgs field is related to the gauge boson masses. Specifically,

$$M_W = \frac{g_2}{2} v, \quad M_Z = \frac{\sqrt{g_1^2 + g_2^2}}{2} v. \quad (1.21)$$

It turns out that $v \approx 246$ GeV. Therefore, the only unknown parameter in the potential energy of the Higgs field is the mass of the Higgs boson.

The naive mass terms of the other particles in the SM, i.e., the leptons and quarks, involve a left-handed and a right-handed fermion, f_L and f_R , which transform differently following the SM gauge group. So they should not appear in the Lagrangian, which means all the fermions in the SM are massless. However, if the Higgs field couples with fermions in the form of Yukawa interactions,

$$\mathcal{L}_f = -y_f \bar{F}_L \cdot \phi f_R + h.c., \quad (1.22)$$

the fermions can have masses after the Higgs field gets its vacuum expectation value,

$$m_f = \frac{1}{\sqrt{2}} y_f v. \quad (1.23)$$

Here F_L denotes the $SU(2)_L$ doublet made of two left-handed fermions, such as the left-handed neutrino and electron, $(\nu_L, e_L)^T$, while f_R is an $SU(2)_L$ singlet.

There are no stringent constraints on the Higgs boson's mass. The unitarity bound is just a very loose constraint, $m_H < 1 \text{ TeV}$ [11]. As a result, it has to be measured by experiments. Given that it couples to the massive gauge boson, it is possible to search for this particle via the associated production of a massive gauge boson, which is one of the main goals at the large electron–positron (LEP) collider. Due to the limited collision energy, at most 209 GeV, these direct searches have only set a lower limit for its mass [12]

$$m_H > 114.4 \text{ GeV}. \quad (1.24)$$

The more powerful hadron collider Tevatron excluded the mass range of $100 \sim 106 \text{ GeV}$ and $147 \sim 179 \text{ GeV}$ based on the analysis of signals of Higgs bosons produced in association with a vector boson ($q\bar{q} \rightarrow W/ZH$), through gluon–gluon fusion ($gg \rightarrow H$), and through vector boson fusion (VBF) ($q\bar{q} \rightarrow q'\bar{q}'H$) [13].

Apart from the direct searches, the parameter m_H affects some electroweak observables through quantum loop effects. For example, the Higgs boson couples to W and Z bosons and changes the relations among electroweak parameters. For example, after considering the quantum effects, the tree-level relation in Eq. (1.15) is modified to

$$M_W^2 \sin^2 \theta_w = M_Z^2 \cos^2 \theta_w \sin^2 \theta_w = \frac{e^2}{4\sqrt{2}G_F} (1 + \Delta_r) \quad (1.25)$$

where Δ_r contains dependence on m_H . The global fitting to the electroweak precision data imposes a stringent constraint, $m_H = 94_{-24}^{+29} \text{ GeV}$, corresponding to a 95 % CL upper limit of $m_H < 152 \text{ GeV}$ [14].

Another parameter, the Higgs self-coupling λ in the potential energy, gets corrections involving the Higgs boson. It would become too large so that the theory is not perturbative and loses its predictability, or is negative so that the vacuum is not stable, as mentioned above. If we want to avoid such cases up to the Planck scale, $M_{Pl} \sim 10^{19} \text{ GeV}$, it is required that $130 \text{ GeV} < m_H < 180 \text{ GeV}$ [15–17]. A more updated investigation of the vacuum stability implies $m_H > 126 \text{ GeV}$ at 98 % CL [18].

A combination of direct searches and electroweak data leads to rather narrow possible ranges for the Higgs boson mass. The final breakthrough was achieved in 2012 at the large hadron collider (LHC), which is the most powerful collider right now. After two years running, the ATLAS and CMS collaborations both reported the discovery of a new particle with a mass of around 125 GeV [6, 7]. The latest combined mass value measured by the ATLAS and CMS collaborations based on events of $h \rightarrow \gamma\gamma$ and $h \rightarrow ZZ^* \rightarrow 4l$ is [19]

$$m_H = 125.09 \pm 0.24 \text{ GeV}, \quad (1.26)$$

which is remarkably close to the constraints set by the precision electroweak data. This coincidence should be considered as a great achievement and a triumph for

the SM, and makes the SM perturbative, unitary, and extrapolable to the very high energy scale.

In addition, the spin of the Higgs boson has been probed in many ways, via its production and decay rates, the kinematics of Higgs production in association with the massive gauge bosons, and angular distributions in the WW , ZZ , $\gamma\gamma$ final states. The spin 1 possibility is excluded by observation of the $\gamma\gamma$ final state due to the Landau-Yang theorem [20, 21], while the spin 2 hypothesis is strongly disfavored [22]. At the same time, it is shown that this particle behaves mainly like a scalar, rather than a pseudoscalar [22, 23].

The discovered mass of the Higgs boson is in a range such that various decay final states can be detected at the LHC. Thus it is possible to measure many couplings of the Higgs boson with the other particles. Because every signal in different final states depends on several Higgs couplings, a global fit to the couplings is required. The result indicates that they are generally compatible with the SM predictions though large uncertainties exist [24].

1.3 Quantum Chromodynamics

The other part of the SM is the theory of QCD based on the gauge group $SU(3)_C$. The subscript C denotes the color space in which each flavor of quark shown in Fig. 1.1 contains three copies with different colors. They form a color triplet such as $(u_r, u_g, u_b)^T$ for the up quark. QCD is established to be the right theory to study the strong interaction. The history and detail of the QCD are left to the next chapter, and we just give a general description in the following paragraphs.

QCD is not a simple extension of the weak interaction by changing the gauge group from $SU(2)$ to $SU(3)$. It is much more complicated and has not been completely understood so far. QCD is not a broken gauge theory in the sense that the force carrier, the gluon, is massless. However, it does not, like the photon, take a long range force because of a special property with QCD, the confinement of quarks. This property indicates that the individual component inside the nucleon cannot be measured separately. In particular, the interaction between two quarks becomes stronger and stronger as they are separated from each other further and further. This behavior is different from the ordinary phenomena in the macro-world where we live and where the main interaction is governed by the theory of QED. Thus the conventional faith that anything could be decomposed into smaller parts is challenged with the appearance of QCD confinement.

On the other hand, if we use high enough energy to probe the inner structure of nucleons, we see the quarks swing around. The interaction between quarks is weak in the very small region. In this circumstance, the different quarks in the nucleon can be separated with high energy. Meanwhile, the high speed quarks would stimulate the vacuum to produce plenty of pairs of (anti-)quarks, and take some of them to fly together and form hadrons in order to comply with the confinement. In this sense, the nucleons can still be decomposed, but not into smaller parts. The decomposed

parts contain additional components that do not exist in the nucleons explicitly but are generated dynamically from the vacuum. As a result, it is conceivable that the decomposed parts may have masses larger than those of hadrons, and that the inner structure of nucleons is not fixed but changes depending on the probing energy.

The strong coupling, g_s , plays a central role in the description of QCD. It also varies depending on the energy. Therefore, different experiments can measure different values for this coupling due to the different energy setting, from a few GeV to a few TeV. The evolution of g_s with respect to the energy is predictable in QCD. After considering this evolution effect, the measured values of g_s from different experiments are in good agreement with each other. Taking the value at the M_Z as a reference, the parameter $\alpha_s \equiv g_s^2/4\pi$ is measured to be [25]

$$\alpha_s(M_Z) = 0.1193 \pm 0.0016, \quad (1.27)$$

which gives $g_s(M_Z) = 1.224 \pm 0.008$, much larger than g_1 and g_2 .

The largest collider LHC employs collisions of proton beams to search for new particles or new interactions. Any prediction on the event generation at the LHC resorts to the understanding of QCD because of the partons in the initial state. Moreover, the processes generated via QCD have significant rates generally due to the large coupling, while the rates of potential processes involving new physics are rather small. It seems that we want to hear a very feeble music in a room full of big noise. The fluctuation of the noise would easily cover the music. Therefore, it is of great importance to predict the noise precisely, which means we need to consider more QCD corrections.

1.4 Open Questions

The SM has been tested by a large number of precision measurements and proved to be a very precise theory of elementary particles and interactions. However, the SM is not a theory about everything. The following questions are still open within the SM and need to be addressed in the future.

- How can gravity be incorporated in the SM?
- What is the nature of dark matter?
- The masses of fermions span from less than 1 eV to larger than 10^{11} eV. Is there any mechanism to arrange them?
- Are the neutrinos Dirac fermions or Majorana fermions?
- Why is the matter much more than antimatter in the universe?
- Why is the coefficient of the quadric term in the Higgs potential negative?

As a result, the SM can be only considered as an effective theory, an approximation of a more complete theory in the low energy limit. It is necessary to extend the SM, and search for new physics beyond the SM.

References

1. P.W. Higgs, Broken symmetries and the masses of gauge bosons. *Phys. Rev. Lett.* **13**, 508–509 (1964)
2. P.W. Higgs, Spontaneous symmetry breakdown without massless bosons. *Phys. Rev.* **145**, 1156–1163 (1966)
3. F. Englert, R. Brout, Broken symmetry and the mass of gauge vector mesons. *Phys. Rev. Lett.* **13**, 321–323 (1964)
4. G. Guralnik, C. Hagen, T. Kibble, Global conservation laws and massless particles. *Phys. Rev. Lett.* **13**, 585–587 (1964)
5. T.W.B. Kibble, Symmetry breaking in nonAbelian gauge theories. *Phys. Rev.* **155**, 1554–1561 (1967)
6. G. Aad et al., ATLAS Collaboration, Observation of a new particle in the search for the standard model Higgs boson with the ATLAS detector at the LHC. *Phys. Lett. B* **716**, 1–29 (2012). [arXiv:1207.7214](https://arxiv.org/abs/1207.7214)
7. S. Chatrchyan et al., CMS Collaboration, Observation of a new boson at a mass of 125 GeV with the CMS experiment at the LHC. *Phys. Lett. B* **716**, 30–61 (2012). [arXiv:1207.7235](https://arxiv.org/abs/1207.7235)
8. S. Glashow, Partial symmetries of weak interactions. *Nucl. Phys.* **22**, 579–588 (1961)
9. S. Weinberg, A model of leptons. *Phys. Rev. Lett.* **19**, 1264–1266 (1967)
10. A. Salam, Weak and electromagnetic interactions. *Conf. Proc.* **C680519**, 367–377 (1968)
11. B.W. Lee, C. Quigg, H. Thacker, Weak interactions at very high-energies: the role of the Higgs boson mass. *Phys. Rev. D* **16**, 1519 (1977)
12. R. Barate et al., LEP Working Group for Higgs boson searches, ALEPH Collaboration, DELPHI Collaboration, L3 Collaboration, OPAL Collaboration, Search for the standard model Higgs boson at LEP. *Phys. Lett. B* **565** (2003) 61–75. [arXiv:hep-ex/0306033](https://arxiv.org/abs/hep-ex/0306033)
13. TEVNP (Tevatron New Phenomena and Higgs Working Group), CDF Collaboration, D0 Collaboration, Combined CDF and D0 search for standard model Higgs boson production with up to 10.0 fb^{-1} of Data. [arXiv:1203.3774](https://arxiv.org/abs/1203.3774)
14. LEP Electroweak Working Group Collaboration, <http://lepewwg.web.cern.ch/LEPEWWG/>
15. M. Sher, Electroweak Higgs potentials and vacuum stability. *Phys. Rept.* **179**, 273–418 (1989)
16. T. Hambye, K. Riessellmann, Matching conditions and Higgs mass upper bounds revisited. *Phys. Rev. D* **55**, 7255–7262 (1997). [arXiv:hep-ph/9610272](https://arxiv.org/abs/hep-ph/9610272)
17. J. Ellis, J. Espinosa, G. Giudice, A. Hoecker, A. Riotto, The probable fate of the standard model. *Phys. Lett. B* **679**, 369–375 (2009). [arXiv:0906.0954](https://arxiv.org/abs/0906.0954)
18. G. Degrandi, S. Di Vita, J. Elias-Miro, J.R. Espinosa, G.F. Giudice et al., Higgs mass and vacuum stability in the standard model at NNLO. *JHEP* **1208**, 098 (2012). [arXiv:1205.6497](https://arxiv.org/abs/1205.6497)
19. G. Aad et al., ATLAS, CMS Collaboration, Combined measurement of the Higgs boson mass in pp and 8 TeV with the ATLAS and CMS experiments. *Phys. Rev. Lett.* **114**, 191803 (2015). [arXiv:1503.07589](https://arxiv.org/abs/1503.07589)
20. L. Landau, On the angular momentum of a two-photon system. *Dokl. Akad. Nauk Ser. Fiz.* **60**, 207–209 (1948)
21. C.-N. Yang, Selection rules for the dematerialization of a particle into two photons. *Phys. Rev.* **77**, 242–245 (1950)
22. G. Aad et al., ATLAS Collaboration, Evidence for the spin-0 nature of the Higgs boson using ATLAS data. *Phys. Lett. B* **726**, 120–144 (2013). [arXiv:1307.1432](https://arxiv.org/abs/1307.1432)
23. S. Chatrchyan et al., CMS Collaboration, Study of the mass and spin-parity of the Higgs boson candidate via its decays to Z boson pairs. *Phys. Rev. Lett.* **110**, no. 8 081803 (2013). [arXiv:1212.6639](https://arxiv.org/abs/1212.6639)
24. T. Corbett, O.J.P. Eboli, D. Gonçalves, J. Gonzalez-Fraile, T. Plehn et al., The Higgs legacy of the LHC run I. *JHEP* **1508**, 156 (2015). [arXiv:1505.05516](https://arxiv.org/abs/1505.05516)
25. K. Olive et al., Particle Data Group Collaboration, Review of particle physics. *Chin. Phys. C* **38**, 090001 (2014)

Chapter 2

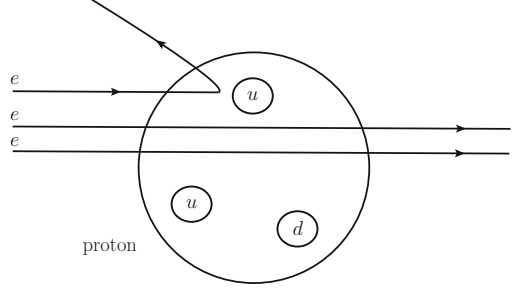
Foundations of the Quantum Chromodynamics

2.1 Origin of QCD

Quantum chromodynamics (QCD) is a theory to describe the strong interaction in hadrons. It was developed in the history of understanding the structure of the hadrons. In the 1950s, a large number of hadrons were discovered in experiments. Some of them are stable, but most are unstable, decaying to more stable particles immediately. This makes it doubtful that all of them could be fundamental particles, and it is proposed that hadrons are composed of more fundamental particles. Later, Gell-Mann et al. discovered that hadrons can be classified according to a method called the eightfold way, which can be explained by an $SU(3)$ flavor symmetry. Consequently, the quark model and three fundamental quarks, called u , d , and s with spin- $\frac{1}{2}$ and fractional charges, were proposed [1–3]. Many experiment results can be understood based on the quark model. However, there are still some phenomena that cannot be explained. For example, the hadron $\Delta^{++}(1232)$ is the ground state composed of three u quarks with spin- $\frac{3}{2}$. As a result, the wave function should be symmetric in both the spin and position spaces. An extra quantum number of the quark, namely *color*, is proposed in order not to violate the spin-statistics theorem. However, the subsequent experiments to discover free quarks all failed, which forced people to presume that the quarks are confined forever in hadrons. In 1972 and 1973, Fritzsche, Gell-Mann and Leutwyler extended the symmetry in the color configuration to $SU(3)$ gauge symmetry, establishing the theory of QCD [4, 5]. This theory can not only explain the properties predicted by the quark model, but can also satisfy the requirement of quark confinement. Later, many other theoretical and experimental developments convinced people that QCD is just the right theory for strong interaction.

One of the most important experiments is the deeply inelastic scattering (DIS) of electrons and protons. This process can be described as $l(p) + N(P) \rightarrow l'(p') + X(p_X)$, where l, l' denotes the in-going and outgoing leptons, respectively, N denotes

The original version of this chapter was revised: Incorrect equation has been corrected. The erratum to this chapter is available at [10.1007/978-3-662-48673-3_8](https://doi.org/10.1007/978-3-662-48673-3_8)

Fig. 2.1 A DIS process

the proton, X represents all the unobserved final states, p , P , p' and p_X are the corresponding momenta. As shown in Fig. 2.1, in the collision of a bunch of electrons with a proton, most electrons go through the proton. Only very few of the electrons change their directions significantly. These processes can be called as the DIS. It happens because the high energy electrons collide with the possible inner small ingredients of the hadron. The ingredients of a hadron are not fixed before any measurement. And the content of the ingredients in a measurement depends on the energy of the measuring particle. The larger the transferred momentum from the lepton $Q \equiv \sqrt{-q^2} = \sqrt{-(p' - p)^2}$ in a DIS, the smaller the measurable ingredients and structure of the hadron. Another important fact in the DIS is that the interaction between the ingredients of a hadron has little impact on the interaction between the lepton and the collided component, because they correspond to interactions with different reaction timescales. For example, if the transferred energy is about 100 GeV, then the interaction of the DIS happens in about 0.67×10^{-26} s, while the interaction between components of hadrons takes place in about 0.67×10^{-22} s after taking into account the time dilation in transferring from the hadron inertial frame to the laboratory frame. This picture was described in the parton (referring to the part of a hadron) model [6], and the scattering cross section of a DIS process is simplified to a sum of contributions from scattering of the lepton with various partons,

$$d\sigma^{\text{DIS}} = \sum_j \int d\xi f_j(\xi) \times d\hat{\sigma}_j, \quad (2.1)$$

where \sum_j is over all partons, $f_j(\xi)$ is the parton distribution function (PDF), and $f_j(\xi)d\xi$ represents the possibility to find a parton j with a momentum fraction of the total momentum of the proton between ξ and $\xi + d\xi$. $\hat{\sigma}_j$ is the scattering cross section between the lepton and partons.

On the other side, according to the general scattering theory, the cross section of the DIS process can be expressed as

$$E' \frac{d\sigma^{\text{DIS}}}{d^3\vec{p}'} \simeq \frac{\pi e^4}{2s} \sum_X \delta^{(4)}(p_X - P - q) |\langle p' | j_\lambda^{\text{lept}} | p \rangle| \frac{1}{q^2} |\langle p_X | j^\lambda | P \rangle|^2 \quad (2.2)$$

$$= \frac{2\alpha^2}{sQ^4} L_{\mu\nu} W^{\mu\nu}, \quad (2.3)$$

where \sqrt{s} is the hadronic center-of-mass energy, and $\alpha = e^2/(4\pi)$ is the fine structure constant. j^λ is the current

$$j^\lambda = \sum_j e_j \bar{\psi}_j \gamma^\lambda \psi_j, \quad (2.4)$$

where ψ_j denote the different partons and e_j are their charges.

The leptonic part in Eq. (2.3) can be calculated easily as

$$L_{\mu\nu} = \frac{1}{2} \text{Tr} \gamma_\nu \not{p} \gamma_\mu \not{p}' = 2(p_\mu p'_\nu + p'_\mu p_\nu - g_{\mu\nu} p \cdot p'). \quad (2.5)$$

The hadronic part in Eq. (2.3) is complicated, and it can be written as

$$W^{\mu\nu} \equiv 4\pi^3 \sum_x \delta^{(4)}(p_X - P - q) \langle P | j^\mu(0) | p_X \rangle \langle p_X | j^\nu(0) | P \rangle \quad (2.6)$$

$$= \frac{1}{4\pi} \int d^4z e^{iq \cdot z} \langle P | j^\mu(z) j^\nu(0) | P \rangle. \quad (2.7)$$

The matrix element in the above equation cannot be calculated analytically due to the non-perturbative properties, but must satisfy the following requirements:

- The current is conserved, i.e., $\partial_\mu j^\mu = 0$ and therefore $q_\mu W^{\mu\nu} = q_\nu W^{\mu\nu} = 0$;
- The P-parity is conserved in QED interactions (weak interaction is omitted);
- The scattering amplitude is unitary, i.e., $W^{\mu\nu}$ is Hermitian, and therefore $(W^{\mu\nu})^* = W^{\nu\mu}$.

Then $W^{\mu\nu}$ should be decomposed to

$$W^{\mu\nu} = \left(-g^{\mu\nu} + \frac{q^\mu q^\nu}{q^2} \right) F_1(x, Q^2) + \frac{(P^\mu - q^\mu P \cdot q / q^2)(P^\nu - q^\nu P \cdot q / q^2)}{P \cdot q} F_2(x, Q^2), \quad (2.8)$$

in which $F_1(x, Q^2)$ and $F_2(x, Q^2)$ are called the structure function, and x is the Bjorken variable, defined as

$$x \equiv \frac{Q^2}{2P \cdot q}. \quad (2.9)$$

Comparing the results in the parton model and the general scattering theory, one obtains

$$F_2(x, Q^2) = \sum_j e_j^2 x f_j(x); \quad F_1(x, Q^2) = \frac{1}{2x} F_2(x, Q^2). \quad (2.10)$$

From the above equation, the structure function has nothing to do with the transferred momentum Q . This behavior is called Bjorken scaling [7], which was verified in experiments at SLAC in 1969. Bjorken scaling is a result of the parton model, and thus its confirmation also supported the parton model.

After a while, Callan and Gross et al. understood that Bjorken scaling implies that the strong interaction is weak at a short distance [8]. At the same time, it was well known that the strong interaction is strong at a long distance. It follows that the strong interaction becomes weaker and weaker as the interaction distance becomes shorter and shorter, i.e., asymptotic freedom. Gross, Wilczek, and Politzer et al. calculated the anomalous dimension of the QCD coupling, and found that it indeed manifests this behavior [9, 10].

2.2 Lagrangian of QCD and Feynman Rules

QCD is a gauge field theory based on the gauge group $SU(3)$ in color space. The Lagrangian of QCD can be written as

$$\mathcal{L}_{QCD} = \mathcal{L}_B + \mathcal{L}_{GF} + \mathcal{L}_G. \quad (2.11)$$

The basic Lagrangian \mathcal{L}_B is

$$\mathcal{L}_B = -\frac{1}{4} F_{\mu\nu}^a F_a^{\mu\nu} + \sum_j \bar{q}_{ja} (i \not{D} - m_j)_{ab} q_{jb}, \quad (2.12)$$

where $F_{\mu\nu}^a$ is the strength tensor with the gluon field \mathcal{A}_μ^a

$$F_{\mu\nu}^a = \partial_\mu \mathcal{A}_\nu^a - \partial_\nu \mathcal{A}_\mu^a + g_s f^{abc} \mathcal{A}_\mu^b \mathcal{A}_\nu^c. \quad (2.13)$$

Here a, b, c are color indices, g_s is the QCD coupling, and f^{abc} is the structure constant of $SU(3)$. $\not{D} = \gamma_\mu D^\mu$ with the covariant derivative is defined as

$$D^\mu = \partial^\mu - i g_s t^a \mathcal{A}_a^\mu, \quad (2.14)$$

where t^a , $a = 1, \dots, 8$ are the generators of $SU(3)$, satisfying

$$\text{Tr}[t^a t^b] = T_F \delta^{ab} = \frac{1}{2} \delta^{ab}. \quad (2.15)$$

m_j denotes the mass of the quark q_j . \mathcal{L}_B is invariant under the gauge transformation

$$q_a(x) \mapsto q'_a(x) = \exp(it \cdot \theta(x))_{ab} q_b(x) \equiv \Omega(x)_{ab} q_b(x), \quad (2.16)$$

$$t \cdot \mathcal{A}_\mu \mapsto t \cdot \mathcal{A}'_\mu = \Omega(x) \left(t \cdot \mathcal{A}_\mu + \frac{i}{g_s} \partial_\mu \right) \Omega^{-1}(x). \quad (2.17)$$

The number of the gluon's physical degree of freedom is less than that the gauge field \mathcal{A}_μ^a has. A well-defined propagator for such a field can only be obtained after

choosing a specific gauge condition. The covariant gauge is generally used, represented by the gauge-fixing Lagrangian

$$\mathcal{L}_{GF} = -\frac{1}{2\lambda} (\partial^\mu \mathcal{A}_\mu^a)^2, \quad (2.18)$$

in which λ is a free parameter. Under this gauge, an additional field, called ghost field, is brought out, whose interaction is contained in the ghost Lagrangian

$$\mathcal{L}_G = \partial_\mu \eta^{a\dagger} (D_{ab}^\mu \eta^b), \quad (2.19)$$

where η^a is a complex scalar field satisfying the anti-communication relation.

When performing the quantization of QCD, the quadratic term of every field is separated to obtain the corresponding propagator. In momentum space, the two-point correlation function of the quark field is

$$\Gamma_{q,ab}^{(2)}(p) = -i\delta_{ab}(\not{p} - m). \quad (2.20)$$

Its inverse gives the quark propagator

$$\Delta_{q,ab}^{(2)}(p) = \frac{i\delta_{ab}}{\not{p} - m + i\epsilon}, \quad (2.21)$$

where $i\epsilon$ with $\epsilon \rightarrow 0$ is a prescription for picking poles coincident with causality. The propagator of the ghost field is

$$\Delta_{\eta,ab}^{(2)}(p) = \frac{i\delta_{ab}}{p^2 + i\epsilon}. \quad (2.22)$$

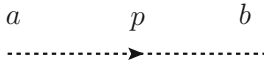
The two-point correlation function of the gluon field under the covariant gauge is

$$\Gamma_{\mathcal{A},ab,\mu\nu}^{(2)}(p) = i\delta_{ab} \left[p^2 g_{\mu\nu} - \left(1 - \frac{1}{\lambda}\right) p_\mu p_\nu \right]. \quad (2.23)$$

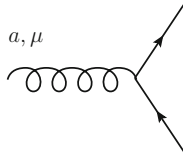
Therefore, the propagator of the gluon field is given as

$$\Delta_{\mathcal{A},ab,\mu\nu}^{(2)}(p) = \frac{i\delta_{ab}}{p^2} \left[-g_{\mu\nu} + (1 - \lambda) \frac{p_\mu p_\nu}{p^2} \right]. \quad (2.24)$$

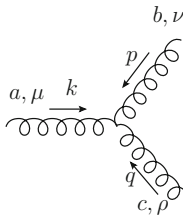
The choice of $\lambda = 1$, corresponding to Feynman gauge, can simplify the calculation significantly in practice. Of course, choosing a general λ and keeping it everywhere in calculation can help to check the correctness of the computation, since the dependence on λ is supposed to be canceled at the end.



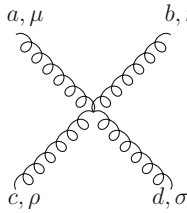
$$\frac{i\delta_{ab}}{p^2 + i\epsilon} \quad (2.32)$$



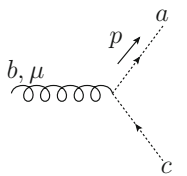
$$ig_s \gamma^\mu t^a \quad (2.33)$$



$$g_s f^{abc} [g^{\mu\nu} (k - p)^\rho + g^{\nu\rho} (p - q)^\mu + g^{\rho\mu} (q - k)^\nu] \quad (2.34)$$



$$-ig_s^2 [f^{abe} f^{cde} (g^{\mu\rho} g^{\nu\sigma} - g^{\mu\sigma} g^{\nu\rho}) + f^{ace} f^{bde} (g^{\mu\nu} g^{\rho\sigma} - g^{\mu\sigma} g^{\nu\rho}) + f^{ade} f^{bce} (g^{\mu\nu} g^{\rho\sigma} - g^{\mu\rho} g^{\nu\sigma})] \quad (2.35)$$



$$g_s f^{abc} p^\mu \quad (2.36)$$

2.3 Renormalization

Making use of the Feynman rules of QCD, one can calculate the amplitudes or cross sections of the hadronic scattering processes. Generally, the amplitudes are hard to be calculated analytically, and should be expanded in a series of the coupling of the strong interaction $\alpha_s = g_s^2/(4\pi) \sim 0.12$.

$$\mathcal{M} = \mathcal{M}_0 + \frac{\alpha_s}{4\pi} \mathcal{M}_1 + \left(\frac{\alpha_s}{4\pi}\right)^2 \mathcal{M}_2 + \dots, \quad (2.37)$$

where $\mathcal{M}_0, \mathcal{M}_1, \mathcal{M}_2$ are referred to as leading order (LO), next-to-leading order (NLO), next-to-next-to-leading order (NNLO) amplitudes, and so forth.

The LO amplitudes are usually easy to calculate. However, the NLO amplitudes are complicated because of the loop integrals in which the momentum of the virtual particles could be infinite, making the integration meaningless. This kind of result is called *ultraviolet-divergent*, a feature of the local field theory. To recover the prediction ability of QCD, renormalization of the theory is needed, which means redefinitions of the parameters in the Lagrangian, such as m_j, g_s . Any observable O is a function of m_j, g_s , i.e., $O(m_j, g_s)$, and meanwhile is finite. Then it is required that the parameters m_j, g_s are also divergent that just cancel the divergences in the loop integrals. It seems unreasonable to use infinite parameters in the calculations. However, if the divergence is universal, which means the structure of infinities in the loop integrals is fixed, then the QCD theory is still predictive after redefinitions of a finite number of parameters. It is remarkable that QCD has been proven to be renormalizable to all orders of α_s [11].

Incorporating infinite parameters in the Lagrangian seems weird at first sight. This is related to the fact that we have considered all fundamental particles as point particles and the interactions are all local.¹ Let us take QED as an example. The electron is charged. If the electron has a finite radius, which has been constrained to be very small experimentally, then the electric potential energy inside the electron would be so large that the individual parts of the electron would be repulsed against each other. As a result, the electron could not be a stable existence. In order to be consistent with reality, the electron is assumed to be point-like. From the uncertainty principle, it is possible that the inside energy of the electron, reflected by the mass, is infinite.

There are two ways to perform renormalization. The first is the bare parameter renormalization. One uses the bare Lagrangian in Eq.(2.11) and its corresponding Feynman rules to calculate the observable $O_1(m_j, g_s)$. Of course, it is divergent. One can use some regularization techniques to represent such divergences, such as $\ln^n(\Lambda/m_j)$ or $1/\epsilon^n$ with $n = 1, 2, \dots$. The former is called cutoff regularization and Λ denotes the upper limit of the loop momentum. The latter is called dimensional regularization and the dimension of the loop momentum is extended from 4 to $4 - 2\epsilon$

¹Here, “local” means that the Lagrangian is a function of fields with the same space-time point. Nonlocal fields and interactions have been discussed in Refs. [12–14].

[15–18]. Taking the renormalization of the mass and coupling as an example, two other observables $O_2(m_j, g_s)$ and $O_3(m_j, g_s)$ are supposed to be calculated before $O_1(m_j, g_s)$ in order to extract the physical or renormalized m_j^R and g_s^R , which are finite. The relations between the bare and renormalized parameters are obtained as

$$m_j^R = m_j + C + \frac{\alpha_s}{4\pi} \frac{1}{\epsilon} + \left(\frac{\alpha_s}{4\pi}\right)^2 \left(\frac{1}{\epsilon^2} + \frac{1}{\epsilon}\right) + \dots, \quad (2.38)$$

$$g_s^R = g_s + C + \frac{\alpha_s}{4\pi} \frac{1}{\epsilon} + \left(\frac{\alpha_s}{4\pi}\right)^2 \left(\frac{1}{\epsilon^2} + \frac{1}{\epsilon}\right) + \dots, \quad (2.39)$$

where C is a finite term and the coefficients of each term have been set to be 1 for simplicity. Then replacing the m_j, g_s in $O_1(m_j, g_s)$ with m_j^R, g_s^R , one finds all divergences cancel out and gets a finite $O_1(m_j^R, g_s^R)$. Notice that the cancelation of divergences takes place order by order in α_s .

The second way is the Bogoliubov-Parasiuk-Hepp-Zimmermann renormalization scheme [19–21]. Since the observables are finite, it is more natural that the parameters they depend on are finite. Therefore, one can use renormalized parameters, such as m_j^R, g_s^R , in the Lagrangian directly and any observable is just a function of renormalized parameters. However, this can be achieved at the cost of adding more interaction terms in the Lagrangian. Explicitly, the fields in the bare Lagrangian should be redefined as

$$q_j = Z_{2,j}^{1/2} q_{j,r}, \quad (2.40)$$

$$A^\mu = Z_3^{1/2} A_r^\mu, \quad (2.41)$$

$$\eta^a = Z_2^{\eta 1/2} \eta_r^a, \quad (2.42)$$

and the Lagrangian in Eq. (2.11) can be rewritten as

$$\mathcal{L}_{QCD} = \mathcal{L}_{QCD}^R + \mathcal{L}_{QCD}^{\text{C.T.}}, \quad (2.43)$$

where $\mathcal{L}_{QCD}^R = \mathcal{L}_{QCD}(m_j \rightarrow m_j^R, g_s \rightarrow g_s^R)$, and $\mathcal{L}_{QCD}^{\text{C.T.}}$ contain counterterms,²

$$\begin{aligned} \mathcal{L}_{QCD}^{\text{C.T.}} = & -\frac{1}{4} \delta_3 (\partial_\mu A_\nu^a - \partial_\nu A_\mu^a)^2 + \sum_j \bar{q}_j (i \delta_2^j \not{\partial} - \delta_m^j) q_j - \delta_2^\eta \eta^{a\dagger} \partial^2 \eta^a \\ & + \sum_j g_s^R \delta_1^j A_\mu^a \bar{q}_j \gamma^\mu q_j - g_s^R \delta_1^{3g} f^{abc} (\partial_\mu A_\nu^a) A_\mu^b A_\nu^c \\ & - \frac{1}{4} g_s^R \delta_1^{A_g} (f^{eab} A_\mu^a A_\nu^b) (f^{ecd} A_\mu^c A_\nu^d) - g_s^R \delta_1^\eta f^{abc} \eta^{a\dagger} \partial^\mu A_\mu^b \eta^c. \end{aligned} \quad (2.44)$$

²All the fields here are renormalized but the subscript 'r' is omitted for simplicity.

Here the various new parameters are defined as

$$\begin{aligned}
\delta_2^j &= Z_{2,j} - 1, & \delta_3 &= Z_3 - 1, & \delta_2^\eta &= Z_2^\eta - 1, & \delta_m^j &= Z_{2,j} m_j - m_j^R, \\
\delta_1^j &= \frac{g_s}{g_s^R} Z_{2,j} Z_3^{1/2} - 1, & \delta_1^{3g} &= \frac{g_s}{g_s^R} Z_3^{3/2} - 1, \\
\delta_1^{4g} &= \frac{g_s^2}{g_s^{R2}} Z_3^2 - 1, & \delta_1^\eta &= \frac{g_s}{g_s^R} Z_2^\eta Z_3^{1/2} - 1.
\end{aligned} \tag{2.45}$$

Now, all the divergences in \mathcal{L}_{QCD} are implicitly incorporated in $\mathcal{L}_{QCD}^{C.T.}$. Specifically, δ_2 (including δ_2^j and δ_2^η), δ_m (including δ_m^j), and δ_3 cancel the divergences in the propagators of quarks, ghosts, and gluons, respectively. δ_1 (including δ_1^j , δ_1^{3g} , δ_1^{4g} , and δ_1^η) cancel the divergences associating vertices. Although they are divergent, they cancel out against the divergences in the loop integrals order by order, resulting in finite predictions on the observables. In general, δ_1 , δ_2 , δ_m , δ_3 can contain arbitrary finite terms. Different finite terms correspond to different renormalized parameters, e.g., m_j^R , g_s^R . It is only required that the same finite terms be used when comparing the predictions on two observables. This means the absolute value of an observable is meaningless as it depends on the definitions of counterterms in the theory. It is the relationship between observables that is predictable and physical. Any specific choice of the finite terms in the counterterms sets a renormalization scheme. The most used are the modified minimal subtraction ($\overline{\text{MS}}$) [22, 23] and on-shell renormalization schemes. The relation between different renormalization schemes is universal. If one has the results in one renormalization scheme, it is easy to translate them to other schemes.

After calculating the counterterms in QCD, i.e., δ_1 , δ_2 , δ_m , δ_3 , the running behaviors of the renormalized parameters m_j^R , g_s^R as a function of the scale are also known. Here the scale refers to the magnitude of the energy. The content of a hadron is different when measured by particles with different energy. Thus, the parameters m_j^R , g_s^R are also different under different energy scale. In QCD, the running equation of g_s^R , i.e., the renormalization group equation (RGE), reads as

$$\beta(g_s^R) \equiv \frac{dg_s^R}{d \ln \mu} = g_s^R \frac{d}{d \ln \mu} [-\ln(1 + \delta_1^j) + \ln(1 + \delta_2^j) + \frac{1}{2} \ln(1 + \delta_3)]. \tag{2.46}$$

The scale μ is a result of choosing the dimensional regularization scheme, where one should make the replacement $g_s^R \rightarrow g_s^R \mu^\epsilon$ so that the mass dimension of g_s^R is still zero. At one-loop level,

$$\beta(g_s^R) = -\frac{g_s^{R3}}{(4\pi)^2} \left(\frac{11}{3} C_A - \frac{4}{3} n_f T_F \right) = -\frac{g_s^{R3}}{3(4\pi)^2} (33 - 2n_f) = -\frac{g_s^R \alpha_s}{4\pi} \beta_0, \tag{2.47}$$

where $C_A = 3$ is the Casimir operator of the adjoint representation in $SU(3)_C$, n_f is the number of active quarks, and $\beta_0 = (11 - \frac{2}{3}n_f)$. The present experiments show $n_f = 6$. Therefore $\beta(g_s^R)$ is negative, which means the strong interaction coupling becomes smaller with the increase of scale. It is just the behavior of asymptotic freedom.

Solving the RGE of $\beta(g_s^R)$ above, one obtains the running coupling at one-loop level,

$$\alpha_s(\mu) = \frac{\alpha_s(\mu_0)}{1 + \frac{\alpha_s(\mu_0)}{4\pi} \beta_0 \ln \frac{\mu^2}{\mu_0^2}}. \quad (2.48)$$

Since $\beta_0 > 0$, when $\mu \rightarrow \infty$, $\alpha_s(\mu) \rightarrow 0$. On the other hand, when $\mu \rightarrow \Lambda_{\text{QCD}} \equiv \mu_0 \exp\left(-\frac{2\pi}{\alpha_s(\mu_0)\beta_0}\right)$, $\alpha_s(\mu) \rightarrow \infty$. It suggests the perturbative QCD is not applicable any more. Λ_{QCD} denotes the lower energy limit in applying perturbative QCD, and is found to be a few hundreds of MeV.

References

1. M. Gell-Mann, Symmetries of baryons and mesons. *Phys. Rev.* **125**, 1067–1084 (1962)
2. G. Zweig, An $SU(3)$ model for strong interaction symmetry and its breaking. CERN-TH **401**
3. G. Zweig, An $SU(3)$ model for strong interaction symmetry and its breaking 2. CERN-TH **412**
4. H. Fritzsch, M. Gell-Mann, Current algebra: quarks and what else? in *eConf C720906V2*, pp. 135–165 (1972). [arXiv:hep-ph/0208010](https://arxiv.org/abs/hep-ph/0208010)
5. H. Fritzsch, M. Gell-Mann, H. Leutwyler, Advantages of the color octet gluon picture. *Phys. Lett. B* **47**, 365–368 (1973)
6. R. Feynman, *Photon Hadron Interactions*. W.A. Benjamin, New York
7. J. Bjorken, Asymptotic sum rules at infinite momentum. *Phys. Rev.* **179**, 1547–1553 (1969)
8. J. Callan, Curtis G., D.J. Gross, Bjorken scaling in quantum field theory. *Phys. Rev. D* **8**, 4383–4394 (1973)
9. D. Gross, F. Wilczek, Ultraviolet behavior of nonabelian gauge theories. *Phys. Rev. Lett.* **30**, 1343–1346 (1973)
10. D. Gross, F. Wilczek, Asymptotically free gauge theories. 1. *Phys. Rev. D* **8**, 3633–3652 (1973)
11. G. 't Hooft, Renormalization of massless yang-mills fields. *Nucl. Phys. B* **33**, 173–199 (1971)
12. H. Yukawa, Quantum theory of nonlocal fields. 1. Free fields. *Phys. Rev.* **77**, 219–226 (1950)
13. H. Yukawa, Quantum theory of nonlocal fields. 2: irreducible fields and their interaction. *Phys. Rev.* **80**, 1047–1052 (1950)
14. A. Pais, G. Uhlenbeck, On field theories with nonlocalized action. *Phys. Rev.* **79**, 145–165 (1950)
15. G. 't Hooft, M.J.G. Veltman, Regularization and renormalization of gauge fields. *Nucl. Phys. B* **44**, 189–213 (1972)
16. C.G. Bollini, J.J. Giambiagi, Lowest order divergent graphs in nu-dimensional space. *Phys. Lett. B* **40**, 566–568 (1972)
17. J.F. Ashmore, A method of gauge invariant regularization. *Lett. Nuovo Cim.* **4**, 289–290 (1972)
18. G.M. Cicuta, E. Montaldi, Analytic renormalization via continuous space dimension. *Lett. Nuovo Cim.* **4**, 329–332 (1972)
19. N. Bogoliubov, O. Parasiuk, *Acta Math.* **97**, 227 (1957)
20. K. Hepp, Proof of the Bogolyubov-Parasiuk theorem on renormalization. *Commun. Math. Phys.* **2**, 301–326 (1966)

21. W. Zimmermann, Convergence of Bogolyubov's method of renormalization in momentum space. *Commun. Math. Phys.* **15**, 208–234 (1969)
22. G. 't Hooft, Dimensional regularization and the renormalization group. *Nucl. Phys. B* **61**, 455–468 (1973)
23. S. Weinberg, New approach to the renormalization group. *Phys. Rev. D* **8**, 3497–3509 (1973)

Chapter 3

QCD Perturbative Calculation of the Scattering Processes at Hadron Colliders

When two high energetic particles A and B collide, a large number of final-state particles can be produced. The differential cross section for the specific process $A(p_A) + B(p_B) \rightarrow X_1(p_1), X_2(p_2), \dots, X_n(p_n)$ is given by

$$d\sigma = \frac{1}{2s} d\Phi_n |\mathcal{M}(p_A, p_B \rightarrow p_1, p_2, \dots, p_n)|^2, \quad (3.1)$$

where \sqrt{s} is the center-of-mass energy. The factor $1/2s$ is obtained in the case that the two colliding particles are massless and moving along the same beam line. It is boost-invariant in the beam line direction. $d\Phi_n$ denotes the phase space of n body final states, defined as

$$d\Phi_n = \left(\prod_{f=1}^n \frac{d^3 p_f}{2E_f (2\pi)^3} \right) (2\pi)^4 \delta^{(4)} \left(p_A + p_B - \sum_{f=1}^n p_f \right), \quad (3.2)$$

It is invariant under Lorentz transformations. $\mathcal{M}(p_A, p_B \rightarrow p_1, p_2, \dots, p_n)$ is the scattering amplitude of the process, which is also Lorentz invariant, calculated by

$$\begin{aligned} & (2\pi)^4 \delta^{(4)} \left(p_A + p_B - \sum_{f=1}^n p_f \right) \mathcal{M}(p_A, p_B \rightarrow p_1, p_2, \dots, p_n) \\ & \equiv \lim_{t_0 \rightarrow \infty(1-i\epsilon)} \left({}_0 \langle p_1 p_2 \dots p_n | T \left(\exp \left[-i \int_{-t_0}^{t_0} dt H_I(t) \right] \right) | p_A p_B \rangle_0 \right)_{\text{C.A.}} \end{aligned} \quad (3.3)$$

where $|p_A p_B\rangle_0$ and $|p_1 p_2 \dots p_n\rangle_0$ denote the wave functions of the initial- and final-state free particles, H_I is the Hamiltonian in the interaction picture, and T is the operator of time-ordering. The subscript ‘‘C.A.’’ means only the connected and amputated Feynman diagrams need to be considered. The right-hand side of the above equation is hard to calculate analytically, and usually expanded in series,

$$\exp \left[-i \int_{-t_0}^{t_0} dt H_I(t) \right] = 1 - i \int_{-t_0}^{t_0} dt H_I(t) + \dots, \quad (3.4)$$

Each contribution from the series can be illustrated by a kind of Feynman diagrams. In the high-energy scattering processes, the QCD coupling is small enough so that the perturbative expansion is applicable.

3.1 Factorization

Since there are quarks or gluons in the initial and final states, the wave functions for the free particles are not well-defined because of color confinement. So σ in Eq. (3.1) does not correspond to any observable. Though the quarks can be considered as free particles in the hard scattering due to asymptotic freedom, the energy scale with the quarks before and after the scattering is in the non-perturbative region. The factorization between these different parts of the process is essential to obtain the prediction for any physical observable. The picture of factorization is illustrated in part by the parton model when discussing the DIS process in the last chapter. The full explanation in QCD can be found in [1].

Here we look at one simple example, i.e., the Drell–Yan process $p(p_A) + \bar{p}(p_B) \rightarrow \mu^+(p_1) + \mu^-(p_2) + X$ at the proton and antiproton collider with the center-of-mass energy of \sqrt{S} . The four momenta of the final-state μ^+ and μ^- can be measured, and therefore the square of the invariant mass of the lepton pair

$$Q^2 = (p_1 + p_2)^2 \quad (3.5)$$

and rapidity

$$y = \frac{1}{2} \ln \frac{(p_1 + p_2) \cdot p_A}{(p_1 + p_2) \cdot p_B} \quad (3.6)$$

can also be obtained from experimental measurements. The factorization theorem gives [1]

$$\begin{aligned} \frac{d\sigma}{dQ^2 dy} \sim & \sum_{a,b} \int_{x_A}^1 d\xi_A \int_{x_B}^1 d\xi_B f_{a/p}(\xi_A, \mu) f_{b/\bar{p}}(\xi_B, \mu) H_{ab} \left(\frac{\xi_A}{x_A}, \frac{\xi_B}{x_B}, Q, \mu, \alpha_s(\mu) \right) \\ & + \mathcal{O} \left(\frac{\Lambda_{\text{QCD}}^2}{Q^2} \right). \end{aligned} \quad (3.7)$$

The first line is called the leading twist contribution while the second line contains higher twist contributions, which are power suppressed by Q^2 . The subscripts a, b denote the partons in the proton and antiproton, respectively. x_A, x_B are defined as

$$x_A = e^y \sqrt{\frac{Q^2}{S}}, \quad x_B = e^{-y} \sqrt{\frac{Q^2}{S}}. \quad (3.8)$$

$H_{ab} \left(\frac{\xi_A}{x_A}, \frac{\xi_B}{x_B}, Q, \mu, \alpha_s(\mu) \right)$ describes the hard scattering process, which can be calculated perturbatively. The non-perturbative effects are all included in the PDFs $f_{a/p}(\xi_A, \mu)$ and $f_{b/\bar{p}}(\xi_B, \mu)$, which denote the possibility to find a parton with a momentum fraction of ξ in the proton. The definitions for the quark and gluon are given by [2]

$$\begin{aligned} f_{q/p}(\xi, \mu) &= \frac{1}{4\pi} \int dx^- e^{-i\xi P^+ x^-} \langle P | \bar{\psi}(0, x^-, 0_\perp) \gamma^+ \mathcal{G} \psi(0, 0, 0_\perp) | P \rangle, \\ f_{g/p}(\xi, \mu) &= \frac{1}{2\pi\xi P^+} \int dx^- e^{-i\xi P^+ x^-} \langle P | F_a(0, x^-, 0_\perp)^{+\nu} \mathcal{G}_{ab} F_b(0, 0, 0_\perp)_\nu^+ | P \rangle. \end{aligned} \quad (3.9)$$

where $P^\pm = (P^0 \pm P^3)/\sqrt{2}$ and

$$\mathcal{G} = \mathcal{P} \exp \left[ig \int_0^{x^-} dy^- A_c^+(0, y^-, 0_\perp) t_c \right], \quad (3.10)$$

with \mathcal{P} being the operator of path-ordering. The PDFs satisfy the RGE

$$\frac{d}{d \ln \mu} f_{a/p}(\xi, \mu) = \sum_b \int_\xi^1 \frac{d\zeta}{\zeta} P_{a/b}(\zeta, \alpha_s(\mu)) f_{b/p}\left(\frac{\xi}{\zeta}, \mu\right), \quad (3.11)$$

with $P_{a/b}(\zeta, \alpha_s(\mu))$ the Altarelli–Parisi splitting function [3]. Notice that Eq. (3.7) is different from Eq. (2.1) because the PDFs, $f_{a/p}(\xi_A, \mu)$ and $f_{b/\bar{p}}(\xi_B, \mu)$, depend on the energy scale.

The factorization form of cross sections is very useful as it divides the complicated process into different two parts. One is related to the non-perturbative low-energy region of QCD, and can be obtained by global fitting with some precise measured processes. The other is governed by QCD in the high-energy region, where asymptotic freedom occurs and thus perturbative calculation can be applied. Although proven explicitly only for a few processes, it is usually considered valid and has been used ubiquitously in perturbative QCD calculations. The agreement between the theoretical predictions and experimental measurements confirms its validation and ensures its application to more general processes.

3.2 Infrared Safety

In the calculation of QCD higher-order corrections, one should include the virtual and real corrections simultaneously. The virtual corrections contain ultraviolet (UV) divergences, which is canceled after renormalization, as well as infrared divergences, i.e., the soft and collinear divergences. The real corrections have infrared divergences only.

In QED, the energy of soft photons is almost vanishing so that the state containing a single electron and the state containing an electron and a bunch of soft photons consist of a degenerate state of the Hamiltonian. The sum of all degenerate states contains no soft divergence. In QCD, the situation is more complicated because of the additional collinear divergence. The state containing a single quark and the state containing a quark and a collinear gluon also consist of a degenerate state of the Hamiltonian. All the infrared divergences cancel out in the sum of all degenerate initial and final states. This is guaranteed by the famous Kinoshita–Lee–Nauenberg (KLN) theorem [4, 5].

In practice, for processes at hadron colliders, the collinear divergences of the virtual and real corrections do not cancel completely since the momenta of initial partons are constrained. However, the left collinear divergence is universal and can be absorbed by renormalization of the PDFs. We can take the Drell–Yan process as an example, of which the LO, virtual and real corrections are shown in Fig. 3.1. The soft divergences in the diagrams (b), (c), and (d) cancel completely, while there are still collinear divergences left. The reason is that the collinear divergent parts in the virtual and real corrections are proportional to the LO amplitude squared with different momenta. In processes with jets in the final state, the collinear divergences in the jets cancel in the sum of the real and virtual corrections.

Any infrared-safe observable should not depend on the number of the soft and collinear particles, i.e., insensitive to the emission of soft and collinear particles. Specifically, the infrared-observable $F_J^n(p_1, p_2, \dots, p_n)$, $n \geq m$ in the general production processes with m jets, containing n partons, must meet the conditions [6]

$$\begin{aligned}
 & F_J^{n+1}(p_1, \dots, p_{j-1}, p_j = \lambda q, p_{j+1}, \dots, p_{n+1}) \\
 & \rightarrow F_J^n(p_1, \dots, p_{j-1}, p_{j+1}, \dots, p_{n+1}) \\
 & \text{if } \lambda \rightarrow 0,
 \end{aligned} \tag{3.12}$$

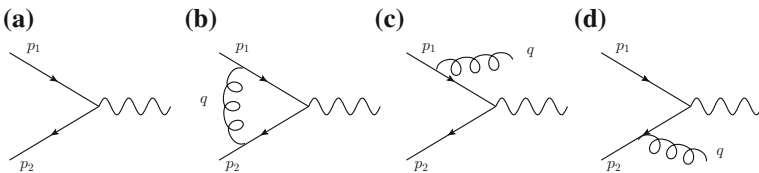


Fig. 3.1 The Feynman diagrams for Drell–Yan production. Diagram **a** is the LO, and diagram **b** is the virtual correction. Diagrams **c** and **d** are the real corrections

$$F_J^{n+1}(p_1, \dots, p_i, \dots, p_j, \dots, p_{n+1}) \rightarrow F_J^n(p_1, \dots, p, \dots, p_{n+1})$$

$$\text{if } p_i \rightarrow zp, p_j \rightarrow (1-z)p, \quad (3.13)$$

$$F_J^n(p_1, \dots, p_n) \rightarrow 0 \text{ if } p_i \cdot p_j \rightarrow 0. \quad (3.14)$$

Equation (3.12) means that the exclusive soft particles cannot be observed. Equation (3.13) requires that the collinear particles should be observed as a whole object. Equation (3.14) guarantees that the LO cross section is finite at a certain order of α_s . The inclusive total cross section of $e^+e^- \rightarrow$ hadrons is a simple example of the infrared-safe observable.

The infrared-safe observable is more complicated when some kinematical information about the final-state particles is required. The theoretical prediction for these kinds of processes involves virtual and real corrections, which have different phase spaces. The infrared divergences can appear in either part. They could be regularized by the dimensional regularization in the similar way to the UV divergence. The dimension of the space-time is extended to $4 - 2\epsilon$. The infrared divergences show up in the form of $1/\epsilon$ and $1/\epsilon^2$ at the one-loop level. The quadratic divergence $1/\epsilon^2$ comes from the both soft and collinear regions. In contrast, the UV divergences show up only in the form of $1/\epsilon$ at the one-loop level. Any infrared-safe observable should contain no such divergences.

For example, the jet algorithm is widely used to cluster the partons generated in hard collisions to experimentally observed jets. In the jet algorithm, a parameter is defined to describe the distance among partons or between the partons and beam lines [7],

$$d_{ij} = \min(k_{ii}^{2p}, k_{jj}^{2p}) \frac{\Delta_{ij}^2}{R^2}, \quad (3.15)$$

$$d_{iB} = k_{ii}^{2p}, \quad (3.16)$$

where $\Delta_{ij}^2 = (y_i - y_j)^2 + (\phi_i - \phi_j)^2$, k_{ii} , y_i , and ϕ_i are the momentum, rapidity, and azimuthal angle of the i -th parton. R is the critical radius, usually chosen in the range $0.4 \sim 1$ at hadron colliders. The exponent p is usually chosen as 1, 0, -1 , corresponding to k_t , Cambridge/Aachen, and anti- k_t algorithm, respectively. All of them are infrared safe. When applying the jet algorithm, the whole partons are included in a set A . The distance parameters d_{ij} and d_{iB} are calculated for the partons in the set A . If the smallest is d_{iB} , then move the i -th parton to another set B . If the smallest is d_{ij} , then combine the i -th and j -th partons to a new parton in the set A , deleting the original i -th and j -th partons. The above procedure is repeated until the set A is empty. The set B contains all the jets clustered from the partons. In the combination of two partons, there are usually two schemes. The first is simply summing the four momenta of the two partons, resulting in massive jets. The other is summing by a

weight E_i , i.e.,

$$E_{t, \text{jet}} = \sum_i E_{ti}, \quad (3.17)$$

$$\eta_{\text{jet}} = \frac{1}{E_{t, \text{jet}}} \sum_i E_{ti} \eta_i, \quad (3.18)$$

$$\phi_{\text{jet}} = \frac{1}{E_{t, \text{jet}}} \sum_i E_{ti} \phi_i, \quad (3.19)$$

which generates massless jets. At the end of the jet clustering, a minimum transverse momentum cut is applied to make sure that a very soft element in the set B is not counted as a measurable jet, ensuring the infrared safety of the observables. A comprehensive review on the jet algorithm can be found in [8]. In practice, the FastJet package can be utilized to implement most of the jet algorithms [9].

3.3 QCD Higher-Order Effects

In the past decades, the SM has been tested by a large number of experiments. The current LHC data also show results consistent with the SM. These agreements impose strong constraints on any new physics model, if exists, and suggest that new physical signal would show up as a small difference from the SM backgrounds. Therefore, precise predictions of the SM background as well as the new physics signal are crucial. The importance of QCD higher-order effects is summarized as

- Decreasing the renormalization scale uncertainty. In principle, the full theoretical prediction does not depend on any scale. But the perturbative theoretical prediction is obtained in a series of α_s . The uncalculated higher order results induce renormalization scale uncertainty. Inclusion of more high-order results could reduce the renormalization scale uncertainty.
- Decreasing the factorization scale uncertainty. The factorization scale involves in the factorization of the cross section at a hadron collider. The non-perturbative part of the cross section can only be obtained by fitting with experiments. But its dependence on the factorization scale can be computed. More precise perturbative calculation would result in less dependence of the cross section on the factorization scale.
- Simulating the jet production accurately. At the LO, each jet contains only a few partons theoretically. At higher order, after applying the jet algorithm, more partons are included in one jet, which is a more accurate simulation of the reality.
- Taking into account the transverse momenta of the initial partons. The total transverse momenta of the initial partons is vanishing at the LO. At higher order, the QCD radiation from the initial partons brings nonvanishing momentum to the

final state.¹ Thus, more accurate prediction of the kinematical distributions of the final state can be obtained.

The QCD higher-order effects consist of the virtual and real corrections for a $n \rightarrow m$ scattering process. At the NLO, they are the one-loop virtual corrections and the tree-level $n \rightarrow m + 1$ cross sections. At the NNLO, they include the two-loop virtual corrections, one-loop $n \rightarrow m + 1$, and tree-level $n \rightarrow m + 2$ cross sections.

In the virtual corrections, the amplitudes are evaluated by reducing the tensor integrals to combination of the scalar integrals and momenta of the external particles, the divergent and convergent parts of which can be numerically computed by programs, such as QCDLoop [10] and LoopTools [11]. This kind of method is generally used in calculating the cross section of $2 \rightarrow 2$ and $2 \rightarrow 3$ processes. Recently, an alternative method, called generalized unitarity method, was developed to deal with more complicated processes involving more external particles in the scattering [12–19]. With this method, the coefficient of the one-loop scalar can be obtained from tree-level amplitudes, which accelerates the calculation. This method has been implemented in a lot of programs, e.g., Helac-NLO/CutTools [20, 21], Golem/Samurai [22, 23], BlackHat/Sherpa [24, 25], Rocket [26], MadLoop [27], GoSam [28], and MCFM [29]. The state of the art is the QCD NLO corrections to W and five jets production at hadron colliders [30].

The two-loop integrals are dealt with the similar methods. But the scalar integrals are not independent any more. The independent ones are chosen as the master integrals, while others can be expressed as a combination of them using the integration by parts (IBP) [31, 32] and Lorentz invariance identities (LI) [33, 34]. This procedure has been automated in the programs, such as AIR [35], FIRE [36], and REDUZE [37]. Therefore, only the master integrals should be evaluated in practice. The Mellin Barnes (MB) representation [38, 39] and the differential equations (DE) [40–42] are widely employed to perform the integration. The basic formula in the MB representation is

$$\frac{1}{(X+Y)^\lambda} = \frac{1}{\Gamma(\lambda)} \frac{1}{2\pi i} \int_{-i\infty}^{+i\infty} dz \Gamma(\lambda+z) \Gamma(-z) \frac{Y^z}{X^{\lambda+z}}. \quad (3.20)$$

It splits the complicate denominator into simpler ones, which is easy to integrate, with the cost of additional integrations. Here, the contour of the integration is chosen such that the poles associating $\Gamma(\dots + z)$, called left poles, are to the left of the contour and the poles associating $\Gamma(\dots - z)$, called right poles, are to the right of the contour. z is the MB integration variable. A normal two-loop integral would reduce to a multifold MB integration. Fortunately, some programs written in the Maple or Mathematica software can help to evaluate them [43–45]. The method of DE makes use of the procedure of reducing all scalar integrals to master integrals. By taking some derivatives of the given master integrals with respect to the known kinematical invariants and masses, one obtains a system of DE that can be solved with appropriate

¹In the case that the final state contains color-charged particles, the QCD radiation from the final state would also make contribution.

boundary conditions. The boundary conditions are the master integrals with some special parameters, which is easier to calculate.

The amplitudes of the real corrections are simpler than those of virtual corrections, but the phase space integrations become more complicated because of the more final-state particle, infrared divergences, and possible kinematical cuts. For the special case with two or three particles in the final state, one can integrate the whole phase space analytically. But for the more general cases with more final-state particles, especially massive particles, or with kinematical cuts imposed, there is almost no way to perform the phase space integration analytically. One has to turn to the numerical integrations. However, the infrared divergences hinder the naive numerical calculation. One still needs to subtract or split the divergent phase space in advance, whose contribution should be added back in an analytical form. The widely used methods to deal with the NLO real corrections are phase space slicing [46–48], dipole subtraction [6, 49, 50], and FKS subtraction [51]. In the two cutoff phase space slicing methods [48], the behavior of the cross section near the infrared divergent region is analytically calculated in the form of $\ln^n(\delta_{s,c})$, with $n = 1, 2$, and $\delta_{s,c}$ define the boundaries between the divergent and nondivergent phase space, i.e., the soft gluon energy is less than $\delta_s\sqrt{s}/2$ and the invariant mass of two collinear particles is less than $\delta_{c,s}$, where \sqrt{s} is the partonic center-of-mass energy. The contribution from the non-divergent region can be numerically integrated. The sum of the two parts does not depend on $\delta_{s,c}$. The dipole and FKS subtraction methods construct the subtraction terms which mimic the real cross section in the infrared divergent region and can also be integrated analytically. At the level up to NLO, the cross section of the m jets production is

$$d\sigma_{\text{NLO}} = \int_{d\Phi_{m+1}} (d\sigma_{\text{NLO}}^{\text{R}} - d\sigma_{\text{NLO}}^{\text{S}})|_{n=4} + \left[\int_{d\Phi_{m+1}} d\sigma_{\text{NLO}}^{\text{S}}|_{n=4-2\epsilon} + \int_{d\Phi_m} d\sigma_{\text{NLO}}^{\text{V}}|_{n=4-2\epsilon} \right], \quad (3.21)$$

where $d\sigma_{\text{NLO}}^{\text{S}}$ is the subtraction corresponding to the real correction $d\sigma_{\text{NLO}}^{\text{R}}$. It has the same behavior as $d\sigma_{\text{NLO}}^{\text{R}}$ in the infrared divergent region. So the difference between them can be just evaluated in the four-dimensional space-time. Meanwhile, $d\sigma_{\text{NLO}}^{\text{S}}$ is simpler than $d\sigma_{\text{NLO}}^{\text{R}}$ so that it can be integrated analytically at the infrared divergent region in $4 - 2\epsilon$ dimensional space-time, giving rise to $1/\epsilon^n$ with $n = 1, 2$, that cancel against the infrared poles in the virtual correction $d\sigma_{\text{NLO}}^{\text{V}}$. At the NNLO level, the phase space slicing and subtraction methods are much more complicated because of the overlap of various divergent regions. Kosower [52, 53] and Weinzierl [54, 55] tried to extend the dipole subtraction method to NNLO, but only obtain the contribution from the leading order result in N_c expansion. The more recent methods of dealing with the real corrections at NNLO include sector decomposition [56–58], antenna subtraction [59–62], q_T subtraction [63–65], STRIPPER subtraction [66], and threshold subtraction [67–71]. The applications of these methods are summarized in Table 3.1. In particular, the q_T subtraction makes use of the formalism of

Table 3.1 The processes at the hadron collider, if not specified, calculated differentially at NNLO in QCD

NNLO calculation methods	Processes
Sector decomposition	Higgs boson production [56, 72]
	Higgs boson decay [73]
	Drell–Yan process [74]
Antenna subtraction	$e^+e^- \rightarrow 3$ jets [75–78]
	$gg \rightarrow 2$ jets [79–82]
	$t\bar{t}$ production [83–85]
	$pp \rightarrow Z + j$ [86]
q_T subtraction	Higgs boson production [87]
	Drell–Yan process [88, 89]
	VH associated production [90, 91]
	VV production [92–95]
STRIPPER subtraction	$t\bar{t}$ production [96–98]
	$pp \rightarrow H + j$ [99, 100]
	Top quark decay [101]
	t -channel single top quark [102]
Threshold subtraction	Top quark decay [67]
	$e^+e^- \rightarrow t\bar{t}$ [68]
	$pp \rightarrow W + j$ [69]
	$pp \rightarrow H + j$ [70]

resummation which is valid to all orders of α_s . The cross section near the infrared divergent region is obtained by expanding the resummation formalism according to α_s . At NNLO, the cross section is divergent like $\ln^n(Q_T/M)$ with $n = 1, 2, 3, 4$, where Q_T defines the boundary between the divergent ($q_T < Q_T$) and nondivergent ($q_T > Q_T$) regions. The result from the nondivergent region depends on Q_T numerically. The sum of the two parts does not depend on Q_T . Notice that the nondivergent ($q_T > Q_T$) region still contains infrared divergence which can be subtracted using the method applicable at NLO.

3.4 Resummation Methods

The QCD perturbative method has proven to be successful in describing the high-energy scattering process. But it has the problem of nonconvergence in some cases. For example, when the total transverse momentum p_T of the final state in the low p_T region is observed or additional radiation of large p_T jets is vetoed, there exists large logarithms of the form $\alpha_s^n/p_T^2 \ln^m(Q^2/p_T^2)$ with $n = 1, \dots$ and $m \leq 2n - 1$. The

expansion in a series of α_s is not valid any more. These kinds of large logarithms should be resummed to all order in α_s .

Resummation of soft gluon effects is a powerful way to surpass the fixed-order perturbative calculations. It is applicable to the processes in which the hard gluon radiations are inhibited, such as a heavy particle production and a jet-vetoed production. These kinds of the regions of the phase space are described by a threshold variable, namely ω , which is defined according to the process involved. For example, it is $1 - T$, with T the thrust, for the e^+e^- annihilation to jets [103], and $1 - M^2/S$ for the Drell–Yan process [104], where M is the invariant mass of the final states and \sqrt{S} is the total available energy. And for the Drell–Yan process at small Q_T , it is $\omega = Q_T^2/Q^2$. It is clear that $\omega \rightarrow 0$ corresponds the threshold region. The fixed-order perturbative calculations in the threshold region is not stable due to the presence of large logarithms $\alpha_s^n \ln^m \omega/\omega$ with $m \leq 2n - 1$, which can be resummed.

The threshold variable ω is chosen to be a dimensionless function of the momenta of the final-state particles and the initial total energy, and to encode the information of the threshold region of the final state. In order to ensure infrared safety, the threshold variable should also respect the relations similar to Eqs. (3.12)–(3.14), such as

$$\omega_n(k_1, \dots, (1 - \alpha)k_{n-1}, \alpha k_{n-1}) = \omega_{n-1}(k_1, \dots, k_{n-1}). \quad (3.22)$$

Since the resummation is closely related to the factorization of the cross section, it is mandatory to figure out the threshold variables in terms of the individual components of the factorized cross section. For illustration, the factorized cross section can be generally written as

$$\begin{aligned} \sigma(\omega) = C \int \prod_{i=H,J,S,1,2} d\omega_i H(\omega_H) \prod_j J_j(\omega_{J,j}) S(\omega_S) f_1(\omega_1) f_2(\omega_2) \\ \delta(\omega - \omega_H - \sum_j \omega_{J,j} - \omega_S - \omega_1 - \omega_2), \end{aligned} \quad (3.23)$$

where H , J , S denote the hard function, jet function, and soft function, respectively. And f_i ($i = 1, 2$) are the PDFs. The coefficient C is chosen such that the leading order (LO) expansion of the formula would recover the LO cross section. The various scales and kinematics dependence are not shown explicitly since we are only interested in the threshold variables here. We should note that the above equation is established only in the threshold region, i.e., $\omega \rightarrow 0$. The individual ω_i is only associated with its corresponding function, which means, for example, that the jet function should not depend on ω_S . The δ function exists due to the assumption that higher order effects, such as contribution scaling as $\mathcal{O}(\omega_S^2)$, are power suppressed and therefore neglected here. The integration is applied to the intermediate threshold variables, not including ω . Because the hard function H does not affect the momenta of the final-state particles, it should provide no contribution to the threshold region. So we can omit ω_H and the corresponding integration. In some cases, certain parts in the above equation are not needed. For instance, there are no f_i in the process of e^+e^-

annihilation to jets. In practice, the individual part would behave as $\alpha_s^n \ln^m \omega_i/\omega_i$ with $m \leq 2n - 1$ near the threshold region. And the integration translates them into $\alpha_s^n \ln^m \omega/\omega$ with $m \leq 2n - 1$. Meanwhile, if some technic, especially RGE,² is employed, then these large logarithms can be resummed.

Actually, the fixed-order calculation would give rise to the singular terms $\alpha_s^n \ln^m \omega/\omega$ with $m = 2n - 1, 2n - 2, \dots, 1$ after the analytical integration of the phase space under certain constraints. More generally, a threshold variable can be defined as $\omega_0 = Q_{\text{low}}^2/Q_{\text{high}}^2 \rightarrow 0$ for the process containing two different scales Q_{low} and Q_{high} with $Q_{\text{low}} \ll Q_{\text{high}}$. The cross section is expected to contain the singular terms $\alpha_s^n \ln^m \omega_0/\omega_0$, $m = 2n - 1, 2n - 2, \dots, 1$. It is crucial to resum these singular terms to provide stable theoretical predictions.

To resum the singular terms, it is better to understand their origin. In the dimensional regularization, they appear along with the divergences, such as at NLO,

$$\frac{1}{\epsilon} \frac{1}{[\omega Q^a]^{1+\epsilon}} \quad (3.24)$$

with $a = 1$ or 2 . Therefore, a thorough understanding of the pole structure can help to resum the large logarithms.

3.4.1 Traditional Resummation Method

Below we illustrate the traditional resummation method in detail through the example of $e^+e^- \rightarrow$ dijet. The cross section in the threshold region can be factorized as [105]

$$\begin{aligned} \sigma(w) = & H \left(\frac{p_1}{\mu}, \frac{p_2}{\mu}, \zeta_i \right) \int \frac{dw_1}{w_1} \frac{dw_2}{w_2} \frac{dw_s}{w_s} J_1 \left(\frac{p_1 \cdot \zeta_1}{\mu}, w_1 \left(\frac{Q}{\mu} \right)^{a_1} \right) \\ & \times J_2 \left(\frac{p_2 \cdot \zeta_2}{\mu}, w_2 \left(\frac{Q}{\mu} \right)^{a_2} \right) S \left(w_s \frac{Q}{\mu}, n_i, \zeta_i \right) \delta(w - w_1 - w_2 - w_s), \end{aligned} \quad (3.25)$$

where the ω s in the denominator are extracted from the jet and soft functions. The soft function depends on the directions n_i of the jets but not the energies of the jets. The constant vectors ζ_1 and ζ_2 ($\zeta_i^2 \neq 0$) are used to gauge the gluon field via $\zeta_i \cdot A = 0$. In such a gauge, the Sudakov double logarithms are encoded in the jet function. The parameter a_i is related to the kinematics of the scattering process. For instance, $a = 1$ and $a = 2$ for the initial- and final-state jets, respectively, in the DIS.

The delta function in above equation shows the convolution of different parts in the cross section, making the analysis complicated. It is more convenient to work in

²In traditional resummation method, the independence of the cross section on the choice of gauge vectors is crucial in resumming the large logarithms.

the Laplace transformed space, where the different parts are multiplied together,

$$\begin{aligned} \tilde{\sigma}(N) = \int_0^\infty dw e^{-Nw} \sigma(w) = H \left(\frac{p_1}{\mu}, \frac{p_2}{\mu}, \zeta_i \right) & \tilde{J}_1 \left(\frac{p_1 \cdot \zeta_1}{\mu}, \frac{Q}{\mu N^{1/a_1}} \right) \\ & \times \tilde{J}_2 \left(\frac{p_2 \cdot \zeta_2}{\mu}, \frac{Q}{\mu N^{1/a_2}} \right) \tilde{S} \left(\frac{Q}{\mu N}, n_i, \zeta_i \right) \end{aligned} \quad (3.26)$$

with

$$\tilde{J}(N) = \int_0^\infty \frac{dw_1}{w_1} e^{-Nw_1} J(w_1), \quad (3.27)$$

$$\tilde{S}(N) = \int_0^\infty \frac{dw_s}{w_s} e^{-Nw_s} S(w_s). \quad (3.28)$$

The region of $w \rightarrow 0$ correspond to the limit $N \rightarrow \infty$. In principle, the integration is valid only for $\omega \rightarrow 0$. But the integration for a large ω is significantly suppressed when taking the limit $N \rightarrow \infty$. Thus, the upper limit of ω can be set to $+\infty$. Actually, $\exp(-Nw) \sim (1-w)^N$ if $\omega \rightarrow 0$, then the Laplace transformation is replaced by the Mellin transformation.

The H , \tilde{J}_i , and \tilde{S} functions should be renormalized and therefore their dependencies on the scale are determined by the anomalous dimensions,

$$\mu \frac{d}{d\mu} \ln H = -\gamma_H(\alpha_s), \quad (3.29)$$

$$\mu \frac{d}{d\mu} \ln \tilde{J}_i = -\gamma_{J_i}(\alpha_s), \quad (3.30)$$

$$\mu \frac{d}{d\mu} \ln \tilde{S} = -\gamma_S(\alpha_s). \quad (3.31)$$

Because the cross section does not depend on the renormalization scale,

$$\gamma_H + \gamma_S + \sum_i \gamma_{J_i} = 0. \quad (3.32)$$

In addition, the cross section on the left side of Eq. (3.26) does not depend on the choice of gauge-fixing vector ζ_i , so that

$$0 = \left(\frac{\partial}{\partial \ln p_1 \cdot \zeta_1} H \right) \tilde{J}_1 \tilde{J}_2 \tilde{S} + H \left(\frac{\partial}{\partial \ln p_1 \cdot \zeta_1} \tilde{J}_1 \right) \tilde{J}_2 \tilde{S} + H \tilde{J}_1 \tilde{J}_2 \left(\frac{\partial}{\partial \ln p_1 \cdot \zeta_1} \tilde{S} \right), \quad (3.33)$$

or

$$\begin{aligned} \frac{\partial}{\partial \ln p_1 \cdot \zeta_1} \ln \tilde{J}_1 \left(\frac{p_1 \cdot \zeta_1}{\mu}, \frac{Q}{\mu N^{1/a_1}} \right) &= - \frac{\partial}{\partial \ln p_1 \cdot \zeta_1} \ln H \left(\frac{p_1}{\mu}, \frac{p_2}{\mu}, \zeta_i \right) \\ &\quad - \frac{\partial}{\partial \ln p_1 \cdot \zeta_1} \ln \tilde{S} \left(\frac{Q}{\mu N}, n_i, \zeta_i \right). \end{aligned} \quad (3.34)$$

The first term on the right side is a function of α_s and $p_1 \cdot \zeta_1 / \mu$, and the second term is a function of α_s and

$$\frac{1}{(n_i \cdot \zeta_i)^{a_1-1}} \frac{Q}{\mu N} = \frac{Q^{a_1}}{(p_i \cdot \zeta_i)^{a_1-1} \mu N} \equiv \frac{Q'_{a_1}}{\mu N}. \quad (3.35)$$

Define

$$G \left(\frac{p_1 \cdot \zeta_1}{\mu}, \alpha_s(\mu) \right) = - \frac{\partial}{\partial \ln p_1 \cdot \zeta_1} \ln H, \quad (3.36)$$

$$K \left(\frac{Q'_{a_1}}{\mu N}, \alpha_s(\mu) \right) = - \frac{\partial}{\partial \ln p_1 \cdot \zeta_1} \ln \tilde{S}. \quad (3.37)$$

The effect of varying the gauge-fixing vector does not involve the divergence associated with the jet, therefore the anomalous dimensions are independent on the gauge-fixing vectors; see Eq. (3.30). As a result,

$$\mu \frac{d}{d\mu} \left[G \left(\frac{p_1 \cdot \zeta_1}{\mu}, \alpha_s(\mu) \right) + K \left(\frac{Q'_{a_1}}{\mu N}, \alpha_s(\mu) \right) \right] = 0. \quad (3.38)$$

Then one can define

$$\mu \frac{d}{d\mu} K = -\gamma_K(\alpha_s(\mu)) = -\mu \frac{d}{d\mu} G, \quad (3.39)$$

where γ_K is the Sudakov anomalous dimension. From the definition given in Eqs. (3.36) and (3.37), G and K correspond to the hard and soft interactions with the intrinsic energy scales of $p_1 \cdot \zeta_1$ and Q'_{a_1}/N , respectively. Notice that $p_1 \cdot \zeta_1 \gg Q'_{a_1}/N$. Any choice of a fixed renormalization scale μ would induce a large logarithm in G or K . In order to avoid such a large logarithm, one should choose the respective intrinsic scales, at which G or K are evaluated individually. And then they are evolved to the common scale μ using the RGE,

$$\begin{aligned} &G \left(\frac{p_1 \cdot \zeta_1}{\mu}, \alpha_s(\mu) \right) + K \left(\frac{Q'_{a_1}}{\mu N}, \alpha_s(\mu) \right) \\ &= G(1, \alpha_s(p_1 \cdot \zeta_1)) + K(1, \alpha_s(Q'_{a_1}/N)) - \int_{Q'_{a_1}/N}^{p_1 \cdot \zeta_1} \frac{d\mu'}{\mu'} \gamma_K(\alpha_s(\mu)) \end{aligned}$$

$$= - \int_{Q_{a_1}/N}^{p_1 \cdot \zeta_1} \frac{d\mu'}{\mu'} A(\alpha_s(\mu')) + A'(\alpha_s(p_1 \cdot \zeta_1)), \quad (3.40)$$

in which

$$A(\alpha_s) = \gamma_K(\alpha_s) + \beta(g) \frac{\partial}{\partial g} K(1, \alpha_s), \quad (3.41)$$

$$A'(\alpha_s) = K(1, \alpha_s) + G(1, \alpha_s). \quad (3.42)$$

Solving Eqs. (3.30) and (3.34), one obtains the jet function

$$\begin{aligned} \tilde{J}\left(\frac{p \cdot \zeta}{\mu}, \frac{Q}{\mu N^{1/a}}, \alpha_s(\mu)\right) &= \tilde{J}(1, 1, \alpha_s(Q/N^{1/a})) \exp\left[-\int_{Q/N^{1/a}}^{\mu} \frac{d\lambda}{\lambda} \gamma_J(\alpha_s(\lambda))\right] \\ &\times \exp\left[-\int_{Q/N^{1/a}}^{p \cdot \zeta} \frac{d\lambda}{\lambda} \left(\int_{Q^a/\lambda^{a-1}N}^{\lambda} \frac{d\xi}{\xi} A(\alpha_s(\xi)) - A'(\alpha_s(\lambda))\right)\right]. \end{aligned} \quad (3.43)$$

In general, $p \cdot \zeta = CQ$ with C a constant. After redefinition of A' , it is possible to set $C = 1$. Combining Eqs. (3.29)–(3.31), one gets the resummed cross section $\tilde{\sigma}(N)$,

$$\begin{aligned} \ln \tilde{\sigma}(N) &= \ln H(1, 1, \alpha_s(Q)) + \ln \tilde{S}(1, \alpha_s(Q/N)) + \sum_{i=1,2} \ln \tilde{J}_i(1, 1, \alpha_s(Q/N^{1/a_i})) \\ &- \sum_i \int_{Q/N^{1/a_i}}^Q \frac{d\lambda}{\lambda} \left[\int_{Q^{a_i}/\lambda^{a_i-1}N}^{\lambda} \frac{d\xi}{\xi} A(\alpha_s(\xi)) - A'(\alpha_s(\lambda)) + \gamma_{J_i}(\alpha_s(\lambda)) \right] \\ &- \int_{Q/N}^Q \frac{d\lambda}{\lambda} \gamma_S(\alpha_s(\lambda)). \end{aligned} \quad (3.44)$$

This resummed result can be expanded in a series of α_s to obtain the approximated fixed-order results. Up to NLO,

$$\ln \tilde{\sigma}(N) = D^{(0)} + \frac{\alpha_s}{\pi} \left[D^{(1)} - A^{(1)} \left(\frac{1}{a}\right) \ln^2 N + 2B^{(1)} \left(\frac{1}{a}\right) \ln N \right]. \quad (3.45)$$

The coefficients $A^{(1)}$, $B^{(1)}$, $D^{(1)}$ are then determined by comparing with the fixed-order result.

The above resummation method can be generalized to the hard scattering process with colored particles in both the initial and final states. Now the soft and hard functions appear in the form of matrix in the color space. The Laplace transformed cross section is given by

$$\begin{aligned}
\tilde{\sigma}(N) &= \int_0^\infty d\omega e^{-N\omega} \sigma(\omega) \\
&= \sum_{IJ} H_{IJ} \left(\frac{p_1}{\mu}, \frac{p_2}{\mu}, \zeta_i \right) \tilde{S}_{IJ} \left(\frac{Q}{\mu N}, n_i, \zeta_i \right) \prod_i \tilde{J}_i \left(\frac{p_i \cdot \zeta_i}{\mu}, \frac{Q}{\mu N^{1/a_i}} \right)
\end{aligned} \tag{3.46}$$

where IJ are color indices. The corresponding anomalous dimensions are also matrices,

$$\mu \frac{d}{d\mu} (\ln H)_{IJ} = (\Gamma_H(\alpha_s))_{IJ}, \tag{3.47}$$

$$\mu \frac{d}{d\mu} (\ln \tilde{J}_i) = \gamma_{J_i}(\alpha_s), \tag{3.48}$$

$$\mu \frac{d}{d\mu} (\ln \tilde{S}_{IJ}) = (\Gamma_S(\alpha_s))_{IJ}, \tag{3.49}$$

which satisfy the condition

$$(\Gamma_H(\alpha_s))_{IJ} + (\Gamma_S(\alpha_s))_{IJ} + \sum_i \gamma_{J_i}(\alpha_s) \delta_{IJ} = 0. \tag{3.50}$$

Other procedure is similar to that in the resummation for $e^+e^- \rightarrow$ dijet.

At the end, the cross section in the momentum space is obtained after performing the inverse Laplace transformation,

$$\sigma(\omega) = \frac{1}{2\pi i} \lim_{y \rightarrow \infty} \int_{x-iy}^{x+iy} e^{\omega N} \tilde{\sigma}(N) dN, \tag{3.51}$$

where x is chosen to make the integration contour in the convergence region of $\tilde{\sigma}(N)$. In the inverse Laplace transformation, N can be so large that the integrand in Eq. (3.44) hits the Landau pole. In this case, one would resort to the Principle Value Resummation or the Minimal Prescription schemes [106–109].

In the above example, the soft gluon effects in the threshold region have been resummed to all orders of α_s . There is another kind of resummation method which only resums the gluon with small transverse momentum. In this case, the transverse momentum of the parton in the hadron should be taken into account and then the factorization formalism is different. The interested reader is encouraged to refer to the original papers, such as Refs. [110–112]. The typical processes in which the large logarithms have been resummed are shown in Table 3.2.

Table 3.2 Typical processes in which the large logarithms have been resummed

High energy scattering processes	Threshold regions	References
$e^+e^- \rightarrow jj$	$T \rightarrow 1$	[113, 114]
DIS process	Bjorken variable $x \rightarrow 1$	[104, 115]
Drell–Yan process	$\tau = M^2/S \rightarrow 1$	[104, 115, 116]
$pp \rightarrow H$	$\tau = M^2/S \rightarrow 1$	[117, 118]
$pp \rightarrow jj$	$\tau = M^2/S \rightarrow 1$	[119]
$pp \rightarrow t\bar{t}$	$\tau = M^2/S \rightarrow 1$	[120]
$pp \rightarrow \gamma + X$	$x_T = 2E_T/\sqrt{S} \rightarrow 1$	[121, 122]
$pp \rightarrow t$	$\tau = M^2/S \rightarrow 1$	[123]
Drell–Yan process at small Q_T	$Q_T \rightarrow 0$	[106]
$pp \rightarrow H$ at small Q_T	$Q_T \rightarrow 0$	[110–112]
$pp \rightarrow \tilde{t}_1$ at small Q_T	$Q_T \rightarrow 0$	[124]
$pp \rightarrow$ single graviton at small Q_T	$Q_T \rightarrow 0$	[125]
$pp \rightarrow$ single slepton at small Q_T	$Q_T \rightarrow 0$	[126]

M and Q_T are the invariant mass and the transverse momentum of the final state, respectively. The threshold variable has another definition in $pp \rightarrow jj$, i.e., $M^2 = p_1 \cdot p_2$ [119] rather than $(p_1 + p_2)^2$, where p_1 and p_2 are the momenta of the two jets

3.4.2 Resummation with SCET

The soft-collinear effective theory (SCET) is a special effective theory of QCD [127–131], which concentrates on the soft and collinear degrees of freedom. The hard freedoms are incorporated in the Wilson coefficient after matching operators from QCD to SCET. It separates the different scales in a complicated process and proves to be an efficient method to deal with the problem of scale hierarchies.

To describe collinear fields in SCET, it is convenient to define a lightlike vector $n_\mu = (1, \mathbf{n})$, $\mathbf{n}^2 = 1$. Any four vectors can be light-cone decomposed with respect to n_μ and $\bar{n}_\mu = (1, -\mathbf{n})$ as

$$l^\mu = l^- \frac{n^\mu}{2} + l^+ \frac{\bar{n}^\mu}{2} + l_{n\perp}^\mu, \quad (3.52)$$

with $l^+ = n \cdot l$ and $l^- = \bar{n} \cdot l$. The momentum of a collinear particle moving along the n^μ direction has the following scaling:

$$p^\mu = (p^+, p^-, p_{n\perp}) \sim (\lambda^2, 1, \lambda), \quad (3.53)$$

while for a soft particle, the momentum scales as

$$q \sim (\lambda^2, \lambda^2, \lambda^2), \quad (3.54)$$

where $\lambda \ll 1$ is a small expansion parameter in SCET. For example, for an energetic jet with invariant mass m_J and energy E_J , $\lambda = m_J/E_J$. From the momentum scaling, one can see that the interaction between collinear fields of different directions n_i and n_j with $n_i \cdot n_j \gg \lambda^2$ will inevitably change the momentum scaling; thus it is forbidden in SCET, but can be included as an external current. The soft fields, on the other hand, can interact with any collinear field without changing the scaling.

In SCET, the n -collinear quark ψ_n and gluon field A_n^μ can be written as

$$\begin{aligned} \chi_n(x) &= W_n^\dagger(x) \xi_n(x) \quad \text{with} \quad \xi_n(x) = \frac{\not{n} \not{\bar{n}}}{4} \psi_n(x), \\ \mathcal{A}_{n\perp}^\mu(x) &= [W_n^\dagger i D_{n\perp}^\mu W_n(x)], \end{aligned} \quad (3.55)$$

where

$$i D_{n\perp}^\mu = \mathcal{P}_{n\perp}^\mu + g_s A_{n\perp}^\mu \quad (3.56)$$

is the collinear covariant derivative and the label operator \mathcal{P} is defined to project out the large momentum component of the collinear field, e.g., $\mathcal{P}_n^\mu \xi_n = \bar{p}^\mu \xi_n$. Here we have split p into a sum of large label momentum and small residue momentum,

$$p^\mu = \bar{p}^\mu + k^\mu \quad \text{with} \quad \bar{p}^\mu = p^\mu - \frac{n^\mu}{2} + p_{n\perp}^\mu. \quad (3.57)$$

The n -collinear Wilson line,

$$W_n(x) = \mathbf{P} \exp \left(i g_s \int_{-\infty}^0 ds \bar{n} \cdot A_n^a(x + s\bar{n}) t^a \right), \quad (3.58)$$

which describes the emission of arbitrary n -collinear gluons from an n -collinear quark or gluon, is constructed to make the collinear fields as defined in Eq. (3.55) invariant under the collinear gauge transformation. The operator \mathbf{P} is the path-ordering operator acting on the color generator t^a .

At the LO in λ , only the $n \cdot A_s$ component of soft gluons can interact with the n -collinear field. Such interaction is eikonal and can be removed by a field redefinition [130]:

$$\begin{aligned} \chi_n(x) &\rightarrow Y_n(x_-) \chi_n(x), \\ \mathcal{A}_{n\perp}^\mu(x) &\rightarrow Y_n(x_-) \mathcal{A}_{n\perp}^\mu(x) Y_n^\dagger(x_-), \end{aligned} \quad (3.59)$$

where

$$Y_n(x) = \mathbf{P} \exp \left(i g_s \int_{-\infty}^0 ds n \cdot A_s^a(x + sn) t^a \right) \quad (3.60)$$

for an incoming Wilson line [130, 132]. And for an outgoing Wilson line, it is defined as

$$\tilde{Y}_n(x) = \bar{\mathbf{P}} \exp \left(-i g_s \int_0^\infty ds n \cdot A_s^a(x + sn) t^a \right), \quad (3.61)$$

with $\bar{\mathbf{P}}$ the anti-path ordering operator.

The soft gluon fields are multipole expanded around x_- to maintain a consistent power counting in λ . For the interaction between the soft gluon fields and massive quark fields, there exists a similar timelike Wilson line [133], for example,

$$Y_v(x) = \mathbf{P} \exp \left(i g_s \int_{-\infty}^0 ds v \cdot A_s^a(x + sv) t^a \right). \quad (3.62)$$

After the field redefinition, the LO SCET Lagrangian is factorized into a sum of different collinear sectors and a soft sector, which do not interact with each other.

$$\mathcal{L}_{\text{SCET}} = \sum_{n_i} \mathcal{L}_{n_i}^{(0)} + \mathcal{L}_s + \dots. \quad (3.63)$$

The decoupling of soft gluons from collinear fields is crucial for deriving the factorization formula.

The advantage of performing resummation with SCET is that the different scales are separated in constructing the effective Lagrangian. The factorization is transparent by integrating out heavier modes step by step in a process, and every part of the factorized matrix element has an explicit field definition, allowing a precise perturbative calculation directly. The resummation is performed by solving the RGE of different parts, which can be expressed in compact form. A comprehensive review on SCET can be found in Ref. [134].

Notice that the resummations in the traditional method and SCET are equivalent in principle though they may produce different theoretical predictions numerically. The similarity and difference between the two methods have been investigated carefully in Refs. [135–140].

References

1. J.C. Collins, D.E. Soper, G.F. Sterman, Factorization of hard processes in QCD. Adv. Ser. Direct. High Energy Phys. **5**, 1–91 (1988). [arXiv:hep-ph/0409313](#)
2. J.C. Collins, D.E. Soper, Parton distribution and decay functions. Nucl. Phys. B **194**, 445 (1982)
3. G. Altarelli, G. Parisi, Asymptotic freedom in parton language. Nucl. Phys. B **126**, 298 (1977)
4. T. Kinoshita, Mass singularities of Feynman amplitudes. J. Math. Phys. **3**, 650–677 (1962)
5. T. Lee, M. Nauenberg, Degenerate systems and mass singularities. Phys. Rev. **133**, B1549–B1562 (1964)
6. S. Catani, M. Seymour, A General algorithm for calculating jet cross-sections in NLO QCD. Nucl. Phys. B **485**, 291–419 (1997). [arXiv:hep-ph/9605323](#)
7. M. Cacciari, G.P. Salam, G. Soyez, The Anti-k(t) jet clustering algorithm. JHEP **0804**, 063 (2008). [arXiv:0802.1189](#)

8. G.P. Salam, Towards jetography. *Eur. Phys. J. C* **67**, 637–686 (2010). [arXiv:0906.1833](#)
9. M. Cacciari, G.P. Salam, G. Soyez, FastJet user manual. *Eur. Phys. J. C* **72**, 1896 (2012). [arXiv:1111.6097](#)
10. R.K. Ellis, G. Zanderighi, Scalar one-loop integrals for QCD. *JHEP* **0802**, 002 (2008). [arXiv:0712.1851](#)
11. T. Hahn, Automatic loop calculations with FeynArts, FormCalc, and LoopTools. *Nucl. Phys. Proc. Suppl.* **89**, 231–236 (2000). [arXiv:hep-ph/0005029](#)
12. Z. Bern, L.J. Dixon, D.C. Dunbar, D.A. Kosower, One loop n point gauge theory amplitudes, unitarity and collinear limits. *Nucl. Phys. B* **425**, 217–260 (1994). [arXiv:hep-ph/9403226](#)
13. Z. Bern, L.J. Dixon, D.C. Dunbar, D.A. Kosower, Fusing gauge theory tree amplitudes into loop amplitudes. *Nucl. Phys. B* **435**, 59–101 (1995). [arXiv:hep-ph/9409265](#)
14. Z. Bern, L.J. Dixon, D.A. Kosower, One loop amplitudes for e+ e- to four partons. *Nucl. Phys. B* **513**, 3–86 (1998). [arXiv:hep-ph/9708239](#)
15. G. Ossola, C.G. Papadopoulos, R. Pittau, Reducing full one-loop amplitudes to scalar integrals at the integrand level. *Nucl. Phys. B* **763**, 147–169 (2007). [arXiv:hep-ph/0609007](#)
16. D. Forde, Direct extraction of one-loop integral coefficients. *Phys. Rev. D* **75**, 125019 (2007). [arXiv:0704.1835](#)
17. R.K. Ellis, W. Giele, Z. Kunszt, A numerical unitarity formalism for evaluating one-loop amplitudes. *JHEP* **0803**, 003 (2008). [arXiv:0708.2398](#)
18. G. Ossola, C.G. Papadopoulos, R. Pittau, On the rational terms of the one-loop amplitudes. *JHEP* **0805**, 004 (2008). [arXiv:0802.1876](#)
19. R.K. Ellis, W.T. Giele, Z. Kunszt, K. Melnikov, Masses, fermions and generalized D -dimensional unitarity. *Nucl. Phys. B* **822**, 270–282 (2009). [arXiv:0806.3467](#)
20. G. Ossola, C.G. Papadopoulos, R. Pittau, CutTools: a program implementing the OPP reduction method to compute one-loop amplitudes. *JHEP* **0803**, 042 (2008). [arXiv:0711.3596](#)
21. A. van Hameren, C. Papadopoulos, R. Pittau, Automated one-loop calculations: a proof of concept. *JHEP* **0909**, 106 (2009). [arXiv:0903.4665](#)
22. P. Mastrolia, G. Ossola, T. Reiter, F. Tramontano, Scattering amplitudes from unitarity-based reduction algorithm at the integrand-level. *JHEP* **1008**, 080 (2010). [arXiv:1006.0710](#)
23. G. Heinrich, G. Ossola, T. Reiter, F. Tramontano, Tensorial reconstruction at the integrand level. *JHEP* **1010**, 105 (2010). [arXiv:1008.2441](#)
24. C. Berger, Z. Bern, L. Dixon, F. Febres, Cordero, D. Forde et al., An automated implementation of on-shell methods for one-loop amplitudes. *Phys. Rev. D* **78**, 036003 (2008). [arXiv:0803.4180](#)
25. C. Berger, Z. Bern, L.J. Dixon, F. Febres, Cordero, D. Forde et al., Next-to-leading order QCD predictions for W+3-jet distributions at hadron colliders. *Phys. Rev. D* **80**, 074036 (2009). [arXiv:0907.1984](#)
26. W. Giele, G. Zanderighi, On the numerical evaluation of one-loop amplitudes: the gluonic case. *JHEP* **0806**, 038 (2008). [arXiv:0805.2152](#)
27. V. Hirschi, R. Frederix, S. Frixione, M.V. Garzelli, F. Maltoni et al., Automation of one-loop QCD corrections. *JHEP* **1105**, 044 (2011). [arXiv:1103.0621](#)
28. G. Cullen, N. Greiner, G. Heinrich, G. Luisoni, P. Mastrolia et al., Automated one-loop calculations with GoSam. *Eur. Phys. J. C* **72**, 1889 (2012). [arXiv:1111.2034](#)
29. J.M. Campbell, R. Ellis, MCFM for the tevatron and the LHC. *Nucl. Phys. Proc. Suppl.* **205–206**, 10–15 (2010). [arXiv:1007.3492](#)
30. Z. Bern, L. Dixon, F. Febres Cordero, S. Hoeche, H. Ita et al., Next-to-leading order $W + 5$ -jet production at the LHC. *Phys. Rev. D* **88** (2013), no. 1 014025. [arXiv:1304.1253](#)
31. K. Chetyrkin, A. Kataev, F. Tkachov, New approach to evaluation of multiloop feynman integrals: the gegenbauer polynomial x space technique. *Nucl. Phys. B* **174**, 345–377 (1980)
32. K. Chetyrkin, F. Tkachov, Integration by parts: the algorithm to calculate beta functions in 4 loops. *Nucl. Phys. B* **192**, 159–204 (1981)
33. T. Gehrmann, E. Remiddi, Differential equations for two loop four point functions. *Nucl. Phys. B* **580**, 485–518 (2000). [arXiv:hep-ph/9912329](#)

34. S. Laporta, High precision calculation of multiloop Feynman integrals by difference equations. *Int. J. Mod. Phys. A* **15**, 5087–5159 (2000). [arXiv:hep-ph/0102033](#)
35. C. Anastasiou, A. Lazopoulos, Automatic integral reduction for higher order perturbative calculations. *JHEP* **0407**, 046 (2004). [arXiv:hep-ph/0404258](#)
36. A.V. Smirnov, *FIRE5: a C++ implementation of Feynman integral reduction*. [arXiv:1408.2372](#)
37. A. von Manteuffel, C. Studerus, *Reduze 2—distributed Feynman integral reduction*. [arXiv:1201.4330](#)
38. M. Bergere, Y.-M.P. Lam, Asymptotic expansion of Feynman amplitudes. Part I: the convergent case. *Commun. Math. Phys.* **39**, 1 (1974)
39. N. Usyukina, On a representation for three point function. *Teor. Mat. Fiz.* **22**, 300–306 (1975)
40. A. Kotikov, Differential equations method: new technique for massive Feynman diagrams calculation. *Phys. Lett. B* **254**, 158–164 (1991)
41. A. Kotikov, Differential equations method: the calculation of vertex type Feynman diagrams. *Phys. Lett. B* **259**, 314–322 (1991)
42. A. Kotikov, Differential equation method: the calculation of N point Feynman diagrams. *Phys. Lett. B* **267**, 123–127 (1991)
43. C. Anastasiou, A. Daleo, Numerical evaluation of loop integrals. *JHEP* **0610**, 031 (2006). [arXiv:hep-ph/0511176](#)
44. M. Czakon, Automated analytic continuation of Mellin-Barnes integrals. *Comput. Phys. Commun.* **175**, 559–571 (2006). [arXiv:hep-ph/0511200](#)
45. J. Gluza, K. Kajda, T. Riemann, AMBRE: a mathematica package for the construction of Mellin-Barnes representations for Feynman integrals. *Comput. Phys. Commun.* **177**, 879–893 (2007). [arXiv:0704.2423](#)
46. R.K. Ellis, D. Ross, A. Terrano, The perturbative calculation of jet structure in e^+e^- annihilation. *Nucl. Phys. B* **178**, 421 (1981)
47. W. Giele, E.N. Glover, Higher order corrections to jet cross-sections in e^+e^- annihilation. *Phys. Rev. D* **46**, 1980–2010 (1992)
48. B. Harris, J. Owens, The two cutoff phase space slicing method. *Phys. Rev. D* **65**, 094032 (2002). [arXiv:hep-ph/0102128](#)
49. K. Fabricius, I. Schmitt, G. Schierholz, G. Kramer, Order α_s^2 correction to jet cross-sections in e^+e^- annihilation. *Phys. Lett. B* **97**, 431 (1980)
50. F. Gutbrod, G. Kramer, G. Schierholz, Higher order QCD corrections to the three jet cross-sections: bare versus dressed jets. *Z. Phys. C* **21**, 235 (1984)
51. S. Frixione, Z. Kunszt, A. Signer, Three jet cross-sections to next-to-leading order. *Nucl. Phys. B* **467**, 399–442 (1996). [arXiv:hep-ph/9512328](#)
52. D.A. Kosower, Multiple singular emission in gauge theories. *Phys. Rev. D* **67**, 116003 (2003). [arXiv:hep-ph/0212097](#)
53. D.A. Kosower, All orders singular emission in gauge theories. *Phys. Rev. Lett.* **91**, 061602 (2003). [arXiv:hep-ph/0301069](#)
54. S. Weinzierl, Subtraction terms at NNLO. *JHEP* **0303**, 062 (2003). [arXiv:hep-ph/0302180](#)
55. S. Weinzierl, Subtraction terms for one loop amplitudes with one unresolved parton. *JHEP* **0307**, 052 (2003). [arXiv:hep-ph/0306248](#)
56. C. Anastasiou, K. Melnikov, F. Petriello, Higgs boson production at hadron colliders: differential cross sections through next-to-next-to-leading order. *Phys. Rev. Lett.* **93**, 262002 (2004). [arXiv:hep-ph/0409088](#)
57. T. Binoth, G. Heinrich, Numerical evaluation of phase space integrals by sector decomposition. *Nucl. Phys. B* **693**, 134–148 (2004). [arXiv:hep-ph/0402265](#)
58. C. Anastasiou, K. Melnikov, F. Petriello, A new method for real radiation at NNLO. *Phys. Rev. D* **69**, 076010 (2004). [arXiv:hep-ph/0311311](#)
59. A. Gehrmann-De Ridder, T. Gehrmann, G. Heinrich, Four particle phase space integrals in massless QCD. *Nucl. Phys. B* **682**, 265–288 (2004). [arXiv:hep-ph/0311276](#)
60. A. Gehrmann-De Ridder, T. Gehrmann, E.N. Glover, Quark-gluon antenna functions from neutralino decay. *Phys. Lett. B* **612** (2005) 36–48. [arXiv:hep-ph/0501291](#)

61. A. Gehrmann-De Ridder, T. Gehrmann, E.N. Glover, Gluon-gluon antenna functions from Higgs boson decay. *Phys. Lett. B* **612**, 49–60 (2005). [arXiv:hep-ph/0502110](#)
62. A. Gehrmann-De Ridder, T. Gehrmann, E.N. Glover, Antenna subtraction at NNLO. *JHEP* **0509**, 056 (2005). [arXiv:hep-ph/0505111](#)
63. S. Catani, M. Grazzini, An NNLO subtraction formalism in hadron collisions and its application to Higgs boson production at the LHC. *Phys. Rev. Lett.* **98**, 222002 (2007). [arXiv:hep-ph/0703012](#)
64. G. Bozzi, S. Catani, D. de Florian, M. Grazzini, The $q(T)$ spectrum of the Higgs boson at the LHC in QCD perturbation theory. *Phys. Lett. B* **564**, 65–72 (2003). [arXiv:hep-ph/0302104](#)
65. M. Grazzini, Soft-gluon effects in WW production at hadron colliders. *JHEP* **0601**, 095 (2006). [arXiv:hep-ph/0510337](#)
66. M. Czakon, A novel subtraction scheme for double-real radiation at NNLO. *Phys. Lett. B* **693**, 259–268 (2010). [arXiv:1005.0274](#)
67. J. Gao, C.S. Li, H.X. Zhu, Top quark decay at next-to-next-to leading order in QCD. *Phys. Rev. Lett.* **110**, 042001 (2013). [arXiv:1210.2808](#)
68. J. Gao, H. X. Zhu, Electroweak production of top-quark pairs in e^+e^- annihilation at NNLO in QCD: the vector contributions. *Phys. Rev.* **D90**(11), 114022 (2014). [arXiv:1408.5150](#)
69. R. Boughezal, C. Focke, X. Liu, F. Petriello, W -boson production in association with a jet at next-to-next-to-leading order in perturbative QCD. *Phys. Rev. Lett.* **115**(6), 062002 (2015). [arXiv:1504.02131](#)
70. R. Boughezal, C. Focke, W. Giele, X. Liu, F. Petriello, Higgs boson production in association with a jet using jetiness subtraction. *Phys. Lett.* **B748**, 5–8 (2015). [arXiv:1505.03893](#)
71. J. Gaunt, M. Stahlhofen, F.J. Tackmann, J.R. Walsh, N -jetiness subtractions for NNLO QCD calculations. *JHEP* **1509**, 058 (2015). [arXiv:1505.04794](#)
72. C. Anastasiou, G. Dissertori, F. Stockli, NNLO QCD predictions for the $H \rightarrow WW \rightarrow l\nu l\nu$ signal at the LHC. *JHEP* **0709**, 018 (2007). [arXiv:0707.2373](#)
73. C. Anastasiou, F. Herzog, A. Lazopoulos, The fully differential decay rate of a Higgs boson to bottom-quarks at NNLO in QCD. *JHEP* **1203**, 035 (2012). [arXiv:1110.2368](#)
74. K. Melnikov, F. Petriello, Electroweak gauge boson production at hadron colliders through $O(\alpha_s^2)$. *Phys. Rev. D* **74**, 114017 (2006). [arXiv:hep-ph/0609070](#)
75. A. Gehrmann-De Ridder, T. Gehrmann, E. Glover, G. Heinrich, Infrared structure of $e^+e^- \rightarrow 3$ jets at NNLO. *JHEP* **0711**, 058 (2007). [arXiv:0710.0346](#)
76. S. Weinzierl, NNLO corrections to 3-jet observables in electron-positron annihilation. *Phys. Rev. Lett.* **101**, 162001 (2008). [arXiv:0807.3241](#)
77. A. Gehrmann-De Ridder, T. Gehrmann, E. Glover, G. Heinrich, Second-order QCD corrections to the thrust distribution. *Phys. Rev. Lett.* **99**, 132002 (2007). [arXiv:0707.1285](#)
78. A. Gehrmann-De Ridder, T. Gehrmann, E. Glover, G. Heinrich, Jet rates in electron-positron annihilation at $O(\alpha_s^3)$ in QCD. *Phys. Rev. Lett.* **100**, 172001 (2008). [arXiv:0802.0813](#)
79. E. Nigel Glover, J. Pires, Antenna subtraction for gluon scattering at NNLO. *JHEP* **1006**, 096 (2010). [arXiv:1003.2824](#)
80. A. Gehrmann-De Ridder, E. Glover, J. Pires, Real-virtual corrections for gluon scattering at NNLO. *JHEP* **1202**, 141 (2012). [arXiv:1112.3613](#)
81. A. Gehrmann-De Ridder, T. Gehrmann, E. Glover, J. Pires, Double virtual corrections for gluon scattering at NNLO. *JHEP* **1302**, 026 (2013). [arXiv:1211.2710](#)
82. A. Gehrmann-De Ridder, T. Gehrmann, E. Glover, J. Pires, Second order QCD corrections to jet production at hadron colliders: the all-gluon contribution. *Phys. Rev. Lett.* **110**, no. 16 162003 (2013). [arXiv:1301.7310](#)
83. G. Abelof, A. Gehrmann-De Ridder, Double real radiation corrections to $t\bar{t}$ production at the LHC: the all-fermion processes. *JHEP* **1204**, 076 (2012). [arXiv:1112.4736](#)
84. G. Abelof, A. Gehrmann-De Ridder, Double real radiation corrections to $t\bar{t}$ channel. *JHEP* **1211**, 074 (2012). [arXiv:1207.6546](#)
85. G. Abelof, O. Dekkers, A. Gehrmann-De Ridder, Antenna subtraction with massive fermions at NNLO: double real initial-final configurations. *JHEP* **1212**, 107 (2012). [arXiv:1210.5059](#)

86. A.G.-D. Ridder, T. Gehrmann, E.W.N. Glover, A. Huss, T.A. Morgan, Precise QCD predictions for the production of a Z boson in association with a hadronic jet. [arXiv:1507.02850](#)
87. M. Grazzini, NNLO predictions for the Higgs boson signal in the $H \rightarrow WW \rightarrow l\nu l\nu$ and $H \rightarrow ZZ \rightarrow 4l$ decay channels. *JHEP* **0802**, 043 (2008). [arXiv:0801.3232](#)
88. S. Catani, L. Cieri, G. Ferrera, D. de Florian, M. Grazzini, Vector boson production at hadron colliders: a fully exclusive QCD calculation at NNLO. *Phys. Rev. Lett.* **103**, 082001 (2009). [arXiv:0903.2120](#)
89. S. Catani, G. Ferrera, M. Grazzini, W Boson, Production at hadron colliders: the lepton charge asymmetry in NNLO QCD. *JHEP* **1005**, 006 (2010). [arXiv:1002.3115](#)
90. G. Ferrera, M. Grazzini, F. Tramontano, Associated WH production at hadron colliders: a fully exclusive QCD calculation at NNLO. *Phys. Rev. Lett.* **107**, 152003 (2011). [arXiv:1107.1164](#)
91. G. Ferrera, M. Grazzini, F. Tramontano, Associated ZH production at hadron colliders: the fully differential NNLO QCD calculation. *Phys. Lett. B* **740**, 51–55 (2015). [arXiv:1407.4747](#)
92. S. Catani, L. Cieri, D. de Florian, G. Ferrera, M. Grazzini, Diphoton production at hadron colliders: a fully-differential QCD calculation at NNLO. *Phys. Rev. Lett.* **108**, 072001 (2012). [arXiv:1110.2375](#)
93. F. Cascioli, T. Gehrmann, M. Grazzini, S. Kallweit, P. Maierhofer et al., ZZ production at hadron colliders in NNLO QCD. *Phys. Lett. B* **735**, 311–313 (2014). [arXiv:1405.2219](#)
94. T. Gehrmann, M. Grazzini, S. Kallweit, P. Maierhofer, A. von Manteuffel et al., W^+W^- production at hadron colliders in next to next to leading order QCD. *Phys. Rev. Lett.* **113**, no. 21 212001 (2014). [arXiv:1408.5243](#)
95. M. Grazzini, S. Kallweit, D. Rathlev, Wgamma and Zgamma production at the LHC in NNLO QCD. *JHEP* **1507**, 085 (2015). [arXiv:1504.01330](#)
96. P. Baernreuther, M. Czakon, A. Mitov, Percent level precision physics at the tevatron: first genuine NNLO QCD corrections to $q\bar{q} \rightarrow t\bar{t} + X$. *Phys. Rev. Lett.* **109**, 132001 (2012). [arXiv:1204.5201](#)
97. M. Czakon, A. Mitov, NNLO corrections to top pair production at hadron colliders: the quark-gluon reaction. *JHEP* **1301**, 080 (2013). [arXiv:1210.6832](#)
98. M. Czakon, P. Fiedler, A. Mitov, Total top-quark pair-production cross section at hadron colliders through $\mathcal{O}(\alpha_s^4)$. *Phys. Rev. Lett.* **110**, 252004 (2013). [arXiv:1303.6254](#)
99. X. Chen, T. Gehrmann, E. Glover, M. Jaquier, Precise QCD predictions for the production of Higgs+jet final states. *Phys. Lett. B* **740**, 147–150 (2015). [arXiv:1408.5325](#)
100. R. Boughezal, F. Caola, K. Melnikov, F. Petriello, M. Schulze, Higgs boson production in association with a jet at next-to-next-to-leading order. *Phys. Rev. Lett.* **115**(8), 082003 (2015). [arXiv:1504.07922](#)
101. M. Brucherseifer, F. Caola, K. Melnikov, $\mathcal{O}(\alpha_s^2)$ corrections to fully-differential top quark decays. *JHEP* **1304**, 059 (2013). [arXiv:1301.7133](#)
102. M. Brucherseifer, F. Caola, K. Melnikov, On the NNLO QCD corrections to single-top production at the LHC. *Phys. Lett. B* **736**, 58–63 (2014). [arXiv:1404.7116](#)
103. S. Catani, L. Trentadue, G. Turnock, B. Webber, Resummation of large logarithms in e+ e- event shape distributions. *Nucl. Phys. B* **407**, 3–42 (1993)
104. G. Sterman, Summation of large corrections to short distance hadronic cross-sections. *Nucl. Phys. B* **281**, 310 (1987)
105. H. Contopanagos, E. Laenen, G. Sterman, Sudakov factorization and resummation. *Nucl. Phys. B* **484**, 303–330 (1997). [arXiv:hep-ph/9604313](#)
106. J.C. Collins, D.E. Soper, G. Sterman, Transverse momentum distribution in Drell-Yan Pair and W and Z boson production. *Nucl. Phys. B* **250**, 199 (1985)
107. S. Catani, M.L. Mangano, P. Nason, L. Trentadue, The resummation of soft gluon in hadronic collisions. *Nucl. Phys. B* **478**, 273–310 (1996). [arXiv:hep-ph/9604351](#)
108. H. Contopanagos, G. Sterman, Principal value resummation. *Nucl. Phys. B* **419**, 77–104 (1994). [arXiv:hep-ph/9310313](#)
109. A. Kulesza, G. Sterman, W. Vogelsang, Joint resummation in electroweak boson production. *Phys. Rev. D* **66**, 014011 (2002). [arXiv:hep-ph/0202251](#)

110. I. Hinchliffe, S.F. Novaes, On the mean transverse momentum of higgs bosons at the SSC. *Phys. Rev. D* **38**, 3475–3480 (1988)
111. R.P. Kauffman, Higgs boson p_T in gluon fusion. *Phys. Rev. D* **44**, 1415–1425 (1991)
112. C.P. Yuan, Kinematics of the higgs boson at hadron colliders: NLO QCD gluon resummation. *Phys. Lett. B* **283**, 395–402 (1992)
113. J.C. Collins, D.E. Soper, Back-to-back jets in QCD. *Nucl. Phys. B* **193**, 381 (1981)
114. J.C. Collins, D.E. Soper, Back-to-back jets: fourier transform from b to k_T . *Nucl. Phys. B* **197**, 446 (1982)
115. S. Catani, L. Trentadue, Resummation of the QCD perturbative series for hard processes. *Nucl. Phys. B* **327**, 323 (1989)
116. S. Catani, L. Trentadue, Comment on QCD exponentiation at large x . *Nucl. Phys. B* **353**, 183–186 (1991)
117. M. Kramer, E. Laenen, M. Spira, Soft gluon radiation in higgs boson production at the LHC. *Nucl. Phys. B* **511**, 523–549 (1998). [arXiv:hep-ph/9611272](#)
118. S. Catani, D. de Florian, M. Grazzini, P. Nason, Soft-gluon resummation for higgs boson production at hadron colliders. *JHEP* **07**, 028 (2003). [arXiv:hep-ph/0306211](#)
119. N. Kidonakis, G. Oderda, G. Sterman, Threshold resummation for dijet cross sections. *Nucl. Phys. B* **525**, 299–332 (1998). [arXiv:hep-ph/9801268](#)
120. R. Bonciani, S. Catani, M.L. Mangano, P. Nason, Nll resummation of the heavy-quark hadroproduction cross-section. *Nucl. Phys. B* **529**, 424–450 (1998). [arXiv:hep-ph/9801375](#)
121. S. Catani, M.L. Mangano, P. Nason, Sudakov resummation for prompt photon production in hadron collisions. *JHEP* **07**, 024 (1998). [arXiv:hep-ph/9806484](#)
122. S. Catani, M.L. Mangano, P. Nason, C. Oleari, W. Vogelsang, Sudakov resummation effects in prompt photon hadroproduction. *JHEP* **03**, 025 (1999). [arXiv:hep-ph/9903436](#)
123. L.L. Yang, C.S. Li, Y. Gao, J.J. Liu, Threshold resummation effects in direct top quark production at hadron colliders. *Phys. Rev. D* **73**, 074017 (2006). [arXiv:hep-ph/0601180](#)
124. T. Plehn, Single stop production at hadron colliders. *Phys. Lett. B* **488**, 359–366 (2000). [arXiv:hep-ph/0006182](#)
125. Q. Li, C.S. Li, L.L. Yang, Soft gluon resummation effects in single graviton production at the cern large hadron collider in the randall-sundrum model. *Phys. Rev. D* **74**, 056002 (2006). [arXiv:hep-ph/0606045](#)
126. L.L. Yang, C.S. Li, J.J. Liu, Q. Li, Soft gluon resummation effects in single slepton production at hadron colliders. *Phys. Rev. D* **72**, 074026 (2005). [arXiv:hep-ph/0507331](#)
127. C.W. Bauer, S. Fleming, M.E. Luke, Summing Sudakov logarithms in $B \rightarrow X_s \gamma$ in effective field theory. *Phys. Rev. D* **63**, 014006 (2000). [arXiv:hep-ph/0005275](#)
128. C.W. Bauer, S. Fleming, D. Pirjol, I.W. Stewart, An effective field theory for collinear and soft gluons: heavy to light decays. *Phys. Rev. D* **63**, 114020 (2001). [arXiv:hep-ph/0011336](#)
129. C.W. Bauer, I.W. Stewart, Invariant operators in collinear effective theory. *Phys. Lett. B* **516**, 134–142 (2001). [arXiv:hep-ph/0107001](#)
130. C.W. Bauer, D. Pirjol, I.W. Stewart, Soft-collinear factorization ineffective field theory. *Phys. Rev. D* **65**, 054022 (2002). [arXiv:hep-ph/0109045](#)
131. T. Becher, M. Neubert, Threshold resummation in momentum space from effective field theory. *Phys. Rev. Lett.* **97**, 082001 (2006). [arXiv:hep-ph/0605050](#)
132. J. Chay, C. Kim, Y.G. Kim, J.-P. Lee, Soft Wilson lines in soft-collinear effective theory. *Phys. Rev. D* **71**, 056001 (2005). [arXiv:hep-ph/0412110](#)
133. G. Korchemsky, A. Radyushkin, Infrared factorization, Wilson lines and the heavy quark limit. *Phys. Lett. B* **279**, 359–366 (1992). [arXiv:hep-ph/9203222](#)
134. T. Becher, A. Broggio, A. Ferroglia, *Introduction to soft-collinear effective theory*. [arXiv:1410.1892](#)
135. T. Becher, M. Neubert, G. Xu, Dynamical threshold enhancement and resummation in Drell-Yan production. *JHEP* **07**, 030 (2008). [arXiv:0710.0680](#)
136. V. Ahrens, T. Becher, M. Neubert, L.L. Yang, Renormalization-group improved prediction for higgs production at hadron colliders. *Eur. Phys. J. C* **62**, 333–353 (2009). [arXiv:0809.4283](#)

137. M. Bonvini, S. Forte, M. Ghezzi, G. Ridolfi, Threshold resummation in SCET vs. perturbative QCD: an analytic comparison. *Nucl. Phys.* **B861**, 337–360 (2012). [arXiv:1201.6364](#)
138. G. Sterman, M. Zeng, Quantifying comparisons of threshold resummations. *JHEP* **1405**, 132 (2014). [arXiv:1312.5397](#)
139. L.G. Almeida, S.D. Ellis, C. Lee, G. Sterman, I. Sung et al., Comparing and counting logs in direct and effective methods of QCD resummation. *JHEP* **1404**, 174 (2014). [arXiv:1401.4460](#)
140. M. Bonvini, S. Forte, G. Ridolfi, L. Rottoli, Resummation prescriptions and ambiguities in SCET vs. direct QCD: higgs production as a case study. *JHEP* **1501**, 046 (2015). [arXiv:1409.0864](#)

Chapter 4

QCD NLO Prediction on the Dark Matter and Photon Associated Production at the LHC

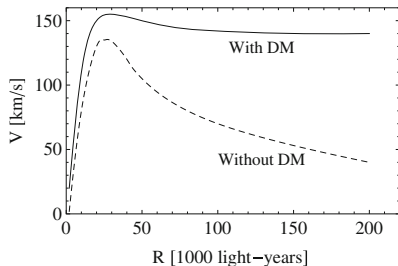
4.1 Introduction

Astrophysical and cosmological observations have confirmed the existence of dark matter (DM) in our universe and the density of DM is about four times larger than that of the visible matter [1]. Here, the visible matter refers to the matter made of all the known particles, e.g., shown in Fig. 1.1. Since any matter that exists for a long time in the Universe must be stable, the visible matter is generally made of electrons and protons, both of which are electricity charged. Thus, they could absorb and radiate photons, allowing them to be observed even if they are far away from us. In contrast, the invisible matter is called the DM, which means that it does not radiate photons, i.e., it is electric neutral, and thus is invisible to telescopes. In order to keep DM stable, DM particles are usually assumed to carry a special quantum number, such as -1 in a global Z_2 transformation, while the SM particles are unchanged under this transformation. The conservation of the quantum number ensures that a single DM particle would not decay into SM particles.

The existence of DM is mainly established from the gravitational effect. Galaxies are the building blocks of the present Universe and the easiest objects we can observe from Earth. A galaxy is a system of stars, gases, and dust, which are bound together and generally rotate around the galaxy center. And most galaxies live together to form a cluster of galaxies. As far as we know, all these movements are controlled by the gravity, whose property is elucidated by Einstein's theory of general relativity. After estimating the mass of the Coma galaxy cluster and the velocities of the galaxy members in it, it was found by Zwicky in 1930s that the visible matter (stars, gas, dust) alone is not enough to attract the galaxy members in the cluster. Thus DM is present and is in much greater amount than luminous matter [2, 3].

More obvious evidence can be found in the observations of the motions of stars in the spiral galaxies. The rotation velocity would drop down with the increasing of the distance if the gravity is produced only by the luminous matter, as shown in Fig. 4.1. However, the observation illustrates that the velocity becomes almost a constant at

Fig. 4.1 The rotation velocity of stars in a galaxy versus the distance from the galaxy center



the long distance, which necessitates the introduction of DM in the galaxy. Detailed investigation proves that the most part of the mass in a galaxy is in the form of DM.

Because most of the matter in the Universe is DM, the existence of DM could also change the structure of the Universe at large scale, and the formation of galaxies. If the DM is made up of slow-moving particles, often called cold DM, the gravitation force among DMs can attract DMs together quickly to form the core of galaxies. If the DM is relativistic particles, called hot DM, then the formation of galaxies is so slow that we can not observe so many galaxies in the present Universe. The latest measurements of microwave background (CMB) anisotropy, the baryon acoustic oscillation (BAO) scale, and the Hubble constant shows that the cold DM density normalized by critical density is [1]

$$\Omega_c = 0.2408^{+0.0093}_{-0.0092}. \quad (4.1)$$

For comparison, the baryon density normalized by critical density is [1]

$$\Omega_b = 0.0472 \pm 0.0010. \quad (4.2)$$

We can see that the cold DM density is about 4 times larger than that of baryon matter. Here, the critical density corresponds to the case that the spatial geometry is flat, which has been measured to be nearly a fact. Since the total normalized density in the Universe should be 1, the other parts are occupied by dark energy density which is still a mystery too.

The DM density measured today is called the relic density of DM. Actually, the precise prediction of the DM relic density requires the knowledge or assumptions about the history of the Universe. In the early hot Universe, there would be a large quantity of matter, including DM and ordinary matter, which are in thermal equilibrium. As the Universe cooled down, they could reduce their densities through pair annihilation and the densities decrease exponentially with decreasing temperature, due to the Boltzmann factor. However, this procedure would not go on forever because that it becomes more and more difficult for particles to find others with which to annihilate, as the their densities decrease. At some point, the annihilation rate becomes smaller than the Hubble expansion rate of the Universe and the densities become constants that are the values measured today. This point is called the

freeze-out epoch, corresponding to the temperature of the Universe $T_{f.o.} \sim m/20$ for a particle of mass m . The resulted densities are determined by the annihilation rate. The greater is the annihilation rate, the less is the relic density. Based on several general assumptions, an approximation equation for the DM relic density reads

$$\Omega_{DM} h^2 \simeq 0.1 \frac{3 \times 10^{-26} \text{ cm}^3/\text{s}}{\langle \sigma_{an} v \rangle}, \quad (4.3)$$

where $h = 0.693 \pm 0.009$ is the rescaled Hubble parameter, related to the Hubble constant H by

$$H = 100h \text{ km s}^{-1} \text{ Mpc}^{-1}. \quad (4.4)$$

v is the relative velocity of the annihilating particles and $\langle \sigma_{an} v \rangle$ is the thermally averaged total annihilation cross section. The typical cross section of the order $3 \times 10^{-26} \text{ cm}^3/\text{s}$ can be obtained if the DMs are massive particles with weak interactions.¹ This kind of DMs are called the weakly interacting massive particles (WIMP), and have been the mostly investigated candidates so far. Since there are no such candidates in the standard model (SM), any discovery of the signal of WIMP imply new physics.

At present, people are making a lot of efforts to search for DM particles with experiment facilities on the Earth, including indirect, direct detections, and collider experiments. The indirect detection receives the signals of DM annihilations in distant zones, such as galaxies centers. These signals should be stable to propagate through the interstellar space and be detected by experiments on the Earth, e.g., PAMELA [4], ATIC [5], HESS [6] and Fermi-LAT [7]. They usually consist of photons, electrons, positrons. If their fluxes are greater than what are expected from the cosmic rays, it is possible that they are products of DM annihilations. This method depends on the assumptions of the distribution of DM and the propagator model. Other astrophysical interpretations, such as pulsars, must be examined carefully.

The direct detection aims to detect the DM in our own galaxy, which may collide with nuclei on the Earth via weak interactions, including the experiments of DAMA [8], CDMS [9], CoGeNT [10], XENON [11], and LUX [12]. The DAMA and CoGeNT experiments reported results that hint a light DM with a mass around 10 GeV. However, these discoveries are not confirmed by CDMS, XENON, and LUX experiments which set upper limits on the WIMP and nucleon spin-dependent and spin-independent cross sections if the mass of the WIMP ranges from 6 to 1000 GeV.

The third approach is to produce the DM in the laboratory directly, such as the Large Hadron Collider (LHC), if DM exists and has interactions with the SM particles. Given that the LHC is operating at such high energies, it is expected it can probe very large parameters regions of DM models. Many investigations have been carried out to search for signals of DM at the LHC in varies of DM models [13–30].

Since a single DM particle would not interact with SM particles, it manifests as missing energy at hadron colliders. It is mandatory to study the process of DM

¹Here weak interactions are not necessarily the interactions mediated by the W and Z bosons.

associated production with some visible particles, e.g., a jet, a lepton, or a photon. Different associating particles leads to different signals and backgrounds, and need to be investigated independently.

In this chapter, we would investigate the signal of DM via its associated production with a photon, since this signal is clear and suffer from fewer backgrounds from the SM than a jet-associated production. Since the LHC is a proton-proton collider, the QCD correction should be considered for any process if we want to make reliable and precise predictions. Thus, in our analysis, we include the next-to-leading (NLO) order QCD effects.

4.2 Effective Operators

The identity of DM is still unknown so far. From the knowledge in the known world, it is possible that they consist of spin-0, spin-1/2, or spin-1 particles. Since ordinary matter is made of spin-1/2 particles while spin-1 particles mediate the forces, the spin-1/2 DM has aroused most interest.

As we have mentioned, the DM relic density hints a weak interaction between DM and SM particles. Effective operators are appropriate to describe such interactions, as they do in the form of Fermi's four-fermion operators. For example, the effective operators between two fermionic WIMPs (χ) and two SM fermions (f) are shown as

$$O_S = \frac{\kappa_S}{\Lambda^2} \bar{\chi} \chi \bar{f} f, \quad (4.5)$$

$$O_P = \frac{\kappa_P}{\Lambda^2} \bar{\chi} \gamma^5 \chi \bar{f} \gamma_5 f, \quad (4.6)$$

$$O_V = \frac{\kappa_V}{\Lambda^2} \bar{\chi} \gamma^\mu \chi \bar{f} \gamma_\mu f, \quad (4.7)$$

$$O_A = \frac{\kappa_A}{\Lambda^2} \bar{\chi} \gamma^\mu \gamma^5 \chi \bar{f} \gamma_\mu \gamma_5 f, \quad (4.8)$$

$$O_T = \frac{\kappa_T}{\Lambda^2} \bar{\chi} \sigma^{\mu\nu} \chi \bar{f} \sigma_{\mu\nu} f. \quad (4.9)$$

Here, the coefficients κ_i , $i = S, P, V, A, T$ denote the effective couplings and are $\mathcal{O}(1)$ numbers. Λ is a large energy scale and can be considered as the masses of new mediators whose effects have been integrated in low energy physics. The most general effective operators involving DM and SM particles can be found in Refs. [23, 27, 31–34]. The effective operators, defined by only a few parameters, simplify the comparison between experiments and various theoretical models, and are very useful before the discovery of any signal of new physics. However, one should keep in mind that there are complicated models, such as the supersymmetry, cannot be correctly described by these effective operators.

We take the scalar operators in Eq. (4.5) as an example to illustrate our method in the following content. We assume that the DM χ is singlet under the SM gauge group $SU(3)_C \otimes SU(2)_L \otimes U(1)_Y$, so that there is no other way to generate the DM

at hadron colliders except for the operator in Eq. (4.5). In addition, we only consider the operators involving SM quarks and rewrite the operator in the form

$$\mathcal{O} = \frac{\kappa}{\Lambda^2} \bar{\chi} \chi \bar{q} q. \quad (4.10)$$

This four-fermion operator has been discussed in Refs. [23, 31, 32, 35]. Here, the new physics scale Λ can be considered as the remnant of integrating a heavy propagator between the SM particles and DM particles. In this picture, the effective operator is valid only in the case that $\Lambda > 2m, \sqrt{\hat{s}}$, where m is the mass of DM and $\sqrt{\hat{s}}$ is the center-of-mass energy of the collision. Generally speaking, it is possible that $\sqrt{\hat{s}} > \Lambda$ for collisions at the LHC. However, the parton distribution functions of the initial partons in the process drops very fast with the increasing of $\sqrt{\hat{s}}$ at the LHC. Therefore, we trust that this limit can be satisfied in practical numerical calculation if we set the default value of Λ above 500 GeV.

4.3 Relic Density

As mentioned in the introduction, the DM relic density is a precision observable in cosmology. The DM we study contributes to the relic density of cold DM. The current density n of WIMPs can be computed from the Boltzmann transport equation and the law of entropy conservation [36]:

$$\frac{dn}{dt} = -3Hn - \langle \sigma_{an} v \rangle (n^2 - n_{\text{EQ}}^2), \quad (4.11)$$

$$\frac{ds}{dt} = -3Hs, \quad (4.12)$$

where t is time, H is the Hubble parameter, and s is the entropy density. The above Boltzmann transport equation is valid for the DM particles χ annihilating with its antiparticles $\bar{\chi}$, and there is no particle-antiparticle asymmetry, $n_\chi = n_{\bar{\chi}} = n$. n_{EQ} is the equilibrium number density, in the non-relativistic limit ($m \gg T$) given by [36]

$$n_{\text{EQ}} = g \left(\frac{mT}{2\pi} \right)^{3/2} \exp\left(-\frac{m}{T}\right), \quad (4.13)$$

where g accounts for the spin degrees of freedom of the particle.

It is convenient to use a new variable $Y \equiv n/s$ to separate out the effect of expansion of the Universe, and change the time to $x = m/T$ with T the photon temperature. It then follows that

$$\frac{dY}{dx} = \frac{1}{3H} \frac{ds}{dx} \langle \sigma_{an} v \rangle (Y^2 - Y_{\text{EQ}}^2). \quad (4.14)$$

In order to solve the above differential equation, we should express every component in terms of the temperature or x .

The Hubble parameter is given by

$$H = \sqrt{\frac{8\pi\rho}{3m_{\text{Pl}}^2}} \quad (4.15)$$

where $m_{\text{Pl}} = 1.22 \times 10^{19}$ GeV is the Planck mass, and ρ is the total energy density of the Universe. In the radiation dominated stage,

$$\rho = \frac{\pi^2}{30} g_*(T) T^4, \quad (4.16)$$

with $g_*(T)$ the effective number of degrees of freedom for the energy density, given by

$$g_*(T) = \sum_{\text{Bose}} g_B \left(\frac{T_i}{T}\right)^4 + \frac{7}{8} \sum_{\text{Fermi}} g_F \left(\frac{T_i}{T}\right)^4, \quad (4.17)$$

where T_i is the temperature of species i , g_B , and g_F denotes the number of degrees of freedom for the bosons and fermions, respectively. The entropy density is defined as

$$s \equiv \frac{S}{V} = \frac{\rho + p}{T} \simeq \frac{2\pi^2}{45} g_{*S}(T) T^3, \quad (4.18)$$

with $g_{*S}(T)$ the effective number of degrees of freedom for the entropy density, given by

$$g_{*S}(T) = \sum_{\text{Bose}} g_B \left(\frac{T_i}{T}\right)^3 + \frac{7}{8} \sum_{\text{Fermi}} g_F \left(\frac{T_i}{T}\right)^3. \quad (4.19)$$

If $T_i = T$, then $g_*(T) = g_{*S}(T) = g_*$ and they are independent of temperature. After defining a new degree of freedom parameter

$$g_{\text{eff}}^{1/2} = \frac{g_{*S}}{g_*^{1/2}} \left(1 + \frac{1}{3} \frac{T}{g_{*S}} \frac{dg_{*S}}{dT}\right), \quad (4.20)$$

Equation (4.14) can be written as

$$\frac{dY}{dx} = -\sqrt{\frac{45}{\pi m_{\text{Pl}}^2}} \frac{g_{\text{eff}}^{1/2} m}{x^2} \langle \sigma_{\text{ann}} v \rangle (Y^2 - Y_{\text{EQ}}^2). \quad (4.21)$$

The equilibrium value Y_{EQ} takes the form in the non-relativistic limit ($x \gg 3$)

$$Y_{\text{EQ}} = \frac{45}{2\pi^4} \left(\frac{\pi}{8}\right)^{1/2} \frac{g}{g_{*S}} x^{3/2} e^{-x}. \quad (4.22)$$

It is instructive to consider the approximation that g_{*S} is independent of T , which is valid most of the time. Then Eq. (4.14) becomes

$$\frac{x}{Y_{\text{EQ}}} \frac{dY}{dx} = -\frac{\Gamma_{an}}{H} \left[\left(\frac{Y}{Y_{\text{EQ}}} \right)^2 - 1 \right], \quad (4.23)$$

with $\Gamma_{an} = n_{\text{EQ}} \langle \sigma_{an} v \rangle$ the equilibrium annihilation rate. At high temperatures, $\Gamma_{an} > H$, Y closely tracks its equilibrium value Y_{EQ} . Since Γ_{an} decreases faster than H with decreasing T , it happens that $\Gamma_{an} \ll H$ so that $dY/dx \simeq 0$, which means that the number of particles per comoving volume becomes constant, i.e., the particles freeze out. The freeze-out epoch $T_{f.o.}$ is thus determined roughly by $\Gamma_{an}(T_{f.o.}) \simeq H(T_{f.o.})$.

The exact analytical solution of Eq. (4.21) does not exist, and it can only be numerically solved with the initial condition $Y = Y_{\text{EQ}}$ at $x \simeq 1$ to obtain the present WIMP abundance Y_0 . However, an approximate solution can be found if the thermally averaged annihilation cross section can be expanded as

$$\langle \sigma_{an} v \rangle = a + b \langle v^2 \rangle + O(v^4), \quad (4.24)$$

where $\sigma_{an} v$ is calculated by [37]

$$\sigma_{an} v = \frac{\beta_f}{64\pi^2 (s - 2m^2)} \int d\Omega |\overline{\mathcal{M}}|^2 \quad (4.25)$$

with

$$\beta_f = \left[1 - \frac{(m_3 + m_4)^2}{s} \right]^{1/2} \left[1 - \frac{(m_3 - m_4)^2}{s} \right]^{1/2}, \quad (4.26)$$

and it is expanded in terms of $s = 4m^2 + m^2 v^2$. Then the freeze-out epoch is evaluated recursively by [38]

$$x_f = \ln \left[c(c+2) \sqrt{\frac{45}{8}} \frac{g m m_{\text{Pl}} (a + 6b/x_f)}{2\pi^3 \sqrt{g_*(x_f)}} \right] \quad (4.27)$$

with $x_f \equiv m/T_{f.o.}$ and c a constant of order unity. The WIMP relic density is given by [36]

$$\Omega_\chi h^2 = \frac{\rho_\chi^0 h^2}{\rho_c^0} = \frac{m s_0 Y_0 h^2}{\rho_c^0} = \frac{1.04 \times 10^9 \text{ GeV}^{-1} x_f}{m_{\text{Pl}} g_{*S} / g_*^{1/2} (a + 3b/x_f)}, \quad (4.28)$$

where ρ_c^0 and s_0 are the present critical density and entropy density respectively, and we have used $T_0 = 2.725\text{K}$ for the present background radiation temperature. For most of the history of the universe all particle species had a common temperature, and g_{*S} can be replaced by g_* . The current experiment value for the relic density of cold DM is [1]

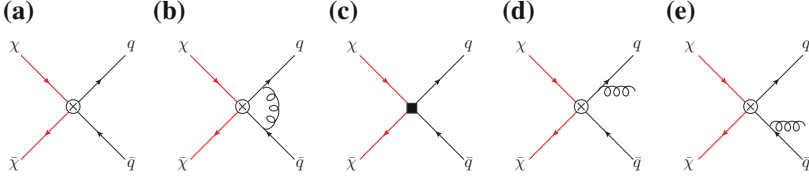


Fig. 4.2 The Feynman diagrams for the DM annihilation. Diagram **a** is the LO. Diagram **b** is the virtual correction while diagram **c** denotes contribution of the counterterm. Diagrams **d** and **e** are the real corrections

$$\Omega_{\text{CDM}}h^2 = 0.1157 \pm 0.0023. \quad (4.29)$$

In our case, we need to calculate the total annihilation cross section of DMs to get the relic density. The leading order (LO) and NLO Feynman diagrams are shown in Fig. 4.2. The LO total annihilation cross section can be calculated according to Eq. (4.25),

$$\sigma_B^{an} v = N_c N_f \frac{\kappa^2}{\Lambda^4} \frac{s(s - 4m^2)}{16\pi(s - 2m^2)}, \quad (4.30)$$

where N_c and N_f are the numbers of color and flavor of quarks, respectively, and we have only considered the massless quarks in the final state because the contribution from heavy quarks are suppressed by the phase space.

There are two parts in the NLO corrections to the total annihilation cross section, i.e., the one-loop virtual corrections and real emission corrections. The virtual corrections contain ultraviolet (UV) divergences which should be canceled after including the counterterm. To deal with UV and infrared (IR) (soft and collinear) divergences in our computation, we use $n = 4 - 2\epsilon$ dimensional regularization to regulate these divergences, and all divergences appear as $1/\epsilon^i$ with $i = 1, 2$. The renormalization constant of the external quark is usually fixed in the on-shell renormalization scheme, while the renormalization of the effective coupling is performed using the $\overline{\text{MS}}$ scheme. Explicitly,

$$\delta Z_2^q = -\frac{\alpha_s C_F}{4\pi} C_\epsilon \left(\frac{1}{\epsilon_{\text{UV}}} - \frac{1}{\epsilon_{\text{IR}}} \right), \quad (4.31)$$

$$\delta \kappa = -\frac{\alpha_s}{\pi} (4\pi e^{-\gamma_E})^\epsilon \frac{1}{\epsilon_{\text{UV}}}. \quad (4.32)$$

where $C_\epsilon = \Gamma(1 + \epsilon)[(4\pi\mu_R^2)/s]^\epsilon$ with μ_R the renormalization scale. We have used the subscripts UV and IR to denote the origins of the divergences. The counterterm of the vertex is defined as

$$\mathcal{O}_0 = Z_{\mathcal{O}} \mathcal{O}_R = (1 + \delta Z_{\mathcal{O}}) \mathcal{O}_R, \quad (4.33)$$

where

$$\delta Z_{\mathcal{O}} = \delta Z_2^q + \delta\kappa. \quad (4.34)$$

Then, the combination of virtual corrections and the counterterm reads

$$\sigma_V^{an} = \sigma_B^{an,\epsilon} \left(\frac{\alpha_s C_F}{2\pi} \right) D_\epsilon \left[-\frac{2}{\epsilon_{\text{IR}}^2} - \frac{3}{\epsilon_{\text{IR}}} - 3 \ln \left(\frac{s}{\Lambda^2} \right) - 2 + \pi^2 \right], \quad (4.35)$$

where $D_\epsilon = (4\pi\mu^2/s)^\epsilon / \Gamma(1-\epsilon)$ and $\sigma_B^{an,\epsilon}$ is the n -dimensional ($n = 4 - 2\epsilon$) LO total annihilation cross section. Because we only consider the massless quarks in the final state, the phase space of the real corrections can be integrated analytically, and the results of real corrections are given by

$$\sigma_R^{an} = \sigma_B^{an,\epsilon} \left(\frac{\alpha_s C_F}{2\pi} \right) D_\epsilon \left(\frac{2}{\epsilon_{\text{IR}}^2} + \frac{3}{\epsilon_{\text{IR}}} + \frac{21}{2} - \pi^2 \right). \quad (4.36)$$

Combining the two parts, we obtain the NLO total annihilation cross section

$$\sigma_{NLO}^{an} = \sigma_B^{an} \left[1 + \frac{\alpha_s C_F}{2\pi} \left(\frac{17}{2} - 3 \ln \left(\frac{s}{\Lambda^2} \right) \right) \right]. \quad (4.37)$$

As we have mentioned above, in order to obtain the relic density, we must expand the cross section by using $s = 4m^2 + m^2 v^2$, then

$$\sigma^{an} v = a + b v^2, \quad (4.38)$$

where

$$\begin{aligned} a &= 0, \\ b &= K^{an} N_c N_f \frac{\kappa^2 m^2}{\Lambda^4 8\pi}, \end{aligned} \quad (4.39)$$

in which K^{an} is the K-factor of the DM annihilation cross section

$$K^{an} = 1 + \frac{\alpha_s C_F}{2\pi} \left[\frac{17}{2} - 3 \ln \left(\frac{4m^2}{\Lambda^2} \right) \right]. \quad (4.40)$$

Here, only the v^2 term contributes to the relic density. This case is called the p -wave annihilation, in contrast to the case of s -wave annihilation that the v^0 term dominates.

Now the result for the relic density can be obtained after putting Eq. (4.39) into Eq. (4.28). We show the results in the left plot of Fig. 4.3. We can see that the new physics scale increases with the increasing of the DM mass in order to produce the present relic density. And the new physics scale becomes larger after the QCD NLO corrections are included. The allowed DM mass as a function of new physics scale is shown in the right plot of Fig. 4.3. Since we do not hold the point of view

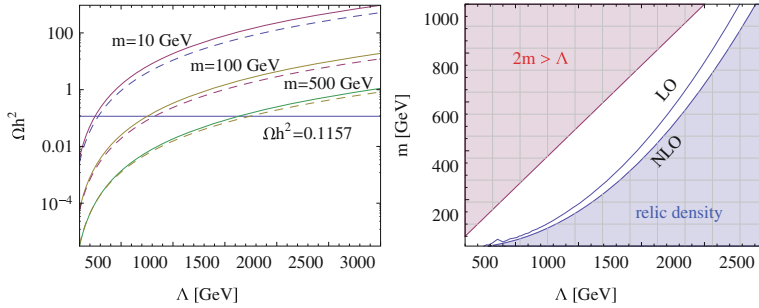


Fig. 4.3 The relic density as a function of the new physics scale and the DM mass (*left plot*) and the allowed DM mass region as a function of the new physics scale (*right plot*). In the *left plot*, the *solid* and *dashed lines* correspond to the LO and NLO results, respectively. In the *right plot*, the *blue* region is excluded by the relic density constraint while the *red* regions represent the parameter regions where the effective theory is not appropriate

that the abundance of the WIMP is determined only by this one kind of DM, the parameter region between the red region and solid lines in the right plot of Fig. 4.3 is allowed. To ensure that the effective theory is appropriate, the red region in the right plot of Fig. 4.3 is not allowed. Comparing the LO and NLO results, we find that the NLO QCD corrections enlarge the allowed parameter regions, with the lower bound decreased by about 10%.

4.4 DM and Photon Associated Production at the LHC

4.4.1 LO Results

Next, we turn to the signal of DM and photon associated production at the LHC. The subprocess of this production at LO is denoted by

$$q(p_1) + \bar{q}(p_2) \rightarrow \chi(p_3) + \bar{\chi}(p_4) + \gamma(p_5), \quad (4.41)$$

whose Feynman diagrams are shown in Fig. 4.4. In the above notation, we have written the momentum of each particle explicitly.

The amplitude involving the DM particles, denoted by \mathcal{M}_{DM} , is easy to calculate. Moreover, due to the special structure of the operator in Eq. (4.10), their contributions to the cross section can be factorized out, so

$$|\mathcal{M}_{DM}|^2 = 2 (s_{34} - 4m^2). \quad (4.42)$$

where $s_{ij} \equiv (p_i + p_j)^2$. Meanwhile, the LO matrix element can be written as

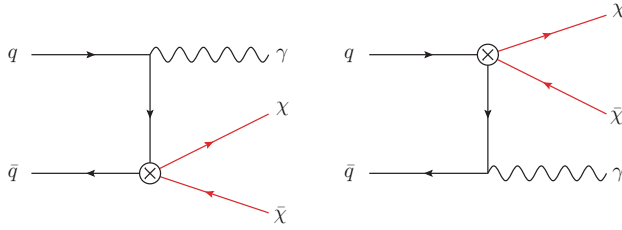


Fig. 4.4 LO Feynman diagrams

$$\mathcal{M}_B = \frac{M_1(-t_{15} - t_{25}) + 2M_2t_{25} - 2M_3t_{15}}{t_{15}t_{25}} \mathcal{M}_{DM}, \quad (4.43)$$

where $t_{ij} \equiv (p_i - p_j)^2$ and M_i , $i = 1, 2, 3$ represent the three independent standard matrix elements, defined by

$$\begin{aligned} M_1 &= \bar{v}(p_2) \not{p}_5 \gamma^\mu u(p_1) \epsilon_\mu(p_5), \\ M_2 &= \bar{v}(p_2) u(p_1) p_1^\mu \epsilon_\mu(p_5), \\ M_3 &= \bar{v}(p_2) u(p_1) p_2^\mu \epsilon_\mu(p_5). \end{aligned} \quad (4.44)$$

The spin and color states of the final-state particles are not observed, thus, the different states should be summed. The polarizations of initial states are not specified before collision, thus, the different states should be averaged. Then, the final summed and averaged LO matrix element squared reads

$$\overline{|\mathcal{M}_B|^2} = \frac{4\pi\alpha\kappa^2}{3\Lambda^4} \frac{s_{12}^2 + s_{34}^2}{t_{15}t_{25}} |\mathcal{M}_{DM}|^2, \quad (4.45)$$

where $\alpha = e^2/4\pi$. The LO partonic cross section is given by

$$\hat{\sigma}_B = \frac{1}{2s_{12}} \int d\Gamma_3 \overline{|\mathcal{M}_B|^2}, \quad (4.46)$$

in which Γ_3 is the three-body phase space. After convoluting with the PDFs $G_{q(\bar{q})}(x)$, it is easy to obtain the LO hadronic cross section

$$\sigma_B = \int dx_1 dx_2 [G_{q/p}(x_1) G_{\bar{q}/p}(x_2) + (x_1 \leftrightarrow x_2)] \hat{\sigma}_B. \quad (4.47)$$

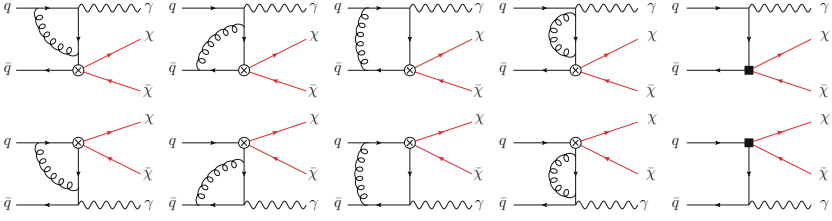


Fig. 4.5 Feynman diagrams for one-loop virtual corrections

4.4.2 NLO Results

The NLO results consist of the one-loop virtual gluon effects and contributions of real gluon and (anti-)quark emissions.

The virtual gluon corrections to DM and photon-associated production include the self-energy, vertex, and box diagrams, as shown in Fig. 4.5. The UV divergences in the virtual corrections are canceled between the loop diagrams and counterterms which are the same as in discussing the relic density. The total virtual gluon corrections to the partonic cross section are

$$\hat{\sigma}_V = \frac{1}{2s_{12}} \int d\Gamma_3 \overline{(\mathcal{M}_B^* \mathcal{M}_V + \mathcal{M}_B \mathcal{M}_V^*)}, \quad (4.48)$$

in which

$$\begin{aligned} \mathcal{M}_V = & \frac{\alpha_s C_F}{4\pi} C_\epsilon \left[\left(\frac{A_2^V}{\epsilon^2} + \frac{A_1^V}{\epsilon^1} + A_0^V \right) \mathcal{M}_B \right. \\ & \left. + \frac{3M_1(t_{15} + t_{25}) - 4M_2 t_{25} + 4M_3 t_{15}}{t_{15} t_{25}} \mathcal{M}_{DM} \right], \end{aligned} \quad (4.49)$$

where

$$\begin{aligned} A_2^V &= -2, \\ A_1^V &= -3, \\ A_0^V &= 3 \ln \frac{\Lambda^2}{s_{12}} + \ln^2 \left(\frac{s_{12}}{t_{15}} \right) + \ln^2 \left(\frac{s_{12}}{t_{25}} \right) + 2\text{Li}_2 \left(-\frac{s_{12} + t_{15}}{t_{25}} \right) \\ &+ 2\text{Li}_2 \left(-\frac{s_{12} + t_{25}}{t_{15}} \right) + 4\text{Li}_2 \left(-\frac{t_{15} + t_{25}}{s_{12}} \right) + 2\pi^2. \end{aligned} \quad (4.50)$$

We can also write Eq. (4.48) in the form

$$d\hat{\sigma}_V = \frac{\alpha_s C_F}{2\pi} C_\epsilon \left[\left(\frac{A_2^V}{\epsilon^2} + \frac{A_1^V}{\epsilon} + A_0^V \right) d\hat{\sigma}_B + d\tilde{\sigma}_V \right], \quad (4.51)$$

with

$$d\tilde{\sigma}_V = -\frac{1}{2s_{12}} \frac{4\pi\alpha\kappa^2}{3\Lambda^4} \frac{4s_{12}^2 + 5(t_{15} + t_{25})s_{12} + 3(t_{15} + t_{25})^2}{t_{15}t_{25}} |\mathcal{M}_{DM}|^2 d\Gamma_3. \quad (4.52)$$

The divergences denoted by A_2^V and A_1^V terms are all IR divergences, which would cancel the IR divergences in real corrections.

The Feynman diagrams for the real gluon emission process

$$q(p_1) + \bar{q}(p_2) \rightarrow \chi(p_3) + \bar{\chi}(p_4) + \gamma(p_5) + g(p_6) \quad (4.53)$$

have been shown in Fig. 4.6. The amplitude squared for this process is easy to get. The difficulty lies in the phase space integration, in which the soft and collinear singularities appear. When discussing the DM annihilations, the phase space integration was obtained analytically. The total cross section is enough to derive the relic density. However, we want to obtain more kinematic information of the final states when studying the signal of DM at the colliders. In addition, the four-body phase space, containing massive particles, is more complicated than that in DM annihilations. Therefore, more advanced technique is needed. We employ the two-cutoff phase space slicing method to separate the regions with singularities and perform the phase space integration analytically in these regions [39]. In this way, the real corrections can be divided into three parts, i.e.,

$$d\hat{\sigma}_R = d\hat{\sigma}_R^S + d\hat{\sigma}_R^{HC} + d\hat{\sigma}_R^{\overline{HC}}, \quad (4.54)$$

where $\hat{\sigma}_R^S$ and $\hat{\sigma}_R^{HC}$ represent the contributions from soft- and hard-collinear regions, respectively. The soft regions are defined by requiring that the energy of the emitted

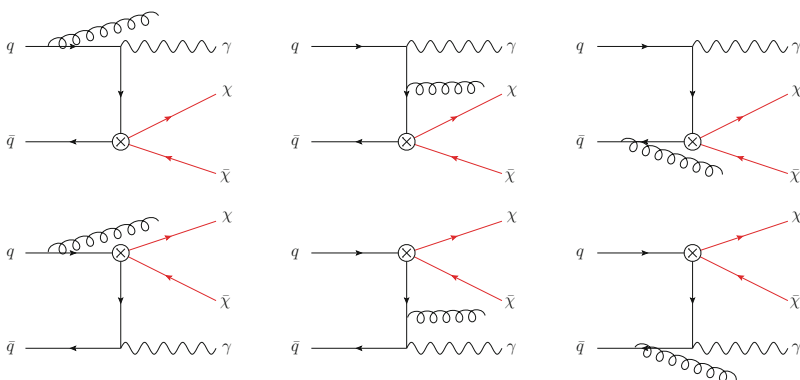


Fig. 4.6 Feynman diagrams for a real gluon emission

gluon $E_6 \leq \delta_s \sqrt{s_{12}}/2$, where δ_s is a small dimensionless cutoff parameter. The hard-collinear regions are defined outside the soft regions by the conditions that $|t_{i6}| < \delta_c s_{12} (t_{i6} = (p_i - p_6)^2, i = 1, 2)$, where δ_c is another cutoff parameter. The hard non-collinear cross section $\hat{\sigma}_R^{\overline{HC}}$ is evaluated in the rest part of the phase space, in which the amplitude squared is finite and can be computed numerically by Monte Carlo method. The optimized phase space integration over these regions are presented in Appendix.

We first deal with the phase space integration in the soft regions. The partonic cross section in soft regions is very simple and can be factorized as

$$d\hat{\sigma}_R^S = (4\pi\alpha_s\mu_R^{2\epsilon})d\hat{\sigma}_B \int dS\Phi_{eik}, \quad (4.55)$$

where dS denotes the integration over the phase space of the soft gluon

$$dS = \frac{1}{2(2\pi)^{3-2\epsilon}} \int_0^{\delta_s \sqrt{s_{12}}/2} dE_6 E_6^{1-2\epsilon} d\Omega_{2-2\epsilon}. \quad (4.56)$$

Here the gluon momentum is parameterized in the center-of-mass frame of the initial partons,

$$p_6 = E_6(1, \dots, \sin\theta_1 \sin\theta_2, \sin\theta_1 \cos\theta_2, \cos\theta_1), \quad (4.57)$$

and the angular integration is defined by

$$d\Omega_{2-2\epsilon} = \sin^{1-2\epsilon}\theta_1 \sin^{-2\epsilon}\theta_2 d\theta_1 d\theta_2 \Omega_{-2\epsilon} \quad (4.58)$$

with the d -dimensional unit sphere is given by

$$\Omega_{d-1} = \frac{2\pi^{d/2}}{\Gamma(d/2)}. \quad (4.59)$$

The factor Φ_{eik} is the amplitude squared in the soft limit except for $|\overline{\mathcal{M}}_B|^2$, defined by

$$\Phi_{eik} = C_F \frac{s_{12}}{t_{16}t_{26}}. \quad (4.60)$$

This special property of the cross section in the soft regions is called the eikonal approximation. After integrating the energy and angular parts in Eq. (4.56) separately, we get

$$d\hat{\sigma}_R^S = d\hat{\sigma}_B \frac{\alpha_s C_F}{2\pi} C_\epsilon \left(\frac{A_2^S}{\epsilon^2} + \frac{A_1^S}{\epsilon} + A_0^S \right), \quad (4.61)$$

with

$$A_2^S = 2, \quad A_1^S = -4 \ln \delta_s, \quad A_0^S = 4 \ln^2 \delta_s - \frac{2\pi^2}{3}. \quad (4.62)$$

The A_2^S term comes from the region in which the soft gluon becomes collinear to the initial partons.

In the hard-collinear regions of this process, the momentum of the emitted gluon become collinear to the initial partons. In this limit, the amplitude squared is approximated by

$$\overline{|\mathcal{M}_R|^2} \approx (4\pi\alpha_s\mu_R^2)\overline{|\mathcal{M}_B|^2} \left[\frac{-2P_{qq}(z, \epsilon)}{zt_{16}} + \frac{-2P_{\bar{q}\bar{q}}(z, \epsilon)}{zt_{26}} \right], \quad (4.63)$$

where z represents the fraction of initial partons' momentum carried by $q(\bar{q})$. $P_{ij}(z, \epsilon)$ are the unregulated splitting functions in n -dimensions which is related to the usual Altarelli-Parisi splitting kernels as $P_{ij}(z, \epsilon) = P_{ij}(z) + \epsilon P'_{ij}(z)$. In our case,

$$P_{qq}(z) = C_F \frac{1+z^2}{1-z}, \quad P'_{qq}(z) = -C_F(1-z). \quad (4.64)$$

In the limit $t_{16} \rightarrow 0$, the four-body phase space can be written as

$$d\Gamma_{4|coll} = d\Gamma_3(s'_{12} = zs_{12}) \frac{(4\pi)^\epsilon}{16\pi^2\Gamma(1-\epsilon)} dz dt_{16} [-(1-z)t_{16}]^{-\epsilon}. \quad (4.65)$$

The integration over t_{16} can be performed,

$$\int_0^{\delta_c s_{12}} d(-t_{16})(-t_{16})^{-1-\epsilon} = -\frac{1}{\epsilon} (\delta_c s_{12})^{-\epsilon}. \quad (4.66)$$

Therefore, we obtain

$$d\sigma_R^{HC} = d\hat{\sigma}_B \frac{\alpha_s}{2\pi} C_\epsilon \left(-\frac{1}{\epsilon}\right) \delta_c^{-\epsilon} \int_{x_i}^{1-\delta_s} \frac{dz}{z} \left(\frac{1-z}{z}\right)^{-\epsilon} [P_{qq}(z, \epsilon) G_{q/p}(x_1/z) G_{\bar{q}/p}(x_2) + P_{\bar{q}\bar{q}}(z, \epsilon) G_{\bar{q}/p}(x_1) G_{q/p}(x_2/z) + (x_1 \leftrightarrow x_2)] dx_1 dx_2. \quad (4.67)$$

The upper limit of z is set by the requirement that the emitted gluon is not soft. If the emitted parton is a (anti-)quark, the upper limit is 1. Therefore, there is only $1/\epsilon$ poles which come from the hard-collinear regions. Some of these collinear singularities can be absorbed into the PDFs. The renormalized PDFs in the $\overline{\text{MS}}$ scheme reads

$$G_{b/p}(x, \mu_F) = G_{b/p}(x) + \left(-\frac{1}{\epsilon}\right) \left[\frac{\alpha_s}{2\pi} \frac{\Gamma(1-\epsilon)}{\Gamma(1-2\epsilon)} \left(\frac{4\pi\mu_R^2}{\mu_F^2}\right)^\epsilon \right] \int_x^1 \frac{dz}{z} P_{ba}(z) G_{a/p}(x/z). \quad (4.68)$$

The above equation can be used to replace $G_{q(\bar{q})/p}$ in the LO hadronic cross section in Eq.(4.47). After that, we combine the result with the hard-collinear contribution in Eq.(4.67). The resulting contribution from hard-collinear regions is

$$\begin{aligned}
d\sigma^{hc} = & d\hat{\sigma}_B \frac{\alpha_s}{2\pi} C_\epsilon \left\{ \tilde{G}_{q/p}(x_1, \mu_F) G_{\bar{q}/p}(x_2, \mu_F) + G_{q/p}(x_1, \mu_F) \tilde{G}_{\bar{q}/p}(x_2, \mu_F) \right. \\
& + \sum_{a=q, \bar{q}} \left[\frac{A_1^{hc}(a \rightarrow ag)}{\epsilon} + A_0^{hc}(a \rightarrow ag) \right] G_{q/p}(x_1, \mu_F) G_{\bar{q}/p}(x_2, \mu_F) \\
& \left. + (x_1 \leftrightarrow x_2) \right\} dx_1 dx_2. \tag{4.69}
\end{aligned}$$

with

$$\begin{aligned}
A_1^{hc}(q \rightarrow qg) &= C_F(2 \ln \delta_s + 3/2), \\
A_0^{hc}(q \rightarrow qg) &= A_1^{hc}(q \rightarrow qg) \ln \left(\frac{s_{12}}{\mu_F^2} \right). \tag{4.70}
\end{aligned}$$

The \tilde{G} functions are given by

$$\tilde{G}_{b/p}(x, \mu_F) = \sum_a \int_x^{1-\delta_s \delta_{ab}} \frac{dy}{y} G_{a/p}(x/y, \mu_F) \tilde{P}_{ba}(y) \tag{4.71}$$

with

$$\tilde{P}_{ba}(y) = P_{ba}(y) \ln \left(\delta_c \frac{1-y}{y} \frac{s_{12}}{\mu_F^2} \right) - P'_{ba}(y). \tag{4.72}$$

The above $1/\epsilon$ pole arises because the integration ranges of z are not the same in Eqs. (4.67) and (4.68).

Then, we consider the (anti)quark emitted processes, such as

$$q(p_1) + g(p_2) \rightarrow \chi(p_3) + \bar{\chi}(p_4) + \gamma(p_5) + q(p_6), \tag{4.73}$$

the Feynman diagrams of which are shown in Fig. 4.7. Due to crossing symmetry, these contributions can be obtained from the results of processes in Eq. (4.53) by $p_1(p_2) \leftrightarrow p_6$. Meanwhile, we should notice that the collinear divergences in these processes can be totally absorbed into the redefinition of the PDFs in Eq. (4.68).

Combing all the pieces above, the NLO cross section for the process $pp \rightarrow \chi\bar{\chi}\gamma$ is

$$\begin{aligned}
\sigma^{NLO} = & \int dx_1 dx_2 \left\{ [G_{q/p}(x_1, \mu_F) G_{\bar{q}/p}(x_2, \mu_F) + (x_1 \leftrightarrow x_2)] (\hat{\sigma}_B + \hat{\sigma}_V + \hat{\sigma}_R^S + \hat{\sigma}_R^{\overline{HC}}) \right\} \\
& + \sigma^{hc} \tag{4.74} \\
& + \sum_{a=q, \bar{q}} \int dx_1 dx_2 [G_{g/p}(x_1, \mu_F) G_{a/p}(x_2, \mu_F) + (x_1 \leftrightarrow x_2)] \hat{\sigma}_R^{\overline{C}}(ga \rightarrow \chi\bar{\chi}\gamma a),
\end{aligned}$$

where \overline{C} in $\hat{\sigma}_R^{\overline{C}}(ga \rightarrow \chi\bar{\chi}\gamma a)$ means that the phase space integration is performed in the non-collinear regions. It is evident that

$$A_2^V + A_2^S = 0, \quad A_1^V + A_1^S + 2A_1^{hc}(q \rightarrow qg) = 0. \tag{4.75}$$

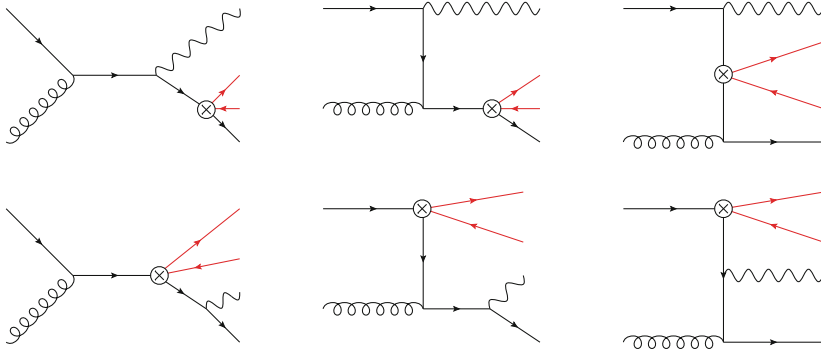


Fig. 4.7 Feynman diagrams for a quark emission. The Feynman diagrams for a anti-quark emission can be obtained by flipping all the arrows on the Fermion lines

Thus there are no singularities left now.

4.4.3 Numerical Results

In this subsection, we present the numerical results for the cross sections of DM and photon-associated production at the LHC. In numerical calculation, we choose the CTEQ6L1 (CTEQ6M) PDF sets [40] and the one (two) loop running strong coupling α_s for the LO (NLO) calculations. The default factorization and renormalization scales, i.e., μ_F and μ_R , are set to be $2m$. We choose the model parameters $(m, \Lambda) = (200 \text{ GeV}, 1000 \text{ GeV})$ and $\kappa = 1$ unless specified otherwise, This choice is consistent with the relic density constraint. We apply the following kinematic cuts

$$\begin{aligned}
 p_T^\gamma &> 100 \text{ GeV}, \\
 |\eta^\gamma| &< 2.4, \\
 p_T^{\text{miss}} &> 100 \text{ GeV},
 \end{aligned}
 \tag{4.76}$$

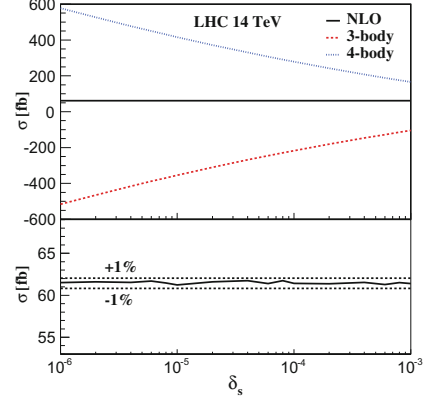
in our numerical calculation. Here p_T^{miss} is the missing transverse momentum, defined as

$$p_T^{\text{miss}} \equiv \begin{cases} p_T^\gamma, & \text{no jets in the final states,} \\ p_T^{\chi\bar{\chi}}, & \text{with jets in the final states,} \end{cases}
 \tag{4.77}$$

where $p_T^{\chi\bar{\chi}}$ is the transverse momentum of the system of the DMs. Jets are defined by the requirements

$$p_T^j > 20 \text{ GeV}, \quad |\eta^j| < 2.5.
 \tag{4.78}$$

Fig. 4.8 Dependence of the NLO cross sections for the DM and photon-associated production at the LHC on the cutoff parameter δ_s with $\delta_c = \delta_s/50$



In order to avoid QED collinear divergences (i.e., the photon becomes collinear to quarks), we also require the photon to be isolated from jets by the prescription [41]

$$\sum_{R_{j\gamma} \in R_0} p_T^j < p_T^\gamma \left(\frac{1 - \cos R_{j\gamma}}{1 - \cos R_0} \right). \quad (4.79)$$

where $R_{j\gamma} \equiv \sqrt{\Delta\phi_{j\gamma}^2 + \Delta\eta_{j\gamma}^2}$ and $R_0 = 0.4$.

Before we show any kinematic distribution, we should validate our calculation first. The most tricky place is that we have divided the real corrections to three parts by two-cutoff parameters; see Eq. (4.54). Each of them depends on the cutoff parameters, but their sum does not. If we calculate each component right, then we would discover this phenomenon. In Fig. 4.8 we show the the NLO cross sections as a function of the cutoff parameters. We change the parameter δ_s from 10^{-6} to 10^{-3} , and the parameter δ_c varies accordingly with $\delta_c = \delta_s/50$. The result of three-body final states includes the LO cross section, virtual corrections, soft, and collinear limits of the cross section of four-body final states. The result of four-body final states consists of the cross section of four-body final states with the singular regions sliced. We see that they change obviously but their sum is almost a constant, within an error of $\pm 1\%$. This can be considered as a strong check on our calculation.

In Fig. 4.9 we show the dependence of the cross sections on m and Λ . The LO (NLO) cross sections decrease from 97.7 (80.6) fb to 26.1 (28.2) fb as m increases from 20 to 500 GeV. The corresponding K-factor, defined as the ratio of the NLO cross sections to the LO ones, varies from 0.82 to 1.08. The LO (NLO)

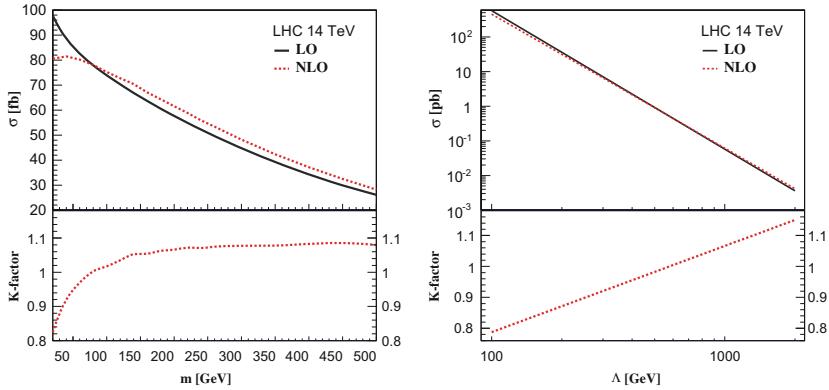


Fig. 4.9 Dependence of the LO and NLO cross sections for the DM and photon associated production at the LHC on the DM mass and the new physics scale Λ . Also shown is the K-factor

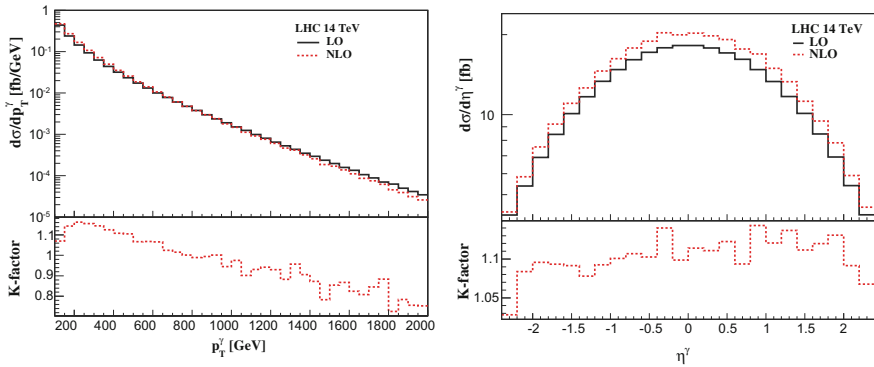
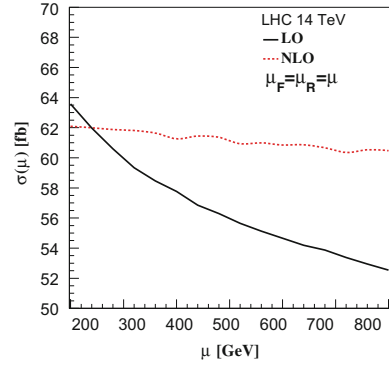


Fig. 4.10 The QCD NLO corrections to the differential distributions. Also shown is the differential K-factor

cross sections decrease from 577 (454) pb to 3.61 (4.15) fb as Λ increases from 100 to 2000 GeV. The corresponding K-factor varies from 0.79 to 1.15. We also show the QCD NLO corrections to the differential distributions in Fig. 4.10. The distribution of the photon's transverse momentum is enhanced and suppressed in the small and large regions, respectively, after including the higher-order correction. The distribution of the photon's rapidity is increased uniformly.

We present the dependence of the cross section on the factorization scale μ_F and renormalization scale μ_R in Fig. 4.11. This kind of theoretical uncertainty is significantly reduced at NLO, which makes the theoretical prediction much more reliable.

Fig. 4.11 Dependence of the LO (NLO) cross sections for the DM and photon associated production at the LHC on the factorization scale μ_F and renormalization scale μ_R



4.5 Backgrounds and Discovery Potential

The dominant SM backgrounds for this process are $pp \rightarrow Z(\rightarrow \nu\bar{\nu}) + \gamma$ and $pp \rightarrow Z(\rightarrow \nu\bar{\nu}) + j$ with the jet misidentified as a photon. Since the NLO QCD corrections for these processes are significant, we use the parton-level Monte Carlo program MCFM [42–45] to calculate these backgrounds at the NLO level. At the Tevatron, the probability $P_{\gamma/j}$ that a jet fakes a photon is almost vanishing if the transverse momentum of the photon p_T^γ is larger than 100 GeV because the hits with large p_T in the central preradiator chambers are counted and thus the prompt photon can be distinguished from meson decays [46]. At the LHC, we set $P_{\gamma/j} = 10^{-4}$ as a conservative estimation, as suggested in Ref. [47].

In Fig. 4.12, we show the differential cross sections of both the signal and backgrounds as a function of p_T^γ and p_T^{miss} . We can see that the $Z\gamma$ production is the dominant background. The distribution of the backgrounds decreases faster than that of the signal with the increasing of p_T^γ and p_T^{miss} . Therefore, the ratio of signal and background will increase if we set a larger p_T^γ or p_T^{miss} cut.

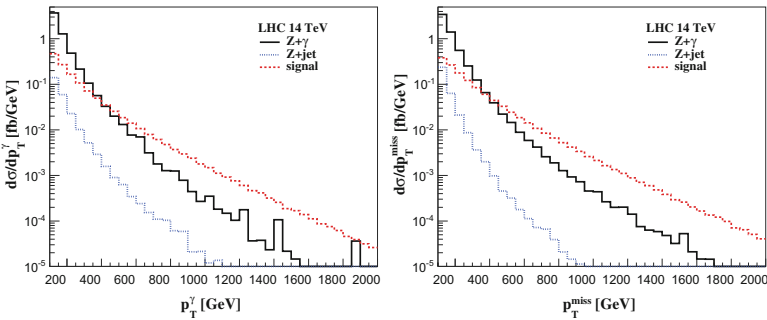
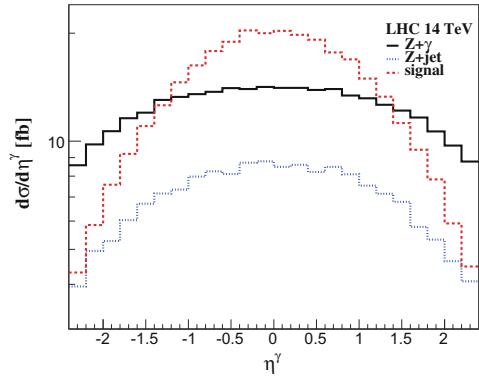


Fig. 4.12 Dependence of the differential cross section on p_T^γ (left) and p_T^{miss} (right)

Fig. 4.13 Dependence of the differential cross section on η^γ



In Fig. 4.13, we show the differential cross section of both the signal and backgrounds as a function of η^γ . We find that the signal is more concentrated in the central region of η^γ than the backgrounds. This is a result of the special structure of the effective operator. This feature may help to select the events in experiments.

Fig. 4.14 shows the new physics scale corresponding to the 5σ ($S/\sqrt{B} = 5$) discovery as a function of the integrated luminosity and the DM mass at the LHC. The physics scale increases fast before the data are accumulated up to 20 fb^{-1} . Beyond that it increases slowly with the increasing of the data. If the real physics scale is around 1500 GeV , then the LHC can discover the DM signal after collecting 30 and 50 fb^{-1} data corresponding to the DM mass $m = 100$ and 200 GeV , respectively. From the right plot in Fig. 4.14, we know the energy scale should be lower than the green line if the signal is discovered with 10 fb^{-1} data. The situations with 50 fb^{-1} and 100 fb^{-1} data are shown as well.

On the other hand, the LHC may not detect this signal with 100 fb^{-1} data. Then, we can derive the exclusion limits on the new physics scale and the DM mass at

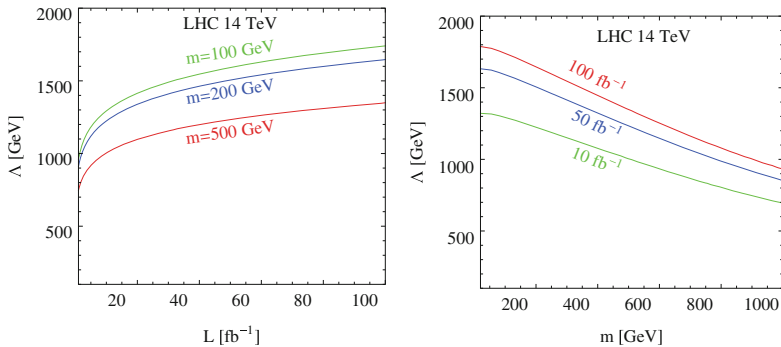
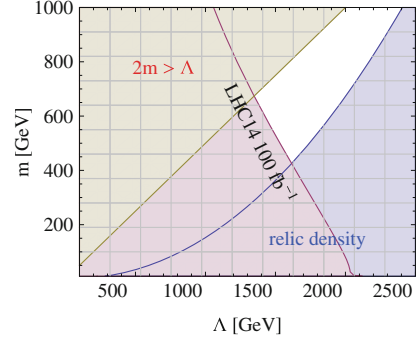


Fig. 4.14 The new physics scale corresponding to the 5σ discovery as a function of the integrated luminosity (*left plot*) and the DM mass (*right plot*) at the LHC

Fig. 4.15 The allowed parameter regions if the DM signal is not observed at the LHC with 100 fb^{-1} data



the 3σ ($S/\sqrt{S+B} = 3$) level in Fig. 4.15. We also show the parameter regions that have been excluded by the relic density and requirement of the theory consistency. We can see that the regions with DM mass $m < 400 \text{ GeV}$ would be totally excluded.

4.6 Conclusions and Comments

The DM is a mystery in our knowledge about the universe. We know it exists, but do not know what is its content. It is interesting to study the possibility of producing DM at colliders on the earth. In this chapter, we investigate the signal of DM and a photon associated production at the LHC induced by a dimension six effective operator at the NLO QCD level. We analyze the parameter regions that have been constrained by the relic density. We also look at the main backgrounds from SM to this signal, i.e., Z boson and a photon associated production with invisible decay of Z boson, and Z boson and a jet production with the jet misidentified as a photon. We find some features of the kinematic distributions that may help to select the events in experiments. After that, we present the new physics scale corresponding to the 5σ discovery. In the case that this signal is not observed with 100 fb^{-1} data, we obtain the exclusion limits on the new physics scale and the DM mass, and compare with those from relic density and theory consistency.

This work just shows an example of predicting the NLO QCD result for mono-photon production induced by an effective operator. It is easy to extend to other operators, such as the vector and pseud-vector operators in Ref. [48], as well as other associated production channels, such as the mono- W [49] and mono- j production [50, 51]. Different production channels are sensitive to different coupling structures, and can help to confirm a future discovery.

On the other hand, the effective operators are just approximations of more complete models. Its validity should be carefully checked when applied to study the DM production at the LHC [23, 32, 33, 52–55]. The minimal requirement that the energy scale should be much larger than the momentum transferred to producing the DM pair is not always guaranteed for the entire region of phase space probed by the

experiment searches at the LHC. It is possible that the mediator (a few TeV) that has been integrated in the effective operators can be accessible in the events with high p_T , rendering the assumption invalid. This issue will be more pressing at the LHC Run-II. As a result, an alternative framework, called simplified models, is proposed to probe the DM interactions [56–71]. The simplified models incorporate the complete degrees of freedom of UV-complete models at the low energy region, but do not describe the interaction by integrating out any propagator. It keeps the simplicity of the effective operator and avoid its drawbacks. Moreover, it may provide new search signals except for the missing energy, such as the search for the mediators. Meanwhile, the simplified model brings some complications. The couplings between the mediator and the DM or SM particles should be specified in calculation, and the width of the mediator needs to be calculated in advance. As a consequence, the result depends on the couplings in a nontrivial way. We are going to investigate these issues in the near future.

References

1. G. Hinshaw et al., W.M.A.P. Collaboration, Nine-year wilkinson microwave anisotropy probe (wmap) observations: cosmological parameter results. *Astrophys. J. Suppl.* **208**, 19 (2013). [arXiv:1212.5226](#)
2. F. Zwicky, Die Rotverschiebung von extragalaktischen Nebeln. *Helv. Phys. Acta.* **6**, 110–127 (1933)
3. F. Zwicky, On the masses of nebulae and of clusters of nebulae. *Astrophys. J.* **86**, 217–246 (1937)
4. O. Adriani et al., PAMELA Collaboration, PAMELA results on the cosmic-ray antiproton flux from 60 MeV to 180 GeV in kinetic energy. *Phys. Rev. Lett.* **105**, 121101 (2010). [arXiv:1007.0821](#)
5. J. Chang et al., An excess of cosmic ray electrons at energies of 300–800 GeV. *Nat.* **456**, 362–365 (2008)
6. F. Aharonian et al., H.E.S.S. Collaboration, The energy spectrum of cosmic-ray electrons at TeV energies. *Phys. Rev. Lett.* **101**, 261104 (2008). [arXiv:0811.3894](#)
7. A.A. Abdo et al., The Fermi LAT Collaboration, Measurement of the cosmic ray e+ plus e- spectrum from 20 GeV to 1 TeV with the fermi large area telescope. *Phys. Rev. Lett.* **102**, 181101 (2009). [arXiv:0905.0025](#)
8. R. Bernabei et al., DAMA Collaboration, First results from DAMA/LIBRA and the combined results with DAMA/NaI. *Eur. Phys. J. C* **56**, 333–355 (2008). [arXiv:0804.2741](#)
9. Z. Ahmed et al., C.D.M.S. Collaboration, Search for weakly interacting massive particles with the first five-tower data from the cryogenic dark matter search at the soudan underground laboratory. *Phys. Rev. Lett.* **102**, 011301 (2009). [arXiv:0802.3530](#)
10. C.E. Aalseth et al., CoGeNT Collaboration, Results from a search for light-mass dark matter with a p- type point contact germanium detector. *Phys. Rev. Lett.* **106**, 131301 (2011). [arXiv:1002.4703](#)
11. E. Aprile et al., XENON100 Collaboration, First dark matter results from the XENON100 experiment. *Phys. Rev. Lett.* **105**, 131302 (2010). [arXiv:1005.0380](#)
12. D. Akerib et al., LUX Collaboration, First results from the LUX dark matter experiment at the sanford underground research facility. *Phys. Rev. Lett.* **112**, 091303 (2014). [arXiv:1310.8214](#)
13. O. Buchmueller et al., Supersymmetry and dark matter in light of LHC 2010 and XENON100 data. *Eur. Phys. J.* **C71**, 1722 (2011). [arXiv:1106.2529](#)

14. T. Li, J.A. Maxin, D.V. Nanopoulos, J.W. Walker, The race for supersymmetric dark matter at XENON100 and the LHC: stringy correlations from no-scale F-SU(5). *JHEP* **1212**, 017 (2012). [arXiv:1106.1165](#)
15. S. Profumo, The quest for supersymmetry: early lhc results versus direct and indirect neutralino dark matter searches. *Phys. Rev.* **D84**, 015008 (2011). [arXiv:1105.5162](#)
16. G. Belanger, S. Kraml, A. Lessa, Light sneutrino dark matter at the LHC. *JHEP* **1107**, 083 (2011). [arXiv:1105.4878](#)
17. J. Kile, A. Soni, Flavored dark matter in direct detection experiments and at LHC. *Phys. Rev.* **D84**, 035016 (2011). [arXiv:1104.5239](#)
18. S. Akula, D. Feldman, Z. Liu, P. Nath, G. Peim, New constraints on dark matter from CMS and ATLAS data. *Mod. Phys. Lett.* **A26**, 1521–1535 (2011). [arXiv:1103.5061](#)
19. D. Feldman, K. Freese, P. Nath, B. D. Nelson, G. Peim, Predictive signatures of supersymmetry: measuring the dark matter mass and gluino mass with early LHC data. *Phys. Rev.* **D84**, 015007 (2011). [arXiv:1102.2548](#)
20. Y. Bai, H.-C. Cheng, Identifying dark matter event topologies at the LHC. *JHEP* **06**, 021 (2011). [arXiv:1012.1863](#)
21. I. Gogoladze, R. Khalid, Y. Mimura, Q. Shafi, Direct and indirect detection and LHC signals of bino- higgsino dark matter. *Phys. Rev. D* **83**, 095007 (2011). [arXiv:1012.1613](#)
22. K. Cheung, K. Mawatari, E. Senaha, P.-Y. Tseng, T.-C. Yuan, The top window for dark matter. *JHEP* **10**, 081 (2010). [arXiv:1009.0618](#)
23. J. Goodman et al., Constraints on dark matter from colliders. *Phys. Rev. D* **82**, 116010 (2010). [arXiv:1008.1783](#)
24. G. Bertone, D.G. Cerdeno, M. Fornasa, R. Ruiz de Austri, R. Trotta, Identification of dark matter particles with LHC and direct detection data. *Phys. Rev. D* **82**, 055008 (2010). [arXiv:1005.4280](#)
25. G.F. Giudice, T. Han, K. Wang, L.-T. Wang, Nearly degenerate gauginos and dark matter at the LHC. *Phys. Rev. D* **81**, 115011 (2010). [arXiv:1004.4902](#)
26. T. Li, W. Chao, Neutrino masses, dark matter and B-L symmetry at the LHC. *Nucl. Phys. B* **843**, 396–412 (2011). [arXiv:1004.0296](#)
27. M. Beltran, D. Hooper, E.W. Kolb, Z.A.C. Krusberg, T.M.P. Tait, Maverick dark matter at colliders. *JHEP* **09**, 037 (2010). [arXiv:1002.4137](#)
28. H. Zhang, C.S. Li, Q.-H. Cao, Z. Li, A dark matter model with non-abelian gauge symmetry. *Phys. Rev. D* **82**, 075003 (2010). [arXiv:0910.2831](#)
29. N. Arkani-Hamed, N. Weiner, LHC signals for a superunified theory of dark matter. *JHEP* **12**, 104 (2008). [arXiv:0810.0714](#)
30. D. Fargion, M.Y. Khlopov, R.V. Konoplich, R. Mignani, On the possibility of searching for heavy neutrinos at accelerators. *Phys. Rev. D* **54**, 4684–4686 (1996)
31. Q.-H. Cao, C.-R. Chen, C.S. Li, H. Zhang, Effective dark matter model: relic density, CDMS II, fermi LAT and LHC. [arXiv:0912.4511](#)
32. Y. Bai, P.J. Fox, R. Harnik, The Tevatron at the frontier of dark matter direct detection. *JHEP* **12**, 048 (2010). [arXiv:1005.3797](#)
33. P.J. Fox, R. Harnik, J. Kopp, Y. Tsai, Missing energy signatures of dark matter at the LHC. *Phys. Rev. D* **85**, 056011 (2012). [arXiv:1109.4398](#)
34. K. Cheung, P.-Y. Tseng, Y.-L.S. Tsai, T.-C. Yuan, Global constraints on effective dark matter interactions: relic density, direct detection, indirect detection, and collider. *JCAP* **1205**, 001 (2012). [arXiv:1201.3402](#)
35. M. Beltran, D. Hooper, E.W. Kolb, Z.A.C. Krusberg, Deducing the nature of dark matter from direct and indirect detection experiments in the absence of collider signatures of new physics. *Phys. Rev. D* **80**, 043509 (2009). [arXiv:0808.3384](#)
36. E.W. Kolb, M.S. Turner, The Early universe. *Front. Phys.* **69**, 1–547 (1990)
37. P. Gondolo, G. Gelmini, Cosmic abundances of stable particles: Improved analysis. *Nucl. Phys. B* **360**, 145–179 (1991)
38. R.J. Scherrer, M.S. Turner, On the relic, cosmic abundance of stable weakly interacting massive particles. *Phys. Rev. D* **33**, 1585 (1986)

39. B. Harris, J. Owens, The two cutoff phase space slicing method. *Phys. Rev. D* **65**, 094032 (2002). [arXiv:hep-ph/0102128](#)
40. J. Pumplin et al., New generation of parton distributions with uncertainties from global QCD analysis. *JHEP* **07**, 012 (2002). [arXiv:hep-ph/0201195](#)
41. S. Frixione, Isolated photons in perturbative QCD. *Phys. Lett. B* **429**, 369–374 (1998). [arXiv:hep-ph/9801442](#)
42. J. M. Campbell, R. K. Ellis, C. Williams, Vector boson pair production at the LHC. [arXiv:1105.0020](#)
43. U. Baur, T. Han, J. Ohnemus, QCD corrections and anomalous couplings in Z gamma production at hadron colliders. *Phys. Rev. D* **57**, 2823–2836 (1998). [arXiv:hep-ph/9710416](#)
44. J. Ohnemus, Order α_s calculations of hadronic W^+ gamma and Z gamma production. *Phys. Rev. D* **47**, 940–955 (1993)
45. W.T. Giele, E.W.N. Glover, D.A. Kosower, Higher order corrections to jet cross-sections in hadron colliders. *Nucl. Phys. B* **403**, 633–670 (1993). [arXiv:hep-ph/9302225](#)
46. D.E. Acosta et al., CDF II Collaboration, Measurement of W gamma and Z gamma production in p anti- p collisions at $\sqrt{s} = 1.96$ TeV. *Phys. Rev. Lett.* **94** (2005) 041803. [arXiv:hep-ex/0410008](#)
47. U. Baur, E.L. Berger, Probing the weak boson sector in Z gamma production at hadron colliders. *Phys. Rev. D* **47**, 4889–4904 (1993)
48. F.P. Huang, C.S. Li, J. Wang, D.Y. Shao, Searching for the signal of dark matter and photon associated production at the LHC beyond leading order. *Phys. Rev. D* **87**, 094018 (2013). [arXiv:1210.0195](#)
49. M. Song, G. Li, W.-G. Ma, R.-Y. Zhang, J.-Y. Guo, Dark matter pair associated with a W boson production at the LHC in next-to-leading order QCD. *JHEP* **1409**, 069 (2014). [arXiv:1403.2142](#)
50. P. J. Fox, C. Williams, Next-to-leading order predictions for dark matter production at hadron colliders. *Phys.Rev.D* **87**(5), 054030 (2013). [arXiv:1211.6390](#)
51. U. Haisch, F. Kahlhoefer, E. Re, QCD effects in mono-jet searches for dark matter. *JHEP* **1312**, 007 (2013). [arXiv:1310.4491](#)
52. G. Busoni, A. De Simone, E. Morgante, A. Riotto, On the validity of the effective field theory for dark matter searches at the LHC. *Phys. Lett. B* **728**, 412–421 (2014). [arXiv:1307.2253](#)
53. O. Buchmueller, M.J. Dolan, C. McCabe, Beyond effective field theory for dark matter searches at the LHC. *JHEP* **1401**, 025 (2014). [arXiv:1308.6799](#)
54. G. Busoni, A. De Simone, J. Gramling, E. Morgante, A. Riotto, On the validity of the effective field theory for dark matter searches at the LHC, part II: complete analysis for the s -channel. *JCAP* **1406**, 060 (2014). [arXiv:1402.1275](#)
55. G. Busoni, A. De Simone, T. Jacques, E. Morgante, A. Riotto, On the validity of the effective field theory for dark matter searches at the LHC part III: analysis for the t -channel. *JCAP* **1409**, 022 (2014). [arXiv:1405.3101](#)
56. J. Alwall, P. Schuster, N. Toro, Simplified models for a first characterization of new physics at the LHC. *Phys. Rev. D* **79**, 075020 (2009). [arXiv:0810.3921](#)
57. D. Alves et al., LHC New Physics Working Group Collaboration, Simplified models for LHC new physics searches. *J. Phys.G* **39**, 105005 (2012). [arXiv:1105.2838](#)
58. J. Goodman, W. Shepherd, LHC bounds on UV-complete models of dark matter. [arXiv:1111.2359](#)
59. H. An, X. Ji, L.-T. Wang, Light dark matter and Z' dark force at colliders. *JHEP* **1207**, 182 (2012). [arXiv:1202.2894](#)
60. M.T. Frandsen, F. Kahlhoefer, A. Preston, S. Sarkar, K. Schmidt-Hoberg, LHC and tevatron bounds on the dark matter direct detection cross-section for vector mediators. *JHEP* **1207**, 123 (2012). [arXiv:1204.3839](#)
61. H. An, L.-T. Wang, H. Zhang, Dark matter with t -channel mediator: a simple step beyond contact interaction. *Phys. Rev. D* **89**(11), 115014 (2014). [arXiv:1308.0592](#)
62. A. DiFranzo, K.I. Nagao, A. Rajaraman, T.M. Tait, Simplified models for dark matter interacting with quarks. *JHEP* **1311**, 014 (2013). [arXiv:1308.2679](#)
63. M. Papucci, A. Vichi, K.M. Zurek, Monojet versus the rest of the world I: t -channel models. *JHEP* **1411**, 024 (2014). [arXiv:1402.2285](#)

64. A. Berlin, D. Hooper, S.D. McDermott, Simplified dark matter models for the galactic center gamma-ray excess. *Phys. Rev. D* **89**(11), 115022 (2014). [arXiv:1404.0022](#)
65. O. Buchmueller, M.J. Dolan, S.A. Malik, C. McCabe, Characterising dark matter searches at colliders and direct detection experiments: vector mediators. *JHEP* **1501**, 037 (2015). [arXiv:1407.8257](#)
66. J. Abdallah, A. Ashkenazi, A. Boveia, G. Busoni, A. De Simone, et al., Simplified models for dark matter and missing energy searches at the LHC. [arXiv:1409.2893](#)
67. S. Malik, C. McCabe, H. Araujo, A. Belyaev, C. Boehm, et al., Interplay and characterization of dark matter searches at colliders and in direct detection experiments. [arXiv:1409.4075](#)
68. M.R. Buckley, D. Feld, D. Goncalves, Scalar simplified models for dark matter. *Phys. Rev. D* **91**(1), 015017 (2015). [arXiv:1410.6497](#)
69. P. Harris, V.V. Khoze, M. Spannowsky, C. Williams, Constraining dark sectors at colliders: beyond the effective theory approach. *Phys. Rev.* **D91**, 055009 (2015). [arXiv:1411.0535](#)
70. T. Jacques, K. Nordstrom, Mapping monojet constraints onto simplified dark matter models. *JHEP* **1506**, 142 (2015). [arXiv:1502.05721](#)
71. U. Haisch, E. Re, Simplified dark matter top-quark interactions at the LHC. *JHEP* **1506**, 078 (2015). [arXiv:1503.00691](#)

Chapter 5

Resummation Prediction on Top Quark Transverse Momentum Distribution at Large p_T

5.1 Introduction

The top quark is one of the third-generation quarks, proposed to exist in 1973 by Kobayashi and Maskawa to explain the observed CP violations in kaon decay [1]. However, it has not been directly observed until 1995 by CDF and DØ collaborations at the Tevatron [2, 3]. The reason is that the top quark is the heaviest particle discovered so far, with a mass close to the electroweak symmetry breaking scale. Because the top quark, as well as the Higgs boson, participate in quantum loop radiative corrections to the W boson mass, the precise measurement of the top quark mass are critical for global electroweak fits which assess the self-consistency within the SM. In addition, because of its large Yukawa coupling, the Higgs boson mass gets an enormous quantum correction from the top quark loop, which makes the mass at about 125 GeV unstable if the energy scale can be extended to the Plank scale. This problem, known as the gauge hierarchy problem in the SM, has motivated a lot of attractive perspectives, such as the minimal supersymmetric standard model (MSSM). The top quark mass also affects the electroweak vacuum stability within the SM. The higher is the top quark mass, the more unstable is the electroweak vacuum. The present value of the top quark mass is $m_t = 173.34 \pm 0.76$ GeV from the combined analysis of the $t\bar{t}$ production at both the Tevatron and the LHC [4]. This mass is measured using a given Monte Carlo event generator, which is different from the pole mass within $\mathcal{O}(1$ GeV) [5, 6]. If we take this value as the top quark pole mass and remember $m_H = 125.09$ GeV and $M_Z = 91.1876$ GeV, then it follows

$$\frac{m_t M_Z}{m_H^2} = 1.010, \quad (5.1)$$

which is very close to 1. It is unclear whether this is just a coincidence or some deeper rules hide here.

Given the above top quark mass, its decay width is $\Gamma_t = 1.3$ GeV [7], corresponding to a life-time of about 5×10^{-25} s, much shorter than the hadronization time.

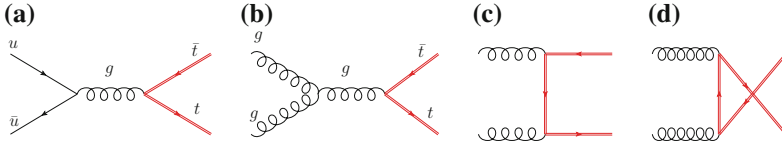


Fig. 5.1 The LO Feynman diagrams for the top quark pair production at hadron colliders. **a** is $q\bar{q}$ channel while **b–d** are gg channel

Thus, the top quarks decay before they can form bound states and the spin information of the top quark is directly transferred to its decay products. This is a unique feature which can be used to detect the coupling structure involving the top quark.

The top quark can decay to Wb and Ws and Wd final states in general. However, the Cabibbo–Kobayashi–Maskawa (CKM) matrix elements V_{ts} and V_{td} , which determine the decay rates, are estimated to be highly suppressed from neutral mesons oscillations and meson rare decays. The matrix element V_{tb} can be determined from top decays assuming the unitarity of the CKM matrix, while the direct measurement of V_{tb} is possible from the single top quark production. The world average value of V_{tb} is [8]

$$|V_{tb}| = 1.021 \pm 0.032. \quad (5.2)$$

This suggests that the top quark almost decays only into Wb .

The main production mode of top quarks at hadron colliders is the $t\bar{t}$ pair production, as shown in Fig. 5.1. Since it is induced by strong interaction, the high-order QCD corrections turn out to be significant. The state of art is the NNLO result combined with soft gluon resummation at NNLL accuracy, which shows that the cross section of top quark pair production is 245.8 and 953.6 pb at the 8 and 14 TeV LHC, respectively [9]. The theoretical uncertainties have been reduced to be less than 6%, allowing precise determination of parton distribution functions (PDFs) and new physics searches in the top quark final state.

The single top production is another main source of top quarks, of which the LO Feynman diagrams are shown in Fig. 5.2. Since it is induced by weak interaction, it is expected the rate is rather small. However, the threshold to produce the single top is less than that to produce the top quark pair, thus the partonic fluxes are relative high. The net effect is that the cross section of the single top production is suppressed with respect to the pair production only by a factor of 2–3. However, due to the

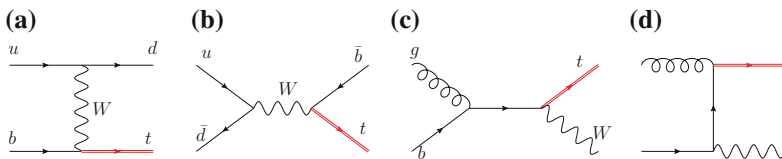
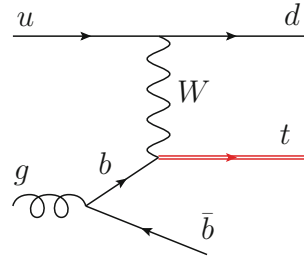


Fig. 5.2 The LO Feynman diagrams for the single top quark production at hadron colliders. **a** is t -channel in five-flavor scheme. **b** is s -channel. **c, d** are tW associated production channel

Fig. 5.3 The LO Feynman diagrams for the single top quark production at hadron colliders in the four-flavor scheme



indistinctive signature and large backgrounds, it takes a long time after the discovery of the top quark for the DØ [10] and CDF [11] collaborations at the Tevatron to observe the single top production. Recently, the ATLAS and CMS collaborations at the LHC have also measured the cross section of the single top production [12–15].

The single top process is sensitive to new physics. A flavor-changing-neutral current involving top quark, such as Zut interaction, induces the same final state. The charged gauge boson W^\pm or Higgs boson H^\pm in some extensions of the SM could be the mediator to generate the single top signal. In order to discover the signal of new physics, it is mandatory to make a precise prediction of the single top production.

There are three single top production modes at hadron colliders, depending on the virtuality Q^2 of the W boson, as shown in Fig. 5.2. If $Q^2 < 0$, it is t -channel. If $Q^2 > m_t^2$, it is s -channel. The associated production corresponds to $Q^2 = M_W^2$. This distinction is obvious at LO, but becomes ambiguous at higher orders. Since the LO result dominates the total cross section, we still use these designations for different modes. The s -channel and associated production are suppressed compared to the t -channel at both the Tevatron and the LHC. As a consequence, the t -channel is of great importance and needs to be studied precisely. This process has been extensively studied first in the five-flavor (5F) scheme [16–23] and then in the four-flavor (4F) scheme [24]. Here, the 5F scheme means that there are five quarks in the proton, including the bottom quark, though the bottom quark is heavier than the proton. In contrast, the 4F scheme indicates that there are only four quarks in the proton, as shown in Fig. 5.3. Therefore, the LO process of the single top production is a $2 \rightarrow 2$ and $2 \rightarrow 3$ scattering in the 5F and 4F scheme, respectively. Because the single top production is induced by electroweak interaction, the QCD correction is not as large as that in top quark pair production. It is reported that the QCD NLO corrections increase the LO cross section in the 5F scheme by about 9 and 5% at the Tevatron and LHC, respectively. In Ref. [24], the NLO result of the t -channel production in the 4F scheme was obtained. The total cross section in the 4F scheme is less than that in the 5F scheme. But the uncertainty in the 4F scheme is larger than that in the 5F scheme. The reason is that the large logarithms of the form $\ln^n(Q^2/m_b^2)$, which would appear in fixed-order calculations in the 4F scheme, has been resummed into the bottom quark PDF in the 5F scheme and thus the scale dependence is significantly reduced.

More effects beyond NLO have been also investigated, such as parton shower [25–27]. Parton shower is designed to resum all the initial and final-state Bremsstrahlung processes. The interested readers are suggested to refer to the introductory review of Ref. [28]. However, the resummation in parton shower is performed at the leading logarithmic (LL) level. More advanced resummation has been carried out in the traditional resummation method [29–31]. But due to the infrared singularities and ambiguities in prescription dependence, as described in Sect. 3.4, the numerical results are not presented. Instead, resummed cross sections are expanded to NNNLO in α_s and subsequently numerical evaluation is performed.

In this chapter, we would perform the resummation of soft and collinear gluon effects in the t -channel single top production in the 5F scheme by using soft collinear effective theory (SCET) [32–36]. As already introduced in Sect. 3.4, SCET is an effective theory of QCD, which was developed specifically to describe the QCD interactions in soft and collinear regions. The interactions in hard regions are encoded in the Wilson coefficients. By construction, it is useful to deal with the scattering processes containing multiple scales, e.g., soft scale and hard scale. Many precise predictions on high energy scattering processes have been obtained in SCET. These processes are divided into two groups, i.e., the timelike and spacelike ones. In the timelike processes, a resonant particle with timelike momentum in the intermediate or final state is produced, such as W/Z boson production [37–40], Higgs boson production [38, 41–45], hadrons production at e^+e^- colliders [46–50], color-octet scalar production [51], direct top quark production via FCNC coupling [52, 53], and s -channel single top production [54]. The spacelike processes contain a particle with spacelike momentum in the intermediate state, including deep-inelastic scattering [36, 55–57], direct photon production [58] and W/Z boson production at large transverse momentum p_T [59]. Besides, some processes are a mix of these two kinds, e.g., the top quark pair production [60–62].

The definition of the threshold variable is the basis of performing resummation of the soft and collinear gluons. It is easy to be defined for timelike processes, for example, $1 - m^2/S$, where m is the invariant mass of the timelike particle and \sqrt{S} is the center-of-mass energy. However, the threshold variable for the spacelike processes is a little subtle. The threshold variable for the deep-inelastic scattering process is given by $1 - x$ with x the Bjorken scaling variable [36, 55–57]. For the direct photon production and $W(Z)$ boson production at large p_T , the threshold region is approached when $S_4 = M^2 \rightarrow 0$, where M is the mass of everything in the final state except the photon (W or Z). The t -channel single top production is a spacelike process involving four colored external particles. We define the threshold variable as $S_4 = P_X^2$, similar to the case of W or Z production at large p_T , where P_X represents the momentum of everything in the final state except the top quark. In the threshold region $S_4 \rightarrow 0$, the cross section can be factorized as

$$\sigma = H \otimes J \otimes S \otimes f_{P_a} \otimes f_{P_b}, \quad (5.3)$$

where H , J , S , and $f_{P_a}(f_{P_b})$ denote the hard function, jet function, soft function and PDF, respectively. The hard function, obtained from virtual corrections, incorporates

the short distance contributions. The jet function describes the collinear interactions inside the outgoing jet. The soft function represents the effects of emitting soft gluons from all colored initial-and final-state particles. The PDF defines the probability of finding an initial-state parton in the proton.

The final states of the t -channel single top production at hadron colliders consist of a single top quark and a light (anti-)quark at the LO. At higher orders in the threshold region, additional soft gluons could be emitted from the colored initial and final-state particles, and the light quark can split into collinear quarks and gluons continuously. These contributions are of higher orders in α_s generally, but can be numerically as significant as the LO results because of the large logarithms. In SCET, the interaction at different scales in a process can be studied separately because that the hard degrees are integrated into the Wilson coefficient and that the soft and collinear degrees are decoupled by redefinitions of the fields [35]. Around each scale, one needs to deal with the only relevant degrees of freedom. The results at different scales are connected together by using the renormalization group (RG) evolution. Therefore, convergent perturbative expansions can be achieved, and the singular terms in the jet and soft functions can be resummed conveniently.

Furthermore, the threshold resummation in t -channel processes is valid only when the final particles have large transverse momenta so that the hard gluon radiations are suppressed and the radiations from the threshold region make the main contribution to the total cross section. In our numerical calculations, we indeed find that for top quark $p_T > 50 \text{ GeV}$, the logarithmic terms approximate the fixed-order calculations well, but for $p_T < 50 \text{ GeV}$, the logarithmic terms do not dominate over the NLO corrections. Thus, we are interested in an improved resummation prediction on the top quark transverse momentum distribution in the region of large p_T . This top quark transverse momentum distribution is also sensitive to new physics. For example, if there is an extra gauge boson W' with a mass around 1 TeV which can decay to $t\bar{b}$, the top quark is highly boosted and generally has a large transverse momentum. In order to distinguish the signal from the SM background, a precise prediction of the t -channel top quark transverse momentum distribution at large p_T in the SM is required.

In Sect. 5.2, we analyze the kinematics of the t -channel single top production in detail and present the definition of the threshold region. In Sect. 5.3, we show the factorization and resummation formalism for the t -channel single top production in momentum space. In Sect. 5.4, we calculate the hard and soft functions at NLO. Then, we investigate the scale independence of the final result analytically. In Sect. 5.5, we discuss the numerical results for t -channel top quark transverse momentum distribution at the Tevatron and the LHC. Conclusion and comments are given in Sect. 5.6.

5.2 Analysis of Kinematics

We introduce the some kinematic variables needed in our analysis. As an example, we consider the subprocess

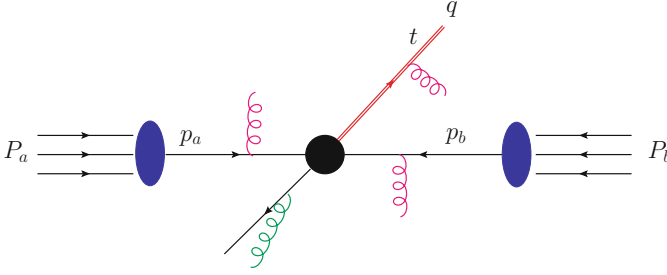


Fig. 5.4 Illustration of the single top quark production near threshold at hadron colliders. The radiated gluons are either collinear or soft

$$u(p_a) + b(p_b) \rightarrow t(q) + X, \quad (5.4)$$

as shown in Fig. 5.4. First of all, we define two lightlike vectors along the beam directions, n_a and n_b . They are related by $n_a = \bar{n}_b$ in the center-of-mass frame. Then we introduce two collinear fields along n_a and n_b to describe the initial partons. In the center-of-mass frame of the hadronic collision, the momenta of the initial hadrons can be written as

$$P_a^\mu = \frac{E_{\text{CM}}}{2} n_a^\mu, \quad P_b^\mu = \frac{E_{\text{CM}}}{2} n_b^\mu, \quad (5.5)$$

where E_{CM} is the center-of-mass energy of the collider and the masses of the hadrons have been neglected. The momenta of the initial partons, with fractions $x_a(x_b)$ of the hadronic momenta, are

$$p_a = x_a \frac{E_{\text{CM}}}{2} n_a^\mu, \quad p_b = x_b \frac{E_{\text{CM}}}{2} n_b^\mu. \quad (5.6)$$

At the hadronic and partonic levels, the momentum conservation manifests as

$$P_a + P_b = q + P_X, \quad (5.7)$$

and

$$p_a + p_b = q + p_X, \quad (5.8)$$

respectively, where q is the momentum of the top quark. We define the partonic jet with momentum p_X including all final-state partons except the top quark, while the hadronic jet with momentum P_X contains all the hadrons in the final state, except the top quark. In threshold region, $p_X = p_1 + k$, where p_1 is the momentum of the final-state collinear partons along the jet and k is the momentum of all soft radiations. Such division of momentum is artificial and we have to integrate over the both p_1 and k to obtain a physical observable.

We also define the Mandelstam variables

$$s = (P_a + P_b)^2, \quad u = (P_a - q)^2, \quad t = (P_b - q)^2 \quad (5.9)$$

at hadronic level, and

$$\hat{s} = (p_a + p_b)^2, \quad \hat{u} = (p_a - q)^2, \quad \hat{t} = (p_b - q)^2 \quad (5.10)$$

at partonic level, respectively. In terms of the Mandelstam variables, the hadronic, and partonic threshold variables are defined by

$$S_4 \equiv P_X^2 = s + t + u - m_t^2, \quad (5.11)$$

$$s_4 \equiv p_X^2 = \hat{s} + \hat{t} + \hat{u} - m_t^2, \quad (5.12)$$

where m_t is the top quark mass. The hadronic threshold limit is taken as $S_4 \rightarrow 0$ [63], where the hard radiations and beam remnants are highly suppressed. And thus the final states consist of a top quark and a narrow jet, as well as the soft radiations. This limit forces $x_a \rightarrow 1$, $x_b \rightarrow 1$, $s_4 \rightarrow 0$ simultaneously. More explicitly, we get

$$\begin{aligned} S_4 &= s_4 + \hat{s}\left(\frac{1}{x_a x_b} - 1\right) + (\hat{t} - m_t^2)\left(\frac{1}{x_b} - 1\right) + (\hat{u} - m_t^2)\left(\frac{1}{x_a} - 1\right) \\ &\approx s_4 + \hat{s}(\bar{x}_a + \bar{x}_b) + (\hat{t} - m_t^2)\bar{x}_b + (\hat{u} - m_t^2)\bar{x}_a \\ &\approx s_4 + (-\hat{t})\bar{x}_a + (-\hat{u})\bar{x}_b, \end{aligned} \quad (5.13)$$

where $\bar{x}_{a,b} = 1 - x_{a,b}$. This expression can help to check the factorization scale independence of the cross section. From the above equation, the hadronic threshold necessitates the partonic threshold. However, the reverse is not true. The partonic threshold $s_4 \rightarrow 0$ does not exclude a significant amount of beam remnants. We notice that in both hadronic and partonic threshold limits, the top quark is, not necessarily produced at rest; i.e., it can have a large transverse momentum.

For later convenience, we rewrite the threshold variable as

$$s_4 = p_X^2 = (p_a + p_b - q)^2 = p_1^2 + 2k^+ E_1 + \mathcal{O}(k^2), \quad (5.14)$$

where $k^+ = n_1 \cdot k$ with k the sum of the momenta of soft radiations. E_1 is the energy of the quark jet and n_1 is the lightlike vector in the jet direction. In the threshold limit ($s_4 \rightarrow 0$), hard radiations are suppressed. Incomplete cancellation between real and virtual corrections leads to singular distributions $\alpha_s^n [\ln^m(s_4/m_t^2)/s_4]_+$ with $m \leq 2n - 1$. It is the purpose of threshold resummation to sum these contributions to all orders in α_s .

The total inclusive cross section of the t -channel single top production can be written as

$$\begin{aligned}
\sigma &= \int dx_a \int dx_b \int d\hat{t} \int d\hat{u} f_{i/P_a}(\mu_F, x_a) f_{j/P_b}(\mu_F, x_b) \frac{1}{2\hat{s}} \frac{d\hat{\sigma}_{ij}}{d\hat{t}d\hat{u}} \\
&= \int_0^{p_{T,\max}^2} dp_T^2 \int_{-y_{\max}}^{y_{\max}} dy \int_{x_{b,\min}}^1 dx_b \int_0^{s_4^{\max}} ds_4 \\
&\quad \frac{1}{2(x_b s + u - m_t^2)} f_{i/P_a}(\mu_F, x_a) f_{j/P_b}(\mu_F, x_b) \frac{d\hat{\sigma}_{ij}}{d\hat{t}d\hat{u}}, \tag{5.15}
\end{aligned}$$

where, we have changed the integration variables to be the squared top quark transverse momentum p_T^2 , rapidity y , x_b , and s_4 . The integration limits are set by

$$\begin{aligned}
p_{T,\max}^2 &= \frac{(s - m_t^2)^2}{4s}, \\
y_{\max} &= \frac{1}{2} \ln \frac{1 + \sqrt{1 - w}}{1 - \sqrt{1 - w}}, \quad \text{with } w = \frac{4s(p_T^2 + m_t^2)}{(s + m_t^2)^2}, \\
x_{b,\min} &= \frac{-u}{s + t - m_t^2}, \\
s_4^{\max} &= x_b(s + t - m_t^2) + u, \tag{5.16}
\end{aligned}$$

with

$$\begin{aligned}
t &= m_t^2 - \sqrt{s} \sqrt{p_T^2 + m_t^2} e^y \\
u &= m_t^2 - \sqrt{s} \sqrt{p_T^2 + m_t^2} e^{-y}. \tag{5.17}
\end{aligned}$$

The other kinematical variables can be expressed in terms of these four integration variables. For example,

$$x_a = \frac{s_4 - m_t^2 + x_b(m_t^2 - t)}{x_b s + u - m_t^2}. \tag{5.18}$$

5.3 Factorization and Resummation Formalism

Now we derive the factorization formula for the t -channel single top production in SCET. We first match the full QCD onto the effective theory. We would follow the convention and formalism in [64, 65], where the matching is performed in momentum space. The relevant operator in QCD responsible for the t -channel single top production is given by

$$O(x) = (\bar{d}_L \gamma^\mu u_L \bar{t}_L \gamma_\mu b_L)(x), \quad (5.19)$$

where, we have adopted the Feynman gauge for the W boson propagator. The denominator of the W propagator is the same in different theories and thus we omit it in the operators. The Dirac matrices do not change in the matching, and therefore, we omit it in the following discussion. This operator consists of three massless (anti-)quarks, which can be described by collinear (anti-)quarks $\chi(x)$ in SCET, and a massive quark, which can be described by $h(x)$ in heavy quark effective theory [66]. Additional soft gluons are compactly represented by the soft gluon Wilson lines $Y(x)$ and $\tilde{Y}(x)$; see Sect. 3.4 for their definitions. Therefore, in the threshold region, the matching from QCD to SCET is given by

$$O(x) \longrightarrow \bar{\chi}_{n_1} \chi_{n_a} \bar{h}_v \chi_{n_b}(x) \tilde{Y}_{n_1}^\dagger Y_{n_a} \tilde{Y}_v^\dagger Y_{n_b}(x). \quad (5.20)$$

The Fourier transform of the above right operators can be written as

$$\begin{aligned} O(p) &= \int \frac{d^4 p_a}{(2\pi)^4} \frac{d^4 p_b}{(2\pi)^4} \frac{d^4 p_1}{(2\pi)^4} \frac{d^4 q}{(2\pi)^4} \frac{d^4 k_s}{(2\pi)^4} \mathcal{C}_I(p_a, p_b; p_1, q) \\ &\times \mathcal{O}_{\text{in}}(p_a, p_b) \mathcal{O}_{\text{out}}(p_1, q) \mathcal{O}_{S,I}(k_s) \\ &\times (2\pi)^4 \delta^{(4)}(p - p_a - p_b + p_1 + q + k_s), \end{aligned} \quad (5.21)$$

where we have written each field in its Fourier transformed form and performed the integration over x . The operator $\mathcal{O}_{\text{in}}(p_a, p_b)$ represents the initial u and b quarks with momenta p_a and p_b ,

$$\mathcal{O}_{\alpha\beta,\text{in}}^{cd} = \chi_\alpha^c(p_a) \chi_\beta^d(p_b), \quad (5.22)$$

with

$$\chi(x) = \int \frac{d^4 p}{(2\pi)^4} e^{ipx} \chi(p). \quad (5.23)$$

The operator $\mathcal{O}_{\text{out}}(p_1, q)$ denotes the final d and t quarks with momenta p_1 and q ,

$$\mathcal{O}_{\gamma\delta,\text{out}}^{ef} = \bar{\chi}_\delta^f(p_1) \bar{h}_{\gamma,v}^e(q), \quad (5.24)$$

with

$$\bar{\chi}(x) = \int \frac{d^4 p}{(2\pi)^4} e^{-ipx} \bar{\chi}(p). \quad (5.25)$$

Notice that we have denoted the top quark in terms of the heavy quark effective field with a label velocity v [66]. Since there are two fermion lines in this process, either of which connects initial and final states, we distinguish them with the explicit Lorentz indices $(\alpha, \beta, \gamma, \delta)$ and color indices (c, d, e, f) . We have retained only quark fields in the operators for simplicity, leaving the other coupling structure in the matching coefficient \mathcal{C}_I , which is at the LO level

$$\mathcal{C}_I^{\delta\alpha,\gamma\beta} = i \frac{g_2^2 V_{ud} V_{tb}}{8(\hat{t} - M_W^2)} (\gamma^\mu (1 - \gamma^5))^{\delta\alpha} (\gamma_\mu (1 - \gamma^5))^{\gamma\beta} \delta_{I1}. \quad (5.26)$$

Here, V_{ij} is the CKM matrix element. We have used the color-singlet-octet basis

$$|c_1\rangle = \delta_{fc} \delta_{ed}, \quad |c_2\rangle = (t^a)_{fc} (t^a)_{ed}, \quad (5.27)$$

and δ_{I1} means that only the basis $|c_1\rangle$ contributes to the t -channel single top production at LO.

In Eq. (5.21), we have separated the soft gluon fields from collinear or massive fields because of the field redefinition in Eq. (3.59). The soft operators $\mathcal{O}_{S,I}$ are given by

$$\begin{aligned} \mathcal{O}_{S,1}^{fced}(k_s) &= \int d^4x e^{ik_s \cdot x} \mathbf{T} \left[\left(\tilde{Y}_{n_1}^\dagger(x) Y_{n_a}(x) \right)^{fc} \left(\tilde{Y}_v^\dagger(x) Y_{n_b}(x) \right)^{ed} \right], \\ \mathcal{O}_{S,2}^{fced}(k_s) &= \int d^4x e^{ik_s \cdot x} \mathbf{T} \left[\left(\tilde{Y}_{n_1}^\dagger(x) t^a Y_{n_a}(x) \right)^{fc} \left(\tilde{Y}_v^\dagger(x) t^a Y_{n_b}(x) \right)^{ed} \right], \end{aligned} \quad (5.28)$$

where the time-ordering operator \mathbf{T} is imposed to ensure the proper ordering of soft gluon fields in the soft Wilson line.

The cross section for t -channel single top production in the threshold region can be written as

$$\begin{aligned} \sigma &= \frac{1}{2s} \sum_x \langle I | \mathcal{O}^\dagger(x=0) | X \rangle \langle X | \mathcal{O}(x=0) | I \rangle (2\pi)^4 \delta^4(P_a + P_b - q - P_X) \\ &= \frac{1}{2s} \sum_x \int d^4x \langle I | \mathcal{O}^\dagger(x=0) | X \rangle \langle X | \mathcal{O}(x) | I \rangle \\ &= \frac{1}{2s} \sum_x \int d^4x \int \frac{d^4k}{(2\pi)^4} e^{-ik \cdot x} \int \frac{d^4p}{(2\pi)^4} \langle I | \mathcal{O}^\dagger(p) | X \rangle \langle X | \mathcal{O}(k) | I \rangle \\ &= \frac{1}{2s} \sum_x \int \frac{d^4p}{(2\pi)^4} \langle I | \mathcal{O}^\dagger(p) | X \rangle \langle X | \mathcal{O}(0) | I \rangle, \end{aligned} \quad (5.29)$$

where $|I\rangle = |P_a P_b\rangle$ denotes the initial-state (anti-)protons. The final state $|X\rangle = |X_t\rangle |X_1\rangle |X_s\rangle$, where $|X_t\rangle$, $|X_1\rangle$ and $|X_s\rangle$ represent the top quark, the jet originating from the d -quark and the remaining soft radiations, respectively. In the second line of Eq. (5.29), we have replaced the delta function with its Fourier form to shift the operator $\mathcal{O}(0)$ to $\mathcal{O}(x)$. In the third line, we have transformed the operators to momentum space, and matched them onto SCET operators.

Before we separate the fields in the operators, we should separate the phase spaces first. We denote the differential phase space as $d\Phi_2 = d^4p_a d^4p_b d^4p_1 d^4q / (2\pi)^{16}$. Then, we can rewrite Eq. (5.29) as

$$\begin{aligned}
\sigma &= \frac{1}{2s} \sum_X \int d\Phi'_2 d\Phi_2 \mathcal{C}_J^*(p'_a, p'_b; p'_1, q') \mathcal{C}_I(p_a, p_b; p_1, q) \\
&\times \int \frac{d^4 k'_s}{(2\pi)^4} \frac{d^4 k_s}{(2\pi)^4} (2\pi)^4 \delta^{(4)}(p_a + p_b - p_1 - q - k_s) \\
&\times \langle P_a P_b | (\mathcal{O}'_{\text{in}} \mathcal{O}'_{\text{out}} \mathcal{O}'_{S,J})^\dagger | X_t X_1 X_s \rangle \langle X_t X_1 X_s | (\mathcal{O}_{\text{in}} \mathcal{O}_{\text{out}} \mathcal{O}_{S,I}) | P_a P_b \rangle. \quad (5.30)
\end{aligned}$$

Since different collinear fields are decoupled among each other and decoupled with the soft fields due to field redefinition, the matrix elements in Eq. (5.30) can be factorized into a product of different matrix elements, each of which obeys corresponding RG equations. Subsequently, we discuss them in detail.

First, the initial-state n_a collinear sector reduces to the convolution with PDF,

$$\begin{aligned}
&\int \frac{d^4 p'_a}{(2\pi)^4} \frac{d^4 p_a}{(2\pi)^4} \langle P_a | \bar{\chi}_{\alpha'}^{c'}(p'_a) \chi_\alpha^c(p_a) | P_a \rangle \\
&= \langle P_a | \bar{\chi}_{\alpha'}^{c'}(x=0) \chi_\alpha^c(x=0) | P_a \rangle \\
&= \frac{1}{2N_c} \delta^{c'c} \int_0^1 \frac{dx_a}{x_a} \left(x_a E_{\text{CM}} \frac{\not{h}_a}{2} \right)_{\alpha\alpha'} f_{u/P_a}(x_a, \mu), \quad (5.31)
\end{aligned}$$

where $f_{u/P_a}(x_a, \mu)$ is defined in Eq. (3.9). The term in bracket is the Dirac structure and $1/2N_c$ denotes the average over the spin and color states. The initial-state n_b collinear sector is similar.

For the final-state d -quark jet sector, we have

$$\begin{aligned}
&\sum_{X_1} \int \frac{d^4 p'_1}{(2\pi)^4} \frac{d^4 p_1}{(2\pi)^4} \langle 0 | \chi_{\delta'}^{f'}(p'_1) | X_1 \rangle \langle X_1 | \bar{\chi}_\delta^f(p_1) | 0 \rangle \\
&= \delta^{f'f} \int \frac{d^4 p_1}{(2\pi)^3} \left(\frac{\not{h}_1}{2} \right)_{\delta'\delta} \theta(p_1^0) \bar{n}_1 \cdot p_1 J(p_1^2), \quad (5.32)
\end{aligned}$$

where the summation over all possible collinear states is performed. The term in bracket and $\bar{n}_1 \cdot p$ are the Dirac structure. $J(p^2)$ is the spin- and color-singlet jet function, defined as

$$\theta(p^0) \bar{n}_1 \cdot p J(p^2) = \frac{1}{8\pi N_c} \int \frac{d^4 p'}{(2\pi)^4} \text{Tr} \langle 0 | \bar{\not{h}}_1 \chi(p') \bar{\chi}(p) | 0 \rangle, \quad (5.33)$$

where Tr denotes the trace over spin and color indices. At LO, it is just $\delta(p^2)$, which means that the jet consists of a single parton. Here, we have constrained the off-shellness of the momenta of all the collinear particles in the jet to be p^2 , since our threshold variable s_4 depends on it. In other cases, different constraints should be imposed in the jet function.

Then, we deal with the top quark sector. Because the soft interactions have been decoupled by field redefinition, the top quark can be regarded as a noninteracting particle, and the corresponding matrix element can be written as

$$\begin{aligned}
& \sum_{X_t} \int \frac{d^4 q'}{(2\pi)^4} \frac{d^4 q}{(2\pi)^4} \langle 0 | h_{\gamma', v'}^{e'}(q') | X_t \rangle \langle X_t | \bar{h}_{\gamma, v}^e(q) | 0 \rangle \\
&= \int \frac{d^3 q}{2E_q (2\pi)^3} (\not{q} + m_t)_{\gamma' \gamma} \delta^{e' e} \\
&= \int \frac{dtdu}{16\pi^2 \hat{s}} (\not{q} + m_t)_{\gamma' \gamma} \delta^{e' e}, \tag{5.34}
\end{aligned}$$

where the summation over the final state $|X_t\rangle$ transforms to the top quark phase space integration. The term in bracket is the Dirac structure.

Finally, the soft function is written in terms of the soft matrix element as

$$\begin{aligned}
\int dk^+ S_{JI}^{d'e'c'f'f'ced}(k^+, \mu) &= \frac{1}{N_c^2} \sum_{X_s} \int dk^+ \frac{d^4 k'_s}{(2\pi)^4} \frac{d^4 k_s}{(2\pi)^4} \langle 0 | \mathcal{O}_{S,J}^{\dagger, d'e'c'f'}(k'_s) | X_s \rangle \\
&\quad \langle X_s | \mathcal{O}_{S,I}^{f'ced}(k_s) | 0 \rangle \delta(k^+ - n_1 \cdot k_s), \tag{5.35}
\end{aligned}$$

where we have inserted an identity operator

$$\mathbf{1} = \int dk^+ \delta[k^+ - n_1 \cdot k_s], \tag{5.36}$$

due to the constraint from Eq. (5.14). This manifests the multipole expansion of a soft field interacting with a collinear field [58]. Notice that the summation over all final states can be performed

$$\sum_{X_s} |X_s(k'_s)\rangle \langle X_s(k_s)| = (2\pi)^4 \delta^{(4)}(k'_s - k_s). \tag{5.37}$$

The color indices in the sectors of the top quark, light jet, and PDFs have been written explicitly, and must be contracted with those in the soft function to obtain

$$S_{II}(k^+, \mu) = \delta^{f'f} \delta^{c'c} \delta^{e'e} \delta^{d'd} S_{JI}^{d'e'c'f'f'ced}(k^+, \mu). \tag{5.38}$$

At the LO, it is given by

$$\mathbf{S}(k^+, \mu) = \delta(k^+) \frac{1}{N_c^2} \begin{pmatrix} C_A^2 & 0 \\ 0 & C_A^2 - 1 \end{pmatrix}, \tag{5.39}$$

where C_A is the Casimir operator in the adjoint representation of $SU(3)_C$. At the NLO, the soft function is obtained after calculating eikonal diagrams [58]. Since the virtual corrections in SCET reduce to scaleless integrals and thus vanish, only real emission diagrams need to be evaluated. The details of the calculation of these diagrams are given in the next section.

Combining the different sectors together, we obtain the cross section in the threshold region

$$\sigma = \int dx_a dx_b d\hat{t} d\hat{u} \frac{1}{2\hat{s}} f_{i/P_a}(x_a, \mu) f_{j/P_b}(x_b, \mu) \frac{d\hat{\sigma}_{ij}^{\text{thres}}}{d\hat{t} d\hat{u}}, \quad (5.40)$$

with

$$\begin{aligned} \frac{d\hat{\sigma}_{ij}^{\text{thres}}}{d\hat{t} d\hat{u}} &= \frac{1}{4N_c^2} \frac{1}{8\pi} \frac{1}{\hat{s}} \lambda_{0,ij} H_{IJ}(\mu) \\ &\times \int dk^+ \int dp_1^2 S_{J_I}(k^+, \mu) J(p_1^2, \mu) \delta(s_4 - p_1^2 - 2k^+ E_1) \end{aligned} \quad (5.41)$$

and

$$\lambda_{0,ij} = g_2^4 |V_{id}|^2 |V_{jt}|^2 \frac{(\hat{s} - m_t^2) \hat{s}}{(\hat{t} - M_W^2)^2}. \quad (5.42)$$

All the elements in the factorized Eq. (5.40) have precise field definitions so that they can be calculated directly and systematically, except for the nonperturbative PDF. The convolution between the jet and soft functions, denoted by the δ function in Eq. (5.41), manifests that the partonic threshold consists of two parts. In the case of $s_4 = 0$, any collinear or soft gluons emissions is excluded. In the small s_4 region, the numbers and momenta of all collinear and soft gluons are constrained.

The hard function is defined by

$$\lambda_{0,ij} H_{IJ} \equiv C_I C_J^*(p_a, p_b; p_1, q), \quad (5.43)$$

where we have included all the Dirac structures in the PDFs, jet function and top quark sector in the matching coefficient so that all Lorentz indices are contracted. Since we have separated the Born amplitude squared into $\lambda_{0,ij}$, the hard function H_{IJ} is normalized to $\delta_{I1} \delta_{J1}$ at the LO. At higher orders, one needs to calculate the loop diagrams of this process in both the full theory and SCET. However, the loop integrals in SCET are scaleless in dimensional regularization scheme and thus vanish. So the hard function is related to the amplitudes of the virtual corrections by [61]

$$\begin{aligned} \lambda_{0,ij} H_{IJ}^{(0)} &= \frac{1}{\langle c_I | c_I \rangle \langle c_J | c_J \rangle} \langle c_I | \mathcal{M}_{\text{ren}}^{(0)} \rangle \langle \mathcal{M}_{\text{ren}}^{(0)} | c_J \rangle, \\ \lambda_{0,ij} H_{IJ}^{(1)} &= \frac{1}{\langle c_I | c_I \rangle \langle c_J | c_J \rangle} \left(\langle c_I | \mathcal{M}_{\text{ren}}^{(1)} \rangle \langle \mathcal{M}_{\text{ren}}^{(0)} | c_J \rangle + \langle c_I | \mathcal{M}_{\text{ren}}^{(0)} \rangle \langle \mathcal{M}_{\text{ren}}^{(1)} | c_J \rangle \right), \end{aligned} \quad (5.44)$$

where H_{IJ} and \mathcal{M}_{ren} have been expanded in series of α_s . The renormalized amplitudes $|\mathcal{M}_{\text{ren}}\rangle$ are obtained in QCD by subtracting the IR divergences in the $\overline{\text{MS}}$ scheme. All the loop integrals in SCET actually contain both IR and UV divergences but in different signs. By construction, the IR structures of integrals in QCD and SCET are the same. So the matching coefficient contains no IR divergences, but can have UV divergences, of which the magnitude is just the negative of the IR divergence of loop integrals in QCD. These UV divergences can be subtracted by counterterms of the matching coefficient. As a result, they control the RG evolution equation of the matching coefficient.

Because this process is induced by electroweak interaction, only the matrix element H_{11} of the hard function contributes to the cross section at the NLO level. The other matrix elements start to make contribution from NNLO, which is beyond our scope in this study. Thus, we neglect them in our calculation, and consider the t -channel single top production as a double deep-inelastic-scattering (DDIS) process [18]. This picture has also been taken in studying the Higgs boson production via vector boson fusion. In this picture, the dynamics associating the two different fermion lines is independent from each other, though the kinematics is still related. As a result, the hard function can be further factorized into two components, i.e., H_{up} and H_{dn} , representing contributions from the up and down fermion lines in Fig. 5.2a, respectively. This factorization is also needed to make a reliable perturbative calculation for the hard function. The reason is that the virtual corrections from the up and down fermion lines contain large logarithms $\ln^2(-\hat{t}/\mu_h^2)$ and $\ln^2((-\hat{t} + m_t^2)/m_t/\mu_h)$, respectively; see Eqs. (5.46)–(5.47). It is hard to choose a single proper hard scale to make both of them small. In the picture of DDIS, the two separate hard functions can be evaluated in different scales so that each has a convergent perturbative expansion. Therefore, we can rewrite Eq. (5.41) as

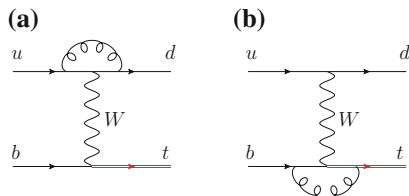
$$\begin{aligned} \frac{d\hat{\sigma}_{ij}^{\text{thres}}}{d\hat{t}d\hat{u}} &= \frac{1}{4N_c^2} \frac{1}{8\pi} \frac{1}{\hat{s}} \lambda_{0,ij} H_{\text{up}}(\mu) H_{\text{dn}}(\mu) \\ &\times \int dk^+ \int dp_1^2 \mathcal{S}(k^+, \mu) J(p_1^2, \mu) \delta(s_4 - p_1^2 - 2k^+ E_1), \quad (5.45) \end{aligned}$$

where $\mathcal{S}(k^+, \mu)$ denotes the component $S_{11}(k^+, \mu)$ in Eq. (5.38).

5.4 Hard, Soft, and Jet Functions at NLO

We now have the factorized cross section at hand, in which the factorized components have explicit definitions. The LO results of them are shown to be trivial. The first nontrivial results start from NLO. That is also what one needs to match the NNLL resummation. Thus we present the explicit expressions of hard, jet, and soft functions in this section.

Fig. 5.5 The one-loop Feynman diagrams for the t -channel single top production



5.4.1 Hard Functions

The hard functions are defined in Eq. (5.43), and can be calculated by Eq. (5.44).

After calculating the one-loop Feynman diagrams in QCD, as shown in Fig. 5.5, we get the hard functions at NLO as follows:

$$H_{\text{up}}(\mu_{h,\text{up}}) = 1 + \frac{C_F \alpha_s(\mu_{h,\text{up}})}{4\pi} \left(-2\ln^2 \frac{-\hat{t}}{\mu_{h,\text{up}}^2} + 6\ln \frac{-\hat{t}}{\mu_{h,\text{up}}^2} + c_1^{H,\text{up}} \right), \quad (5.46)$$

$$H_{\text{dn}}(\mu_{h,\text{dn}}) = 1 + \frac{C_F \alpha_s(\mu_{h,\text{dn}})}{4\pi} \left(-4\ln^2 \frac{-\hat{t} + m_t^2}{\mu_{h,\text{dn}} m_t} + 10\ln \frac{-\hat{t} + m_t^2}{\mu_{h,\text{dn}} m_t} + c_1^{H,\text{dn}} \right), \quad (5.47)$$

where

$$c_1^{H,\text{up}} = -16 + \frac{\pi^2}{3}, \quad (5.48)$$

$$c_1^{H,\text{dn}} = -\frac{2}{\lambda} \ln(1-\lambda) + 2\ln^2(1-\lambda) + 6\ln(1-\lambda) + 4\text{Li}_2(\lambda) - 12 - \frac{\pi^2}{6} + \frac{2m_t^2 \hat{u}}{\hat{t}(\hat{s} - m_t^2)} \ln \frac{m_t^2}{m_t^2 - \hat{t}}, \quad (5.49)$$

with $\lambda = \hat{t}/(\hat{t} - m_t^2)$. These results are in complete agreement with Ref. [18]. In order to avoid large double logarithms, the scales $\mu_{h,\text{up}}$ and $\mu_{h,\text{dn}}$ should be chosen around $\sqrt{-\hat{t}}$ and $(-\hat{t} + m_t^2)/m_t$, respectively. Then its value at the other scales, such as the factorization scale, is obtained by running the RG equations.

The RG equations for hard functions are determined by the counterterms of the matching coefficient, or the IR divergence of the loop amplitudes in QCD. The latter is embodied in the soft and jet functions in SCET, both of which are process independent and have been predicted up to two-loop level or even higher level [67, 68]. Therefore, the RG evolutions of the hard functions are fully understood up to two-loop level. For t -channel single top production, the RG equations for hard functions as

$$\frac{d}{d \ln \mu_{h,\text{up}}} H_{\text{up}}(\mu_{h,\text{up}}) = \left(2\Gamma_{\text{cusp}} \ln \frac{-\hat{t}}{\mu_{h,\text{up}}^2} + 2\gamma_{\text{up}}^V \right) H_{\text{up}}(\mu_{h,\text{up}}), \quad (5.50)$$

$$\frac{d}{d \ln \mu_{h,\text{dn}}} H_{\text{dn}}(\mu_{h,\text{dn}}) = \left(2\Gamma_{\text{cusp}} \ln \frac{-\hat{t} + m_t^2}{\mu_{h,\text{dn}} m_t} + 2\gamma_{\text{dn}}^V \right) H_{\text{dn}}(\mu_{h,\text{dn}}), \quad (5.51)$$

where Γ_{cusp} is the cusp anomalous dimension of Wilson loops with lightlike segments [69], which governs the double logarithmic terms. The anomalous dimensions γ_{up}^V and γ_{dn}^V control the single logarithmic terms. All their explicit expressions up to two-loop level are shown in appendix.

The above evolution equations are just differential equations with initial state $H(\mu_h)$. The general solutions at an arbitrary scale μ are obtained by

$$H_{\text{up}}(\mu) = \exp[4S(\mu_{h,\text{up}}, \mu) - 2a_{\text{up}}^V(\mu_{h,\text{up}}, \mu)] \left(\frac{-\hat{t}}{\mu_{h,\text{up}}^2} \right)^{-2a_{\Gamma}(\mu_{h,\text{up}}, \mu)} H_{\text{up}}(\mu_{h,\text{up}}), \quad (5.52)$$

$$H_{\text{dn}}(\mu) = \exp[2S(\mu_{h,\text{dn}}, \mu) - 2a_{\text{dn}}^V(\mu_{h,\text{dn}}, \mu)] \left(\frac{-\hat{t} + m_t^2}{\mu_{h,\text{dn}} m_t} \right)^{-2a_{\Gamma}(\mu_{h,\text{dn}}, \mu)} H_{\text{dn}}(\mu_{h,\text{dn}}), \quad (5.53)$$

where the two functions $S(\mu_{h,\text{up}}, \mu)$ and $a_{\text{up}}^V(\mu_{h,\text{up}}, \mu)$ are defined by [70]

$$S(\mu_{h,\text{up}}, \mu) = - \int_{\alpha_s(\mu_{h,\text{up}})}^{\alpha_s(\mu)} d\alpha \frac{\Gamma_{\text{cusp}}(\alpha)}{\beta(\alpha)} \int_{\alpha_s(\mu_{h,\text{up}})}^{\alpha} \frac{d\alpha'}{\beta(\alpha')}, \quad (5.54)$$

$$a_{\Gamma}(\mu_{h,\text{up}}, \mu) = - \int_{\alpha_s(\mu_{h,\text{up}})}^{\alpha_s(\mu)} d\alpha \frac{\Gamma_{\text{cusp}}(\alpha)}{\beta(\alpha)}. \quad (5.55)$$

Similar expressions for other functions are understood.

5.4.2 Soft Function

The soft function $\mathcal{S}(k^+, \mu)$, defined in Eq. (5.35), describes soft gluon emission from all colored particles. Since the eikonal approximation is the same in both QCD and SCET. Therefore, it can be directly calculated in QCD. The LO result has been shown in Eq. (5.39). The NLO result can be obtained by calculating the real emission diagrams, as shown in Fig. 5.6. The results of diagrams (a) and (b) are given by

$$S_{bt}^{(1)}(k, \mu) = \frac{2g_s^2 C_F \mu^{2\epsilon}}{(2\pi)^{d-1}} \frac{1}{2} \int_0^\infty dq^+ \int_0^\infty dq^- \int d^{d-2} q_\perp \delta(q^+ q^- - q_\perp^2) \delta(k - n_1 \cdot q) \frac{n_b \cdot v}{(q \cdot n_b)(q \cdot v)}, \quad (5.56)$$

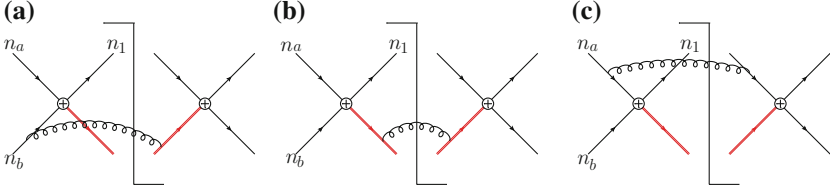


Fig. 5.6 The real emission diagrams contributing to the soft function at NLO. The contributions from the (a) and (b) diagrams are denoted as $S_{bt}^{(1)}$ and $S_{tt}^{(1)}$, respectively. The result of the (c) diagram is vanishing

and

$$S_{tt}^{(1)}(k, \mu) = \frac{-g_s^2 C_F \mu^{2\epsilon}}{(2\pi)^{d-1}} \frac{1}{2} \int_0^\infty dq^+ \int_0^\infty dq^- \int d^{d-2} q_\perp \delta(q^+ q^- - q_\perp^2) \delta(k - n_1 \cdot q) \frac{1}{(q \cdot v)^2}, \quad (5.57)$$

respectively. The result of the diagram (c) is vanishing due to scaleless integral. The above two integrals can be calculated as shown in appendix. We just show the final results here,

$$S_{bt}^{(1)}(k, \mu) = \frac{2C_F \alpha_s}{4\pi} \left\{ 4 \left[\frac{\ln \frac{k}{\tilde{\mu}}}{k} \right]_*^{[k, \tilde{\mu}]} + \delta(k) c_{bt}^S \right\},$$

and

$$S_{tt}^{(1)}(k, \mu) = \frac{2C_F \alpha_s}{4\pi} \left\{ - \left[\frac{2}{k} \right]_*^{[k, \tilde{\mu}]} + \delta(k) c_{tt}^S \right\}, \quad (5.58)$$

respectively, where $\tilde{\mu} = \mu / \sqrt{(2n_{bb})/n_1^{+2}} = (\mu(-\hat{u})m_t)/(2(-\hat{t} + m_t^2)E_1)$. The explicit expressions of c_{bt}^S and c_{tt}^S can be found in appendix. The star distribution is defined by [50]

$$[f(x)]_*^{[x, a]} = f(x) \text{ for } x > 0, \quad (5.59)$$

$$\int_0^a dx [f(x)]_*^{[x, a]} g(x) = \int_0^a dx f(x) [g(x) - g(0)], \quad (5.60)$$

where $g(x)$ is a normal function of x and not divergent as $x \rightarrow 0$. The total soft function is

$$S(k, \mu) = S_{bt}(k, \mu) + S_{tt}(k, \mu). \quad (5.61)$$

The RG equation of the soft function can be obtained from the divergent part of the soft function, which is also given in appendix. We have

$$\frac{d}{d \ln \mu} \mathcal{S}(k, \mu) = \left[-2\Gamma_{\text{cusp}} \ln \frac{k}{\tilde{\mu}} + 2\gamma^S \right] \mathcal{S}(k, \mu) + 2\Gamma_{\text{cusp}} \int_0^k dk' \frac{\mathcal{S}(k, \mu) - \mathcal{S}(k', \mu)}{k - k'}, \quad (5.62)$$

where γ^S is the anomalous dimensions of the soft function. It has been shown explicitly in the appendix. Different from the RG equation of the hard function, this is an integro-differential equation. The solution to this equation is not easy to get. It is convenient to work with the Laplace transformed soft function

$$\tilde{s} \left(\ln \frac{\Lambda}{\tilde{\mu}}, \mu \right) = \int_0^\infty dk e^{-k/\Lambda'} \mathcal{S}(k, \mu) \quad (5.63)$$

with $\Lambda' = e^{\gamma_E} \Lambda$. The inverse transformation is

$$\mathcal{S}(k, \mu) = \frac{1}{2\pi i} \int_{c-i\infty}^{c+i\infty} d\xi e^{\xi k} \tilde{s} \left(\ln \frac{1}{e^{\gamma_E} \xi \tilde{\mu}}, \mu \right), \quad (5.64)$$

where the real number c is chosen to be greater than all the real part of the singularities of $\tilde{s} \left(\ln \frac{1}{e^{\gamma_E} \xi \tilde{\mu}}, \mu \right)$. Then the Laplace transformed soft function satisfies the RG equation

$$\frac{d}{d \ln \mu} \tilde{s} \left(\ln \frac{\Lambda}{\tilde{\mu}}, \mu \right) = \left[-2\Gamma_{\text{cusp}} \ln \frac{\Lambda}{\tilde{\mu}} + 2\gamma^S \right] \tilde{s} \left(\ln \frac{\Lambda}{\tilde{\mu}}, \mu \right), \quad (5.65)$$

which can be solved analogous to the hard function. And transforming back to the momentum space, we get

$$\mathcal{S}(k, \mu) = \exp \left[-2S(\mu_s, \mu) - 2a^S(\mu_s, \mu) \right] \tilde{s}(\partial_{\eta_s}, \mu_s) \frac{1}{k} \left(\frac{k}{\tilde{\mu}_s} \right)^{\eta_s} \frac{e^{-\gamma_E \eta_s}}{\Gamma(\eta_s)}, \quad (5.66)$$

with $\eta_s = 2a_\Gamma(\mu_s, \mu)$. The Laplace transformed soft function $\tilde{s}(L, \mu)$ up to $\mathcal{O}(\alpha_s)$ is given by

$$\tilde{s}(L, \mu) = 1 + \frac{\alpha_s}{4\pi} \left(\Gamma_0 L^2 - 2\gamma_0^S L + c_1^S \right), \quad (5.67)$$

with $c_1^S = (2c_{bt}^S + 2c_{tt}^S + \frac{2\pi^2}{3})C_F$.

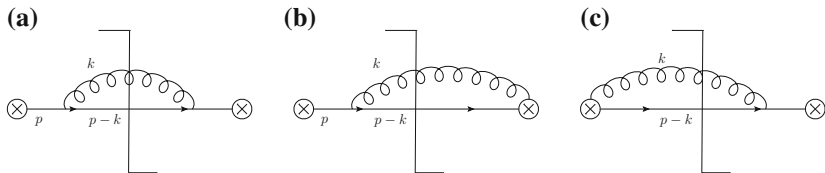


Fig. 5.7 The jet function calculated at NLO. In diagrams **b** and **c**, the effective vertices with a gluon are obtained after contracting a highly off-shell particles in SCET. The vanishing virtual corrections are not shown explicitly here

5.4.3 Jet Function

The jet function $J(p^2, \mu)$, defined in Eq. (5.33), describes the probability of a quark with invariant mass squared p^2 evolving to a jet. It is process independent and has been obtained by calculating the diagrams of the discontinuity of the propagator. The relevant Feynman diagrams at NLO are shown in Fig. 5.7.

Introducing the direction vectors $n(\bar{n})$ parallel (anti-parallel) the jet momentum, the contribution of the diagram *a* is given by

$$J_a = \frac{1}{8\pi\bar{n} \cdot p} \int d\Phi_J |\mathcal{M}_a|^2, \quad (5.68)$$

where the phase space integration is

$$\begin{aligned} \int d\Phi_J &= \int \frac{d^d k}{(2\pi)^d} (-2\pi i)^2 \delta(k^2) \delta((p-k)^2) \frac{1}{p^2} \\ &= -\frac{(4\pi)^\epsilon}{8\pi\Gamma(1-\epsilon)} \frac{1}{p^2} \left(\frac{p^2}{\mu^2}\right)^{-\epsilon} (p^-)^{-1+2\epsilon} \int_0^{p^-} dk^- (k^-(p^- - k^-))^{-\epsilon} \end{aligned} \quad (5.69)$$

and the matrix element reads

$$|\mathcal{M}_a|^2 = -4g_s^2 C_F (d-2) k^-. \quad (5.70)$$

After performing the integration, we get

$$J_a = -\frac{C_F \alpha_s}{4\pi} \delta(p^2) \frac{1}{\epsilon} + \frac{C_F \alpha_s}{4\pi} \left[\left(\frac{1}{p^2}\right)_*^{[p^2, \mu^2]} - \delta(p^2) \right]. \quad (5.71)$$

The matrix elements of diagram (b) is

$$|\mathcal{M}_b|^2 = -8C_F g_s^2 \frac{p^-(p^- - k^-)}{k^-}. \quad (5.72)$$

Then, the contribution of diagram (b) is given by

$$J_b = \frac{C_F \alpha_s}{2\pi} \left\{ \delta(p^2) \frac{1}{\epsilon^2} - \left[\left(\frac{1}{p^2} \right)_*^{[p^2, \mu^2]} - \delta(p^2) \right] \frac{1}{\epsilon} \right\} \\ + \frac{C_F \alpha_s}{4\pi} \left[2 \left(\frac{\ln p^2 / \mu^2}{p^2} \right)_*^{[p^2, \mu^2]} - 2 \left(\frac{1}{p^2} \right)_*^{[p^2, \mu^2]} + \left(4 - \frac{\pi^2}{2} \right) \delta(p^2) \right]. \quad (5.73)$$

The diagram (c) has a same result, $J_c = J_b$. Therefore, we get the NLO quark jet function

$$J^{(1)}(p^2, \mu) = \frac{C_F \alpha_s}{4\pi} \left[4 \left(\frac{\ln p^2 / \mu^2}{p^2} \right)_*^{[p^2, \mu^2]} - 3 \left(\frac{1}{p^2} \right)_*^{[p^2, \mu^2]} + (7 - \pi^2) \delta(p^2) \right], \quad (5.74)$$

which agrees with the results in Ref. [55]. The NNLO quark jet function has been obtained in Ref. [71]. The RG evolution of the jet function is given by

$$\frac{dJ(p^2, \mu)}{d \ln \mu} = \left(-2\Gamma_{\text{cusp}} \ln \frac{p^2}{\mu^2} - 2\gamma^J \right) J(p^2, \mu) + 2\Gamma_{\text{cusp}} \int_0^{p^2} dq^2 \frac{J(p^2, \mu) - J(q^2, \mu)}{p^2 - q^2}, \quad (5.75)$$

where γ^J is the anomalous dimensions of the jet function. It has been shown explicitly in the appendix. Similar to the soft function, it is better to use the Laplace transformed jet function [36, 70]

$$\tilde{j}(\ln \frac{Q^2}{\mu^2}, \mu) = \int_0^\infty dp^2 \exp\left(-\frac{p^2}{Q^2 e^{\gamma_E}}\right) J(p^2, \mu), \quad (5.76)$$

which satisfies the RG equation

$$\frac{d}{d \ln \mu} \tilde{j}(\ln \frac{Q^2}{\mu^2}, \mu) = \left(-2\Gamma_{\text{cusp}} \ln \frac{Q^2}{\mu^2} - 2\gamma^J \right) \tilde{j}(\ln \frac{Q^2}{\mu^2}, \mu). \quad (5.77)$$

Thus, we get the jet function at arbitrary scale μ

$$J(p^2, \mu) = \exp[-4S(\mu_j, \mu) + 2a^J(\mu_j, \mu)] \tilde{j}(\partial_{\eta_j}, \mu_j) \frac{1}{p^2} \left(\frac{p^2}{\mu_j^2} \right)^{\eta_j} \frac{e^{-\gamma_E \eta_j}}{\Gamma(\eta_j)}, \quad (5.78)$$

where $\eta_j = 2a_\Gamma(\mu_j, \mu)$. The scale dependent part of the Laplace transformed jet function $\tilde{j}(L, \mu)$ is determined by the anomalous dimensions of the jet function from Eq.(5.77), while the scale independent part can be obtained only by fixed-order calculations. At NLO, it is

$$\tilde{j}(L, \mu) = 1 + \frac{\alpha_s}{4\pi} \left(\frac{\Gamma_0}{2} L^2 + \gamma_0^J L + c_1^J \right) \quad (5.79)$$

with $c_1^J = (7 - \frac{2}{3}\pi^2) C_F$.

5.4.4 Scale Invariance

The scale invariance is an essential property of any physical observable in principle. In practice, the theoretical predictions cannot be calculated to all orders. As a result, there is remaining scale dependence in theoretical predictions. This scale dependence resides in the unknown high-order contributions. The higher order results we obtain, the less scale dependence we get.

In the factorized cross section in Eq. (5.45), the hard function, jet function and soft function have their intricate scales, at which the perturbative expansion is reliable. The results at a common scale are estimated by evolving the RG equations, as shown in the last section. The independence on the intricate scales can be checked order by order in α_s . For example, we can expand the exponents in Eq. (5.52) in a series of $\alpha_s(\mu)$, then the dependence of the right hand of the equation on the intermediate hard scale $\mu_{h,\text{up}}$ cancel up to $\mathcal{O}(\alpha_s)$. The same cancellation happens for $\mu_{h,\text{dn}}$ in Eq. (5.53).

The case for the jet scale in Eq. (5.76) is more complicated due to the partial derivative operator and the distributions in fixed order arising from the expansion

$$\frac{1}{p^2} \left(\frac{p^2}{\mu_j^2} \right)^{\eta_j} = \frac{\delta(p^2)}{\eta_j} + \left[\frac{1}{p^2} \right]_{\star}^{[p^2, \mu_j^2]} + \eta_j \left[\frac{\ln(p^2/\mu_j^2)}{p^2} \right]_{\star}^{[p^2, \mu_j^2]} + \mathcal{O}(\eta_j^2). \quad (5.80)$$

Each term above is defined in the sense of an integration with a regular test function. Thus, it is difficult to confirm the cancellation of μ_j in this form. However, we can transform into the Laplace space in which the jet function has a similar expansion to the hard function; see Eq. (5.79). In this space, the cancellation of μ_j up to $\mathcal{O}(\alpha_s)$ is easy to be checked. The case for the soft scale is similar.

Next, we discuss the dependence on the common scale. Since each part of the cross section near the threshold in Eq. (5.45) depends on the common scale, we need to consider the hadronic cross section,

$$\begin{aligned} \frac{d\sigma}{dS_4 dy} \propto \int dx_a dx_b \int dp_1^2 \int dk^+ \frac{1}{s} f_{i/P_a}(x_a, \mu) f_{j/P_b}(x_b, \mu) H_{\text{up}}(\mu) H_{\text{dn}}(\mu) \\ J(p_1^2, \mu) S(k^+, \mu) \delta(S_4 - (-\hat{t})(1-x_a) - (-\hat{u})(1-x_b) - p_1^2 - 2k^+ E_1), \end{aligned} \quad (5.81)$$

where we have used $dS_4 dy$ instead of $dp_T^2 dy$ because of the δ constraint. The RG equation of the jet function with argument p^2 , i.e., $J(p^2, \mu)$ depends on the jet functions with other argument, i.e., $J(p'^2, \mu)$. The RG equations of the soft function and PDFs are of the same feature. Meanwhile, the arguments of the jet function, soft function, and PDFs are connected by the δ function. To get rid of the correlation, it is convenient to apply the Laplace transformation to the above equation and we obtain

$$\frac{d\tilde{\sigma}}{dQ^2 dy} = \int_0^\infty dS_4 \exp\left(-\frac{S_4}{Q^2 e^{\gamma_E}}\right) \frac{d\sigma}{dS_4 dy}. \quad (5.82)$$

The Laplace transformed jet function and its RG evolution are given in Eqs. (5.76) and (5.77). The Laplace transformed soft function is similar, but satisfies the RG equation

$$\frac{d}{d \ln \mu} \tilde{s}\left(\ln \frac{Q^2(-\hat{t} + m_t^2)}{\mu(-\hat{u})m_t}, \mu\right) = \left(-2\Gamma_{\text{cusp}} \ln \frac{Q^2(-\hat{t} + m_t^2)}{\mu(-\hat{u})m_t} + 2\gamma^S\right) \tilde{s}\left(\ln \frac{Q^2(-\hat{t} + m_t^2)}{\mu(-\hat{u})m_t}, \mu\right). \quad (5.83)$$

The Laplace transformed PDF near the endpoint ($x \rightarrow 1$) is given by

$$\tilde{f}_{i/P}(\tau, \mu) = \int_0^1 dx \exp\left(-\frac{1-x}{\tau e^{\gamma_E}}\right) f_{i/P_a}(x, \mu), \quad (5.84)$$

which satisfies the RG equation

$$\frac{d}{d \ln \mu} \tilde{f}_{i/P}(\tau, \mu) = (2\Gamma_{\text{cusp}} \ln \tau + 2\gamma^\phi) \tilde{f}_{i/P}(\tau, \mu). \quad (5.85)$$

From the δ function in Eq.(5.81), the variables $\tau_{a,b}$ in the Laplace transformed PDF are given by

$$\tau_a = \frac{Q^2}{-\hat{t}} \quad \text{for} \quad \tilde{f}_{i/P_a}(\tau_a, \mu), \quad \text{and} \quad \tau_b = \frac{Q^2}{-\hat{u}} \quad \text{for} \quad \tilde{f}_{j/P_b}(\tau_b, \mu). \quad (5.86)$$

Last, the RG equations for the hard functions have been given by Eqs.(5.50) and (5.51).

Now we are ready to check the scale independence of the final results. Given the relation between anomalous dimensions given in Eq.(7.30), we can immediately obtain

$$\frac{d}{d \ln \mu} \left[\tilde{f}_{i/P_a}(\tau_a, \mu) \tilde{f}_{j/P_b}(\tau_b, \mu) H_{\text{up}}(\mu) H_{\text{dn}}(\mu) \tilde{j}\left(\ln \frac{Q^2}{\mu^2}, \mu\right) \tilde{s}\left(\ln \frac{Q^2(-\hat{t} + m_t^2)}{\mu(-\hat{u})m_t}, \mu\right) \right] = 0. \quad (5.87)$$

Even more precisely, we have two separate equations

$$\begin{aligned} \frac{d}{d \ln \mu} \left[\tilde{f}_{i/P_a}(\tau_a, \mu) H_{\text{up}}(\mu) \tilde{j} \left(\ln \frac{Q^2}{\mu^2}, \mu \right) \right] &= 0, \\ \frac{d}{d \ln \mu} \left[\tilde{f}_{j/P_b}(\tau_b, \mu) H_{\text{dn}}(\mu) \tilde{s} \left(\ln \frac{Q^2(-\hat{t} + m_t^2)}{\mu(-\hat{u})m_t}, \mu \right) \right] &= 0, \end{aligned} \quad (5.88)$$

which manifest the scale invariance of the cross section. We point out that the scale invariance discussed in this section is valid given that all functions have been known to all orders. In practice, there would be scale dependence in the cross section due to the unknown high-order contributions.

5.4.5 Final RG Improved Differential Cross Section

Combining the hard, jet, and soft functions together, we obtain the resummed differential cross section for t -channel single top production

$$\begin{aligned} \frac{d\hat{\sigma}^{\text{thres}}}{d\hat{t}d\hat{u}} &= \sum_{ij} \frac{\lambda_{0,ij}}{64\pi N_c^2 \hat{s}^2} \\ &\exp[4S(\mu_{h,\text{up}}, \mu_{F,\text{up}}) - 2a_{\text{up}}^V(\mu_{h,\text{up}}, \mu_{F,\text{up}})] \left(\frac{-\hat{t}}{\mu_{h,\text{up}}^2} \right)^{-2a_\Gamma(\mu_{h,\text{up}}, \mu_{F,\text{up}})} \\ &H_{\text{up}}(\mu_{h,\text{up}}) \\ &\exp[2S(\mu_{h,\text{dn}}, \mu_{F,\text{dn}}) - 2a_{\text{dn}}^V(\mu_{h,\text{dn}}, \mu_{F,\text{dn}})] \left(\frac{-\hat{t} + m_t^2}{\mu_{h,\text{dn}} m_t} \right)^{-2a_\Gamma(\mu_{h,\text{dn}}, \mu_{F,\text{dn}})} \\ &H_{\text{dn}}(\mu_{h,\text{dn}}) \\ &\exp[-4S(\mu_j, \mu_{F,\text{up}}) + 2a^J(\mu_j, \mu_{F,\text{up}})] \left(\frac{m_t^2}{\mu_j^2} \right)^{\eta_j} \\ &\exp[-2S(\mu_s, \mu_{F,\text{dn}}) - 2a^S(\mu_s, \mu_{F,\text{dn}})] \left(\frac{m_t(-\hat{t} + m_t^2)}{\mu_s(-\hat{u})} \right)^{\eta_s} \\ &\tilde{j}(\partial_\eta + L_j, \mu_j) \tilde{s}(\partial_\eta + L_s, \mu_s) \frac{1}{s_4} \left(\frac{s_4}{m_t^2} \right)^\eta \frac{e^{-\gamma_E \eta}}{\Gamma(\eta)}, \end{aligned} \quad (5.89)$$

where $\eta = \eta_j + \eta_s$ and $L_j = \ln(m_t^2/\mu_j^2)$, $L_s = \ln[m_t(-\hat{t} + m_t^2)/\mu_s(-\hat{u})]$. In the above expression, the hard function H_{up} and jet function (H_{dn} and soft function) have been evolved from their intrinsic scales to the factorization scale $\mu_{F,\text{up}}$ ($\mu_{F,\text{dn}}$). Though the t -channel single top production can be considered as double DIS processes, the convolution between the jet and soft functions, as expressed in terms of the partial derivative operator acting on the same kernel function, violates this simple picture and relates the two DIS processes nontrivially.

If we set scales $\mu_{h,\text{up}}, \mu_{h,\text{dn}}, \mu_j, \mu_s$ all equal to the factorization scale $\mu_{F,\text{up}} = \mu_{F,\text{dn}} = \mu_F$, then we reproduce the singular plus distributions, which should appear in the fixed-order calculations. Up to $\mathcal{O}(\alpha_s^2)$, we have

$$\left(\frac{\lambda_{0,ij}}{64\pi N_c^2 \hat{s}^2}\right)^{-1} \frac{d\hat{\sigma}_{ij}^{\text{thres}}}{d\hat{t}d\hat{u}} = \delta(s_4) + \frac{\alpha_s}{4\pi} \left\{ A_2 D_2 + A_1 D_1 + A_0 \delta(s_4) \right\} + \left(\frac{\alpha_s}{4\pi}\right)^2 \left\{ B_4 D_4 + B_3 D_3 + B_2 D_2 + B_1 D_1 + B_0 \delta(s_4) \right\}, \quad (5.90)$$

where

$$D_n = \left[\frac{\ln^{n-1}(s_4/m_t^2)}{s_4} \right]_{\star}^{[s_4, m_t^2]}. \quad (5.91)$$

The A_n and B_n coefficients are given by

$$A_2 = 3\Gamma_0, \quad (5.92)$$

$$A_1 = (L_j + 2L_s)\Gamma_0 + \gamma_0^J - 2\gamma_0^S, \quad (5.93)$$

$$A_0 = \left(-\frac{1}{2}L_{h,\text{up}}^2 - L_{h,\text{dn}}^2 + \frac{1}{2}L_j^2 + L_s^2 - \frac{\pi^2}{4} \right) \Gamma_0 - \gamma_{\text{up},0}^V L_{h,\text{up}} - 2\gamma_{\text{dn},0}^V L_{h,\text{dn}} + \gamma_0^J L_j - 2\gamma_0^S L_s + c_1^H + c_1^J + c_1^S, \quad (5.94)$$

$$B_4 = \frac{A_2^2}{2}, \quad (5.95)$$

$$B_3 = \frac{9}{2}A_1\Gamma_0 - \frac{5}{2}\beta_0\Gamma_0, \quad (5.96)$$

$$B_2 = A_1^2 + A_2A_0 - \frac{3\pi^2}{2}\Gamma_0^2 - \beta_0\Gamma_0(L_j + 4L_s) - \beta_0(\gamma_0^J - 4\gamma_0^S) + 3\Gamma_1, \quad (5.97)$$

$$B_1 = A_1 \left(A_0 - \frac{\pi^2}{2}\Gamma_0 \right) + 9\zeta_3\Gamma_0^2 - \beta_0\Gamma_0 \left(\frac{1}{2}L_j^2 + 2L_s^2 - \frac{5}{12}\pi^2 \right) - \beta_0(c_1^J + 2c_1^S + \gamma_0^J L_j - 4\gamma_0^S L_s) + \gamma_1^J - 2\gamma_1^S + \Gamma_1(L_j + 2L_s), \quad (5.98)$$

where $\zeta_3 = 1.20206\dots$, $L_{h,\text{dn}} = \ln[(-\hat{t} + m_t^2)/\mu m_t]$, $L_{h,\text{up}} = \ln(-\hat{t}/\mu^2)$ and $c_1^H = c_1^{H,\text{up}} + c_1^{H,\text{dn}}$.

To obtain most precise predictions, we resum the singular terms to all orders and also include the nonsingular terms up to NLO. The nonsingular terms are obtained by subtracting from the exact NLO results the singular terms. Therefore, we obtain the final RG improved differential cross section

$$\frac{d\hat{\sigma}_{\text{Resum}}}{d\hat{t}d\hat{u}} = \frac{d\hat{\sigma}^{\text{thres}}}{d\hat{t}d\hat{u}} + \left(\frac{d\hat{\sigma}_{\text{NLO}}}{d\hat{t}d\hat{u}} - \frac{d\hat{\sigma}^{\text{thres}}}{d\hat{t}d\hat{u}} \right) \Big|_{\text{expanded to NLO}}. \quad (5.99)$$

In the threshold regions, the second term in the above equation almost vanishes because the expansion of the resummed result approaches the fixed-order one, and thus, the threshold contribution dominates. In the regions far from the threshold limit, the resummation effect is not important and the final prediction is almost determined by the fixed-order result.

5.5 Numerical Results

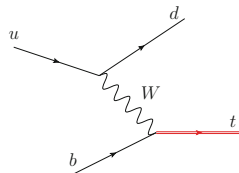
In this section, we discuss the numerical results of threshold resummation effects in the t -channel single top production at the Tevatron ($\sqrt{s} = 1.96$ TeV) and the LHC ($\sqrt{s} = 8$ TeV). The top quark mass is chosen to be $m_t = 173.2$ GeV [72] and the rapidity of the top quark is integrated over the region $(-2.4, 2.4)$. The W boson mass is taken to be $M_W = 80.4$ GeV. The Fermi constant is $G_F = 1.1664 \times 10^{-5}$ GeV $^{-2}$. The CKM matrix is given by

$$V_{CKM} = \begin{pmatrix} 0.9751 & 0.2215 & 0.0035 \\ 0.2210 & 0.9743 & 0.0410 \\ 0 & 0 & 1 \end{pmatrix}. \quad (5.100)$$

Throughout the numerical calculations, we use the MSTW2008NNLO PDF sets [73] and associated strong coupling constant. The factorization scales are set at m_t unless specified otherwise.

There are four immediate scales, i.e., $\mu_{h,\text{up}}$, $\mu_{h,\text{dn}}$, μ_j , μ_s in the RG improved cross section. Though the cross section in all orders does not depend on them, at a fixed order, they must be properly set so that the hard, jet and soft functions have stable perturbative expansions. This requires that each function should not contain large logarithms. From Eqs. (5.46) and (5.47), we can see that if we choose $\mu_{h,\text{up}} = Q \equiv \sqrt{-\hat{t}}$ and $\mu_{h,\text{dn}} = (Q^2 + m_t^2)/m_t$, then the large logarithms in the hard function vanish. On the other hand, if we combine the two hard functions into one hard function, we cannot choose a proper hard scale to eliminate all the possible large logarithms simultaneously. This is due to the fact that the W boson connects interactions at different scales intrinsically. Actually, we can take another viewpoint on the t -channel single top production, i.e., considering it as a fusion process $Wb \rightarrow t$, as shown in Fig. 5.8. The W boson, emitted from an initial-state up quark, collides with a bottom quark to produce a top quark. There is no specific constraint on the

Fig. 5.8 The Feynman diagrams for the single top production via the fusion of a W boson and a bottom quark



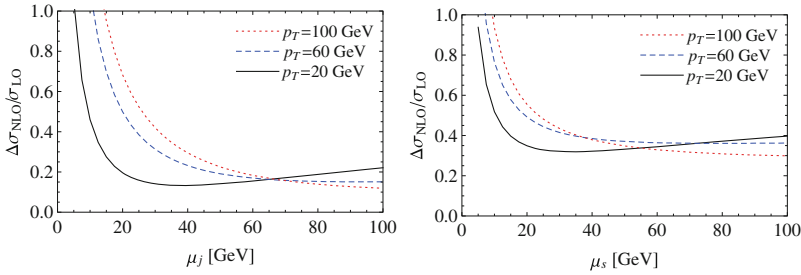


Fig. 5.9 The contributions from fixed-order jet and soft functions normalized by the LO cross section [74]

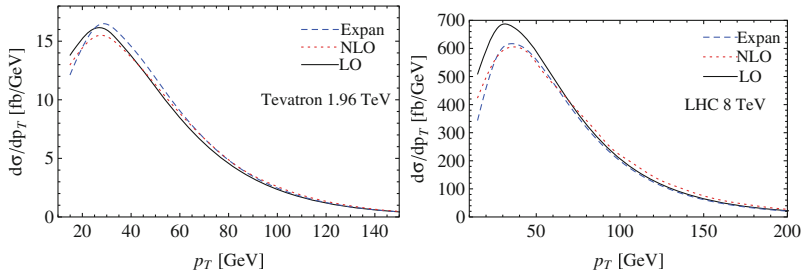


Fig. 5.10 The singular terms contribution and fixed-order cross sections for t -channel single top production at the Tevatron (*left*) and the LHC (*right*) [74]. The *dashed line* represents the contributions from the singular terms up to $\mathcal{O}(\alpha_s)$ which is given in Eq. (5.90)

virtuality of the W boson in its production. However, the mass and momentum of the final-state top quark impose constraints on the W boson. As a result, the typical scales of the interactions involving the light quarks and heavy quarks are different, and need to be set separately.

The choices of jet and soft scales are a little tricky. From Eqs. (5.66), (5.67), (5.78) and (5.79) the intrinsic jet and soft scales should be $\sqrt{p^2}$ and $2kE_1(-\hat{t} + m_t^2)/(-\hat{u})/m_t$, respectively. But these two scales are integrated over so that they do not have fixed values. Moreover, they can be so small that the theory would become nonperturbative. Therefore, in practice, we choose the intrinsic jet and soft scales numerically. In Fig. 5.9, we show the contributions of the fixed-order jet and soft functions normalized by the LO cross section. The top quark transverse momentum is fixed at three specific values, i.e., $p_T = 20, 60, 100$ GeV, while the jet (soft) scale changes from 5 to 100 GeV. We can see that the contributions are very large when the jet or soft scale is too small. In order to make the perturbative expansions of the jet and soft functions converge fast, we choose the intrinsic jet and soft scales as 80 and 50 GeV, respectively, and the scale uncertainties due to these choices will be discussed below. From Fig. 5.9, we can also see that the contributions of the jet and soft functions are positive, about 20 and 40 % at the intrinsic scales. For comparison, we also estimate the contributions of the hard functions, and find that

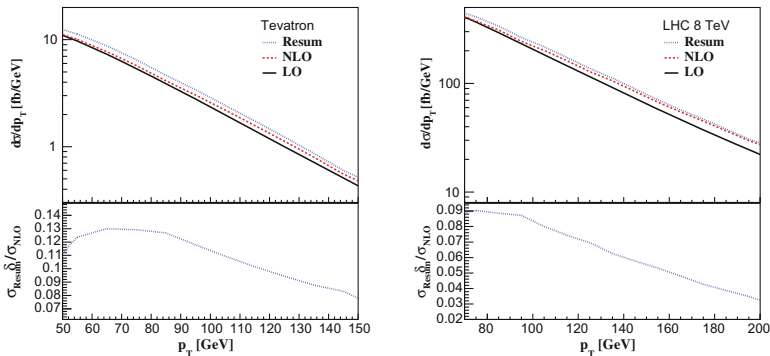


Fig. 5.11 The RG improved (*dashed*) and fixed-order cross sections for t -channel single top production at the Tevatron (*left*) and the LHC (*right*). We have defined $\delta\sigma_{\text{Resum}} = d\sigma_{\text{Resum}} - d\sigma_{\text{NLO}}$

the hard functions give negative contributions, about -15% at the intrinsic scales [74].

Before discussing the numerical results of the RG improved cross section, it is important to compare the contributions from singular terms with the fixed-order calculations. In Fig. 5.10, we present the contribution from singular terms and fixed-order cross sections. We can see that the NLO cross sections are well approximated by the singular terms only if the top quark transverse momentum p_T is greater than 50 (70) GeV at the Tevatron (LHC). Since we can predict the singular terms to higher orders, we may know the approximate cross sections at higher orders. Therefore, it is useful to resum the singular terms in the large p_T region. In the small p_T region, the singular terms do not dominate the NLO corrections, so high-order results of the cross sections cannot be known from the high-order singular terms, and one needs to calculate the exact high-order corrections. In the following content, we only discuss the numerical results in single top production with $p_T > 50$ (70) GeV at the Tevatron (LHC).

As read from Fig. 5.10, the NLO QCD correction is small for t -channel single top production. This may due to the fact that the large positive contributions from the soft and jet functions cancel with the large negative contributions from the hard functions, as illustrated above. It is interesting to see whether the cancellation still happens after these large contributions are resummed to all orders.

Then, we present the numerical results of the cross section. When discussing each scale dependence, we fix the other scales at the intrinsic scales discussed above. We show the RG improved cross sections as a function of the top quark p_T in Fig. 5.11. We can see that the distribution is increased by about 9–13% and 4–9% for $p_T > 50$ and 70 GeV at the Tevatron and LHC, respectively, compared to the NLO results. In Fig. 5.12, we give the uncertainties of the resummation results due to the change of intermediate scales $\mu_{h,\text{up}}$, $\mu_{h,\text{dn}}$, μ_j , μ_s independently by a factor of two. The uncertainties arising from $\mu_{h,\text{up}}$, $\mu_{h,\text{dn}}$ and μ_j are less than $\pm 1\%$, and for μ_s are about $\pm 2\%$. In Fig. 5.13, we show the scale uncertainties of the resummation results

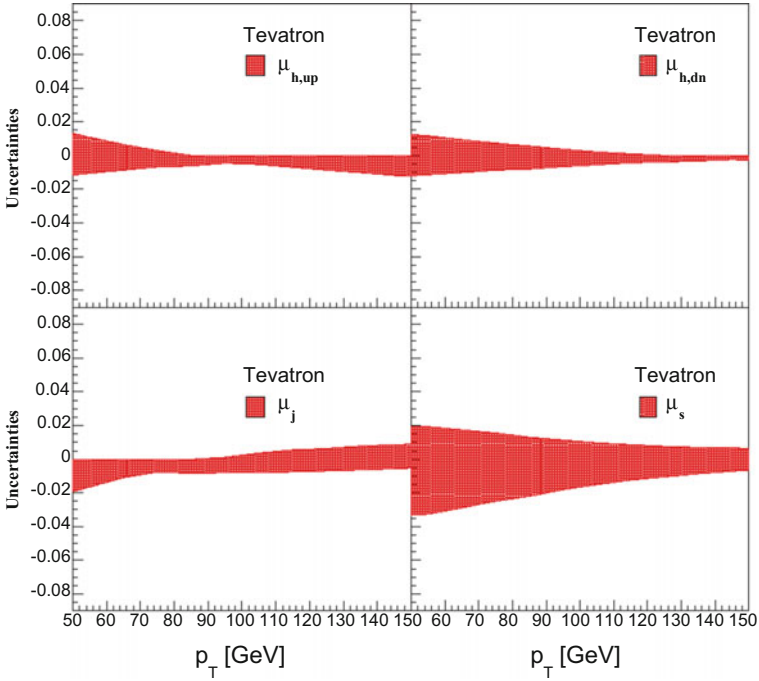


Fig. 5.12 The scale uncertainties of the resummation results due to the variations of $\mu_{h,\text{up}}$, $\mu_{h,\text{dn}}$, μ_j , μ_s , respectively

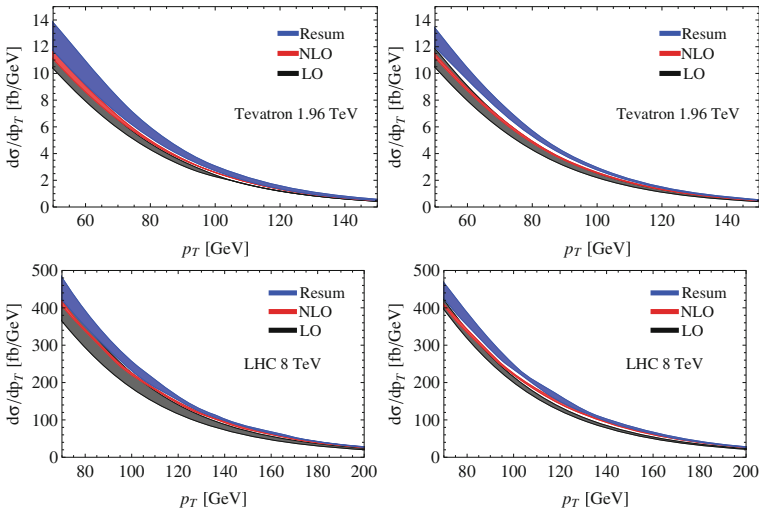


Fig. 5.13 The scale uncertainties due to the variations of $\mu_{F,\text{dn}}$ (left) and $\mu_{F,\text{up}}$ (right), respectively [74]. The bands in each plots from top to bottom denote the resummation, NLO and LO results, respectively

due to the variations of $\mu_{F,\text{dn}}$ and $\mu_{F,\text{up}}$ by a factor of two, and do not see scale uncertainties are decreased, compared to the NLO results. In principle, the scale uncertainties should vanish, as illustrated analytically in the last section. However, the analysis is based on the assumption that the PDF is evaluated near the endpoint. But in practice, this is not always true because the center-of-mass energy of the Tevatron or LHC is much larger than the invariant mass of the final states. And the dynamical enhancement mechanism [39] is not appropriate for a t -channel process. On the other hand, when approaching the threshold region, i.e., with the increasing of the top quark p_T , the scale uncertainties of the resummed cross sections are significantly reduced, as shown in Fig. 5.13.

5.6 Conclusions and Comments

The top quark is closely related to the precision electroweak fit, Higgs physics as well as extensions of the SM. The single top quark production plays an important role in determining the CKM matrix element V_{tb} and is also sensitive to new physics. In this chapter, we present the renormalization group improved prediction on the t -channel top quark transverse momentum distribution at large p_T in the SM at both the Tevatron and the LHC with SCET. This is the first spacelike process studied in SCET involving both massless and massive colored particles in the final states. The cross section in the threshold region can be factorized into a convolution of hard, jet, soft, and PDFs. In particular, we first calculate the NLO soft functions in this process. The renormalization group improved cross section is obtained by evolving the scales in different functions to a common scale. We find that the resummation effects increase the NLO results by about 9–13% and 4–9% when the transverse momentum of the top quark is larger than 50 and 70 GeV at the Tevatron and the 8 TeV LHC, respectively. Our prediction on the transverse momentum distribution of the top quark in the large p_T region is important in the search for new physics, e.g., a heavy W' which can induce the single top production through the s -channel. In addition, we discuss the scale independence of the cross section both analytically and numerically, and show how to choose the proper scales at which the perturbative expansion can converge fast.

Here, we want to mention two main latest developments of the theoretical prediction on the single top production. One is the prediction on the transverse momentum spectrum of the top quark in traditional resummation method which has already been obtained in Ref. [75], where a different threshold variable is used. Explicitly, the S_4 there is given by

$$\begin{aligned} S_4 &\equiv s + t + u - m_t^2 \\ &= (P_a + P_b)^2 + (P_a - p_1)^2 + (P_b - p_1)^2 - m_t^2. \end{aligned} \quad (5.101)$$

The corresponding partonic threshold variable s_4 for the underlying partonic process $u(p_a) + b(p_b) \rightarrow d(p_1) + t(q)$ is given by

$$\begin{aligned}
s_4 &\equiv (p_a + p_b)^2 + (p_a - p_1)^2 + (p_b - p_1)^2 - m_t^2 \\
&= \hat{s} + \hat{t} + \hat{u} - m_t^2 \\
&= (q + k)^2 - m_t^2 + p_1^2 \\
&= p_1^2 + 2q \cdot k + k^2 \\
&\simeq p_1^2 + 2q \cdot k.
\end{aligned} \tag{5.102}$$

Here, the momenta of additional radiation have been divided, compared to Born level scattering, into the collinear part, denoted by p_1 , and the soft part, denoted by k . The hadronic threshold limit $S_4 \rightarrow 0$ implies the partonic threshold limit $s_4 \rightarrow 0$ as well as no initial remnants in the final state. More explicitly, in the threshold region,

$$S_4 \approx s_4 + (-\hat{u}_1)\bar{x}_a + (-\hat{t}_1)\bar{x}_b, \tag{5.103}$$

with $\hat{t}_1 = \hat{t} - m_t^2$, $\hat{u}_1 = \hat{u} - m_t^2$. The threshold variable embodies the information of the threshold region. We see from Eq. (5.102) that radiation of soft gluons ($k \rightarrow 0$) or collinear gluons ($p_1^2 \rightarrow 0$) implies $s_4 \rightarrow 0$. This fact means that the method in Ref. [31] resums both the soft and the collinear gluon effects.

However, there is a difference. In the soft gluon limit, i.e., $k \rightarrow 0$,

$$s_4 \approx 2q \cdot k \tag{5.104}$$

in traditional resummation method, while

$$s_4 \approx 2p_1 \cdot k \tag{5.105}$$

in SCET. Given that q and p_1 are massive and massless, respectively, the magnitudes of s_4 are not the same for a fixed k . This difference can be traced back to the theory in which the resummation is performed. In traditional resummation method, the soft gluon is described by its small energy in the partonic center-of-mass frame, similar to HQET. In SCET, the soft gluon interacts with collinear particles only through its small component in the light-cone frame of the collinear particle. This difference also induce the different method in calculating the individual part of the factorized cross section. Thought the result given in Ref. [75] is similar to our calculation, it is interesting to compare the two resummation methods in more detail, which is left to future work.

The other eminent development is the fully differential QCD NNLO correction to the t -channel single top production in the approximation that all dynamical cross-talk between corrections to the light and heavy quark lines are not considered [76]. The results show that the NNLO correction is rather small but reduces the scale uncertainties to less than 1 %. This small increase is the result of significant cancellations between various sources of QCD corrections. For example, NLO QCD corrections in the bq partonic channel increase the leading order cross section by 10 %, which is largely canceled by the quark–gluon channel that appears at NLO. The similar cancellation happens at NNLO corrections. In our work, the soft gluon effect in the

bq partonic channel has been resummed to all order while the quark–gluon channel is only kept at NLO. Therefore, a few percent increase is expected for the transverse momentum of the top quark.

References

1. M. Kobayashi, T. Maskawa, CP violation in the renormalizable theory of weak interaction. *Prog. Theor. Phys.* **49**, 652–657 (1973)
2. F. Abe et al., CDF Collaboration, Observation of top quark production in $\bar{p}p$ collisions. *Phys. Rev. Lett.* **74**, 2626–2631 (1995). [arXiv:hep-ex/9503002](#)
3. S. Abachi et al., D0 Collaboration, Observation of the top quark. *Phys. Rev. Lett.* **74**, 2632–2637 (1995). [arXiv:hep-ex/9503003](#)
4. ATLAS, CDF, CMS, D0 Collaboration, First combination of Tevatron and LHC measurements of the top-quark mass. [arXiv:1403.4427](#)
5. A.H. Hoang, I.W. Stewart, Top mass measurements from jets and the tevatron top-quark mass. *Nucl. Phys. Proc. Suppl.* **185**, 220–226 (2008). [arXiv:0808.0222](#)
6. A. Buckley, J. Butterworth, S. Gieseke, D. Grellscheid, S. Hoche et al., General-purpose event generators for LHC physics. *Phys. Rept.* **504**, 145–233 (2011). [arXiv:1101.2599](#)
7. J. Gao, C.S. Li, H.X. Zhu, Top quark decay at next-to-next-to leading order in QCD. *Phys. Rev. Lett.* **110**, 042001 (2013). [arXiv:1210.2808](#)
8. K. Olive et al., Particle Data Group Collaboration, Review of particle physics. *Chin. Phys. C* **38**, 090001 (2014)
9. M. Czakon, P. Fiedler, A. Mitov, Total top-quark pair-production cross section at hadron colliders through $\mathcal{O}(\alpha_s^4)$. *Phys. Rev. Lett.* **110**, 252004 (2013). [arXiv:1303.6254](#)
10. V.M. Abazov et al., D0 Collaboration, Observation of single top-quark production. *Phys. Rev. Lett.* **103**, 092001 (2009). [arXiv:0903.0850](#)
11. T. Aaltonen et al., CDF Collaboration, First observation of electroweak single top quark production. *Phys. Rev. Lett.* **103**, 092002 (2009). [arXiv:0903.0885](#)
12. G. Aad et al., ATLAS Collaboration, Measurement of the t-channel single top-quark production cross section in pp collisions at $\sqrt{s} = 7$ TeV with the ATLAS detector. *Phys. Lett. B* **717**, 330–350 (2012). [arXiv:1205.3130](#)
13. S. Chatrchyan et al., CMS Collaboration, Measurement of the single-top-quark t-channel cross section in pp collisions at $\sqrt{s} = 7$ TeV. *JHEP* **1212**, 035 (2012). [arXiv:1209.4533](#)
14. V. Khachatryan et al., C.M.S. Collaboration, Measurement of the t-channel single-top-quark production cross section and of the $|V_{tb}| = 8$ TeV. *JHEP* **1406**, 090 (2014). [arXiv:1403.7366](#)
15. G. Aad et al., ATLAS Collaboration, Comprehensive measurements of t TeV with the ATLAS detector. *Phys. Rev. D* **90**(11), 112006 (2014). [arXiv:1406.7844](#)
16. G. Bordes, B. van Eijk, Calculating QCD corrections to single top production in hadronic interactions. *Nucl. Phys. B* **435**, 23–58 (1995)
17. T. Stelzer, S. Willenbrock, Single top quark production via $q\bar{q} \rightarrow t\bar{b}$. *Phys. Lett. B* **357**, 125–130 (1995). [arXiv:hep-ph/9505433](#)
18. B.W. Harris, E. Laenen, L. Phaf, Z. Sullivan, S. Weinzierl, The Fully differential single top quark cross-section in next to leading order QCD. *Phys. Rev. D* **66**, 054024 (2002). [arXiv:hep-ph/0207055](#)
19. Z. Sullivan, Understanding single-top-quark production and jets at hadron colliders. *Phys. Rev. D* **70**, 114012 (2004). [arXiv:hep-ph/0408049](#)
20. J.M. Campbell, R.K. Ellis, F. Tramontano, Single top production and decay at next-to-leading order. *Phys. Rev. D* **70**, 094012 (2004). [arXiv:hep-ph/0408158](#)
21. Q.-H. Cao, C.P. Yuan, Single top quark production and decay at next-to-leading order in hadron collision. *Phys. Rev. D* **71**, 054022 (2005). [arXiv:hep-ph/0408180](#)

22. Q.-H. Cao, R. Schwienhorst, J.A. Benitez, R. Brock, C.P. Yuan, Next-to-leading order corrections to single top quark production and decay at the tevatron: 2. t -channel process. *Phys. Rev. D* **72**, 094027 (2005). [arXiv:hep-ph/0504230](#)
23. J.M. Campbell, R. Frederix, F. Maltoni, F. Tramontano, NLO predictions for t -channel production of single top and fourth generation quarks at hadron colliders. *JHEP* **10**, 042 (2009). [arXiv:0907.3933](#)
24. J.M. Campbell, R. Frederix, F. Maltoni, F. Tramontano, Next-to-leading-order predictions for t -channel single-top production at hadron colliders. *Phys. Rev. Lett.* **102**, 182003 (2009). [arXiv:0903.0005](#)
25. S. Frixione, E. Laenen, P. Motylinski, B.R. Webber, Single-top production in MC@NLO. *JHEP* **03**, 092 (2006). [arXiv:hep-ph/0512250](#)
26. S. Frixione, E. Laenen, P. Motylinski, B.R. Webber, C.D. White, Single-top hadroproduction in association with a W boson. *JHEP* **07**, 029 (2008). [arXiv:0805.3067](#)
27. S. Alioli, P. Nason, C. Oleari, E. Re, NLO single-top production matched with shower in POWHEG: s- and t-channel contributions. *JHEP* **09**, 111 (2009). [arXiv:0907.4076](#)
28. S. Hoche, Introduction to parton-shower event generators, in *Theoretical Advanced Study Institute in Elementary Particle Physics: Journeys Through the Precision Frontier: Amplitudes for Colliders (TASI 2014) Boulder*, Colorado, 2–27 June, 2014. [arXiv:1411.4085](#)
29. N. Kidonakis, Single top production at the tevatron: threshold resummation and finite-order soft gluon corrections. *Phys. Rev. D* **74**, 114012 (2006). [arXiv:hep-ph/0609287](#)
30. N. Kidonakis, Higher-order soft gluon corrections in single top quark production at the LHC. *Phys. Rev. D* **75**, 071501 (2007). [arXiv:hep-ph/0701080](#)
31. N. Kidonakis, Next-to-next-to-leading-order collinear and soft gluon corrections for t-channel single top quark production. *Phys. Rev. D* **83**, 091503 (2011). [arXiv:1103.2792](#)
32. C.W. Bauer, S. Fleming, M.E. Luke, Summing Sudakov logarithms in $B \rightarrow X_s \gamma$ in effective field theory. *Phys. Rev. D* **63**, 014006 (2000). [arXiv:hep-ph/0005275](#)
33. C.W. Bauer, S. Fleming, D. Pirjol, I.W. Stewart, An effective field theory for collinear and soft gluons: heavy to light decays. *Phys. Rev. D* **63**, 114020 (2001). [arXiv:hep-ph/0011336](#)
34. C.W. Bauer, I.W. Stewart, Invariant operators in collinear effective theory. *Phys. Lett. B* **516**, 134–142 (2001). [arXiv:hep-ph/0107001](#)
35. C.W. Bauer, D. Pirjol, I.W. Stewart, Soft-collinear factorization in effective field theory. *Phys. Rev. D* **65**, 054022 (2002). [arXiv:hep-ph/0109045](#)
36. T. Becher, M. Neubert, Threshold resummation in momentum space from effective field theory. *Phys. Rev. Lett.* **97**, 082001 (2006). [arXiv:hep-ph/0605050](#)
37. A. Idilbi, X.-D. Ji, Threshold resummation for Drell-Yan process in soft-collinear effective theory. *Phys. Rev. D* **72**, 054016 (2005). [arXiv:hep-ph/0501006](#)
38. A. Idilbi, X.-D. Ji, F. Yuan, Transverse momentum distribution through soft-gluon resummation in effective field theory. *Phys. Lett. B* **625**, 253–263 (2005). [arXiv:hep-ph/0507196](#)
39. T. Becher, M. Neubert, G. Xu, Dynamical threshold enhancement and resummation in Drell-Yan production. *JHEP* **07**, 030 (2008). [arXiv:0710.0680](#)
40. I.W. Stewart, F.J. Tackmann, W.J. Waalewijn, Factorization at the LHC: from PDFs to initial state jets. *Phys. Rev.* **D81**, 094035 (2010). [arXiv:0910.0467](#)
41. Y. Gao, C.S. Li, J.J. Liu, Transverse momentum resummation for Higgs production in soft-collinear effective theory. *Phys. Rev. D* **72**, 114020 (2005). [arXiv:hep-ph/0501229](#)
42. V. Ahrens, T. Becher, M. Neubert, L.L. Yang, Origin of the large perturbative corrections to higgs production at hadron colliders. *Phys. Rev. D* **79**, 033013 (2009). [arXiv:0808.3008](#)
43. V. Ahrens, T. Becher, M. Neubert, L.L. Yang, Renormalization-group improved prediction for higgs production at hadron colliders. *Eur. Phys. J. C* **62**, 333–353 (2009). [arXiv:0809.4283](#)
44. H.X. Zhu, C.S. Li, J.J. Zhang, H. Zhang, Z. Li, Threshold resummation effects in neutral higgs boson production by bottom quark fusion at the CERN large hadron collider. *Phys. Rev. D* **79**, 113005 (2009). [arXiv:0903.5047](#)
45. S. Mantry, F. Petriello, Factorization and resummation of Higgs boson differential distributions in soft-collinear effective theory. *Phys. Rev.* **D81**, 093007 (2010). [arXiv:0911.4135](#)

46. C. Lee, G. Sterman, Momentum flow correlations from event shapes: factorized soft gluons and soft-collinear effective theory. *Phys. Rev. D* **75**, 014022 (2007). [arXiv:hep-ph/0611061](#)
47. S. Fleming, A.H. Hoang, S. Mantry, I.W. Stewart, Jets from massive unstable particles: top-mass determination. *Phys. Rev. D* **77**, 074010 (2008). [arXiv:hep-ph/0703207](#)
48. S. Fleming, A.H. Hoang, S. Mantry, I.W. Stewart, Top jets in the peak region: factorization analysis with NLL resummation. *Phys. Rev. D* **77**, 114003 (2008). [arXiv:0711.2079](#)
49. C.W. Bauer, S.P. Fleming, C. Lee, G. Sterman, Factorization of e+e- event shape distributions with hadronic final states in soft collinear effective Theory. *Phys. Rev. D* **78**, 034027 (2008). [arXiv:0801.4569](#)
50. M.D. Schwartz, Resummation and NLO matching of event shapes with effective field theory. *Phys. Rev. D* **77**, 014026 (2008). [arXiv:0709.2709](#)
51. A. Idilbi, C. Kim, T. Mehen, Factorization and resummation for single color-octet scalar production at the LHC. *Phys. Rev. D* **79**, 114016 (2009). [arXiv:0903.3668](#)
52. L.L. Yang, C.S. Li, Y. Gao, J.J. Liu, Threshold resummation effects in direct top quark production at hadron colliders. *Phys. Rev. D* **73**, 074017 (2006). [arXiv:hep-ph/0601180](#)
53. L.L. Yang, C.S. Li, J. Gao, J. Wang, NNLL momentum-space threshold resummation in direct top quark production at the LHC. *JHEP* **12**, 123 (2014). [arXiv:1409.6959](#)
54. H.X. Zhu, C.S. Li, J. Wang, J.J. Zhang, Factorization and resummation of s-channel single top quark production. *JHEP* **1102**, 099 (2011). [arXiv:1006.0681](#)
55. A.V. Manohar, Deep inelastic scattering as $x \rightarrow 1$ using soft-collinear effective theory. *Phys. Rev. D* **68**, 114019 (2003). [arXiv:hep-ph/0309176](#)
56. J. Chay, C. Kim, Deep inelastic scattering near the endpoint in soft-collinear effective theory. *Phys. Rev. D* **75**, 016003 (2007). [arXiv:hep-ph/0511066](#)
57. P.-Y. Chen, A. Idilbi, X.-D. Ji, QCD factorization for deep-inelastic scattering at large Bjorken $x(B)$ approx. 1-O(Λ_{QCD}/Q). *Nucl. Phys. B* **763**, 183–197 (2007). [arXiv:hep-ph/0607003](#)
58. T. Becher, M.D. Schwartz, Direct photon production with effective field theory. *JHEP* **02**, 040 (2010). [arXiv:0911.0681](#)
59. T. Becher, C. Lorentzen, M.D. Schwartz, Resummation for W and Z production at large pT. *Phys. Rev. Lett.* **108**, 012001 (2012). [arXiv:1106.4310](#)
60. V. Ahrens, A. Ferroglia, M. Neubert, B.D. Pecjak, L.L. Yang, Threshold expansion at order α_s^4 for the t-tbar invariant mass distribution at hadron colliders. [arXiv:0912.3375](#)
61. V. Ahrens, A. Ferroglia, M. Neubert, B.D. Pecjak, L.L. Yang, Renormalization-group improved predictions for top-quark pair production at Hadron colliders. [arXiv:1003.5827](#)
62. M. Beneke, P. Falgari, S. Klein, C. Schwinn, Hadronic top-quark pair production with NNLL threshold resummation. *Nucl. Phys. B* **855**, 695–741 (2012). [arXiv:1109.1536](#)
63. E. Laenen, G. Oderda, G. Sterman, Resummation of threshold corrections for single particle inclusive cross-sections. *Phys. Lett. B* **438**, 173–183 (1998). [arXiv:hep-ph/9806467](#)
64. C.W. Bauer, A. Hornig, F.J. Tackmann, Factorization for generic jet production. *Phys. Rev. D* **79**, 114013 (2009). [arXiv:0808.2191](#)
65. C.W. Bauer, N.D. Dunn, A. Hornig, Factorization of boosted multijet processes for threshold resummation. *Phys. Rev. D* **82**, 054012 (2010). [arXiv:1002.1307](#)
66. N. Isgur, M.B. Wise, Weak decays of heavy mesons in the static quark approximation. *Phys. Lett. B* **232**, 113 (1989)
67. V. Ahrens, M. Neubert, L. Vernazza, Structure of infrared singularities of gauge-theory amplitudes at three and four loops. *JHEP* **1209**, 138 (2012). [arXiv:1208.4847](#)
68. T. Becher, M. Neubert, Infrared singularities of QCD amplitudes with massive partons. *Phys. Rev. D* **79**, 125004 (2009). [arXiv:0904.1021](#)
69. I. Korchemskaya, G. Korchemsky, On light-like wilson loops. *Phys. Lett. B* **287**(1–3), 169–175 (1992)
70. T. Becher, M. Neubert, B.D. Pecjak, Factorization and momentum-space resummation in deep-inelastic scattering. *JHEP* **01**, 076 (2007). [arXiv:hep-ph/0607228](#)
71. T. Becher, M. Neubert, Toward a NNLO calculation of the $\bar{B} \rightarrow X_s + \gamma$ decay rate with a cut on photon energy. II: Two-loop result for the jet function. *Phys. Lett. B* **637**, 251–259 (2006). [arXiv:hep-ph/0603140](#)

72. Tevatron Electroweak Working Group, CDF, D0 Collaboration, Combination of CDF and D0 results on the mass of the top quark using up to 5.8 fb⁻¹ of data. [arXiv:1107.5255](#)
73. A.D. Martin, W.J. Stirling, R.S. Thorne, G. Watt, Parton distributions for the LHC. *Eur. Phys. J. C* **63**, 189–285 (2009). [arXiv:0901.0002](#)
74. J. Wang, C.S. Li, H.X. Zhu, Resummation prediction on top quark transverse momentum distribution at large p_T . *Phys. Rev. D* **87**(3), 034030 (2013). [arXiv:1210.7698](#)
75. N. Kidonakis, Top-quark transverse-momentum distributions in t-channel single-top production. *Phys. Rev. D* **88**(3), 031504 (2013). [arXiv:1306.3592](#)
76. M. Brucherseifer, F. Caola, K. Melnikov, On the NNLO QCD corrections to single-top production at the LHC. *Phys. Lett. B* **736**, 58–63 (2014). [arXiv:1404.7116](#)

Chapter 6

Search for the Signal of Monotop Production at the Early LHC

6.1 Introduction

The main tasks of the LHC are to answer the fundamental questions in particle physics: whether the Higgs boson exist or not; are there new physics beyond the SM such as supersymmetry (SUSY), extra dimension, etc., at the TeV scale? The first stage of the LHC has discovered a scalar resonance closely resembling the SM Higgs boson, but provides no clue on the new physics beyond the SM. Instead, stringent constraints have been imposed from experiments on the possible extensions of the SM. Facing this fact, both theorists and experimentalists become interested in the more signature-based strategy, focusing on unusual final states which are difficult to detect or have not been considered yet by experimental collaborations so far. In this way, we may discover some new physics that is not included by any known models. Thus it provides more opportunities to explore the unknown world. This method is also inspired by the fact that many new theories are established in history to explain some new phenomena discovered previously. For example, the energy nonconservation of all visible particles in β -decay was discovered before the proposal of the neutrino. It is already a great achievement to discover some new phenomena, even though it cannot be predicted or explained by any existing theory.

It is naturally believed that top quark may have strong connections with new physics due to its large mass close to the scale of electroweak symmetry breaking. Searching for this kind of new physics has been delicately designed and carried out. Though it is possible that some new physics effects can occur in the quantum loop corrections to some precise measured processes involving top quarks, it is more evident to discover them via the top quark associated productions. The production modes of top quark pair production with or without missing transverse energy E_T have been extensively investigated [1–10]. However the production mode of a top and E_T , which is so-called monotop¹ [11], has only been discussed recently

¹We remind that the single top production discussed in the last chapter contains a top and a jet in the final state.

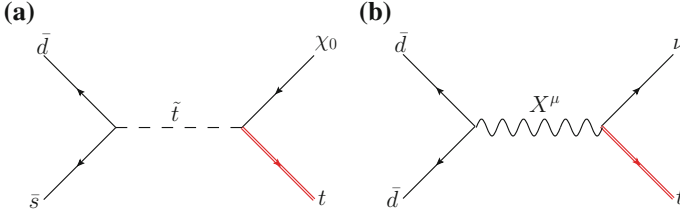


Fig. 6.1 Feynman diagrams for monotop production in some specific models

[12, 13]. This signal is absent in the SM because of loop suppression and the Glashow–Iliopoulos–Maiani mechanism. But it exists in models such as R -parity violating SUSY and $SU(5)$ grand unification model as decay products of some resonances. For example, in R -parity violating SUSY [14], a stop can be produced by the fusion of two down-type antiquarks through the Yukawa-like trilinear interaction $\lambda''_{ijk} U_i^c D_j^c D_k^c$, where U_i, D_i are left-handed chiral superfields and the superscript c denotes the charge conjugate, and then the stop decays into a top quark and a neutralino, the supersymmetric partner of the Higgs or neutral gauge bosons, as shown in Fig. 6.1a. This neutralino can be stable enough so that it escapes from the detector. Another example is the $SU(5)$ model [15], in which the gauge bosons X^μ , in one case, can transform quarks to antiquarks assigned to the **10** representation; in another case, they couple to quarks and leptons in the **5** representation. As a result, they can be resonantly produced and decay into a top and a neutrino at hadron colliders, as shown in Fig. 6.1b. Therefore, any discovery of such signal imply new physics, and can help us to explore the fundamental questions mentioned above.

In this work, we propose the general model-independent renormalizable effective Lagrangian with $SU(3)_C \otimes SU(2)_L \otimes U(1)_Y$ gauge symmetry of the SM

$$\begin{aligned}
 \mathcal{L} = & \lambda_S^{ij} \epsilon^{\alpha\beta\gamma} \phi_\alpha \bar{d}_{i\beta R}^c d_{j\gamma R} + a_S^i \phi_\alpha \bar{u}_{iR}^\alpha \chi \\
 & + \lambda_V^{ij} \epsilon^{\alpha\beta\gamma} X_{\mu,\alpha} \bar{d}_{i\beta L}^c \gamma^\mu d_{j\gamma R} + a_V^i X_{\mu,\alpha} \bar{u}_{iL}^\alpha \gamma^\mu \chi \\
 & + h.c., \tag{6.1}
 \end{aligned}$$

where there is a summation over the generation indices $i, j = 1, 2, 3$, and $SU(3)_C$ gauge indices $\alpha, \beta, \gamma = 1, 2, 3$. The superscript c denotes charge conjugation. The neutral fermion χ is a singlet under the SM gauge group and manifests as missing energy at colliders. The scalar field ϕ is color triplet and $SU(2)_L$ singlet resonance. The vector field X_μ is color triplet and $SU(2)_L$ doublet resonance. They can appear in some models, which obtain their masses at high energy scales. This Lagrangian could further be generalized, such as shown in Ref. [11], although it may not be gauge invariant any more. One can also add the interaction involving left-handed quarks, such as $\phi' \bar{q}_L^c q_L$ with ϕ' $SU(2)_L$ triplet [16] and $\varphi \bar{q}_L \chi$ with φ $SU(2)_L$ doublet [16, 17]. The free parameters in Eq. (6.1) are masses of the resonances and missing particle, i.e., m_ϕ, m_X and m_χ , and couplings $\lambda_{S,V}^{ij}$ and $a_{S,V}^i$, which should be constrained by

current precise data, and will be investigated carefully in this paper. Here, we only consider the case of scalar resonance field ϕ , and the case of vector resonance field X_μ will be studied elsewhere.

The scenario of monotop production has been explored in Ref. [11], where they only consider the mode of top hadronic decay. In the case of resonant monotop production, they assume the branching fraction of $\phi \rightarrow t\chi$ equal to one and neglect the decay channel of $\phi \rightarrow \bar{d}\bar{s}$, which would lead to an overestimation of the signal. In our study, we will take into account all decay channels of the resonance, which turns out to be very important for estimating the sensitivity to detect the signal at the LHC. Moreover, we also discuss the mode of semileptonic decay of top quark in addition to the hadronic decay mode. Although the cross section of the backgrounds for semileptonic decay mode are very large, the discovery of the signal in this mode is still possible once appropriate cuts are imposed.

This chapter is organized as follows. In Sect. 6.2, we consider the constraints on the model parameters from experiments such as $K^0 - \bar{K}^0$ mixing, Z hadronic decay branching ratio and dijet productions at the LHC. In Sect. 6.3, we investigate the signal and backgrounds of monotop production in detail and then analyze the discovery potential at the early LHC. Conclusions and comments are given in Sect. 6.4.

6.2 Experiment Constraints

To describe the signal of monotop, we propose the Lagrangian in Eq. (6.1). The model parameters include the couplings of the interaction vertices as well as the masses of the new particles. It is important to know the parameter regions which are allowed to make predictions. We consider the constraints from experiments that are related to the Lagrangian in Eq. (6.1). First of all, we notice that some constraints have been obtained on the stop production and decay in R -parity violating SUSY so far, the signal of which is similar to the monotop. For example, the H1 [18] and ZEUS [19] collaborations at HERA have studied the stop resonant production by electron-quark fusion $e^+d \rightarrow \tilde{t}$, followed either by a direct R -parity violating decay or by the gauge decay to $b\tilde{\chi}_1^+$. The stop pair production and decay into dielectron plus dijet at the Tevatron has also been discussed [20]. However, these results can not be converted to constraints on the parameters in our case because they contain interactions with leptons. We are going to discuss the more relevant experiments including $K^0 - \bar{K}^0$ mixing, Z hadronic decay branching ratio and dijet production at the LHC.

6.2.1 $K^0 - \bar{K}^0$ Mixing

The neutral kaon K^0 is a meson consisting of a down quark and a strange antiquark. Its antiparticle \bar{K}^0 , containing a down antiquark and a strange quark, is also neutral. They are copiously produced via strong interaction in the same way. When propagating

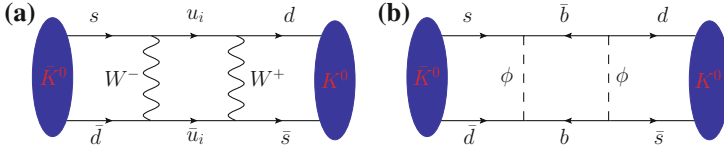


Fig. 6.2 Sample Feynman diagrams for $K^0 - \bar{K}^0$ mixing. **a** is the contribution from the SM. **b** is induced by the new particle ϕ

in space, they would transform into each other because of the weak interaction, as shown in Fig. 6.2a. As a result, they are not the mass eigenstates, which are denoted by K_1 and K_2 . K_1 is the difference of the two neutral kaons $K_1 = (K^0 - \bar{K}^0)/\sqrt{2}$ and has a quantum number of $CP = +1$. In contrast, $K_2 = (K^0 + \bar{K}^0)/\sqrt{2}$ and has $CP = -1$. Depending on their lifetime under decays via weak interactions, there are also two weak eigenstates, called the K_S and K_L . If CP is conserved, then $K_S = K_1$ and $K_L = K_2$, and thus they would have different masses. However, the difference is rather small because it arises from weak interaction. If CP is violated slightly, then there would be a small portion of K_2 in K_S , and K_1 in K_L .

The $K^0 - \bar{K}^0$ mixing is the reason of the mass difference between K_S and K_L , which has been measured very precisely. Therefore, it is a sensitive probe of new physics beyond the SM. The typical Feynman diagram for $K^0 - \bar{K}^0$ mixing is shown in Fig. 6.2.

The SM contribution to the $K_L - K_S$ mass difference Δm_K is given by [21]

$$\Delta m_K^{SM} = 2\text{Re}\langle K^0 | \mathcal{H}_{SM}^{\Delta S=2} | \bar{K}^0 \rangle = 2C_1 \text{Re}\langle K^0 | Q_1 | \bar{K}^0 \rangle, \quad (6.2)$$

where Q_1 is the operator $\bar{d}_L^\alpha \gamma^\mu s_L^\alpha \bar{d}_L^\beta \gamma^\mu s_L^\beta$, and C_1 is its Wilson coefficient. The matrix element $\langle K^0 | Q_1 | \bar{K}^0 \rangle$ can be parameterized as

$$\langle K^0 | Q_1 | \bar{K}^0 \rangle = \frac{1}{3} m_K f_K^2 B_K(\mu) \quad (6.3)$$

where m_K is the mass of K^0 (497.6 MeV), f_K is kaon decay constant (160 MeV), and $B_K(\mu)$ is related to the renormalization group invariant parameter \hat{B}_K by

$$\hat{B}_K = B_K(\mu) b(\mu). \quad (6.4)$$

where

$$b(\mu) = (\alpha_s(\mu))^{-2/9} \left(1 + \frac{307}{162} \frac{\alpha_s(\mu)}{4\pi} \right) \quad (6.5)$$

contains the renormalization scale dependence [22]. In our numerical analysis we will use the following result [23]:

$$\hat{B}_K = 0.75 \pm 0.15. \quad (6.6)$$

And finally, the SM contribution is

$$\Delta m_K^{SM} = \frac{G_F^2}{6\pi^2} f_{\tilde{K}}^2 \hat{B}_K m_K M_W^2 \text{Re}[\lambda_c^{*2} \eta_1 S_0(x_c) + \lambda_t^{*2} \eta_2 S_0(x_t) + 2\lambda_c^* \lambda_t^* \eta_3 S_0(x_c, x_t)] \quad (6.7)$$

where $\lambda_i = V_{is}^* V_{is}$, and V_{ij} are the CKM matrix elements. The functions S_0 are given by

$$\begin{aligned} S_0(x_t) &= \frac{4x_t - 11x_t^2 + x_t^3}{4(1-x_t)^2} - \frac{3x_t^3 \ln x_t}{2(1-x_t)^3}, \\ S_0(x_c) &= x_c, \\ S_0(x_c, x_t) &= x_c \left[\ln \frac{x_t}{x_c} - \frac{3x_t}{4(1-x_t)} - \frac{3x_t^2 \ln x_t}{4(1-x_t)^2} \right] \end{aligned} \quad (6.8)$$

with $x_i = m_i^2/M_W^2$. The next-to-leading values of η_i have been chosen according to Refs. [24–26]:

$$\eta_1 = 1.38 \pm 0.20, \quad \eta_2 = 0.57 \pm 0.01, \quad \eta_3 = 0.47 \pm 0.04. \quad (6.9)$$

The contribution from the new physics, illustrated in Fig. 6.2b, can be estimated by straightforward calculations. We obtain

$$\mathcal{H}_{eff}^{\Delta S=2} = \tilde{C}_1 \tilde{Q}_1, \quad (6.10)$$

where \tilde{Q}_1 is the operator $\bar{d}_R^\alpha \gamma^\mu s_R^\alpha \bar{d}_R^\beta \gamma^\mu s_R^\beta$, and \tilde{C}_1 is its Wilson coefficient,

$$\tilde{C}_1 = \frac{(\lambda_S^{13})^2 (\lambda_S^{23})^2}{2\pi^2} \left[\frac{m_\phi^4 - m_b^4 - 2m_b^2 m_\phi^2 \ln \frac{m_\phi^2}{m_b^2}}{(m_\phi^2 - m_b^2)^3} \right] b(\mu). \quad (6.11)$$

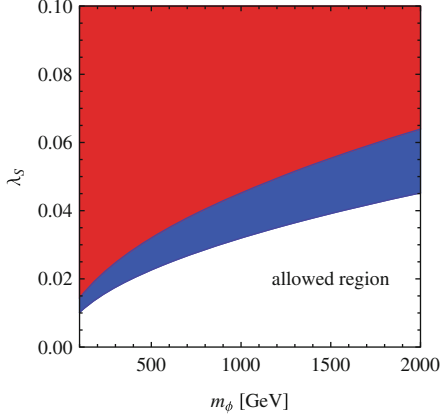
Our result is in agreement with those in Refs. [27, 28]. Then, the contribution to the $K_L - K_S$ mass difference is given by

$$\Delta m_K^{NP} = 2\text{Re}\langle K^0 | \mathcal{H}_{eff}^{\Delta S=2} | \bar{K}^0 \rangle = 2\tilde{C}_1 \text{Re}\langle K^0 | \tilde{Q}_1 | \bar{K}^0 \rangle. \quad (6.12)$$

The matrix element $\langle K^0 | \tilde{Q}_1 | \bar{K}^0 \rangle$ is the same as $\langle K^0 | Q_1 | \bar{K}^0 \rangle$ since the strong interaction preserve parity.

We require that the contribution to Δm_K , including both the SM and new physics result, is not larger than the experimental value $\Delta m_K^{\text{exp}} = (3.483 \pm 0.006) \times 10^{-15}$ GeV [29] within 1σ level, assuming the CPT conservation. In Fig. 6.3, we show the allowed region for λ_S as a function of m_ϕ for the cases of $\lambda_S^{13} = \lambda_S^{23} = \lambda_S$, $\lambda_S^{13}/2 = \lambda_S^{23} = \lambda_S$ and $\lambda_S^{13} = \lambda_S^{23}/2 = \lambda_S$. We can see that the constraint on λ_S is very stringent, generally less than 0.06 or 0.04 in different cases. We also notice that

Fig. 6.3 The allowed region of λ_S by $K^0 - \bar{K}^0$ mixing as a function of m_ϕ . The *red region* is excluded for $\lambda_S = \lambda_S^{13} = \lambda_S^{23}$ where the *blue region* is excluded for $\lambda_S = \lambda_S^{13} = \lambda_S^{23}/2$ or $\lambda_S = \lambda_S^{13}/2 = \lambda_S^{23}$



these couplings involves the third generation quarks, the parton distribution functions (PDFs) of which are small compared with those of the first two generations. Therefore, we choose $\lambda_S^{13} = \lambda_S^{23} = 0$ in the following discussion on the experiments at hadron colliders.

6.2.2 Z Hadronic Decay Branching Ratio

The tree-level amplitude of a Z boson decaying into a pair of quarks in the SM can be represented as

$$\mathcal{M} = g_Z \bar{q}(p_1) \gamma^\mu (a_L^q P_L + a_R^q P_R) q(p_2) \epsilon_\mu, \quad (6.13)$$

with

$$g_Z = \frac{e}{s_W c_W}, \quad (6.14)$$

$$a_L^q = T_q^3 - Q_q s_W^2, \quad (6.15)$$

$$a_R^q = -Q_q s_W^2. \quad (6.16)$$

Here, $s_W \equiv \sin \theta_W$ and $c_W \equiv \cos \theta_W$. T_q^3 and Q_q denote the $SU(2)_L$ and charge quantum numbers, respectively. P_L and P_R are the projection operators for the left- and right-handed components, respectively.

The interactions in Eq. (6.1) may affect the hadronic decay of the Z boson, as shown in Fig. 6.4, and thus contribute to the branching fraction of Z boson hadronic decay. This variable has been very precisely measured experimentally, and impose constraints on R-parity violating SUSY parameters [30]. Notice that the quarks in the interaction are right-handed, so only the couplings of right-handed quarks with

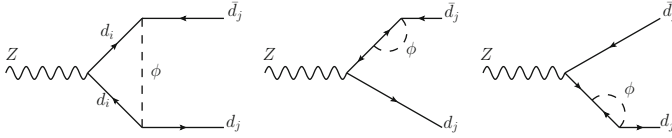


Fig. 6.4 Feynman diagrams for hadronic Z boson decay induced by the particle ϕ

Z boson are modified if all the quarks are taken to be massless. After calculating the Feynman diagrams in Fig. 6.4, we find that the coefficient a_R^q is adjusted by multiplying a factor

$$\xi = 1 + \Delta_f = 1 + \frac{\lambda_f^2}{8\pi^2} g(a), \quad (6.17)$$

where $a = M_Z^2/m_\phi^2$ and $f = 1, 2, 3$ corresponds to the decay of the Z boson into $d\bar{d}$, $s\bar{s}$ and $b\bar{b}$ final state, respectively. λ_f is related to the interaction couplings as

$$\lambda_1^2 = 4[(\lambda_S^{12})^2 + (\lambda_S^{13})^2], \quad (6.18)$$

$$\lambda_2^2 = 4[(\lambda_S^{12})^2 + (\lambda_S^{23})^2], \quad (6.19)$$

$$\lambda_3^2 = 4[(\lambda_S^{13})^2 + (\lambda_S^{23})^2], \quad (6.20)$$

where we have used the relation that $\lambda_S^{ij} = -\lambda_S^{ji}$ due to the antisymmetry property of the $\epsilon^{\alpha\beta\gamma}$ couplings in Eq. (6.1). The explicit expression of the function $g(a)$ reads

$$g(a) = \frac{(a-4)a - 2\ln(a)((a-2)a + 2\ln(a+1)) - 4\text{Li}_2(-a)}{4a^2}. \quad (6.21)$$

This function is positive as long as $m_\phi > 75$ GeV. The ultraviolet poles of the triangle and self-energy diagrams in Fig. 6.4 cancel with each other, and we finally obtain a finite result. In this calculation, all the masses of quarks have been neglected since they are too small compared with the Z boson mass. The result in Eq. (6.21) seems singular in the limit $a \rightarrow 0$ because of the a^2 denominator. However, expanding the result around $a = 0$, we get the approximate form

$$g(a) = \left(\frac{1}{9} - \frac{\ln(a)}{3}\right)a + \left(\frac{\ln(a)}{4} - \frac{1}{16}\right)a^2 + \left(\frac{1}{25} - \frac{\ln(a)}{5}\right)a^3 + O(a^4), \quad (6.22)$$

which vanishes obviously in the limit $a \rightarrow 0$. This result reflects the decoupling property of the heavy virtual particle ϕ in the large m_ϕ limit.

The change of coefficient a_R^q affects two experimental observables. One is $R_l \equiv \Gamma_h/\Gamma_l$, where Γ_h and Γ_l are the widths of Z boson decaying into hadrons and leptons, respectively. The correction to R_l is given by

$$\begin{aligned}\delta R_l &= \frac{\Gamma_h - \Gamma_h^{SM}}{\Gamma_l^{SM}} \\ &= \frac{2(\Delta_1 \Gamma_{dR}^{SM} + \Delta_2 \Gamma_{sR}^{SM} + \Delta_3 \Gamma_{bR}^{SM})}{\Gamma_l^{SM}},\end{aligned}\quad (6.23)$$

where Γ_{qR}^{SM} , $q = d, s, b$ denote the widths of Z boson decaying into only right-handed q quarks in the SM. The other is $R_b \equiv \Gamma_b / \Gamma_h$ with Γ_b the width into $b\bar{b}$. Explicitly, we can write the corrected R_b as

$$\begin{aligned}R_b &= \frac{\Gamma_b}{\Gamma_h} \\ &= \frac{1 + 2\Delta_3 \frac{\Gamma_{bR}^{SM}}{\Gamma_b^{SM}}}{1 + 2\Delta_1 \frac{\Gamma_{dR}^{SM}}{\Gamma_h^{SM}} + 2\Delta_2 \frac{\Gamma_{sR}^{SM}}{\Gamma_h^{SM}} + 2\Delta_3 \frac{\Gamma_{bR}^{SM}}{\Gamma_h^{SM}}} \frac{\Gamma_b^{SM}}{\Gamma_h^{SM}}.\end{aligned}\quad (6.24)$$

Thus, the correction to R_b is given by

$$\delta R_b \approx 2 \left[\Delta_3 \frac{\Gamma_{bR}^{SM}}{\Gamma_b^{SM}} \left(1 - \frac{\Gamma_b^{SM}}{\Gamma_h^{SM}} \right) - \Delta_1 \frac{\Gamma_{dR}^{SM}}{\Gamma_d^{SM}} \frac{\Gamma_d^{SM}}{\Gamma_h^{SM}} - \Delta_2 \frac{\Gamma_{sR}^{SM}}{\Gamma_s^{SM}} \frac{\Gamma_s^{SM}}{\Gamma_h^{SM}} \right] R_b^{SM}. \quad (6.25)$$

These experimental observables are measured to be $R_e = 20.804 \pm 0.050$, $R_\mu = 20.785 \pm 0.033$, $R_\tau = 20.764 \pm 0.045$ and $R_b = 0.2163 \pm 0.0007$, respectively, while the corresponding SM values are $R_e^{SM} = R_\mu^{SM} = 20.735$, $R_\tau^{SM} = 20.780$ and $R_b^{SM} = 0.2158$ [29]. The requirement that the corrected $R_{e,\mu,\tau,b}$ agree with the measured values in the 1σ range imposes constraints on the parameters

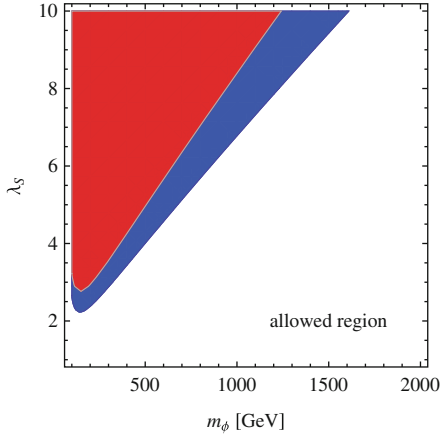
$$(\lambda_1^2 + \lambda_2^2 + \lambda_3^2) \frac{g(a)}{4\pi^2} < 0.829, 0.578, 0.202 \quad \text{for } R_e, R_\mu, R_\tau, \text{ respectively,} \quad (6.26)$$

and

$$-0.0289 < [0.78\lambda_3^2 - 0.22(\lambda_1^2 + \lambda_2^2)] \frac{g(a)}{4\pi^2} < 0.173 \quad \text{for } R_b. \quad (6.27)$$

In order to illustrate these constraints in more obvious way, we choose the couplings as $\lambda_S^{12} = \lambda_S$, $\lambda_S^{13} = \lambda_S^{23} = 0$ since $\lambda_S^{13,23}$ are constrained by the neutral kaon mixing, and show the allowed region by the constraints from R_τ and R_b in Fig. 6.5. We see that the variable R_b imposes more stringent constraint than R_τ . However, this constraint on the parameter is very weak. This is due to the fact that only right-handed couplings of the Z boson are affected, and the widths of the Z boson decaying into right-handed quarks are much less than into left-handed quarks.

Fig. 6.5 The allowed region by Z boson hadronic decay branching fraction. The *blue* and *red regions* are excluded by the limits from R_b and R_τ respectively. We have chosen $\lambda_S^{12} = \lambda_S$, $\lambda_S^{13} = \lambda_S^{23} = 0$



6.2.3 Dijet Production at the LHC

The process of dijet production is the most dominant process at the LHC. New resonances, such as excited quarks, axigluons, Randall–Sundrum gravitons, diquarks and string resonances that are predicted in many extensions of the SM, would decay into dijet and manifest themselves in the dijet invariant mass distribution. It is of high priority to probe the new resonance at the LHC. The events of dijet production have been analyzed at the early stage [31–35] or the complete Run-I stage [36, 37]. The negative discovery of any new resonance has set upper limits on the product of cross section (σ_{jj}) and signal acceptance (\mathcal{A}). Since the new particle ϕ would induce the dijet production, as illustrated in Fig. 6.6, the parameters in the effective Lagrange in Eq. (6.1) are necessarily constrained by the limits.

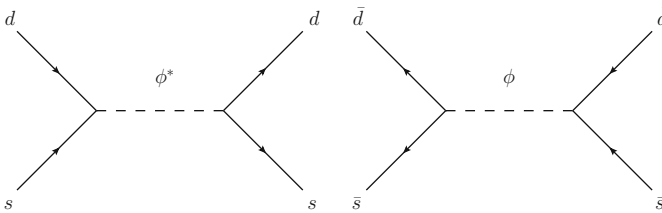


Fig. 6.6 Feynman diagrams for the dijet production at the LHC

The cross section of the resonance ϕ production and decay depends on the total width of ϕ , which is given by

$$\Gamma_\phi = \Gamma_{\phi \rightarrow d\bar{s}} + \Gamma_{\phi \rightarrow u_i \bar{\chi}}, \quad (6.28)$$

where

$$\begin{aligned} \Gamma_{\phi \rightarrow d\bar{s}} &= \frac{(\lambda_S^{12})^2}{2\pi} m_\phi, \\ \Gamma_{\phi \rightarrow u_i \bar{\chi}} &= \frac{|a_S^i|^2}{16\pi m_\phi^3} (m_\phi^2 - m_{u_i}^2 - m_\chi^2) \lambda^{1/2}(m_\phi^2, m_{u_i}^2, m_\chi^2) \end{aligned} \quad (6.29)$$

with

$$\lambda(a, b, c) = a^2 + b^2 + c^2 - 2ab - 2bc - 2ca. \quad (6.30)$$

The effect of these widths is included in our numerical calculation below. Since the width of ϕ is very small compared to its mass, we do not consider the interference between the diagrams in Fig. 6.6 and those in the SM. We use MadGraph5v1.3.3 [38] to calculate the cross section with the effective Lagrangian implemented by FeynRules [39]. For comparison with the experiments at the LHC, we have calculated the dijet production at both the 7 and 8 TeV collisions. The CTEQ6L1 PDF set [40] is chosen and the factorization (renormalization) scales are set at m_ϕ . We fixed the couplings at $\lambda_S^{12} = a_S^3 = 0.2$, $a_S^1 = a_S^2 = 0$ and the mass $m_\chi = 50$ GeV. The mass of ϕ is changed from 500 to 2500 GeV with a step of 100 GeV. We choose the same kinematic cuts as in the experiments [31, 34]:

$$|\eta_j| < 2.5, \quad |\eta_{j_1} - \eta_{j_2}| < 1.3. \quad (6.31)$$

The cross sections of the dijet signal after the cuts are listed in Table 6.1.

It is required that theoretical prediction of the dijet production $\sigma_{jj} \cdot \mathcal{A}$ is not larger than the observed 95 % C.L. upper limit in the dijet experiment [31, 34, 36]. Therefore, the parameter regions of $\lambda_S (= \lambda_S^{12})$ as a function of m_ϕ are constrained, as shown in Fig. 6.7. We have chosen the acceptance $\mathcal{A} = 0.6$ as in Ref. [34]. The bump of the curve in the region of $500 \text{ GeV} < m_\phi < 1000 \text{ GeV}$ is due to the fact that we use the data in this region and the other regions corresponding to different integrated luminosities collected by the CMS experiment at the LHC. We see that the upper limit on λ_S is about 0.2 for $1200 \text{ GeV} < m_\phi < 1500 \text{ GeV}$, and larger than 0.2 in other regions.

Table 6.1 The cross sections of dijet production induced by the resonance of ϕ , assuming $\lambda_S^{12} = a_S^3 = 0.2, a_S^1 = a_S^2 = 0$

m_ϕ (GeV)	σ_{jj} (pb)	Upper limit (pb)
500	16.2	118
600	7.13	182
700	3.52	90.7
800	1.84	70.8
900	0.998	52.7
1000	0.566	1.098
1100	0.322	0.777
1200	0.320	0.23
1300	0.201	0.18
1400	0.129	0.1
1500	8.43×10^{-2}	0.06
1600	5.57×10^{-2}	0.074
1700	3.64×10^{-2}	0.13
1800	2.41×10^{-2}	0.14
1900	1.64×10^{-2}	0.1
2000	1.11×10^{-2}	0.06
2100	7.45×10^{-3}	0.035
2200	4.98×10^{-3}	0.026
2300	3.37×10^{-3}	0.025
2400	2.33×10^{-3}	0.023
2500	1.60×10^{-3}	0.02

Also shown is the upper limits at the 95 % CL on $\sigma_{jj} \cdot \mathcal{A}$. The limits for $m_\phi < 1200$ GeV are taken from Refs. [31, 34] at the 7 TeV LHC while the others are from Ref. [36] at the 8 TeV LHC

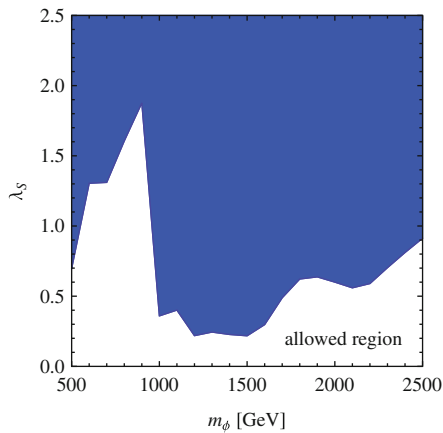


Fig. 6.7 The allowed region of $\lambda_S (= \lambda_S^{12})$ by dijet experiments at the LHC as a function of m_ϕ

6.3 Signals and Backgrounds

The signals of the monotop production have different final states depending on the decay mode of the top quark. If the top quark decays hadronically, then the signal is

$$pp \rightarrow t + \bar{\chi} \rightarrow b + W^+ + \bar{\chi} \rightarrow b + j + j + \cancel{E}_T, \quad (6.32)$$

called the hadronic mode. While the top quark decays semileptonically, the signal is

$$pp \rightarrow t + \bar{\chi} \rightarrow b + W^+ + \bar{\chi} \rightarrow b + \bar{l} + \cancel{E}_T, \quad (6.33)$$

called the semileptonic mode. The Feynman diagrams are both shown in Fig. 6.8. The symbol b and j denote a b -tagged jet and light quark or gluon jet, respectively, and l represents the first two generation charged leptons, i.e., e and μ . The two modes have different final states, and thus different backgrounds in the SM. We would discuss them separately in the following part. The hadronic mode has been studied in Ref. [11] where the branching fraction $R(\phi \rightarrow t\bar{\chi})$ is assumed to be equal to one. In fact, this assumption is over optimistic. From Eq. (6.29) we can get the branching fraction $R(\phi \rightarrow t\bar{\chi})$,

$$R(\phi \rightarrow t\bar{\chi}) = \frac{\Gamma_{\phi \rightarrow t\bar{\chi}}}{\Gamma_{\phi \rightarrow t\bar{\chi}} + \Gamma_{\phi \rightarrow \bar{d}s}} = \frac{1}{1+z}, \quad (6.34)$$

with

$$z = \frac{8(\lambda_S^{12})^2}{|a_S^3|^2} \frac{m_\phi^4}{(m_\phi^2 - m_t^2 - m_\chi^2)\lambda^{1/2}(m_\phi^2, m_t^2, m_\chi^2)}. \quad (6.35)$$

In the case of $\lambda_S^{12} = a_S^3 = 0.2$, $m_t = 173.1$ GeV, $m_\phi = 500$ GeV and $m_\chi = 50$ GeV, we obtain $\Gamma_{\phi \rightarrow t\bar{\chi}} = 0.300$ GeV, $\Gamma_{\phi \rightarrow \bar{d}s} = 3.183$ GeV, and thus the branching fraction of $\phi \rightarrow t\bar{\chi}$ is just about 0.1. Here we have neglected the decay widths $\Gamma_{\phi \rightarrow u\bar{\chi}}$ and $\Gamma_{\phi \rightarrow c\bar{\chi}}$ because they depend on different parameters. If they are taken into account,

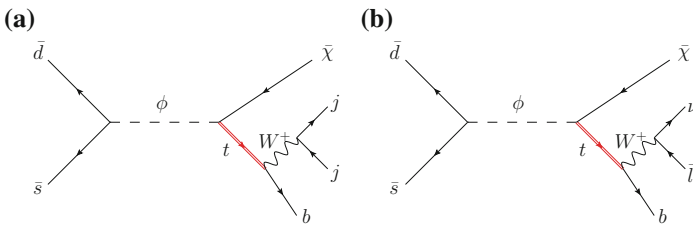


Fig. 6.8 Feynman diagrams for the monotop production at the LHC. **a** is the hadronic decay mode while, **b** is the semileptonic decay mode

then the branching fraction of $\phi \rightarrow t\bar{\chi}$ would be even smaller. Therefore, we include the effects of both ϕ decay channels in our discussion.

Before discussing the signal and backgrounds in detail, we first have to choose the parameter m_χ . Some implications can be obtained from the search for the lightest neutralino. In SUSY without the assumption of gaugino mass unification, there is no general constraints on the mass of the lightest neutralino at e^+e^- colliders [29]. The indirect constraints from the experiments such as $(g-2)_\mu, b \rightarrow s\gamma$ and $B \rightarrow \mu^+\mu^-$ indicate that the lightest neutralino mass may be as low as about 6 GeV [41]. In our calculation, we choose the default value $m_\chi = 50$ GeV and vary m_χ in the range 5–100 GeV when discussing the discovery significance.

As mentioned in the introduction of this chapter, the particle χ can be taken as missing energy at hadron colliders. This is not guaranteed by a new quantum number of χ , for example -1 under a Z_2 symmetry, since we do not consider χ as a dark matter candidate. Instead, it is caused by the small width of χ . Actually, χ is not stable and can decay into SM particles, as shown in Fig. 6.9. We show the calculation of the width in the decay channel

$$\chi(p_1) \rightarrow d(p_2)s(p_3)b(p_4)\nu(p_5)l^+(p_6). \quad (6.36)$$

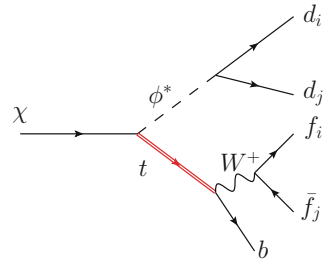
The decay width of χ is estimated by

$$\Gamma_\chi = \frac{1}{2m_\chi} \int |\overline{\mathcal{M}}|^2 d\Gamma_5, \quad (6.37)$$

where $|\overline{\mathcal{M}}|^2$ is the matrix element squared for the decay process with the initial- and final-state spins and colors averaged and summed. When the masses of all the final-state particles are neglected, the five-body phase space integration can be written as

$$\int d\Gamma_5 = \frac{1}{32768\pi^7} \frac{1}{m_\chi^2} \int_0^{m_\chi^2} ds_{23} \int_0^{(m_\chi - \sqrt{s_{23}})^2} ds_{456} \int_0^{s_{456}} ds_{45} \lambda^{1/2}(m_\chi^2, s_{23}, s_{456}) \left(1 - \frac{s_{45}}{s_{456}}\right), \quad (6.38)$$

Fig. 6.9 Feynman diagram for χ decay



with $s_{ij} = (p_i + p_j)^2$ and $s_{ijk} = (p_i + p_j + p_k)^2$. In the mass range of χ we are interested in, the momenta of the decay products of the W boson are too small compared with the mass of the W boson so that we neglect them in the matrix element. Moreover, we assume that the charged lepton l^+ carries about one-fifth of the energy of χ on average. Then, the matrix element squared is simply given by

$$|\overline{\mathcal{M}}|^2 \approx \frac{96}{5} g_W^4 (\lambda_S^{12})^2 (a_S^3)^2 \frac{m_\chi^2}{m_\phi^4 m_t^2 M_W^4} s_{23} s_{45}. \quad (6.39)$$

where g_W is the coupling of the W boson with left-handed fermions. Now performing the integration in Eq. (6.37), we obtain

$$\Gamma_\chi \approx 1.82 \times 10^{-19} \text{GeV} \left(\frac{\lambda_S^{12}}{0.2} \right)^2 \left(\frac{a_S^3}{0.2} \right)^2 \frac{(m_\chi/50\text{GeV})^{11}}{(m_\phi/500\text{GeV})^4 (m_t/173.1\text{GeV})^2 (M_W/80.4\text{GeV})^4}, \quad (6.40)$$

where we have included the contribution from the other decay channels.

The ATLAS collaboration has searched for displaced vertices arising from decays of new heavy particles and found that the efficiency for detecting displaced vertices almost vanishes for a distance between the primary and the displaced vertex larger than 0.35 m [43]. The produced $\tilde{\chi}$ at hadron colliders, as a decay product of a massive particle, usually has such a large energy that it moves nearly in the speed of light. The decay width can be translated to the the distance traveled before its decay, as shown in Fig. 6.10. We can see that the distance sensitively depends on the mass

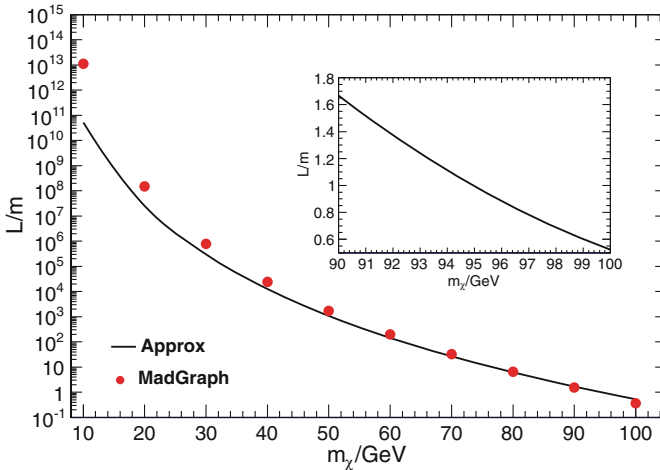


Fig. 6.10 The distance traveled by the particle $\tilde{\chi}$ before its decay as a function of its mass [42]. The solid line is obtained from Eq. (6.40) while the dots denote the results of MadGraph. The relevant parameters are chosen as $\lambda_S^{12} = a_S^3 = 0.2$, $m_t = 173.1$ GeV, $M_W = 80.4$ GeV, and $m_\phi = 500$ GeV

of χ and decreases with the increasing of m_χ . We also calculate the decay width numerically by the MadGraph in some parameter points. The results of MadGraph are well approximated by those obtained from Eq. (6.40) in the large m_χ region. In the low mass region, there are obvious difference since the mass of final-state particle in Eq. (6.40) can not be neglected. But this discrepancy between them in the low mass region is not important because they are both much larger than the size of the detector at the LHC. In the region $m_\chi \leq 100$ GeV, the distance traveled by $\bar{\chi}$ before its decay is larger than 0.35 m. Therefore, it is reasonable to consider the particle χ with $m_\chi \leq 100$ GeV as missing energy at the LHC.

6.3.1 Hadronic Decay Mode

In the hadronic decay mode, the signal consists of a b -jet, two light jets and missing energy. The main backgrounds arise from $pp \rightarrow jjjZ(\rightarrow \nu\bar{\nu})$, with a jet misidentified as a b -jet, and $pp \rightarrow b\bar{b}jZ(\rightarrow \nu\bar{\nu})$ with a b -jet not tagged. The $pp \rightarrow t\bar{t}$ and $pp \rightarrow t(\bar{t})j$ processes with hadronic top quark decay may also contribute to the backgrounds if some jets are not detected. The signal and backgrounds are simulated by MadGraph5v1.3.3 [38] and ALPGEN [44] interfaced with PYTHIA [45, 46] to perform the parton shower and hadronization.

In the following numerical calculation, the default values of relevant parameters are chosen as $\lambda_S^{12} = a_S^3 = 0.2$, $\lambda_S^{13} = \lambda_S^{23} = 0$, $a_S^1 = a_S^2 = 0$, $m_t = 173.1$ GeV, $m_\phi = 500$ GeV and $m_\chi = 50$ GeV. The CTEQ6L1 PDF [40] is used, and the renormalization and factorization scales are set at m_ϕ . We apply the following basic selection cuts

$$p_T^{b,j} > 30 \text{ GeV}, \quad |\eta^{b,j}| < 2.4, \quad \Delta R_{bb,bi,jj} > 0.5. \quad (6.41)$$

Moreover, we choose a b -tagging efficiency of 50% while the misidentification rates for a light jet faking a b -jet are 8% for charm quark and 0.2% for gluon and other light quarks [47].

To determine the missing transverse energy cut, we investigate the normalized spectrum of the missing transverse energy for the signal and backgrounds [42]. Because the missing transverse energy of the background comes from either an invisible decayed Z boson or non-detected jets, which are produced mainly via t -channel, the backgrounds concentrate in the region $E_T < 100$ GeV. In contrast, the missing transverse energy of the signal originates from the decay of a heavy resonance so that it can be large. Therefore we choose the missing transverse energy cut

$$E_T > 100 \text{ GeV}. \quad (6.42)$$

Meanwhile, the missing transverse energy of the signal is similar to the distribution $E_T/\sqrt{E_T^{\max 2} - E_T^2}$ with an edge at $E_T^{\max} = \lambda^{1/2}(m_\phi^2, m_t^2, m_\chi^2)/2m_\phi$ due to the heavy

resonance mass. This feature may help to specify the masses of the resonance and the missing particle.

In this mode, the momentum of three jets, and therefore momentum of the W boson and top quark, can be reconstructed, which leads to efficient event selection. We also study the reconstructed top quark mass distribution for the signal and backgrounds processes using the three leading jets [42]. We do not consider all the combinations of three jets in the final state to reconstruct the top quark. This kind of reconstruction can efficiently suppress the $t\bar{t}$ and $t(\bar{t})j$ backgrounds. We find that there is a peak around 173 GeV for the signal while the distributions of backgrounds have no obvious bumps. So we impose the invariant mass cut

$$120 \text{ GeV} < m_{t,r} < 200 \text{ GeV}. \quad (6.43)$$

The cross sections of the signal and backgrounds after a series of cuts at the LHC ($\sqrt{s} = 7 \text{ TeV}$) are listed in Table 6.2. It can be seen that the backgrounds decrease dramatically when the invariant mass cuts are imposed, The $t\bar{t}$ and $t(\bar{t})j$ processes are mainly suppressed by the missing transverse energy cut. We also notice that the cross section of $b\bar{b}jZ(\nu\bar{\nu})$ is not less than that of $jjjZ(\nu\bar{\nu})$ after all cuts imposed.

We also estimate the signal after all the above cuts as a function of the parameters m_χ and m_ϕ in Fig. 6.11. The cross section is not sensitive to m_χ , but decreases very fast with the increasing of m_ϕ .

We present the parameter region for a discovery of the monotop signal in Fig. 6.12. The coupling $\lambda_S^{12} = a_S^3 = \lambda_S$ needs to be larger than 0.06 and 0.034 at $m_\phi = 500 \text{ GeV}$ in order to discover the signal at 5σ level at the LHC with the integrated luminosity of 1 fb^{-1} and 10 fb^{-1} , respectively. And it increases vary fast as m_ϕ increases. The needed λ_S with 10 fb^{-1} data is larger than 1 if $m_\phi > 1500 \text{ GeV}$. We also show the parameter regions for a discovery at the 3σ level. These regions can be compared with the constraint imposed by the dijet experiment. We see that the regions at $m_\phi > 1200 \text{ GeV}$ have been excluded by the dijet experiment, while regions at $m_\phi < 1200 \text{ GeV}$ are still allowed. However, we notice that $\lambda_S = \lambda_S^{12}$ in the dijet constraint. If a larger value of a_S^3 is chosen, then there would be more parameter regions allowed by the dijet experiment.

Table 6.2 The cross sections of the signal and backgrounds after various cuts in the hadronic mode at the LHC ($\sqrt{s} = 7 \text{ TeV}$) [42]

σ (fb)	Basic	E_T	$m_{t,r}$	b-tagging	ϵ_{cut}
Signal	902	811	502	251	27.1 %
$jjjZ(\nu\bar{\nu})$	7.03×10^4	7.87×10^3	944	9.35	0.013 %
$b\bar{b}jZ(\nu\bar{\nu})$	1.70×10^3	143	19.4	9.67	0.57 %
$t\bar{t}$	2.80×10^4	34.6	0.28	0.14	5×10^{-6}
$t(\bar{t})j$	2.35×10^4	10.9	0.24	0.12	5×10^{-6}

The cut acceptance ϵ_{cut} is also listed. The entries after the $m_{t,r}$ cut for $t\bar{t}$ and $t(\bar{t})j$ processes are estimated by considering that one out of the total events we have generated for analysis can survive various kinematic cuts

Fig. 6.11 The cross section of the signal in the hadronic mode at the LHC ($\sqrt{s} = 7$ TeV) as a function of m_χ and m_ϕ . The black band consists of twenty *solid lines* from the bottom up corresponding to the value of m_χ varying from 5 to 100 GeV with a step of 5 GeV

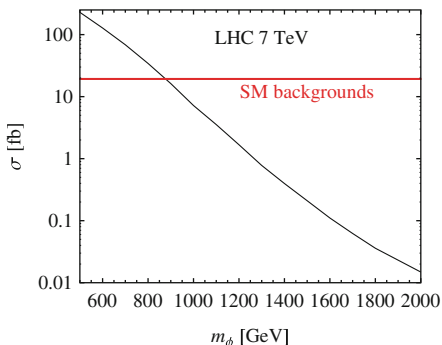
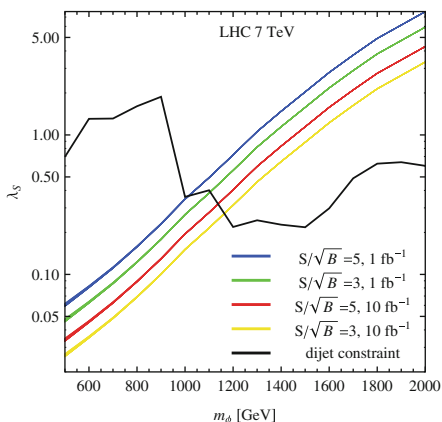


Fig. 6.12 The parameter region for a discovery of the monotop signal in the hadronic mode at the LHC ($\sqrt{s} = 7$ TeV). Each colorful band consists of twenty *solid lines* from the bottom up corresponding to the value of m_χ varying from 5 to 100 GeV with a step of 5 GeV. We have taken $\lambda_S = \lambda_S^{12} = a_S^3$



In this mode, the full kinematic information of the top quark can be reconstructed from its decay products, so the mass of the resonance ϕ can be obtained by

$$m_\phi = \sqrt{\vec{p}_t^2 + m_\chi^2} + \sqrt{\vec{p}_t^2 + m_t^2} \quad (6.44)$$

$$\approx \sqrt{\vec{p}_t^2} + \sqrt{\vec{p}_t^2 + m_t^2} \quad \text{if } m_\chi^2 \ll \vec{p}_t^2 \quad (6.45)$$

with

$$\vec{p}_t^2 = p_{t,x}^2 + p_{t,y}^2 + p_{t,z}^2, \quad (6.46)$$

in which $p_{t,x}$, $p_{t,y}$, $p_{t,z}$ are the three-vector momentum of the top quark. This information, combined with the missing transverse energy distribution, may help to specify the masses of the resonance and the missing particle.

6.3.2 Semileptonic Decay Mode

In the semileptonic decay mode, the signal is a b -jet, a charged lepton and missing energy. The dominant backgrounds include $pp \rightarrow W^+(\rightarrow l^+\nu)j$ with the jet misidentified as a b -jet and $pp \rightarrow tj$ with semileptonic top quark decay. The W^+j background is very large because there are only two final-state particles, compared with four final-state particles in the $pp \rightarrow jjjZ$ and $pp \rightarrow b\bar{b}jZ$ backgrounds in the hadronic mode. Besides, the final state of the signal contains two missing particles, i.e., $\tilde{\chi}$ and ν , which makes the reconstruction of the mass of the top quark very challenging. Nevertheless, the semileptonic mode is still promising if appropriate cuts are imposed. The signal and backgrounds are simulated by MadGraph5v1.3.3 [38] interfaced with PYTHIA [45]. We choose the same default parameters as in the hadronic mode, and the basic cuts are

$$p_T^b > 30 \text{ GeV}, \quad p_T^l > 20 \text{ GeV}, \quad |\eta^{b,l}| < 2.4, \quad \Delta R_{bl} > 0.5. \quad (6.47)$$

We investigate the normalized spectrum of the missing transverse energy in the semileptonic mode at the LHC with $\sqrt{s} = 7 \text{ TeV}$ [42]. The signal increases while the backgrounds decrease in the range $30 \text{ GeV} < E_T < 150 \text{ GeV}$. The reason is that the missing particles of the signal originate from a resonance of a large mass, and thus could be produced with large transverse momentum. In contrast, the missing particle of the backgrounds is ν , coming from the W boson. Meanwhile the W^+j and single top production are t -channel processes, in which the momentum of final-state particles tend to be collinear to those of the initial-state particles. Therefore, we impose the missing transverse energy cut

$$E_T > 120 \text{ GeV} \quad (6.48)$$

to suppress the backgrounds.

In the process containing a leptonic decayed W boson, the transverse mass is a useful variable, defined as [29]

$$M_T = \sqrt{(E_T + E_T^l)^2 - (\vec{p}_T + \vec{p}_T^l)^2}, \quad (6.49)$$

where E_T and \vec{p}_T are the missing transverse energy and missing transverse momentum, respectively. If the missing particle and the lepton are both decay products of a W boson, then the upper limit of the distribution of M_T is the W boson mass. This is just the case of the backgrounds here. However the signal contains additional missing particle so that M_T can be very large. Therefore, we impose the transverse mass cut

$$M_T > 120 \text{ GeV} \quad (6.50)$$

to suppress the backgrounds.

Table 6.3 The cross sections of the signal and backgrounds after various cuts in the semileptonic mode at the LHC ($\sqrt{s} = 7$ TeV) [42]

σ (fb)	Basic	p_T^l	E_T	M_T	b-tagging	ϵ_{cut}
Signal	399	376	231	218	109	27.3%
$W(l\nu)j$	1.83×10^6	1.53×10^6	3.45×10^4	1.83	0.003	2×10^{-9}
$t(\bar{t})j$	9.09×10^3	7.33×10^3	185	2.15	1.08	0.012%

The cut acceptance ϵ_{cut} is also listed. The entries after the M_T cut for $W(l\nu)j$ process are estimated by considering that one out of the total events we have generated for analysis can survive various kinematic cuts

The cross sections of the signal and backgrounds after a series of cuts at the LHC ($\sqrt{s} = 7$ TeV) are listed in Table 6.3. We find that the backgrounds nearly vanish after the transverse mass cut is imposed. This indicates that it is very promising to detect the signal of monotops in the semileptonic mode.

We also calculate the signal after all the above cuts as a function of the parameters m_χ and m_ϕ in Fig. 6.13. Same as in the hadronic mode, the cross section is not sensitive to m_χ , but decreases very fast with the increasing of m_ϕ . The cross point when the cross section of the signal is equal to that of the backgrounds is about 1350 GeV, higher than that in the hadronic mode. This implies that the discovery potential in the semileptonic mode would be better than in the hadronic mode.

We present the parameter region for a discovery of the monotop signal in Fig. 6.14. The coupling $\lambda_S^{12} = a_S^3 = \lambda_S$ needs to be larger than 0.043 and 0.024 at $m_\phi = 500$ GeV in order to discover the signal at 5σ level at the LHC with the integrated luminosity of 1 fb^{-1} and 10 fb^{-1} , respectively. And it increases vary fast as m_ϕ increases. The needed λ_S with 10 fb^{-1} data is larger than 0.4 if $m_\phi > 1500$ GeV. We also show the parameter regions for a discovery at the 3σ level. These regions can be compared with the constraint imposed by the dijet experiment. We see that the regions at $m_\phi > 1400$ GeV have been excluded by the dijet experiment while regions at $m_\phi < 1400$ GeV are still allowed. However, we notice that $\lambda_S = \lambda_S^{12}$ in the dijet constraint. If a larger value of a_S^3 is chosen, then there would be more parameter regions allowed by the dijet experiment.

Fig. 6.13 The cross section of the signal in the semileptonic mode at the LHC ($\sqrt{s} = 7$ TeV) as a function of m_χ and m_ϕ . The black band consists of twenty *solid lines* from the bottom up corresponding to the value of m_χ varying from 5 to 100 GeV with a step of 5 GeV

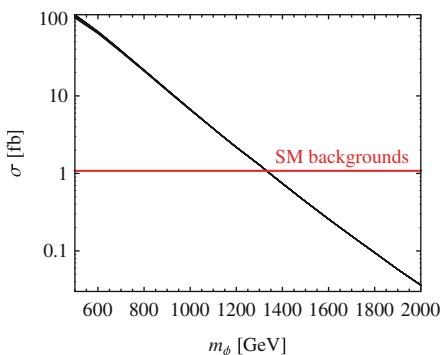
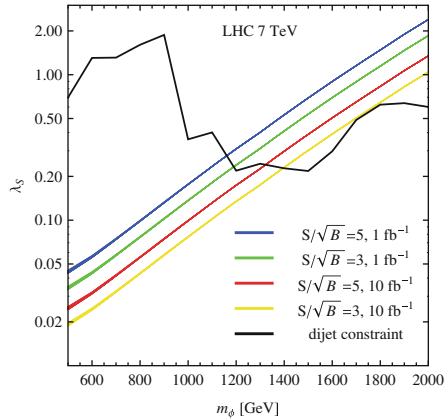


Fig. 6.14 The parameter region for a discovery of the monotop signal in the semileptonic mode at the LHC ($\sqrt{s} = 7$ TeV). Each colorful band consists of twenty *solid lines* from the bottom up corresponding to the value of m_χ varying from 5 to 100 GeV with a step of 5 GeV. We have taken $\lambda_S = \lambda_S^{12} = a_S^3$



6.4 Conclusions and Comments

The monotop signal is predicted in many extensions of the SM and has a feature easy to be discovered. In this chapter, we propose a gauge invariant Lagrangian to describe the production of monotop signal. And we study the allowed regions of the parameters in the Lagrangian by the present data of $K^0 - \bar{K}^0$ mixing, Z boson hadronic decay branching ratio and dijet production at the LHC. After that, we investigate the potential of the early LHC to discover the signal of monotop production in both the hadronic and semileptonic modes. We present the parameters that corresponds to a discovery at the 5σ or 3σ level with an integrated luminosity of 1 or 10 fb^{-1} . We also find that in the hadronic mode the information from the missing transverse energy and reconstructed resonance mass distributions can be used to specify the masses of the resonance and the missing particle. Moreover, from our estimation, the semileptonic mode is more promising to discover the signal. This signature has attracted the interest of the ATLAS collaboration and an analysis has been presented where a similar limit on the coupling to that predicted by us is set [48].

The analysis has just made use of the monotop production at the LHC. Actually, the mono-antitop production at the LHC is also interesting and should be investigated in detail. It has the same final state with monotop production in the hadronic decay mode, while the lepton in the semileptonic mode has a different sign. Moreover, it is expected the cross section of mono-antitop production is significantly larger than monotop production due to the enhancement of PDFs of initial-state quarks.

The pattern of the monotop production studied in this chapter is the resonant production mode. There are several other production modes that have been investigated so far. One of them is the top quark and a vector boson associated production via flavor-changing neutral interaction and the vector boson decays into invisible particles, as shown in Fig. 6.15. It is possible that this vector is just the Z boson in the SM. However, the flavor-changing neutral current Zqt ($q = u, c$) has been tightly constrained by the top quark decay at the LHC. The branching fraction of $t \rightarrow Zq$

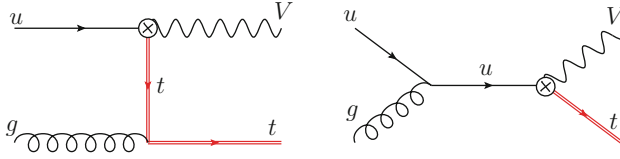


Fig. 6.15 Feynman diagrams for $gq \rightarrow tV$ production at the LHC

greater than 0.05 % has been excluded at a confidence level of 95 % [49]. The vector can also be a new particle in a hidden sector which is heavier than the top quark. Then the present constraint on the Zqt is not applicable, and the process of $gq \rightarrow tV$ may be detectable at the LHC. The relevant Lagrangian is given by

$$\mathcal{L}_{\text{FCNC}} = a_{\text{FCNC}} V_\mu \bar{q} \gamma^\mu (a_L P_L + a_R P_R) t + \text{h.c.}, \quad (6.51)$$

where P_L and P_R are the projector operators to select the left- and right-handed components of the quarks, respectively. The prospect to discover such a signal has been analyzed in Ref. [50]. Both the ATLAS and CMS collaborations have searched for the monotop signature induced by this FCNC interaction, and an upper limit on the coupling or a lower limit on the mass of the invisible particle have been set [48, 51].

References

1. E. Alvarez, L. Da Rold, J.I.S. Vietto, A. Szykman, Phenomenology of a light gluon resonance in top-physics at Tevatron and LHC. *JHEP* **1109**, 007 (2011). [arXiv:1107.1473](#)
2. U. Haisch, S. Westhoff, Massive Color-octet bosons: bounds on effects in top-quark pair production. *JHEP* **1108**, 088 (2011). [arXiv:1106.0529](#)
3. E.L. Berger, Q.-H. Cao, C.-R. Chen, H. Zhang, Top quark polarization as a probe of models with extra gauge bosons. *Phys. Rev. D* **83**, 114026 (2011). [arXiv:1103.3274](#)
4. J. Cao, L. Wu, J.M. Yang, New physics effects on top quark spin correlation and polarization at the LHC: a comparative study in different models. *Phys. Rev. D* **83**, 034024 (2011). [arXiv:1011.5564](#)
5. C. Degrande, J.-M. Gerard, C. Grojean, F. Maltoni, G. Servant, Non-resonant new physics in top pair production at hadron colliders. *JHEP* **03**, 125 (2011). [arXiv:1010.6304](#)
6. M. Battaglia, G. Servant, Four-top production and $t\bar{t}$ + missing energy events at multi TeV e^+e^- colliders. *Nuovo Cim.* **co33N2**, 203–208 (2011). [arXiv:1005.4632](#)
7. Q.-H. Cao, D. McKeen, J.L. Rosner, G. Shaughnessy, C.E.M. Wagner, Forward-backward asymmetry of top quark pair production. *Phys. Rev. D* **81**, 114004 (2010). [arXiv:1003.3461](#)
8. J. Alwall, J.L. Feng, J. Kumar, S. Su, Dark matter-motivated searches for exotic 4th generation quarks in tevatron and early LHC data. *Phys. Rev. D* **81**, 114027 (2010). [arXiv:1002.3366](#)
9. T. Han, R. Mahbubani, D.G. Walker, L.-T. Wang, Top quark pair plus large missing energy at the LHC. *JHEP* **0905**, 117 (2009). [arXiv:0803.3820](#)
10. V. Barger, T. Han, D.G. Walker, Top quark pairs at high invariant mass: a model-independent discriminator of new physics at the LHC. *Phys. Rev. Lett.* **100**, 031801 (2008). [arXiv:hep-ph/0612016](#)

11. J. Andrea, B. Fuks, F. Maltoni, Monotops at the LHC. *Phys. Rev.* **D84**, 074025 (2011). [arXiv:1106.6199](#)
12. J.F. Kamenik, J. Zupan, Discovering dark matter through flavor violation at the LHC. *Phys. Rev.* **D84**, 111502 (2011). [arXiv:1107.0623](#)
13. Z. Dong, G. Durieux, J.-M. Gerard, T. Han, F. Maltoni, Baryon number violation at the LHC: the top option. *Phys. Rev.* **D85**, 016006 (2012). [arXiv:1107.3805](#)
14. R. Barbier, C. Berat, M. Besancon, M. Chemtob, A. Deandrea et al., R-parity violating supersymmetry. *Phys. Rept.* **420**, 1–202 (2005). [arXiv:hep-ph/0406039](#)
15. S.M. Barr, A new symmetry breaking pattern for SO(10) and proton decay. *Phys. Lett. B* **112**, 219 (1982)
16. I. Boucheneb, G. Cacciapaglia, A. Deandrea, B. Fuks, Revisiting monotop production at the LHC. *JHEP* **1501**, 017 (2015). [arXiv:1407.7529](#)
17. R. Allahverdi, M. Dalchenko, B. Dutta, Y. Gao, T. Kamon, Distinguishing standard model extensions using monotop chirality at the LHC. [arXiv:1507.02271](#)
18. A. Aktas et al., H1 Collaboration, Search for squark production in R parity violating supersymmetry at HERA. *Eur. Phys. J. C* **36**, 425–440 (2004). [arXiv:hep-ex/0403027](#)
19. S. Chekanov et al., ZEUS Collaboration, Search for stop production in R-parity-violating supersymmetry at HERA. *Eur. Phys. J. C* **50**, 269–281 (2007). [arXiv:hep-ex/0611018](#)
20. S. Chakrabarti, M. Guchait, N.K. Mondal, Constraining top squark in R parity violating SUSY model using existing Tevatron data. *Phys. Rev. D* **68**, 015005 (2003). [arXiv:hep-ph/0301248](#)
21. M. Ciuchini, V. Lubicz, L. Conti, A. Vladikas, A. Donini, et al., Delta M(K) and epsilon(K) in SUSY at the next-to-leading order. *JHEP* **9810**, 008 (1998). [arXiv:hep-ph/9808328](#). Erratum added online, Mar/29/2000
22. S. Herrlich, U. Nierste, Indirect CP violation in the neutral kaon system beyond leading logarithms. *Phys. Rev. D* **52**, 6505–6518 (1995). [arXiv:hep-ph/9507262](#)
23. A.J. Buras, Weak Hamiltonian, CP violation and rare decays. [arXiv:hep-ph/9806471](#)
24. A.J. Buras, M. Jamin, P.H. Weisz, Leading and next-to-leading QCD corrections to epsilon parameter and B0—anti-B0 mixing in the presence of a heavy top quark. *Nucl. Phys. B* **347**, 491–536 (1990)
25. S. Herrlich, U. Nierste, Enhancement of the K(L) – K(S) mass difference by short distance QCD corrections beyond leading logarithms. *Nucl. Phys. B* **419**, 292–322 (1994). [arXiv:hep-ph/9310311](#)
26. J. Urban, F. Krauss, U. Jentschura, G. Soff, Next-to-leading order QCD corrections for the B0 anti-B0 mixing with an extended Higgs sector. *Nucl. Phys. B* **523**, 40–58 (1998). [arXiv:hep-ph/9710245](#)
27. B. de Carlos, P.L. White, R-parity violation and quark flavour violation. *Phys. Rev. D* **55**, 4222–4239 (1997). [arXiv:hep-ph/9609443](#)
28. P. Slavich, Constraints on R-parity violating stop couplings from flavor physics. *Nucl. Phys. B* **595**, 33–43 (2001). [arXiv:hep-ph/0008270](#)
29. K. Nakamura et al., Particle Data Group Collaboration, Review of particle physics. *J. Phys. G* **G37**, 075021 (2010)
30. G. Bhattacharyya, D. Choudhury, K. Sridhar, New LEP bounds on B violating scalar couplings: R-parity violating supersymmetry or diquarks. *Phys. Lett. B* **355**, 193–198 (1995). [arXiv:hep-ph/9504314](#)
31. V. Khachatryan et al., CMS Collaboration, Search for dijet resonances in 7 TeV pp collisions at CMS. *Phys. Rev. Lett.* **105**, 211801 (2010). [arXiv:1010.0203](#)
32. G. Aad et al., ATLAS Collaboration, Search for New Particles in Two-Jet final states in 7 TeV Proton-Proton collisions with the ATLAS detector at the LHC. *Phys. Rev. Lett.* **105**, 161801 (2010). [arXiv:1008.2461](#)
33. G. Aad et al., ATLAS Collaboration, Search for new physics in dijet mass and angular distributions in pp collisions at $\sqrt{s} = 7$ TeV measured with the ATLAS detector. *New J. Phys.* **13** 053044 (2011). [arXiv:1103.3864](#)
34. S. Chatrchyan et al., CMS Collaboration, Search for resonances in the dijet mass spectrum from 7 TeV pp collisions at CMS. *Phys. Lett.* **B704**, 123–142 (2013). [arXiv:1107.4771](#)

35. G. Aad et al., ATLAS Collaboration, Search for new physics in the dijet mass distribution using 1 fb^{-1} TeV collected by the ATLAS detector. *Phys. Lett.* **B708**, 37–54 (2013). [arXiv:1108.6311](#)
36. V. Khachatryan et al., CMS Collaboration, Search for resonances and quantum black holes using dijet mass spectra in proton-proton collisions at $\sqrt{s} = 8 \text{ TeV}$. *Phys. Rev. D* **91**(5), 052009 (2015). [arXiv:1501.04198](#)
37. G. Aad et al., ATLAS Collaboration, Search for new phenomena in the dijet mass distribution using $p - p$ with the ATLAS detector. *Phys. Rev. D* **91**(5), 052007 (2015). [arXiv:1407.1376](#)
38. J. Alwall, M. Herquet, F. Maltoni, O. Mattelaer, T. Stelzer, MadGraph 5: going beyond. *JHEP* **06**, 128 (2011). [arXiv:1106.0522](#)
39. N.D. Christensen, C. Duhr, FeynRules—Feynman rules made easy. *Comput. Phys. Commun.* **180**, 1614–1641 (2009). [arXiv:0806.4194](#)
40. J. Pumplin et al., New generation of parton distributions with uncertainties from global QCD analysis. *JHEP* **07**, 012 (2002). [arXiv:hep-ph/0201195](#)
41. G. Belanger, F. Boudjema, A. Cottrant, A. Pukhov, S. Rosier-Lees, Lower limit on the neutralino mass in the general MSSM. *JHEP* **0403**, 012 (2004). [arXiv:hep-ph/0310037](#)
42. J. Wang, C.S. Li, D.Y. Shao, H. Zhang, Search for the signal of monotop production at the early LHC. *Phys. Rev. D* **86**, 034008 (2012). [arXiv:1109.5963](#)
43. G. Aad et al., ATLAS Collaboration, Search for displaced vertices arising from decays of new heavy particles in 7 TeV pp collisions at ATLAS. *Phys. Lett. B* **707**, 478–496 (2012). [arXiv:1109.2242](#)
44. M.L. Mangano, M. Moretti, F. Piccinini, R. Pittau, A.D. Polosa, ALPGEN, a generator for hard multiparton processes in hadronic collisions. *JHEP* **0307**, 001 (2003). [arXiv:hep-ph/0206293](#)
45. T. Sjostrand, S. Mrenna, P.Z. Skands, A. Brief, A brief introduction to PYTHIA 8.1. *Comput. Phys. Commun.* **178**, 852–867 (2008). [arXiv:0710.3820](#)
46. T. Sjostrand, S. Mrenna, P.Z. Skands, PYTHIA 6.4 physics and manual. *JHEP* **0605**, 026 (2006). [arXiv:hep-ph/0603175](#)
47. G. Aad et al., The ATLAS Collaboration, Expected performance of the ATLAS experiment—detector, trigger and physics. [arXiv:0901.0512](#)
48. G. Aad et al., ATLAS Collaboration, Search for invisible particles produced in association with single-top-quarks in proton-proton collisions at $\sqrt{s} = 8 \text{ TeV}$ with the ATLAS detector. *Eur. Phys. J. C* **75**(2), 79 (2015). [arXiv:1410.5404](#)
49. S. Chatrchyan et al., CMS Collaboration, Search for flavor-changing neutral currents in top-quark decays $t \rightarrow Zq$ TeV. *Phys. Rev. Lett.* **112**(17), 171802 (2014). [arXiv:1312.4194](#)
50. J.-L. Agram, J. Andrea, M. Buttignol, E. Conte, B. Fuks, Monotop phenomenology at the large hadron collider. *Phys. Rev. D* **89**(1), 014028 (2014). [arXiv:1311.6478](#)
51. V. Khachatryan et al., CMS Collaboration, Search for monotop signatures in Proton-Proton collisions at $\sqrt{s} = 8 \text{ TeV}$. *Phys. Rev. Lett.* **114**(10), 101801 (2015). [arXiv:1410.1149](#)

Chapter 7

Summary and Outlook

The desire to understand the fundamental constituents of the world and ourselves has led to the standard model (SM) of the particle physics today after a huge number of efforts of both theorists and experimentalists over several centuries. The theory has proven very beautiful and successful, which accurately describes three kinds of interactions, i.e., the electromagnet, weak, and strong interactions, in a unified way. The idea of symmetries, especially gauge symmetries, is the core of the theory, and has been reflected by a lot of predictions and confirmations of experiments, such as the discovery of the W^+ , W^- , and Z particles. The inner structure of protons or neutrons can be fortunately described by the perturbation-theory of QCD at high energy collisions. The problem of particles' masses is elegantly solved by the Higgs mechanism and the predicted Higgs boson has been finally found in 2012 at CERN after searched for about half a century. However, the model is very far from being the final theory; there are still many puzzles in our understanding.

The LHC has collected data with the integrated luminosity of about 20 fb^{-1} at the center-of-mass energy of 7 and 8 TeV, and started running with the collisions at 13 TeV, which explores a new region of energy scale. It provides opportunities to make a detailed study of the Higgs boson and search for new physics. In order to give more stable and precise predictions for the processes at the hadron collider, it is essential to consider the QCD high-order effects, including fixed order corrections and soft gluon resummations.

The existence of the dark matter is one of the strongest indications for physics beyond the standard model, because no known particle can be attributed to dark matter. Though the dark matter outnumbers the ordinary matter by a factor of about 4, the particles constituting the dark matter remain unclear so far. A lot of candidates of dark matter are predicted by many theories beyond the standard model with a largely unconstrained mass range from $\mathcal{O}(\text{GeV})$ to $\mathcal{O}(\text{TeV})$. It is of high priority to obtain the information and determine the quantum numbers of the dark matter. The way to achieve these aims includes direct detection, indirect detection, and collider experiments. They are complementary to each other and sensitive to different

parameter regions. The signal of dark matter at the LHC appears as missing energy associated with some visible particles. In this thesis, we investigate the dark matter and a photon-associated production at the LHC in the frame of effective operators, including the QCD NLO corrections. After comparing the signal and backgrounds, we find that the kinematic distributions of the photon can help to select the events in experiments. In the end, we present the region of new physics scale for a discovery or a exclusion at the LHC.

The top quark is the heaviest particle discovered so far and has a close relation with many extensions of the standard model. There are millions of top quarks produced every year at the LHC, providing a good place to study its properties. The single top quark production is sensitive to the electroweak interactions and related new physics. Therefore, it is necessary to consider the precision prediction for the kinematic distributions of the top quark. We have studied the renormalization group improved prediction for the transverse momentum spectrum at large p_T region with the soft-collinear effective theory. We discuss the factorization of the cross section into hard, jet and soft functions, and calculate the soft function in detail. The resummed cross section is increased by a few percent at the LHC, compared to the NLO result. This prediction can be used in searching for heavy bosons which decay into top quark and a jet.

The signal of monotop production has a very simple final state, which does not exist in the SM. It is easy to be identified and distinguished and thus has a potential to be discovered at the LHC. We study this signal induced by the general model-independent renormalizable operators with the SM gauge symmetries, though there are some models predicting it. After checking the constraints from the present experiment data, including the neutral meson mixing, Z boson decay, and dijet experiments, we simulate the signal and backgrounds in both hadronic and semileptonic decay modes at the LHC. The final discovery potential is presented as a function of the parameters in the operators. This signal has attracted the interest of the ATLAS and CMS collaborations and a lower limit on the mass of the invisible particle or an upper limit on the couplings of the operators have been set.

The topics studied above can be further extended. For example, given that the dark matter may couple with the SM particles in different structures, is it possible to find some observables to distinguish them? If there is a new gauge boson W' which could induce the single top production but have a different mass and coupling structure from the W boson, what is the most precise prediction for the kinematical distributions of the signal? For the current analysis in monotop productions, only LO predictions are used. What is the effect of QCD NLO corrections and soft gluon resummations? Besides, after the discovery of the Higgs boson, it is of significant importance to narrow the uncertainties of its couplings, which requires not only more accumulated data but also accurate theoretical predictions on various production channels. Last, to search and determine new physics with the LHC, the world's most powerful particle accelerator, the backgrounds should be precisely understood before any meaningful discovery.

Erratum to: Foundations of the Quantum Chromodynamics

Erratum to:
Chapter 2 in: J. Wang, *QCD Higher-Order Effects and Search for New Physics*, Springer Theses,
DOI [10.1007/978-3-662-48673-3_2](https://doi.org/10.1007/978-3-662-48673-3_2)

The original version of the book was inadvertently published with an incorrect Eq. 2.29 in chapter 2. The chapter and the book have been updated with the change.

The updated original online version for this chapter can be found
[10.1007/978-3-662-48673-3_2](https://doi.org/10.1007/978-3-662-48673-3_2)

J. Wang (✉)
Johannes Gutenberg University, Mainz, Germany
e-mail: jian.wang@uni-mainz.de

© Springer-Verlag Berlin Heidelberg 2016
J. Wang, *QCD Higher-Order Effects and Search for New Physics*,
Springer Theses, DOI [10.1007/978-3-662-48673-3_8](https://doi.org/10.1007/978-3-662-48673-3_8)

Appendix A

Phase Space Integration

The phase space in a collision is an indispensable component of the cross section. In practice, it causes a lot of complexities in the calculations. As a consequence, numerical integration is usually implemented. However, in some special phase spaces, the corresponding scattering amplitudes approach analytical poles, making the numerical results converge very slowly. Therefore, it is highly demanded that the numerical integration near the special phase spaces be optimized. In this Appendix, we present our method in performing the phase space integration in the dark matter and photon associated productions.

The general phase space is defined in Eq. (3.2). We begin with the two-body final state,

$$d\Phi_2 = \left(\prod_{f=3}^4 \frac{d^3 p_f}{2E_f (2\pi)^3} \right) (2\pi)^4 \delta^{(4)} \left(p_1 + p_2 - \sum_{f=3}^4 p_f \right). \quad (\text{A.1})$$

Because the phase space is Lorentz invariant, it is better to choose the center-of-mass frame of the final-state two particles. Then,

$$d\Phi_2 = \frac{1}{16\pi^2} \frac{|\vec{p}_3|}{\sqrt{s}} \sin \theta d\theta d\phi, \quad (\text{A.2})$$

where \sqrt{s} is the center-of-mass energy of the initial states, and \vec{p}_3 is the momentum of the first final-state particle. The polar angle and azimuthal angle are denoted by θ and ϕ , respectively. The length of \vec{p}_3 is given by

$$|\vec{p}_3| = \frac{\sqrt{s}}{2} \lambda^{1/2}(1, m_3^2/s, m_4^2/s), \quad (\text{A.3})$$

with

$$\lambda(a, b, c) \equiv a^2 + b^2 + c^2 - 2ab - 2bc - 2ca. \quad (\text{A.4})$$

The four-momenta p_3^μ and p_4^μ are determined by θ , ϕ , and s .

Then we discuss the three-body final state,

$$d\Phi_3 = \left(\prod_{f=3}^5 \frac{d^3 p_f}{2E_f (2\pi)^3} \right) (2\pi)^4 \delta^{(4)} \left(p_1 + p_2 - \sum_{f=3}^5 p_f \right). \quad (\text{A.5})$$

We consider that the phase space is factorized into two two-body phase spaces. First, the phase space is divided to be p_5 and $p_{34} \equiv p_3 + p_4$. Then the phase space of p_{34} is divided to be p_3 and p_4 . As a result, we have

$$d\Phi_3 = \frac{1}{2\pi} \int_{(m_3+m_4)^2}^{(\sqrt{s}-m_5)^2} ds_{34} d\Phi_2(s, m_5^2, s_{34}) d\Phi_2(s_{34}, m_3^2, m_4^2), \quad (\text{A.6})$$

where we have written the center-of-mass energy and two masses in two-body phase spaces explicitly. The four-momenta p_3^μ and p_4^μ are generated in the center-of-mass frame of p_{34} and should be boosted and rotated back to the center-of-mass frame of the initial states in which the four-momentum p_5^μ is generated.

This procedure of recursive division of phase space can be easily extended to the four-body final state. We would obtain

$$d\Phi_4 = \frac{1}{2\pi} \int_{(m_3+m_4+m_5)^2}^{(\sqrt{s}-m_6)^2} ds_{345} d\Phi_2(s, m_6^2, s_{345}) d\Phi_3(s_{345}, m_3^2, m_4^2, m_5^2). \quad (\text{A.7})$$

In our calculation of the real correction to the dark matter and photon associated productions,

$$q(p_1) + \bar{q}(p_2) \rightarrow \chi(p_3) + \bar{\chi}(p_4) + \gamma(p_5) + g(p_6), \quad (\text{A.8})$$

the amplitude becomes divergent in the phase space with $t_{16} \equiv (p_1 - p_6)^2 \rightarrow 0$ or $t_{26} \equiv (p_2 - p_6)^2 \rightarrow 0$. In practice, we have used two cutoff phase space slicing methods to separate the divergent regions with $|t_{16}| < \delta_c s$ and $|t_{26}| < \delta_c s$, which can be integrated analytically. The remaining parts of phase space integration would generate the terms like $\ln^2 \delta_c$ which are numerically large since $\delta_c \sim 10^{-5}$. To get more stable numerical result, we must separate such terms out of the phase space integration.

Let us define $s_{345}^{\min} = (m_3 + m_4 + m_5)^2$ and

$$t_{16} = (s_{345}^{\min} - s) \left(\frac{\delta_c s}{s - s_{345}^{\min}} \right)^{u_1}, \quad u_1 \in [0, 1], \quad (\text{A.9})$$

$$t_{26} = (s_{345}^{\min} - s) \left(\frac{\delta_c s}{s - s_{345}^{\min}} \right)^{u_2}, \quad u_2 \in [0, 1]. \quad (\text{A.10})$$

Then we obtain

$$ds_{345}d\Phi_2(s, 0, s_{345}) = \frac{t_{16}t_{26}}{16\pi^2s} \ln^2 \frac{\delta_c s}{s - s_{345}^{\min}} \Theta[t_{16} + t_{26} + s - s_{345}^{\min}] \Theta[-\delta_s s - t_{16} - t_{26}] du_1 du_2 d\phi, \quad (\text{A.11})$$

where the Θ functions are inserted to ensure that the integration does not include the soft regions that have been integrated analytically. We have checked that numerical convergence can be greatly improved after applying the above method.

Appendix B

Calculation of the Soft Functions

In this Appendix, we present the details of the calculation of the two $\mathcal{O}(\alpha_s)$ soft functions $S_{bt}^{(1)}(k, \mu)$ and $S_{tt}^{(1)}(k, \mu)$ that appear in Chap. 5. We choose to perform the calculation in the rest frame of the top quark, in which the four-velocity of the top quark is $v^\mu = (1, 0, 0, 0)$. In this frame, the denominators are simple but the content of the delta function is complex. We have also carried out the calculation in the frame where the content of the delta function is simple but the singularities in the denominators are hard to isolate, using the method in Ref. [1]. We obtain the same results, which can be considered as a cross-check of our calculations.

In the rest frame of the top quark, we choose the direction $n_b^\mu = (1, 0, 0, 1)$. Then, we have

$$q^\mu = q^+ \frac{\bar{n}_b^\mu}{n_{b\bar{b}}} + q^- \frac{n_b^\mu}{n_{b\bar{b}}} + q_\perp^\mu, \quad n_1^\mu = n_1^+ \frac{\bar{n}_b^\mu}{n_{b\bar{b}}} + n_1^- \frac{n_b^\mu}{n_{b\bar{b}}} + n_{1\perp}^\mu, \quad (\text{B.1})$$

and

$$q \cdot n_1 = \frac{q^+ n_1^- + q^- n_1^+}{n_{b\bar{b}}} - |q_\perp| |n_{1\perp}| \cos \theta, \quad q \cdot v = q \cdot \frac{(n_b + n_{\bar{b}})}{2} = \frac{(q^+ + q^-)}{2}. \quad (\text{B.2})$$

Inserting these expressions into Eq. (5.56), we get

$$S_{bt}^{(1)}(k, \mu) = \frac{g_s^2 C_F \mu^{2\epsilon}}{(2\pi)^{d-1}} \int_0^\infty dq^+ \int_0^\infty dq^- \int d\Omega_{d-2} \left(\frac{2q^+ q^-}{n_{b\bar{b}}} \right)^{-\epsilon} \delta\left(k - \frac{q^+ n_1^- + q^- n_1^+}{n_{b\bar{b}}} + |q_\perp| |n_{1\perp}| \cos \theta\right) \frac{n_b \cdot v}{q^+(q^+ + q^-)}. \quad (\text{B.3})$$

Let us redefine the integration variables q^+ and q^- and take $a = \frac{n_1^+}{n_1^-}$, then

$$S_{bt}^{(1)}(k, \mu) = \frac{g_s^2 C_F \mu^{2\epsilon}}{(2\pi)^{d-1}} \int_0^\infty dq^+ \int_0^\infty dq^- \int d\Omega_{d-2} \left(\frac{2n_{b\bar{b}}}{n_1^+ n_1^-} \right)^{-\epsilon} \delta(k - q^+ - q^- + 2\sqrt{q^+ q^-} \cos \theta) \frac{n_b \cdot v}{q^+(aq^+ + q^-)}. \quad (\text{B.4})$$

Introducing other two variables x and y satisfying $q^+ = kyx$ and $q^- = ky(1-x) = ky\bar{x}$, we obtain

$$S_{bt}^{(1)}(k, \mu) = \frac{g_s^2 C_F \mu^{2\epsilon}}{(2\pi)^{d-1}} \left(\frac{2n_{b\bar{b}}}{n_1^+ n_1^-} \right)^{-\epsilon} k^{-1-2\epsilon} \int d\Omega_{d-2} \int_0^1 dx x^{-1-\epsilon} \frac{(1-2\sqrt{x\bar{x}} \cos \theta)^{2\epsilon} \bar{x}^{-\epsilon}}{ax + \bar{x}}. \quad (\text{B.5})$$

The singularity in the integrand can be isolated by

$$x^{-1-\epsilon} = -\frac{1}{\epsilon} \delta(x) + \left(\frac{1}{x} \right)_+ - \epsilon \left(\frac{\ln x}{x} \right)_+ + \mathcal{O}(\epsilon^2). \quad (\text{B.6})$$

It is straight to calculate the above three parts separately. After making use of

$$\frac{1}{k^+} \left(\frac{\tilde{\mu}}{k^+} \right)^{2\epsilon} = -\frac{1}{2\epsilon} \delta(k^+) + \left[\frac{1}{k^+} \right]_\star^{[k^+, \tilde{\mu}]} - 2\epsilon \left[\frac{1}{k^+} \ln \frac{k^+}{\tilde{\mu}} \right]_\star^{[k^+, \tilde{\mu}]} + \mathcal{O}(\epsilon^2), \quad (\text{B.7})$$

we get the divergent and finite parts

$$S_{bt,div}^{(1)}(k, \mu) = \frac{2C_F \alpha_s (4\pi \mu^2 e^{-\gamma_E})^\epsilon}{4\pi} \left\{ \frac{\delta(k)}{\epsilon^2} - \frac{2}{\epsilon} \left[\frac{1}{k} \right]_\star^{[k, \tilde{\mu}]} \right\}, \quad (\text{B.8})$$

$$S_{bt,fin}^{(1)}(k, \mu) = \frac{2C_F \alpha_s}{4\pi} \left\{ 4 \left[\frac{\ln \frac{k}{\tilde{\mu}}}{k} \right]_\star^{[k, \tilde{\mu}]} + \delta(k) c_{bt}^S \right\}, \quad (\text{B.9})$$

with $c_{bt}^S = -\ln^2(1 + \frac{1}{a}) - 2\text{Li}_2(\frac{1}{1+a}) + \frac{\pi^2}{12}$.

With the same method, we get

$$S_{tt,div}^{(1)}(k, \mu) = \frac{2C_F \alpha_s (4\pi \mu^2 e^{-\gamma_E})^\epsilon}{4\pi} \left\{ \frac{\delta(k)}{\epsilon} \right\}, \quad (\text{B.10})$$

$$S_{tt,fin}^{(1)}(k, \mu) = \frac{2C_F \alpha_s}{4\pi} \left\{ - \left[\frac{2}{k} \right]_\star^{[k, \tilde{\mu}]} + \delta(k) c_{tt}^S \right\}, \quad (\text{B.11})$$

with $c_{tt}^S = 2\ln(1 + \frac{1}{a})$.

When performing the Laplace transformation from $S(k, \mu)$ to $\tilde{S}(L, \mu)$, the following replacements prove useful:

$$\left[\frac{\ln \frac{k}{\mu}}{k} \right]_{\star}^{[k, \mu]} \rightarrow \frac{L^2}{2} + \frac{\pi^2}{12}, \quad (\text{B.12})$$

$$\left[\frac{1}{k} \right]_{\star}^{[k, \mu]} \rightarrow L. \quad (\text{B.13})$$

Appendix C

Anomalous Dimensions

The various anomalous dimensions needed in our calculations are available, e.g., in Refs. [2–4]. We show them below for the convenience of the reader. The QCD β function is expanded as

$$\beta(\alpha_s) = -2\alpha_s \left[\beta_0 \frac{\alpha_s}{4\pi} + \beta_1 \left(\frac{\alpha_s}{4\pi} \right)^2 + \dots \right], \quad (\text{C.1})$$

with expansion coefficients

$$\begin{aligned} \beta_0 &= \frac{11}{3}C_A - \frac{4}{3}T_F n_f, \\ \beta_1 &= \frac{34}{3}C_A^2 - \frac{20}{3}C_A T_F n_f - 4C_F T_F n_f, \\ \beta_2 &= \frac{2857}{54}C_A^3 + \left(2C_F^2 - \frac{205}{9}C_F C_A - \frac{1415}{27}C_A^2 \right) T_F n_f + \left(\frac{44}{9}C_F + \frac{158}{27}C_A \right) T_F^2 n_f^2, \end{aligned} \quad (\text{C.2})$$

where $C_A = 3$, $C_F = 4/3$, $T_F = 1/2$ for QCD, and n_f is the number of active quark flavors.

The cusp anomalous dimension is given as

$$\Gamma_{\text{cusp}}(\alpha_s) = \Gamma_0 \frac{\alpha_s}{4\pi} + \Gamma_1 \left(\frac{\alpha_s}{4\pi} \right)^2 + \dots, \quad (\text{C.3})$$

with

$$\begin{aligned} \Gamma_0 &= 4C_F, \\ \Gamma_1 &= 4C_F \left[\left(\frac{67}{9} - \frac{\pi^2}{3} \right) C_A - \frac{20}{9} T_F n_f \right], \end{aligned}$$

$$\Gamma_2 = 4C_F \left[C_A^2 \left(\frac{245}{6} - \frac{134}{27}\pi^2 + \frac{11}{45}\pi^4 + \frac{22}{3}\zeta_3 \right) + C_A T_{Fnf} \left(-\frac{418}{27} + \frac{40}{27}\pi^2 - \frac{56}{3}\zeta_3 \right) + C_F T_{Fnf} \left(-\frac{55}{3} + 16\zeta_3 \right) - \frac{16}{27} T_F^2 n_f^2 \right]. \quad (\text{C.4})$$

The other anomalous dimensions are expanded as Eq. (C.3), and the expansion coefficients are

$$\begin{aligned} \gamma_q^0 &= -3C_F, \\ \gamma_q^1 &= C_F^2 \left(-\frac{3}{2} + 2\pi^2 - 24\zeta_3 \right) + C_F C_A \left(-\frac{961}{54} - \frac{11}{6}\pi^2 + 26\zeta_3 \right) \\ &\quad + C_F T_{Fnf} \left(\frac{130}{27} + \frac{2}{3}\pi^2 \right), \\ \gamma_Q^0 &= -2C_F, \\ \gamma_Q^1 &= C_F C_A \left(\frac{2}{3}\pi^2 - \frac{98}{9} - 4\zeta_3 \right) + \frac{40}{9} C_F T_{Fnf}, \\ \gamma_\phi^0 &= 3C_F, \\ \gamma_\phi^1 &= C_F^2 \left(\frac{3}{2} - 2\pi^2 + 24\zeta_3 \right) + C_F C_A \left(\frac{17}{6} + \frac{22}{9}\pi^2 - 12\zeta_3 \right) - C_F T_{Fnf} \left(\frac{2}{3} + \frac{8}{9}\pi^2 \right), \\ \gamma_j^0 &= -3C_F, \\ \gamma_j^1 &= C_F^2 \left(-\frac{3}{2} + 2\pi^2 - 24\zeta_3 \right) + C_F C_A \left(-\frac{1769}{54} - \frac{11}{9}\pi^2 + 40\zeta_3 \right) \\ &\quad + C_F T_{Fnf} \left(\frac{242}{27} + \frac{4}{9}\pi^2 \right). \end{aligned} \quad (\text{C.5})$$

In the single top production, γ_{up}^V , γ_{dn}^V and γ^S can be obtained from the above anomalous dimensions by the following equations:

$$\begin{aligned} \gamma_{up}^V &= 2\gamma_q, \\ \gamma_{dn}^V &= \gamma_q + \gamma_Q, \\ \gamma^S &= -\gamma_\phi - \gamma_{dn}^V. \end{aligned} \quad (\text{C.6})$$

References

1. R. Kelley, M.D. Schwartz, Threshold hadronic event shapes with effective field theory. Phys. Rev. D **83**, 033001 (2011). [arXiv:1008.4355](#)
2. T. Becher, M. Neubert, B.D. Pecjak, Factorization and momentum-space resummation in deep-inelastic scattering. JHEP **01**, 076 (2007). [arXiv:hep-ph/0607228](#)
3. T. Becher, M. Neubert, G. Xu, Dynamical threshold enhancement and resummation in Drell-Yan Production. JHEP **07**, 030 (2008). [arXiv:0710.0680](#)
4. T. Becher, M.D. Schwartz, Direct photon production with effective field theory. JHEP **02**, 040 (2010). [arXiv:0911.0681](#)